## General Disclaimer

## One or more of the Following Statements may affect this Document

- This document has been reproduced from the best copy furnished by the organizational source. It is being released in the interest of making available as much information as possible.

- This document may contain data, which exceeds the sheet parameters. It was furnished in this condition by the organizational source and is the best copy available.

- This document may contain tone-on-tone or color graphs, charts and/or pictures, which have been reproduced in black and white.

- This document is paginated as submitted by the original source.

- Portions of this document are not fully legible due to the historical nature of some of the material. However, it is the best reproduction available from the original submission.

# FINAL REPORT

# STRAPDOWN MINIATURE ELECTROSTATIC GYRO (SDMEG) DEVELOPMENT AND EVALUATION

John C. Wacker

March 1969

JPL Contract No. 951149
(Subcontract under NASA Contract NAS 7-100)

"This work was performed for the Jet Propulsion Laboratory, California Institute of Technology, sponsored by the National Aeronautics and Space Administration under Contract NAS 7-100."



Honeywell Inc.
Aerospace Division
Minneapolis, Minnesota

FINAL REPORT

# STRAPDOWN MINIATURE ELECTROSTATIC GYRO (SDMEG) DEVELOPMENT AND EVALUATION

John C. Wacker

March 1969

JPL Contract No. 951149
(Subcontract under NASA Contract NAS 7-100)

NOTICE

This report was prepared as an account of Government-sponsored work. Neither the United States, nor the National Aeronautics and Space Administration (NASA), nor any person acting on behalf of NASA:

a. Makes warranty or representation, expressed or implied, with respect to the accuracy, completeness, or usefulness of the information contained in this report, or that the use of any information, apparatus, method, or process disclosed in this report may not infringe privately-owned rights; or

b. Assumes any liabilities with respect to the use of, or for damages resulting from the use of any information, apparatus, method, or process disclosed in this report.

As used above, "person acting on behalf of NASA" includes any employee or contractor of NASA, or employee of such contractor, to the extent that such employees or contractor of NASA, or employee of such contractor prepares, disseminates, or provides access to, any information pursuant to his employment with such contractor.

Requests for copies of this report should be referred to:

National Aeronautics and Space Administration
Office of Scientific and Technical Information
Washington 25, D.C.

Attention AFSS A

## FOREWORD

This development and evaluation study was conducted as part of the Jet Propulsion Laboratory Contract No. 951149 (Subcontract under NASA Contract NAS 7-100). Mr. Tom Donlin of the Jet Propulsion Laboratory was the Project Monitor. The work was conducted during the period 1 June 1965 through 28 March 1969. This report consists of this volume and a classified attachment.

This report was prepared by the Inertial Components Group of the Aerospace Division, Honeywell Inc., 2600 Ridgway Road, Minneapolis, Minnesota 55413.

The document number assigned to this report by the Honeywell Aerospace Division is 20302-FR.

TABLE OF CONTENTS

TABLES OF CONTENTS -- CONTINUED

## LIST OF ILLUSTRATIONS

LIST OF ILLUSTRATIONS -- CONTINUED

LIST OF ILLUSTRATIONS -- CONTINUED

LIST OF ILLUSTRATIONS -- CONCLUDED

## LIST OF TABLES

# SECTION I
# INTRODUCTION

A study program was initiated in June, 1963 to determine the feasibility of implementing a strapdown electrically suspended gyro in an attitude reference system for a spacecraft. Under the sponsorship of JPL Contract No. 950607, the concept of the SDMEG was developed. It featured a suspension system capable of low-power operation in a low-g environment and an approach toward automatically starting the gyro in space. New technological advances were employed to successfully miniaturize some of the critical subsystems of the gyro.

In June, 1965 an evaluation program of the SDMEG began under sponsorship of JPL Contract 951149. Major tasks of the contract included:

- Building a complete gyro assembly for the evaluation program
- Developing and building the equipment needed to conduct the SDMEG evaluation tests
- Coding and checking out a software system of drift test data reduction programs for the SDMEG
- Conducting tests to demonstrate the performance potential of the SDMEG

Concurrent with this program, JPL Contract No. 951148 sponsored a program to build and test a second model of the SDMEG.

The evaluation program was designed to test the capability of the gyro to be started and operated as an inertial component of a spacecraft attitude reference system after the craft has been separated from the launch vehicle. The starting tests included the simulation of vehicle angular motion. Other environmental tests included operating temperature range tests and acceleration capability tests. They showed the SDMEG to be capable of starting under automatic control, of operating in moderate temperature ranges, and of maintaining suspension in expected space acceleration environments, even in a low-power mode of suspension operation.

Other major accomplishments include:

- Development of techniques for calibrating critical readout parameters

- Development of a theoretical torque model which predicts the drift behavior of the SDMEG
- Development of a technique for calibrating the coefficients of the torque model from test data

These developments were helpful in evaluating the nature of the torque model and verifying from test data the drift behavior of the gyro as predicted by the ESG torque theory.

The results of these tests indicate a need for further improvements in readout accuracy and further refinement of readout parameter calibration techniques. Such improvements, when followed by additional studies of the drift characteristics of the gyro, can lead to further improvement in predicting the drift behavior of the gyro. The existing SDMEG hardware and test data can usefully serve as vehicles for further study in these fields.

New developments in ESG technology offer the promise of further reductions of size, weight, and power consumption which now characterize the SDMEG. Such developments can be implemented in flight test versions of the SDMEG.

# SECTION II
# GYRO ASSEMBLY AND DEVELOPMENT

## INTRODUCTION

During the feasibility study program conducted under JPL Contract 950607, new concepts were developed and tested at the piece part and subassembly level. Such items as a rotor, housing parts, optical pickoffs, and electronic circuits were built and thoroughly tested during that program.

For this development and evaluation program, additional components to produce a fully operating gyro were added. Some modifications were made to the existing gyro hardware where the results of the feasibility study program indicated that modifications would be beneficial to gyro performance. The added components and the modifications are briefly described in this section.

Improvements were made to the gyro suspension by converting it to the type using separate sensing frequencies. The suspension in its present form is described in this section. Current schematics are included.

## FABRICATION AND MODIFICATION OF SDMEG COMPONENTS

During the feasibility study program conducted in 1963 and 1964, a number of SDMEG piece parts were built so that the new concepts could be tested with hardware. These piece parts, however, did not comprise a complete gyro assembly. Under the present contract, the additional components needed to complete the assembly were built. At the same time, design modifications were made according to the findings of the feasibility study program.

### Pickoffs

Two pickoffs were built and tested in the feasibility study program. A third pickoff was assembled to provide a complete set for the gyro.

Early in the program, tests were conducted to determine a means of reducing the noise output of the optical pickoffs caused by pickup from the support electrodes. The tests showed that a metal shield around the pickoff sensor reduced the total noise from 1 volt to 50 millivolts peak-to-peak, and the pickoff design was modified to incorporate this shield. In its present form, the shield also serves as a field stop by making the opening in front of the

sensor the correct size. The field stop formerly located in front of the light source was enlarged to serve as a scatter stop.

A significant improvement in signal level was accomplished in 1966 by replacing the RCA sensors with Fairchild FPM200 units. Later in the program, some difficulties were encountered in locating the optical axis of some pickoffs in line with the object lens (which also served as the window of the housing). To correct the problem, the pickoffs were modified in 1967 so that the optical axis could be adjusted concentric with the center of the cylindrical housing of the pickoff.

Spin and Damping Coils

New spin and damping coils were built with 25 percent more turns than those which were built during the feasibility study program. These changes were designed to provide greater damping power and to increase the spin rate to 20 rps per minute.

Ion Pump

To sever the gyro from the large vacuum system used in the feasibility study, an ion pump was built. The ion pump is similar to units used in other ESG designs.

Alignment Mirrors

Two alignment mirrors were added to the gyro for alignment reference purposes. These mirrors, clamped to the electrode assembly, are located directly opposite two of the three optical pickoffs. The mirror normals, nominally at right angles to each other, define a case-fixed reference coordinate system from which pickoff alignment parameters are defined.

Gyro Frame

The aluminum gyro frame was modified to accommodate the larger spin coils. Other modifications included provisions for mounting the ion pump and for clamping the alignment mirrors to the gyro housing.

Rotors

A second rotor was fabricated as a backup to the rotor built under the feasibility study program. Both rotors were identical and were built to the following design parameters:

- Outside Diameter — 1.9970 inches
- Polar Wall Thickness — 0.030 inch
- Equatorial Wall Thickness — 0.065 inch
- Mass — 20 gm
- Moment of Inertia — 90 gm $cm^2$

At one point in the development and evaluation program, a buildup of surface blemishes necessitated rotor rework. A drift performance test in 1966 showed that electric torques were larger than predicted during the feasibility study. To reduce their effect, the rotors were prolated slightly during the last rework so that they would distort to a spherical shape near an operating speed of 200 rps.

The pattern originally applied to the rotors is of the cosine type illustrated in Figure 1. The figure consists of a cosine pattern line, a meridional reference line, and a wider meridional logic line to identify the other lines in the readout logic.

After the last rework, the pattern was changed to the double cosine type shown in Figure 2. A pattern optimization study conducted under Air Force sponsorship had shown this pattern to be insensitive to errors which are a function of pattern line slope. Since the pattern was already designed and an application master was available after the rework, no inconvenience, delay, or extra expense was encountered in adopting this pattern for the JPL program.

## Terminal Boards and Connectors

Terminal boards and connectors were added to the gyro assembly to facilitate connection to the control console and suspension electronics subassembly. Two miniature connectors are used -- one carrying output signals and the other input power.

The high-voltage leads consist of individually shielded cables running from the electronics subassembly to the electrode pins brazed into the ceramic envelope. These cables are flexed and twisted in the performance of readout system calibration tests. One gyro failure was attributed to a fatigued high-voltage lead which was probably produced by the flexing.

To avoid a recurrence of this type of failure, the envelope end of the high-voltage leads was redesigned. Until then, the cable had no means of strain relief to support the conductor where it is soldered onto the terminal insert. The new design provided for strain relief at the terminal insert connection point.

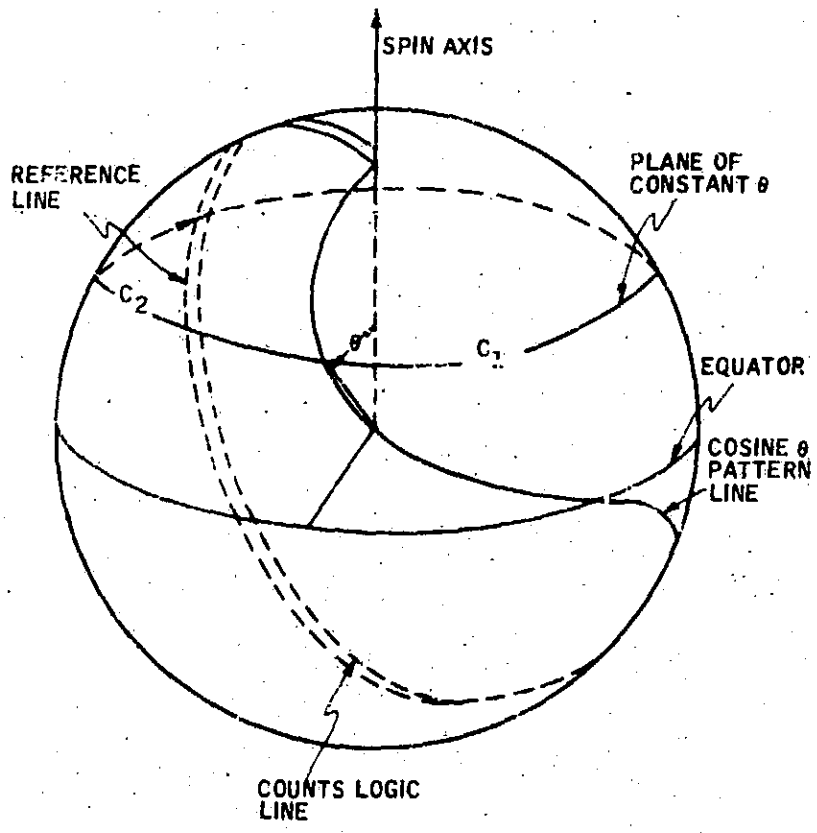


Figure 1. SDMEG Cosine Pattern

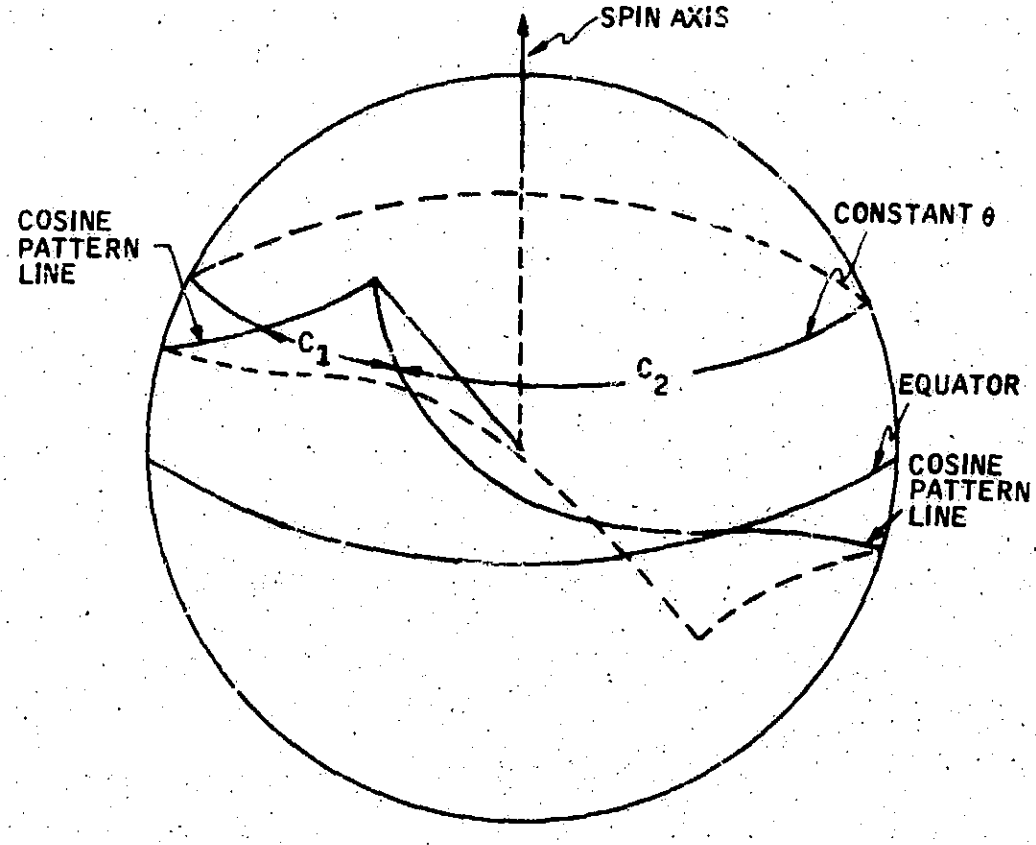


Figure 2. Double Cosine Pattern

Magnetic Shield Covers

To complete the mechanical subassembly, covers which served as a magnetic shield for the gyro were designed and built. Access ports were located in optimum locations for feeding through the high-voltage leads and the connectors and for viewing the reference mirrors mounted on the gyro housing.

## GYRO SUBASSEMBLY

Figure 3 is a view of the gyro subassembly with the pickoffs removed. The X-axis pickoff window is visible between two of the four spin coils. At the top is the ion pump used to maintain the vacuum inside the envelope. In Figure 4 the opposite end of the subassembly is shown. Located between the two terminal connectors is the damping coil mounting plate which also serves as a coil heat sink. The damping coil is recessed into the frame and envelope to achieve maximum proximity with the rotor.

Shown in Figure 5 is the gyro subassembly mounted in the test fixture. The X-axis pickoff is shown mounted in place. The high-voltage leads to the electrode pins are also connected. Figure 6 shows another view of the mounted gyro subassembly. The X-axis mirror is shown mounted in place between two spin coils.

Figure 7 shows the SDMEG with the magnetic shield covers in place. The gyro is shown here mounted for acceleration tests on the centrifuge.

Under JPL Contract 951148, a second complete gyro subassembly was built for acceptance testing and delivery to JPL. A spare rotor was also fabricated as a backup to this gyro. A spare set of envelope parts was also built as a backup to the two gyros produced under the contracts.

## ELECTRONICS SUBASSEMBLY

The electronics subassembly consists of the suspension and the height-insensitive trigger (HIT) for each of the pickoff signals. The suspension and the HIT are housed in a slope-faced cabinet with a volume of approximately 1700 cubic inches.

The construction of the electronics is of the plug-in card type to allow maximum flexibility for checkout and any necessary adjustments and circuit modifications. Figure 8 shows the subassembly cabinet with five of the suspension cards displayed in front. The blank card is one of several copper cards which are inserted between circuit cards for shielding.

At the end of the feasibility study program, the suspension occupied nine cards. Mounted physically to the cabinet chassis were the output transformers, power

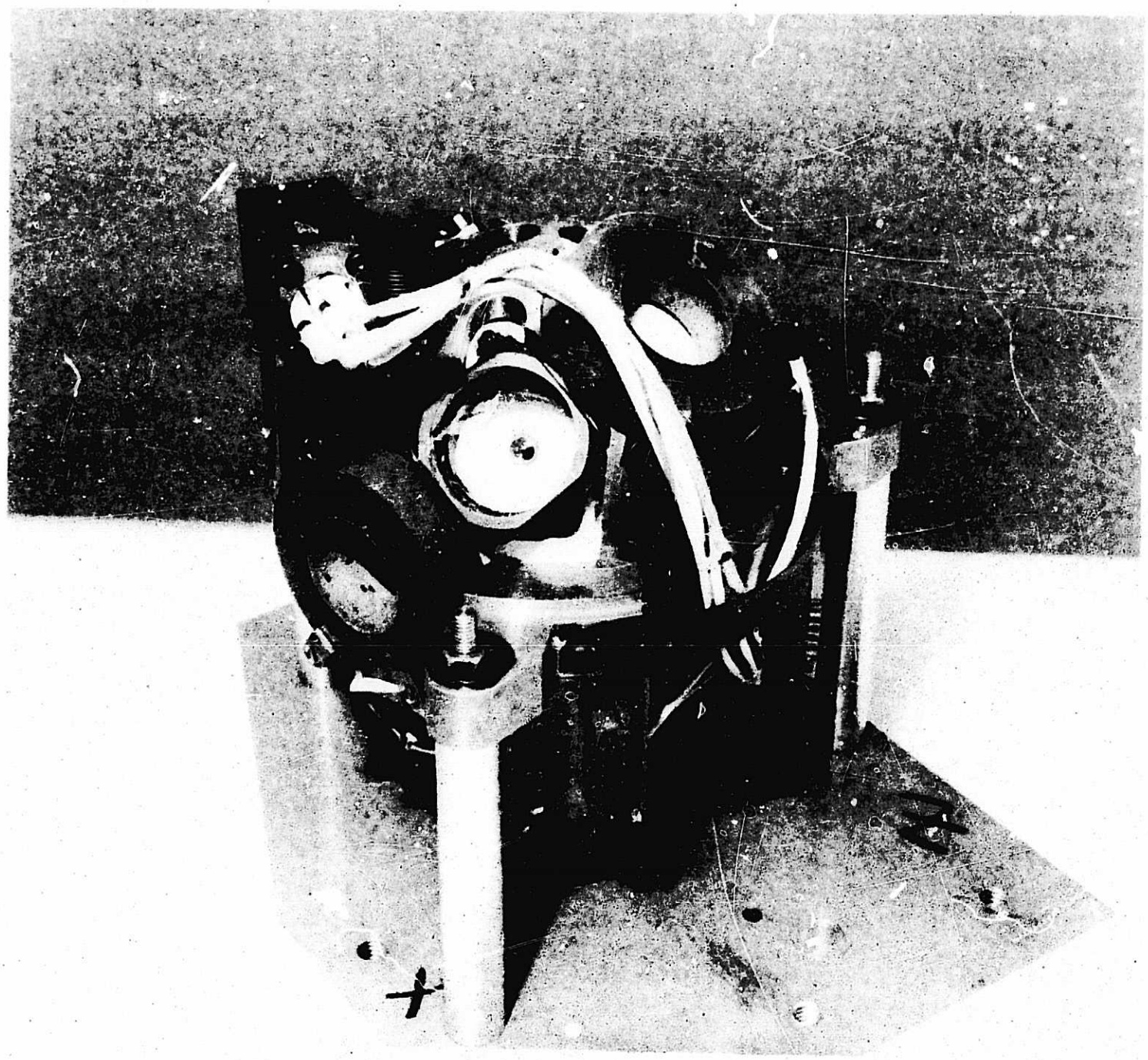

Figure 3. Top View of SDMEG Housing Assembly

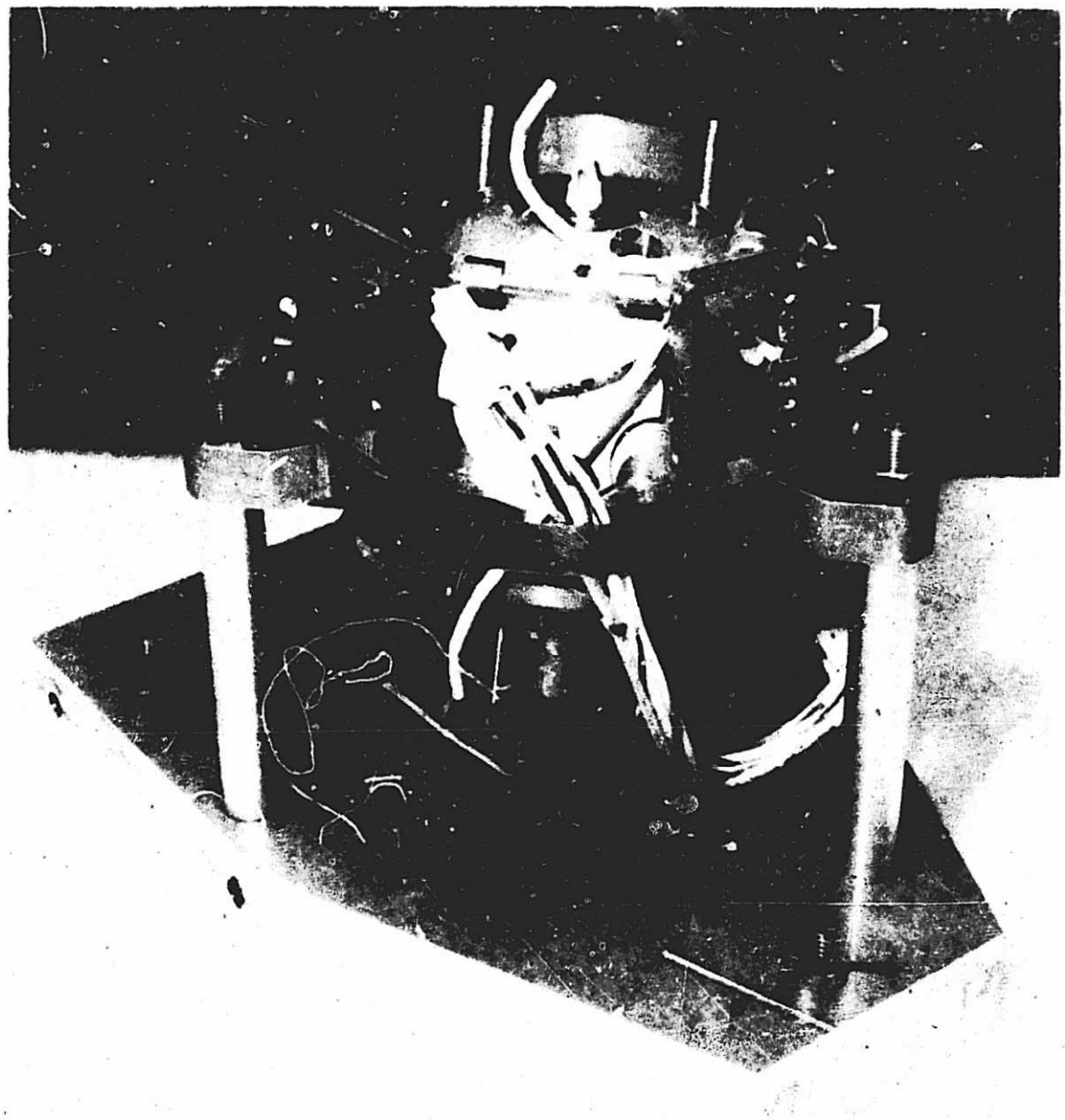

Figure 4. Bottom View of SDMEG Housing Assembly

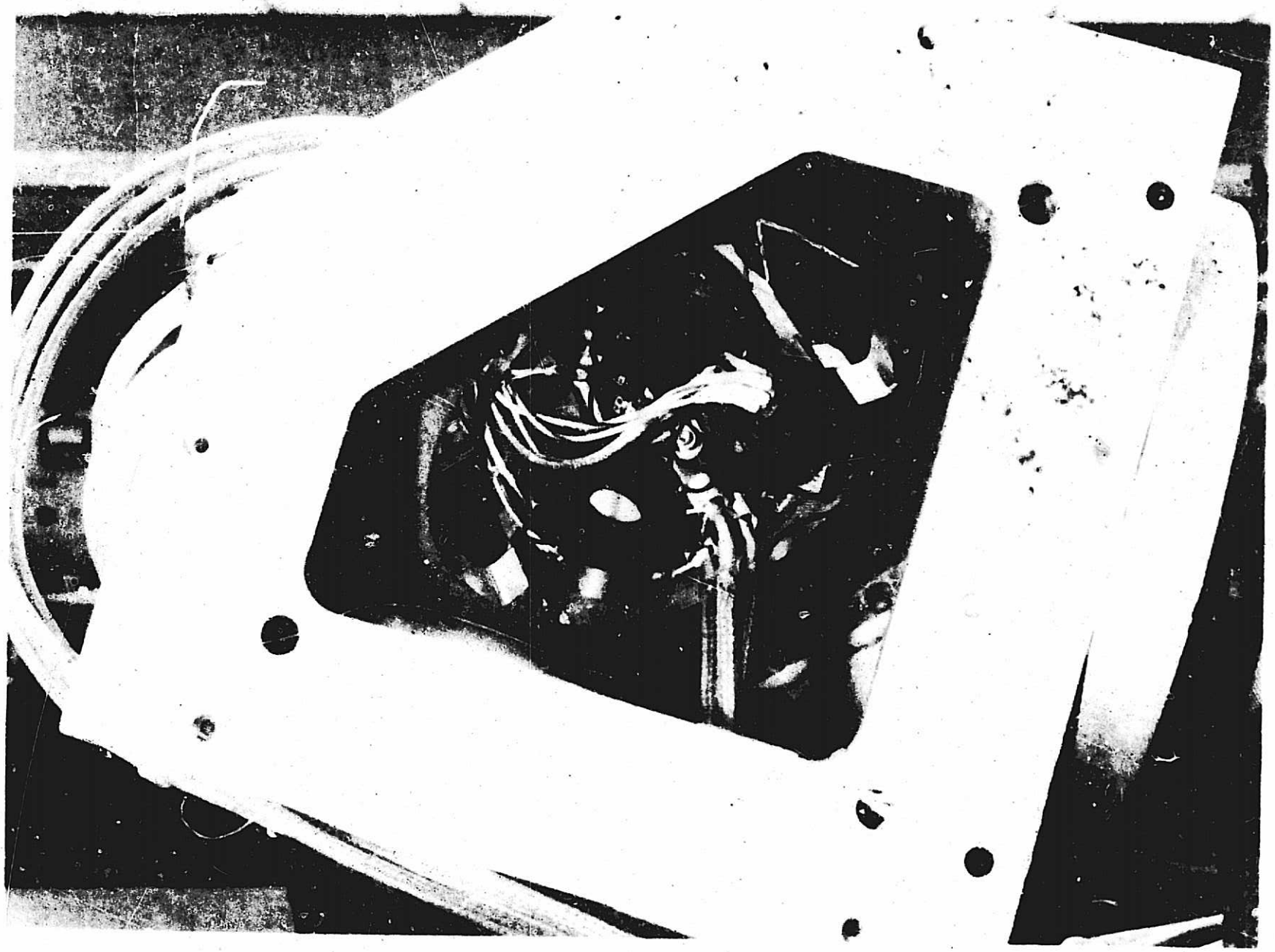

Figure 5. Top View, Gyro Subassembly in Test Fixture

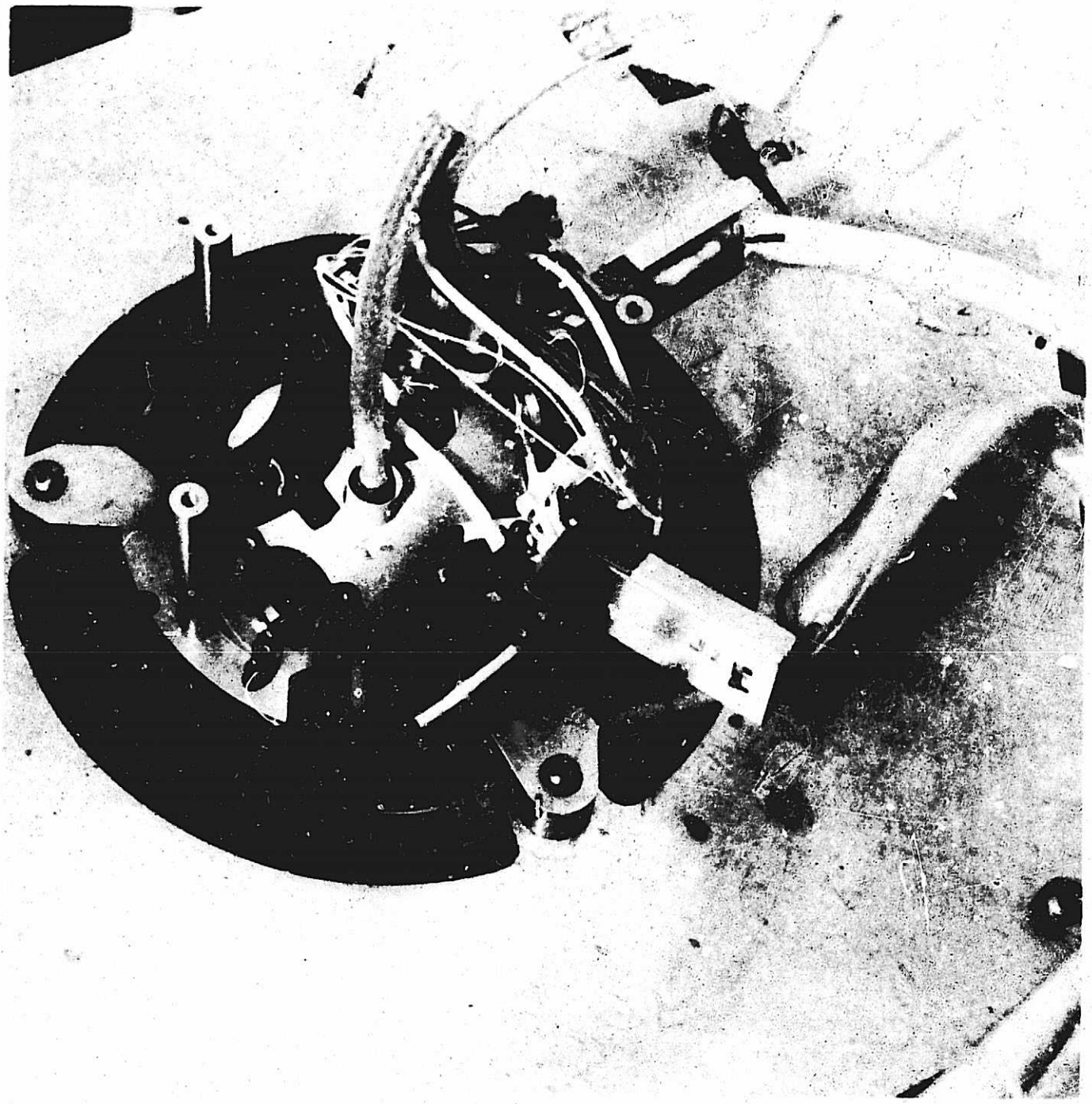

Figure 6. Bottom View, Gyro Subassembly in Test Fixture

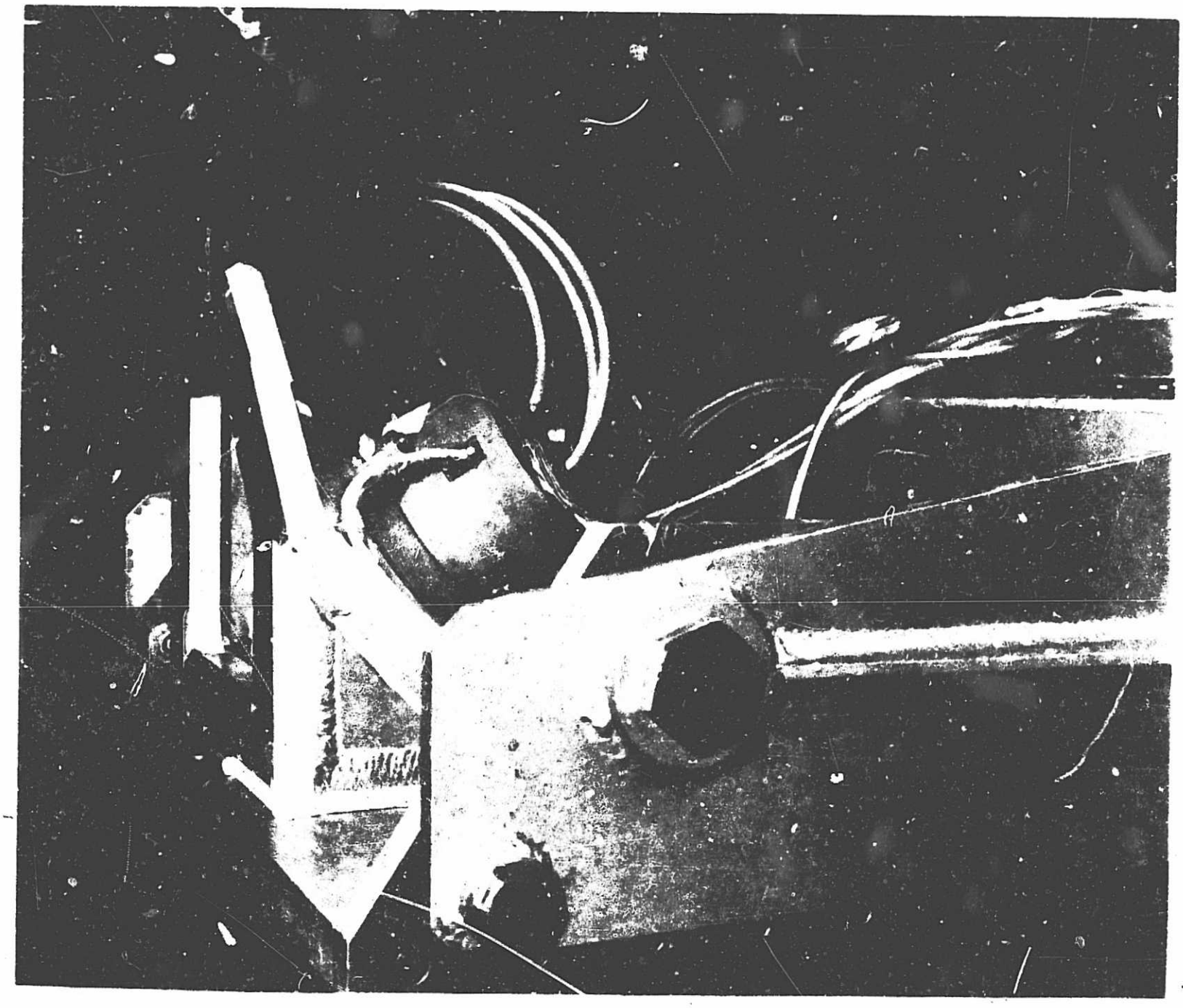

Figure 7. SDMEG Gyro Subassembly with Covers Mounted

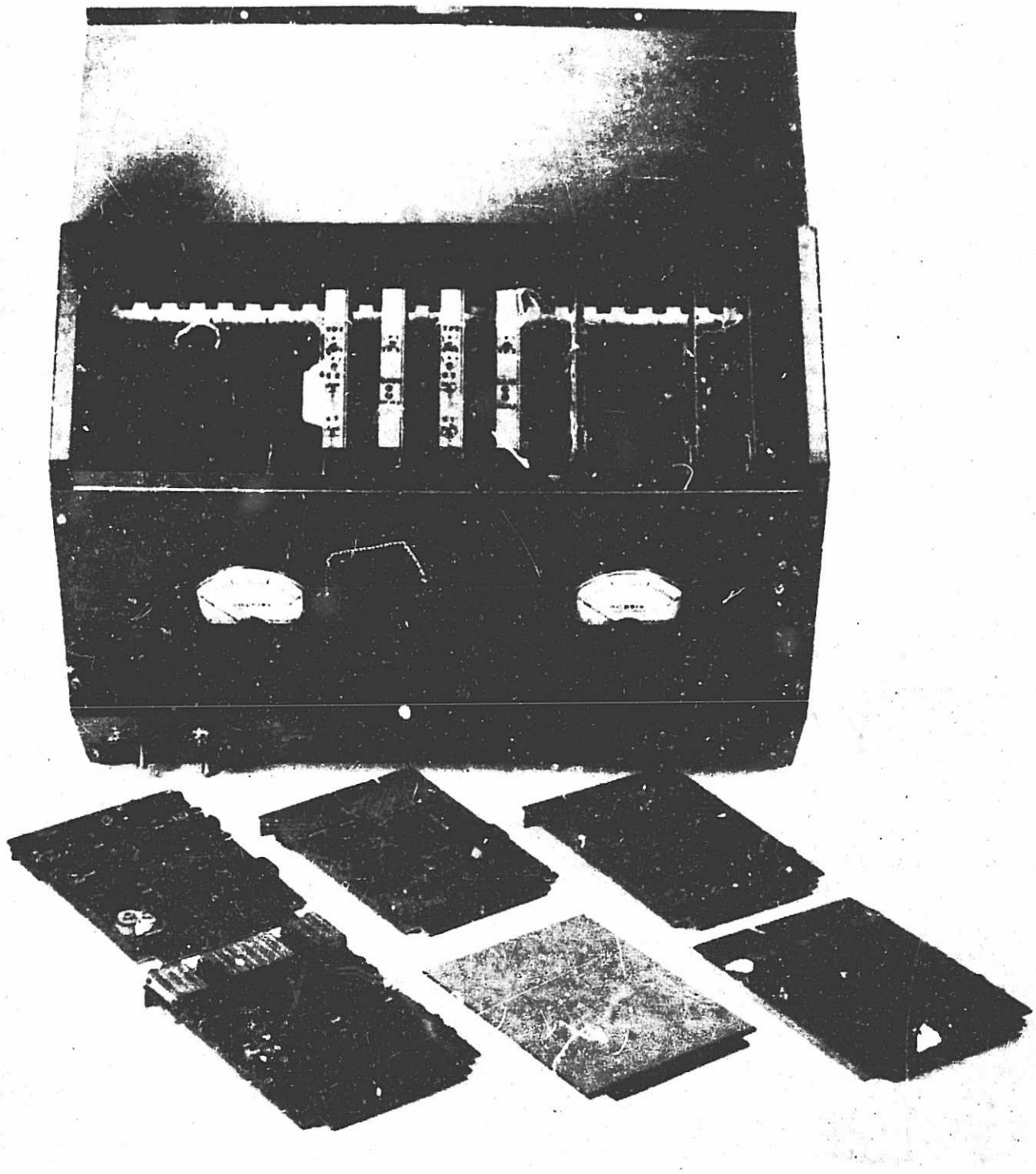

Figure 8. SDMEG Electronics Cabinet and Cards

transistors, and power decoupling circuits; these components are shown in Figure 9. During this program a tenth card, on which the capacitance bridge circuits are mounted, was added to the suspension. Completing the subassembly are two cards containing the HIT circuits and their power decoupling circuits; they occupy the right-hand side of the cabinet. At the extreme right is room for an extender card used in checking circuits on the plug-in cards.

A second set of suspension electronics, also of the plug-in card type, was built under Contract 951148. This set was mated with the second gyro subassembly for acceptance testing and delivery to JPL. Because the construction of the two sets of suspension electronics is similar, many of the cards in the two suspension sets are interchangeable.

The power consumption of the suspension was designed to be a minimum in each of the two operating modes -- a high-g mode and a low-g mode. The design is such that rotor-electrode capacitance changes increase the power and decrease relative stability. For this reason, the suspension undergoes a tuning process as it is mated to a gyro subassembly to optimize stability and power.

Since rotor-electrode capacitance changes with temperature, the suspension design imposes limits on the gyro operating temperature range. Temperature tests conducted before the suspension was modified indicated that the gyro could be operated safely over temperature ranges from 60° to 120°F if the gyro was tuned for operation at 80°F. The operating range could be extended further if limits were placed on the difference in temperature between the envelope and the rotor; however, if a situation occurred that required an emergency shutdown, there would be no assurance that safe operation limits would not be exceeded in the extended ranges.

Some failures which occurred during preliminary tests and suspension confidence checks led to a major suspension modification in 1966, one utilizing separate sensing frequencies for each channel. The separate sensing frequency design has several advantages over the single-frequency design:

- Less susceptible to rotor charge
- Relatively insensitive to the environmental temperature vibrations
- Increased bandwidth and vibration capability in the low-g mode
- External adjustment of rotor position relative to gyro case

The former design accomplished three-channel forcing and sensing functions using only a single-frequency, three phase 20 kHz signal. The present form uses three phase 20 kHz for forcing signals and 1250 kHz, 1510 kHz, and 1740 kHz for three-axis sensing. Both suspension sets were modified to the separate sensing frequency design.

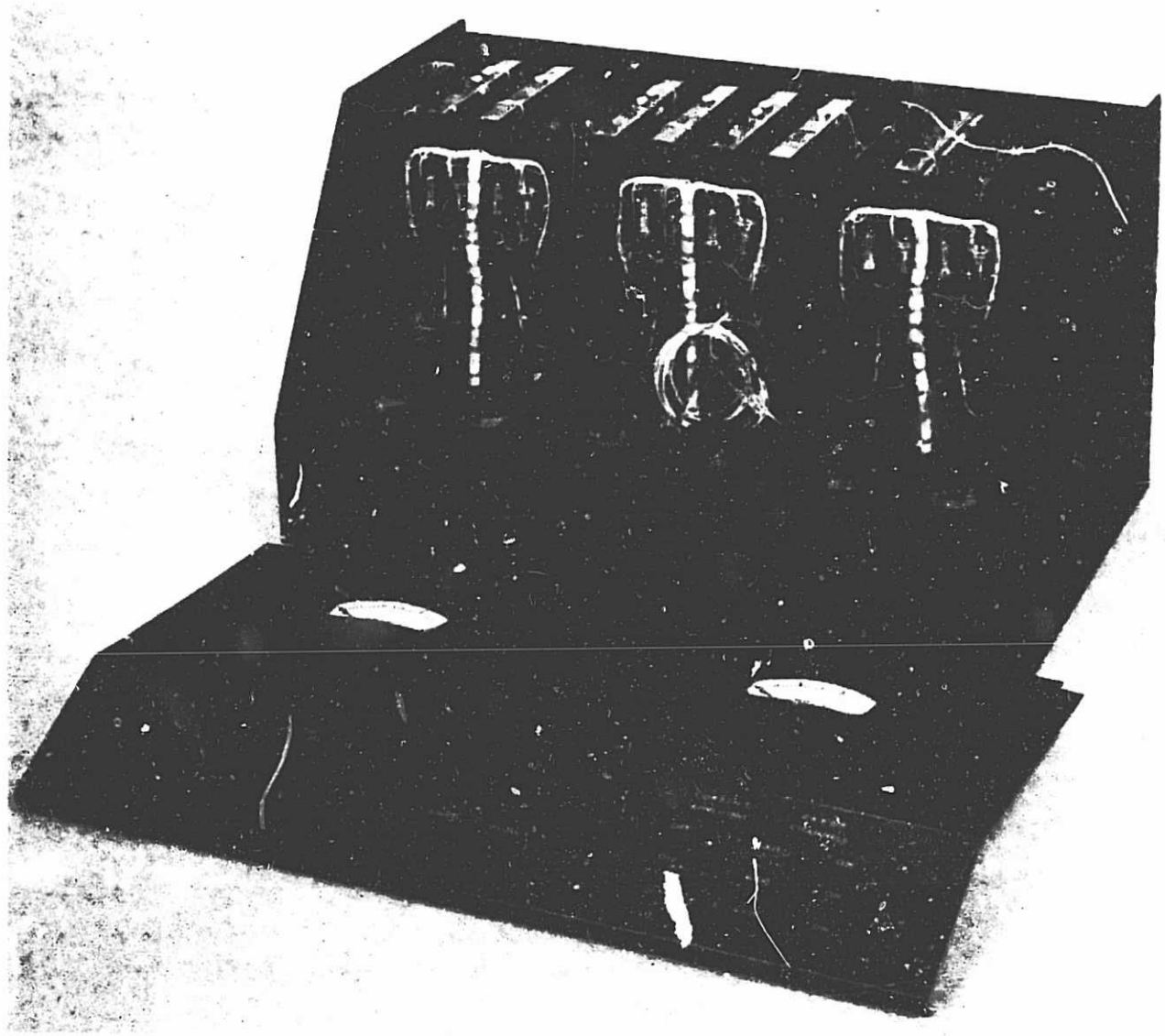

Figure 9. SDMEG Electronics Subassembly with Output Circuits Exposed

The addition of the capacitance bridge and the modification to the suspension caused an increase in the suspension power consumption. Power measurements made on the suspension built under Contract 951148 are given in Table I. The line voltage quoted in the table is that from which the cha sis-mounted power transistors draw their power; the error channel, signa source, and capacitance bridge circuits are not switched from the ±22-volt supply.

Table I. SDMEG Suspension Currents

| Mode of Operation | Current (milliamp) Drawn From | | | | Suspension |
|---|---|---|---|---|---|
| | +22 volts | -22 volts | +12 volts | -12 volts | Power (watts) |
| High g, 22-volt | 720 | 885 | | | 35.3 |
| Low g, 22-volt | 530 | 695 | | | 27.0 |
| Low g, 12-volt | 135 | 270 | 310 | 315 | 16.4 |

## ELECTRONICS SUBASSEMBLY DESCRIPTION AND DRAWINGS

Figure 10 shows a block diagram of the suspension electronics as modified during this program. A complete list of all circuit diagrams for the electronics subassembly is given in Table II. Included in the table is a figure reference of the diagrams which are included in this section.

### Wiring Diagram

An overall wiring diagram of the electronics subassembly chassis is shown in Figure 11. The exit terminals of all circuit cards and terminal boards have been identified on the hardware to facilitate suspension checkout and any troubleshooting which might arise.

In Figure 11, each block represents either an entire circuit card or terminal board, or a portion of a circuit card or terminal board, as identified within the block. The circled letters or numbers at the borders of the blocks represent exit pins or terminals on the cards or terminal boards, respectively. The test points shown on the block borders are test points on the cards. Test points 1, 2, and 3 of the HIT circuits are located on the chassis front panel.

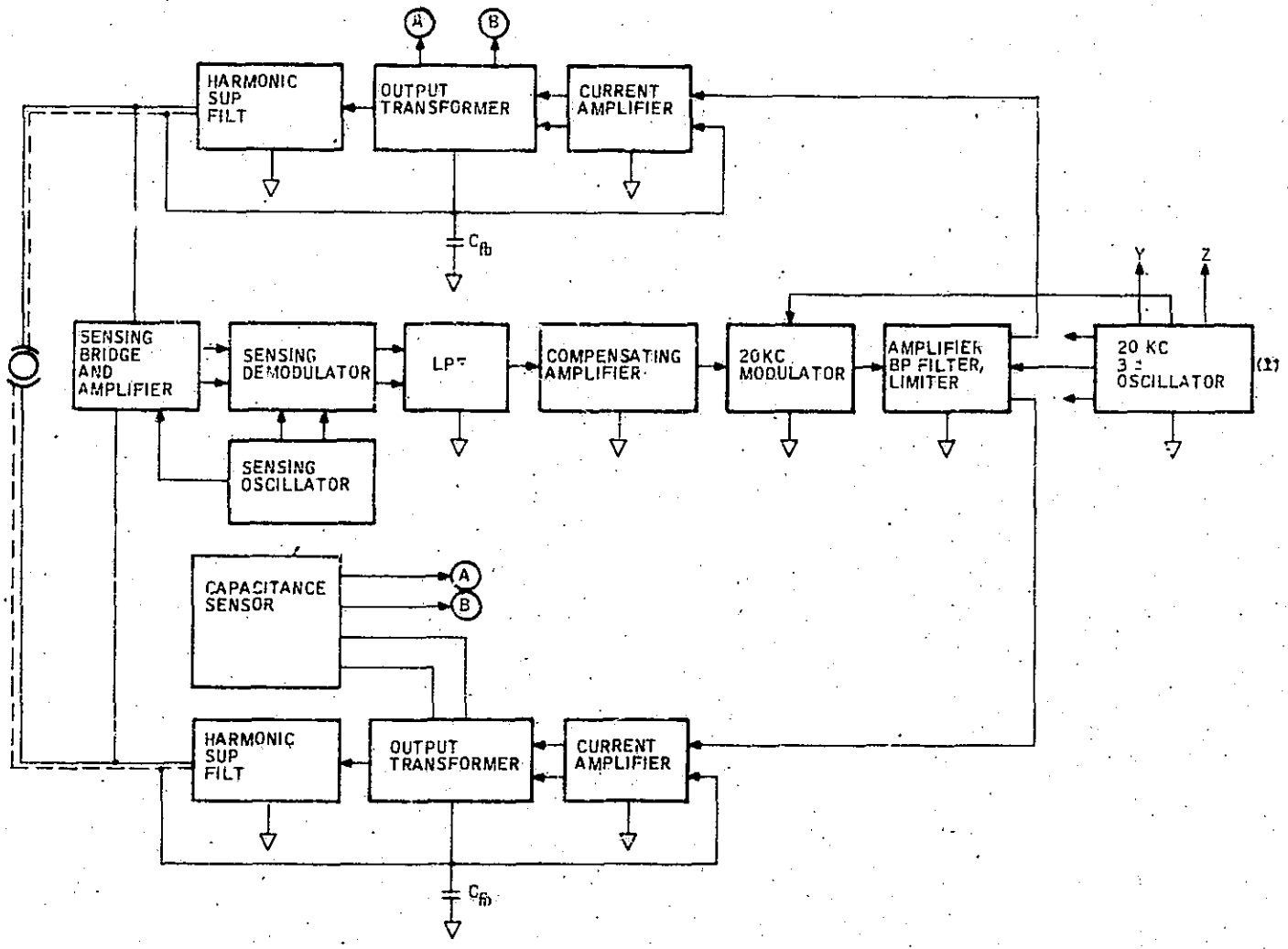


Figure 10. SDMEG Suspension Electronics Block Diagram

Table II. Circuit Diagrams for the SDMEG Suspension Chassis

| Figure | Honeywell Dwg. No. | Title |
|---|---|---|
| 11 | C13194 | Electronic Subassembly Wiring Diagram |
| 12 | C13196 | Signal Source |
| 13 | C12992 | Schematic Diagram of Error Channel Suspension Electronics |
| 14 | C13193-1 | Schematic Diagram of X and Y Channel Current Amplifier Preamplifier Card |
| 15 | C13193-2 | Schematic Diagram of Z Channel Current Amplifier Preamplifier Card |
| 16 | C13993-4 | Schematic Diagram of Current Amplifier, Output Stage, Chassis Mounted |
| 17 | C13193-5 | Schematic Diagram of Current Amplifier Bias Terminal Board (TB7, TB8) |
| 18 | C13193-8 | Schematic Diagram of Current Amplifier, Driver and Decoupling Board |
| 19 | C13193-6 | Schematic Diagram of Current Amplifier, Harmonic Suppression Filter Terminal Board |
| 20 | C13193-7 | Schematic Diagram of Current Amplifier, Feedback Isolation Terminal Board |
| 21 | C13197 | Capacitance Bridge |
| 22 | C13198 | Schematic Diagram of Height-Insensitive Triggers |

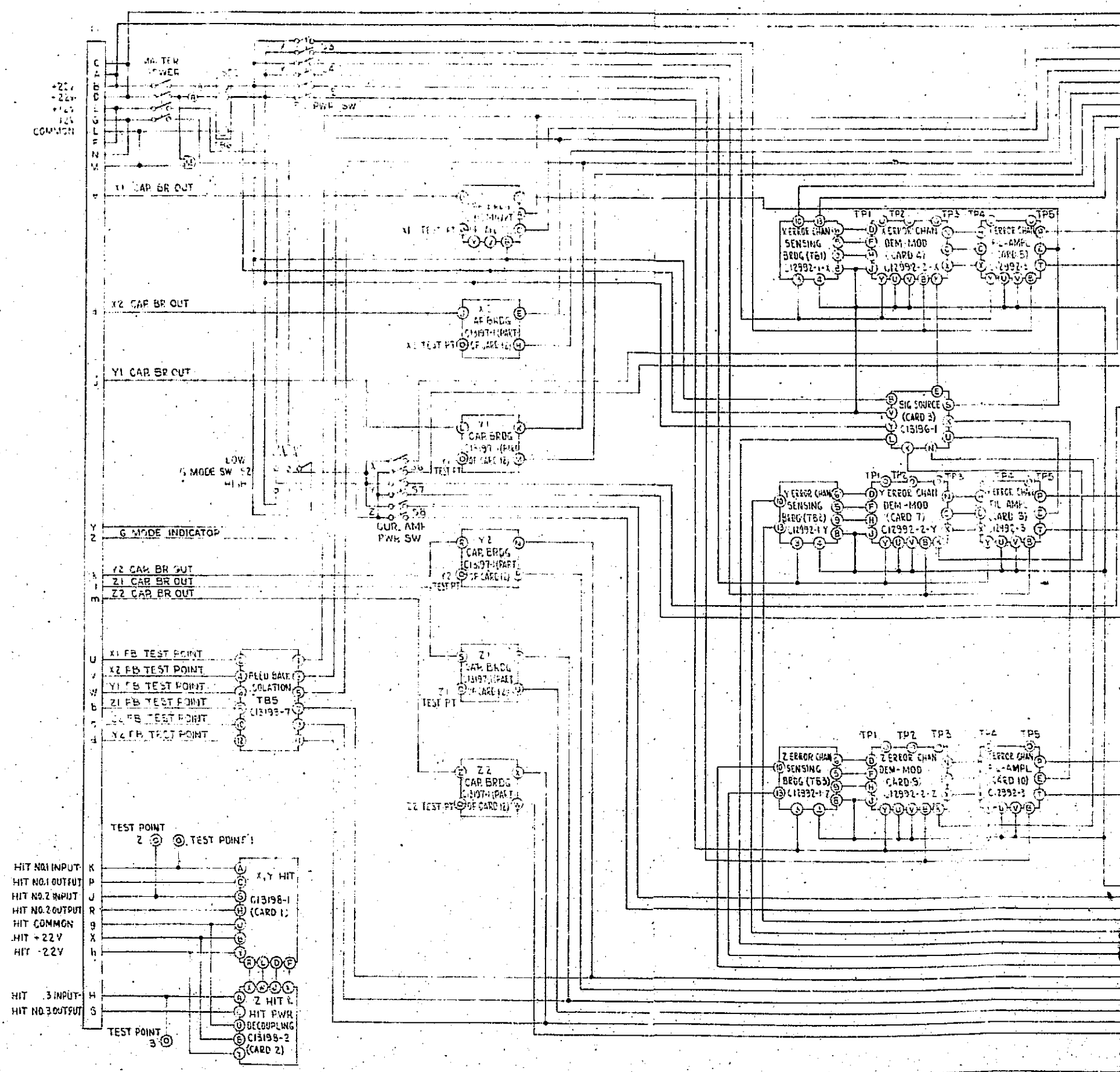


| TEST POINTS LOCATED ON CARDS | | |
|---|---|---|
| CARDS | TEST PT | DESCRIPTION |
| 4, 7, 9 | TP1 | LOW PASS FIL OUTPUT |
| 4, 7, 9 | TP2 | MOD INPUT |
| 4, 7, 9 | TP3 | LOCAL GROUND |
| 5, 8, 10 | TP4 | ERROR CHAN OUTPUT |
| 5, 8, 10 | TP5 | ERROR CHAN LIM SHORTING |
| 12 | TPX1 | X1 CAP BR OUTPUT |
| 12 | TPX2 | X2 |
| 12 | TPY1 | Y1 |
| 12 | TPY2 | Y2 |
| 12 | TPZ1 | Z1 |
| 12 | TPZ2 | Z2 |

Figure 11. Electronic Subassembly

FOLDOUT FRAME 4

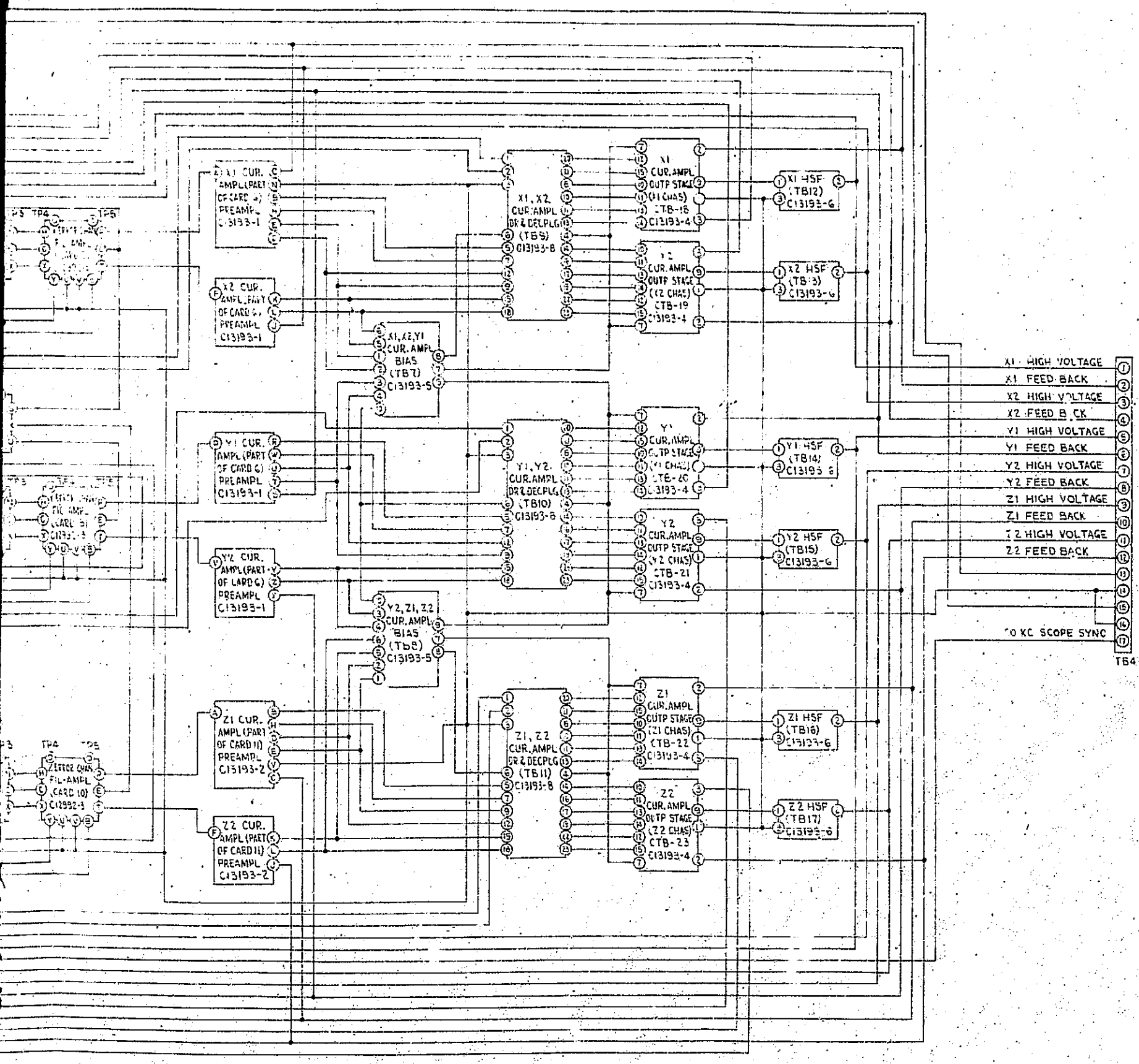


| TEST PT | POINTS LOCATED ON CARDS DESCRIPTION |
|---|---|
| TP1 | LOW PASS FIL OUTPUT |
| TP2 | MOD INPUT |
| TP3 | LOCAL GROUND |
| TP4 | ERROR CHAN OUTPUT |
| TP5 | ERROR CHAN LIM SHORTING J |
| TPX1 | X1 CAP BR OUTPUT |
| TPX2 | X2 |
| TPY1 | Y1 |
| TPY2 | Y2 |
| TPZ1 | Z1 |
| TPZ2 | Z2 |



hic Subassembly Wiring Diagram

FOLDOUT FRAME B

Signal Source

Figure 12 shows the signal source schematic diagram. During this program, capacitive interstage coupling was added between transistors Q4 and Q5, consisting of capacitor C13 and bias inductor L1. This reduced the transient occurring when the preload is switched between the high-g and low-g levels.

Error Channel

The complete error channel schematic is shown in Figure 13. Each error channel is physically separated into three portions, an enclosed terminal board located on the under side of the chassis and two plug-in circuit cards. The sensing bridge (C 12992-1) consists of the bridge capacitors (C1, C2, C7, and C8), the bridge drive transformer (T1), the 20 kHz shunting filter (L1, L2, and C6), and inverting amplifier (Q1 with associated components). Inductor L1 with transformer T1 resonates with the bridge capacitors at the sensing frequency to provide maximum drive signal for a given sensing oscillator power consumption.

Demodulator-Modulator Card

The error channel input card (C 12992-2 of Figure 13) contains the sensing oscillator, sensing demodulator, low-pass filter, compensating amplifier, and the 20 kHz modulator. Transistor Q3 with associated components forms a modified Colpitts oscillator with outputs for demodulator drive. The 30-volt oscillator output signal is fed into the bridge transformer. The oscillator frequency is set by inductor L2 in series resonance with capacitors C16, C19, and C20.

Diode quads CR3 and CR4, acting as DPST switches, alternately switch the normal and inverted bridge outputs to ground, thus functioning as a full-wave demodulator. Resistors R1, R2, R12, and R13 are part of the demodulator, with resistors R5 and R20 providing a bias path for the compensating amplifier.

The low-pass filter is a third-order Chebychev, 1-db ripple filter cutting off at 11,500 Hz. Inductor L1, capacitors C3 and C7, resistor R6, and the demodulator resistors form the filter.

Micro-amplifier AR1 acts as a compensating amplifier, providing phase lead necessary for servo loop stability and phase lag compensation to provide decreased rotor sag at low frequencies. The voltage transfer function for amplifier is of the form

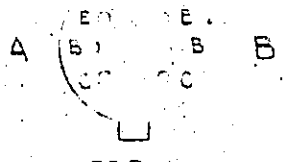





Figure 12. Signal Sou

FOLDOUT FRAME

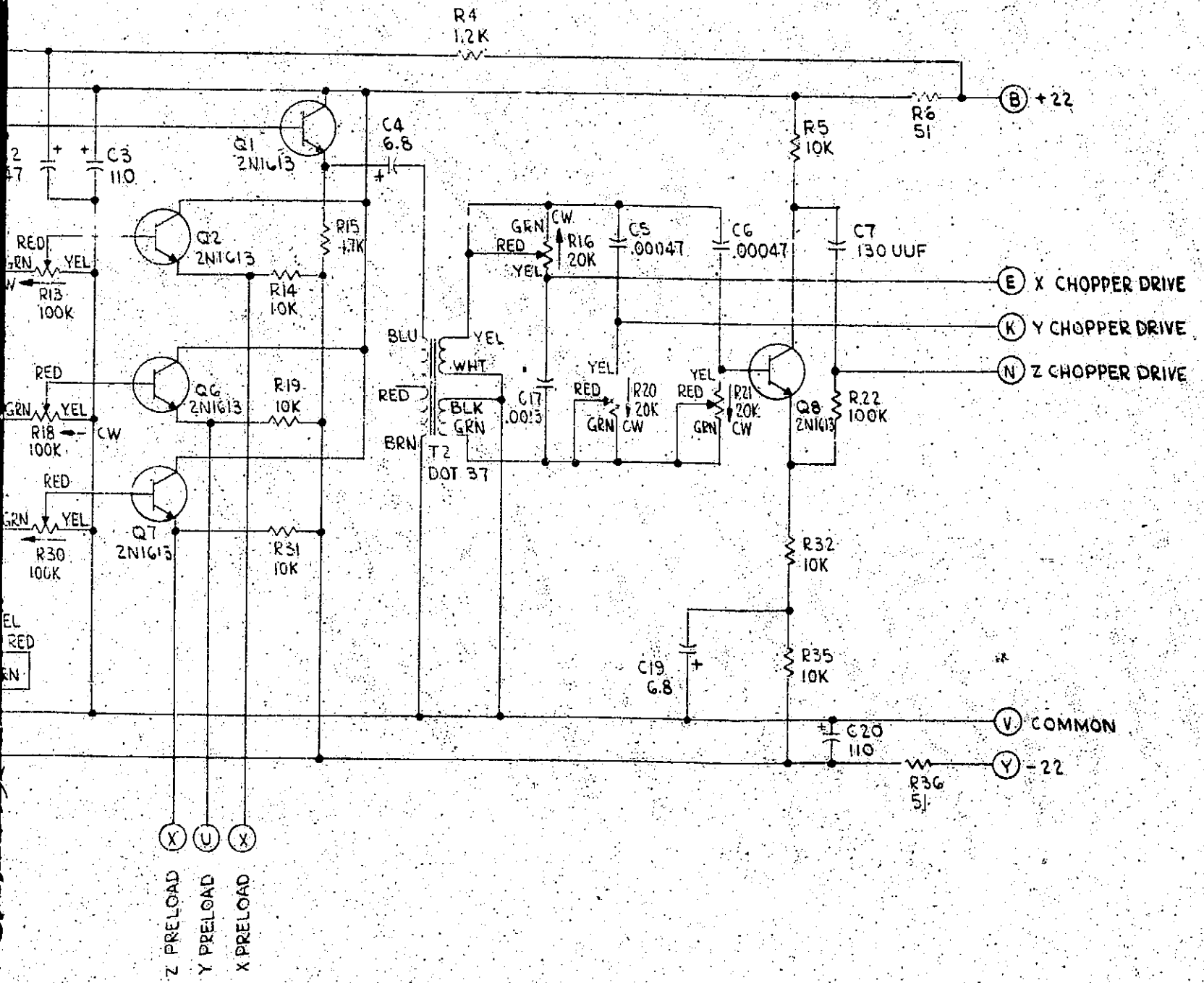


2. Signal Source



FOLDOUT FRAME 5

| TERMINAL BD DESIGNATION | RESONANT FREQ OF TANK | NOMINAL VALUE OF INDUCTOR L1 | NOMINAL VALUE OF INDUCTOR L2 | OSCILLATOR FREQ |
|---|---|---|---|---|
| TB1 | 1250 KC | 136 UH | 73.5 UH | NONE |
| TB2 | 1510 KC | 93 UH | 50.5 UH | ↓ |
| TB3 | 1740 KC | 70 UH | 38.1 UH | |
| NONE | NONE | NONE | 31.2 UH | 1250 KC |
| ↓ | ↓ | ↓ | 21.4 UH | 1510 KC |
| | | | 16.1 UH | 1740 KC |


BASE DIAGRAM
FSP-15

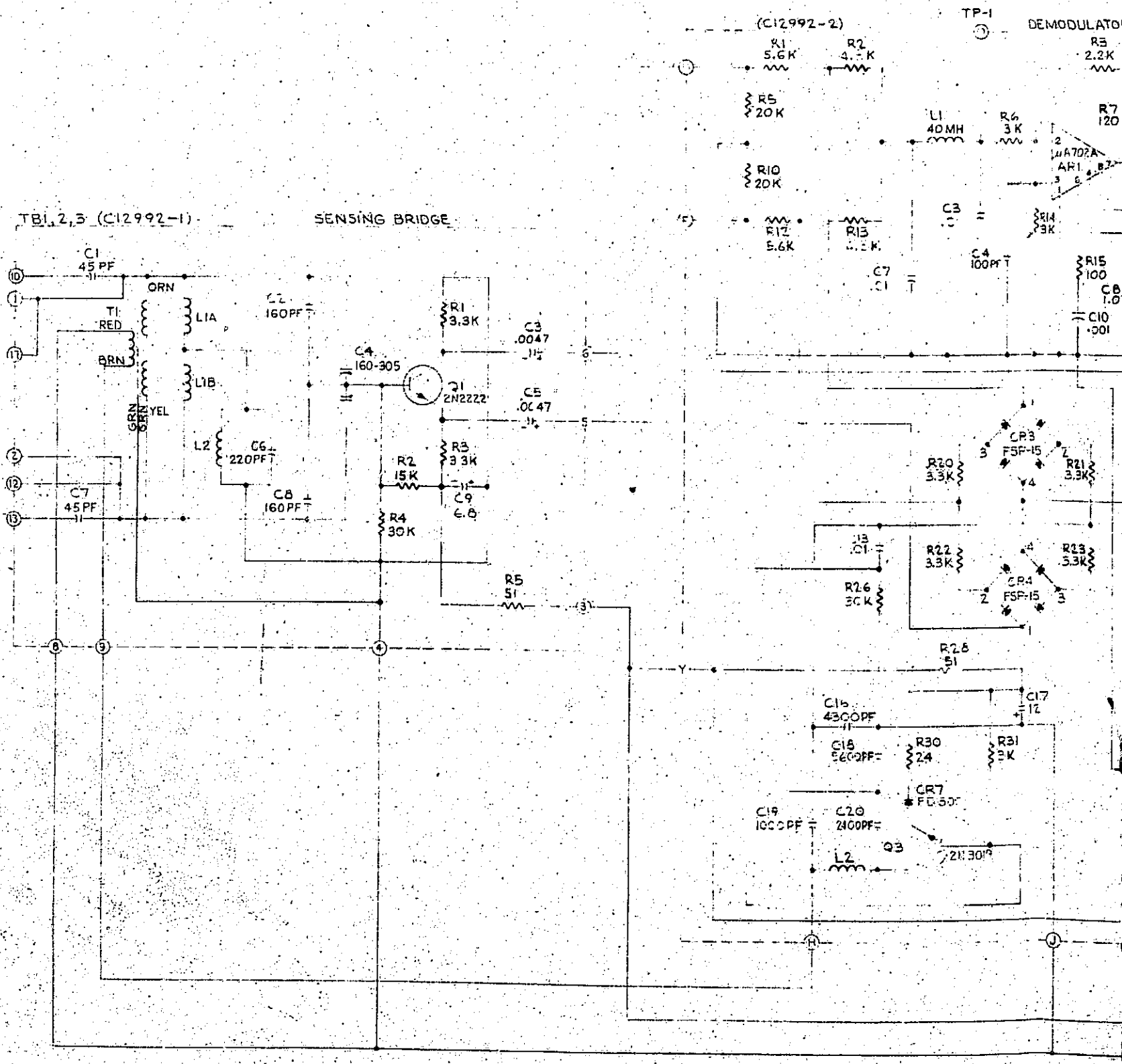


2- TAB OF μA702A ALIGNED WITH RED MARK ON SOCKET

1- ALL RESISTANCES ARE IN OHMS AND ALL CAPACITANCES ARE IN UF UNLESS OTHERWISE SPECIFIED

FOLDOUT FRAME 4

**Figure 13.** Schematic D
Suspension E

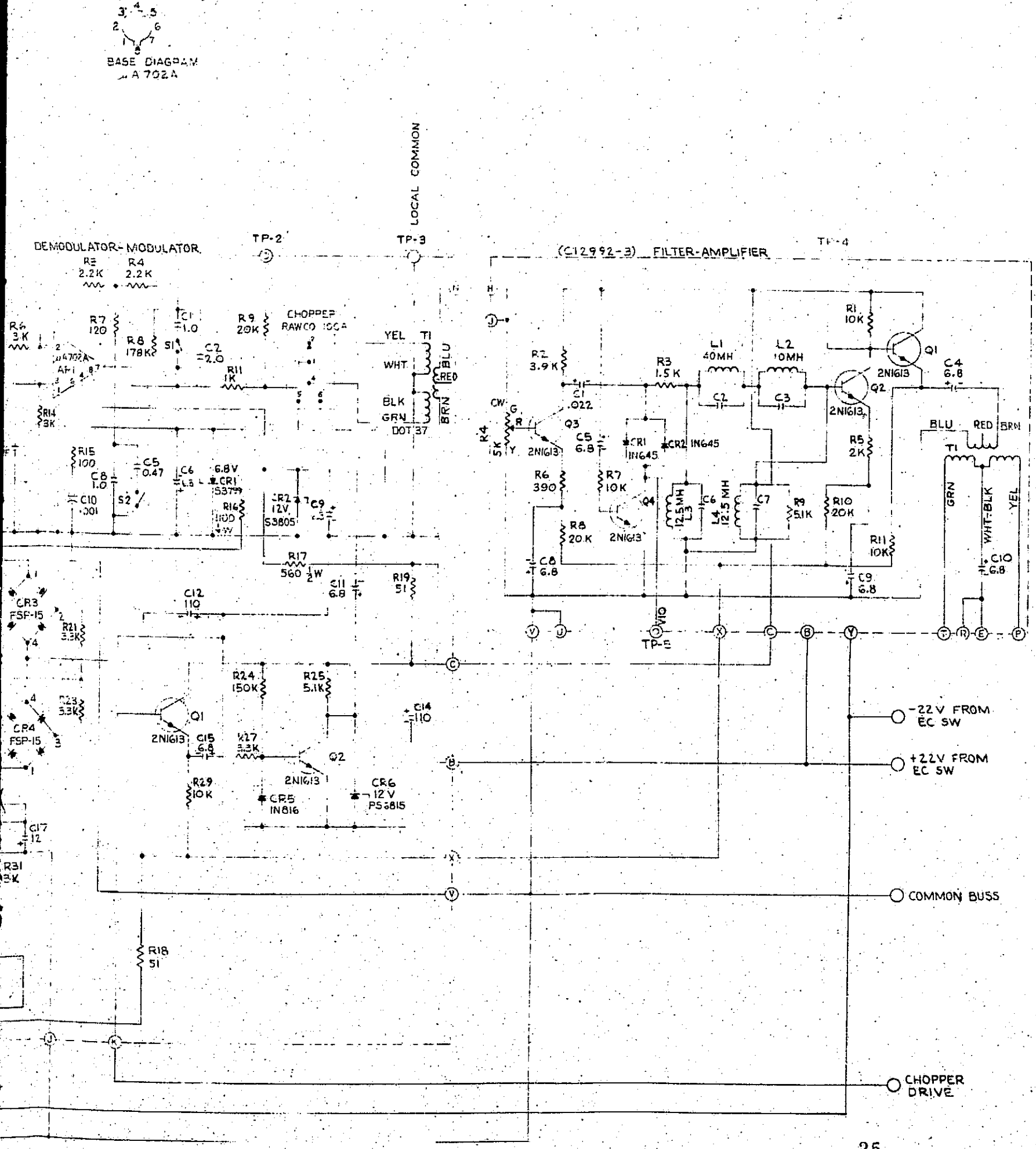


25

hematic Diagram of Error Channel
spension Electronics

FOLDOUT FRAME 13

$$G(s) = K \frac{\left(1 + \frac{S}{2\pi f_2}\right)\left(1 + \frac{S}{2\pi f_3}\right)}{\left(1 + \frac{S}{2\pi f_1}\right)\left(1 + \frac{S}{2\pi f_4}\right)}$$

where

$f_1 < f_2 < f_3 < f_4$

$f_1$, $f_2$, $f_3$, $f_4$ are amplifier break frequencies

S is LaPlace operator ($S = j2\pi f$, $j = \sqrt{-1}$ )

K is a gain constant

G(s) is the amplifier voltage transfer function

The amplifier break frequencies for both the high-g mode (S1 and S2 open) and the low-g mode (S1 and S2 closed) are given in Table III.

Table III. Compensating Amplifier Break Frequencies
(Component Values as Shown on C12992-2 of Figure 13)

| Break Frequency | High-g Mode (Hz) | Low-g Mode (Hz) |
|---|---|---|
| $f_1$ | $\frac{1}{2\pi R_8 C_2} = 0.45$ | $\frac{1}{2\pi R_8 (C_1 + C_2)} = 0.30$ |
| $f_2$ (approximate) | $\frac{1}{2\pi (R_3 + R_4) C_2} = 18$ | $\frac{1}{2\pi (R_3 + R_4)(C_1 + C_2)} = 12$ |
| $f_3$ (approximate) | $\frac{1}{2\pi \left(R_7 + \frac{R_3 R_4}{R_3 + R_4}\right) C_8} = 130$ | $\frac{1}{2\pi \left(R_7 + \frac{R_3 R_4}{R_3 + R_4}\right)(C_5 + C_8)} = 89$ |
| $f_4$ | $\frac{1}{2\pi R_7 C_8} = 1300$ | $\frac{1}{2\pi R_7 (C_5 + C_8)} = 890$ |

The solid-state chopper operating as a SPDT switch into transformer T1, operating at 20 kHz, serves as a 20-kHz, full-wave modulator.

Test points on this card are low-pass filter output (TP1), modulator input (TP2), and a local ground (TP3) for grounding scope probes during checkout.

Filter Amplifier Card

The error channel output card (C12992-3 of Figure 13) contains an amplifier, a band-pass filter, and a voltage limiter.

Potentiometer R4 is suspension gain adjustment feeding amplifier stage Q3.

Transistor Q4 acts as a switch which grounds the voltage limiting diodes (CR1 and CR2).

Capacitive biasing on Q4 "closes" the switch for the first 200 milliseconds after application of power and results in a steady-state "open switch". The function of the limiter is to limit the maximum error channel output and consequently limit the electrode-to-rotor voltage gradients during rotor lifting. The limiter then ceases to limit after initial lift, allowing increased suspension servo vibration capability.

Inductors L1, L2, L3, and L4 with their respective capacitors and with resistors R2, R3, and R9 form the 20-kHz band-pass filter. The band-pass filter, attenuating the harmonics of the 20-kHz modulator, is required to prevent suspension instability and to reduce the power consumption of the current amplifiers. The current amplifier output stages are resonant to 20 kHz and not to harmonics of 20 kHz.

Transistors Q2 and Q1 form an amplifier driving transformer T1. Since the center tap of T1 is driven by the preload output of the signal source, then the two-error channel outputs at points P and T are the "preload plus the rebalance" and the "preload minus the rebalance", each of which feeds one current amplifier of one channel.

Current Amplifier

Each current amplifier consists of a preamplifier and a class AB Darlington connected output stage operating into a high-voltage output transformer. A high degree of current feedback around the amplifier is utilized to make the output current into the load relatively independent of load capacitance. The inductance of the transformer resonates with the rotor-to-electrode capacitance and the cable capacitance at the carrier frequency, resulting in minimum power consumption.

A drawing of the X and Y channel preamplifier card is shown in Figure 14. Figure 15 is a drawing of the Z channel preamplifier card. The chassis-mounted output transistors and the output transformer are shown in Figure 16. Figure 17 presents the bias circuitry, and Figure 18 shows the driver transistors and power decoupling. Figure 19 shows the harmonic suppression filter, while Figure 20 presents the isolation capacitors for the feedback test points.

## Capacitance Bridge

The capacitance bridge circuit consists of two carrier frequency bridges, each of which is connected to a tap winding on the output transformer. The sum of reference (feedback) capacitor voltage and tap voltage produces a nulled output at a particular value of load (rotor-electrode plus cable) capacitance. Voltage output about this null point is produced by rotor-electrode capacitance variations which include relative size change between the rotor and housing as well as rotor displacement.

The schematic diagram of the six capacitance bridges is shown in Figure 21. Each capacitance bridge consists of a 20-kHz bridge, an isolation amplifier, and a low-pass filter. The bridge outputs are a 20-kHz sinusoid with amplitudes proportional to change in rotor-to-electrode capacitances from nominal.

## Height-Insensitive Trigger (HIT)

The HIT, as explained in Section VI, is to produce a gating pulse at a fixed proportion of the pickoff pulse height instead of at a fixed voltage. A schematic diagram of the two HIT circuit cards is shown in Figure 22. Three HIT circuits, one for each pickoff, and the associated decoupling components are mounted on these cards.

Card C13198-1 is the X and Y HIT circuits located on one HIT card. C13198-2 is the Z HIT circuit and the power decoupling for the X, Y, and Z HIT circuits located on the second card.

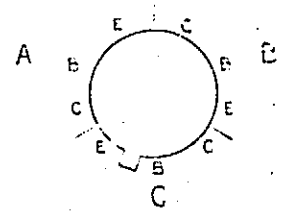


FSP113
BASE DIAGRAM

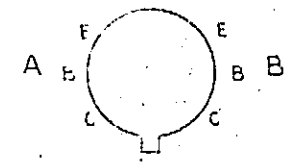


SP8309
BASE DIAGRAM

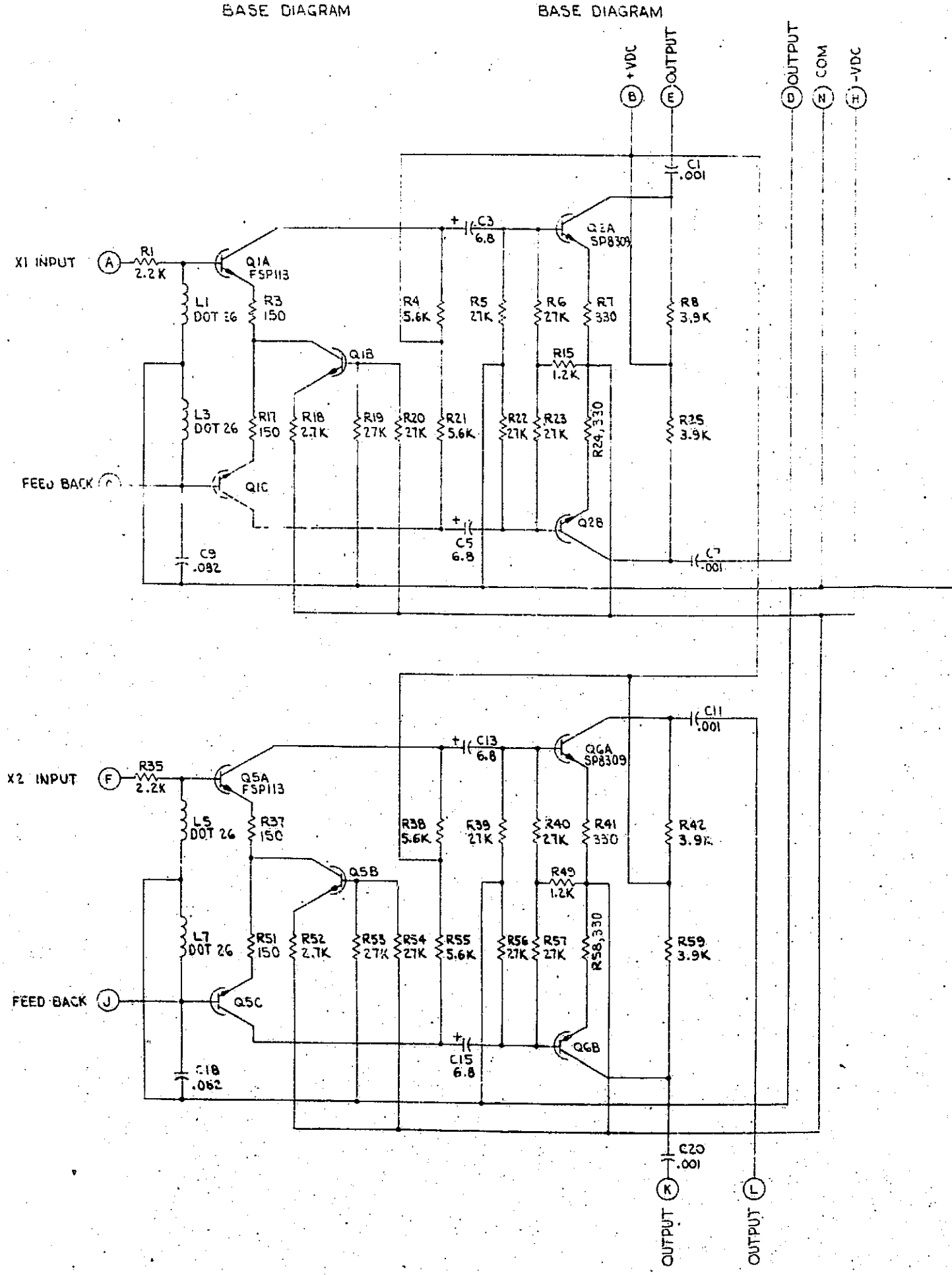


Figure 14. Schematic Diagram of
Amplifier Preamplifier

FOLDOUT FRAME

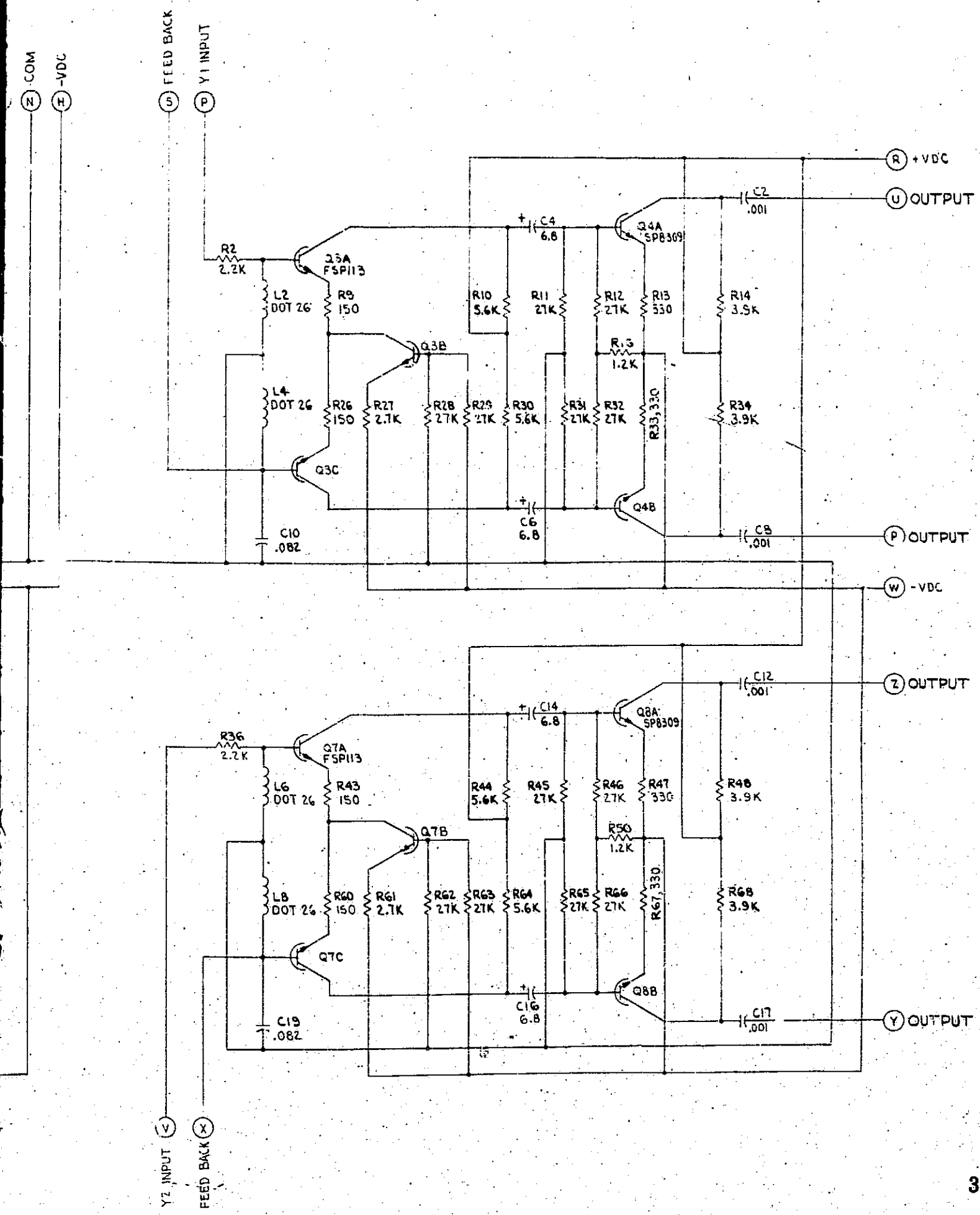


ic Diagram of X and Y Channel Current
er Preamplifier Card



FOLDOUT FRAME 13

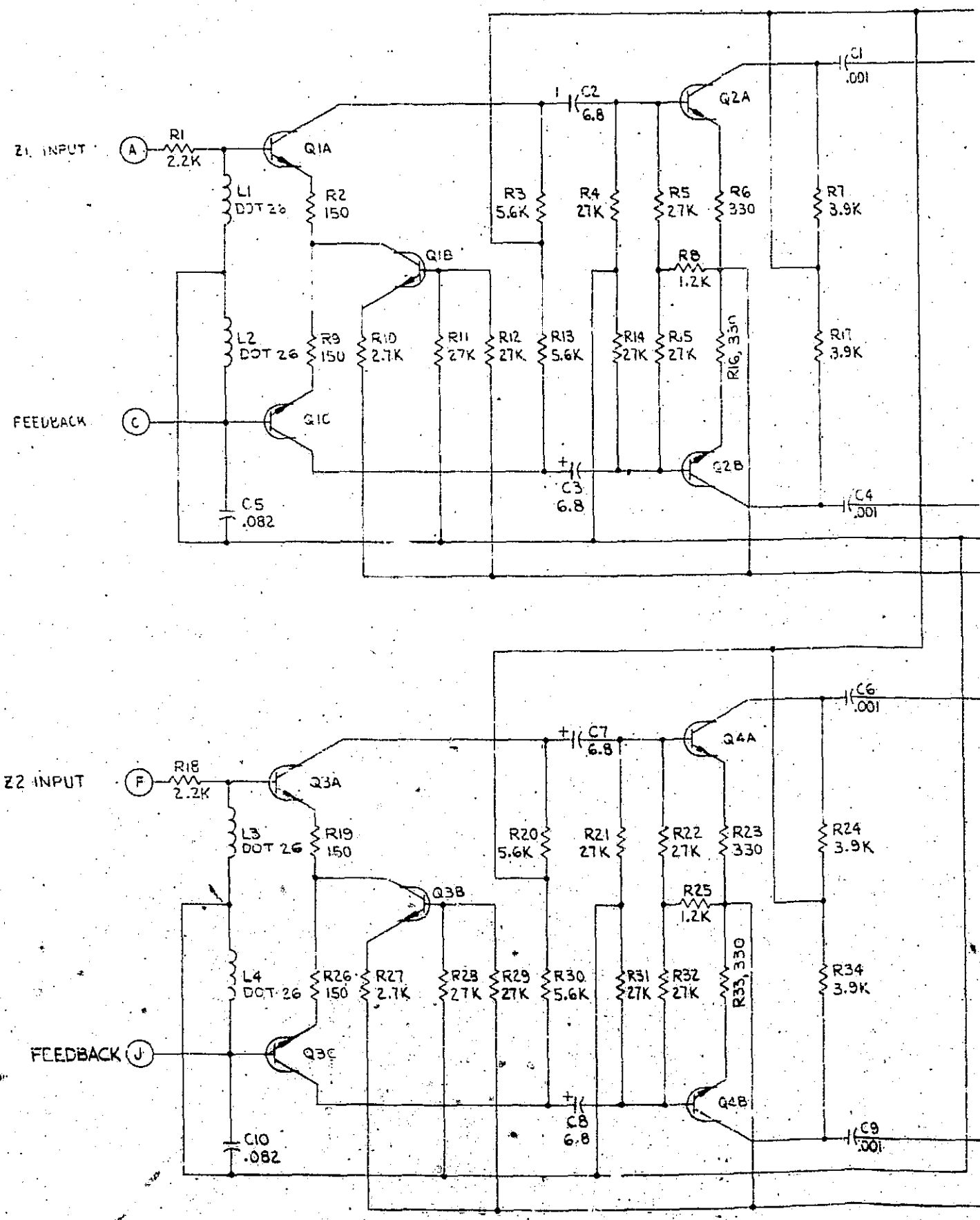


Figure 15. Schematic Diagram of Z Amplifier Preamplifier

1 - ALL RESISTANCE ARE IN OHMS AND ALL CAPACITANCE ARE IN UF UNLESS OTHERWISE SPECIFIED

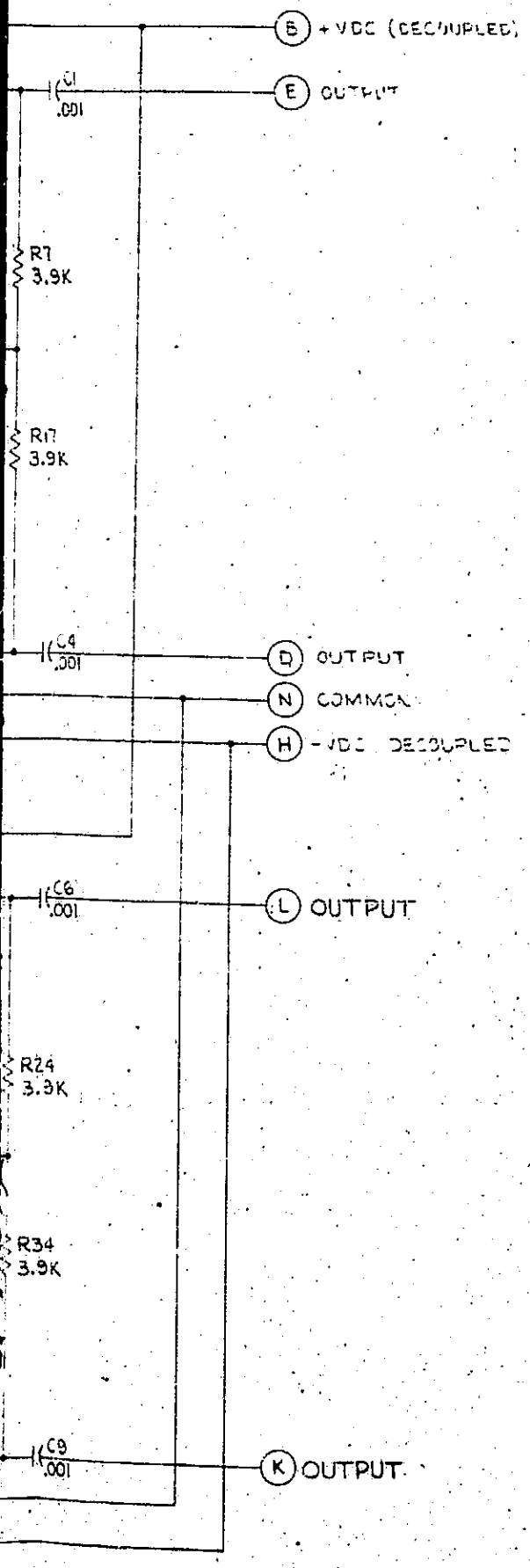


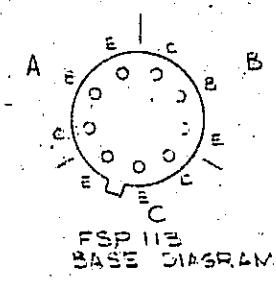


FSP 113
BASE DIAGRAM

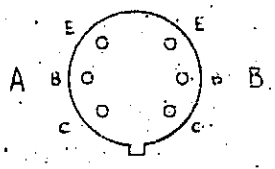


SP8309
BASE DIAGRAM

iagram of Z Channel Current
reamplifier Card



FOLDOUT FRAME 2

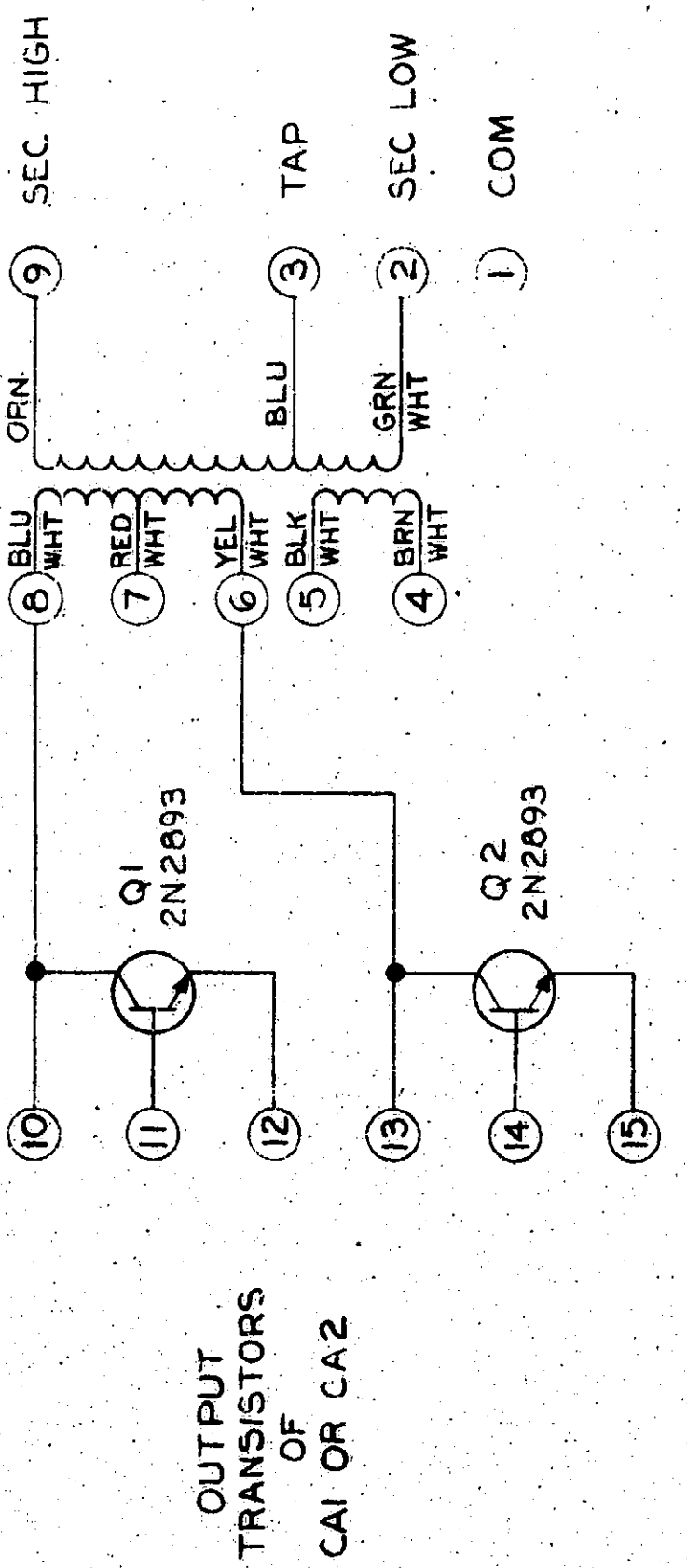


Figure 16. Schematic Diagram of Current Amplifier, Output Stage, Chassis Mounted

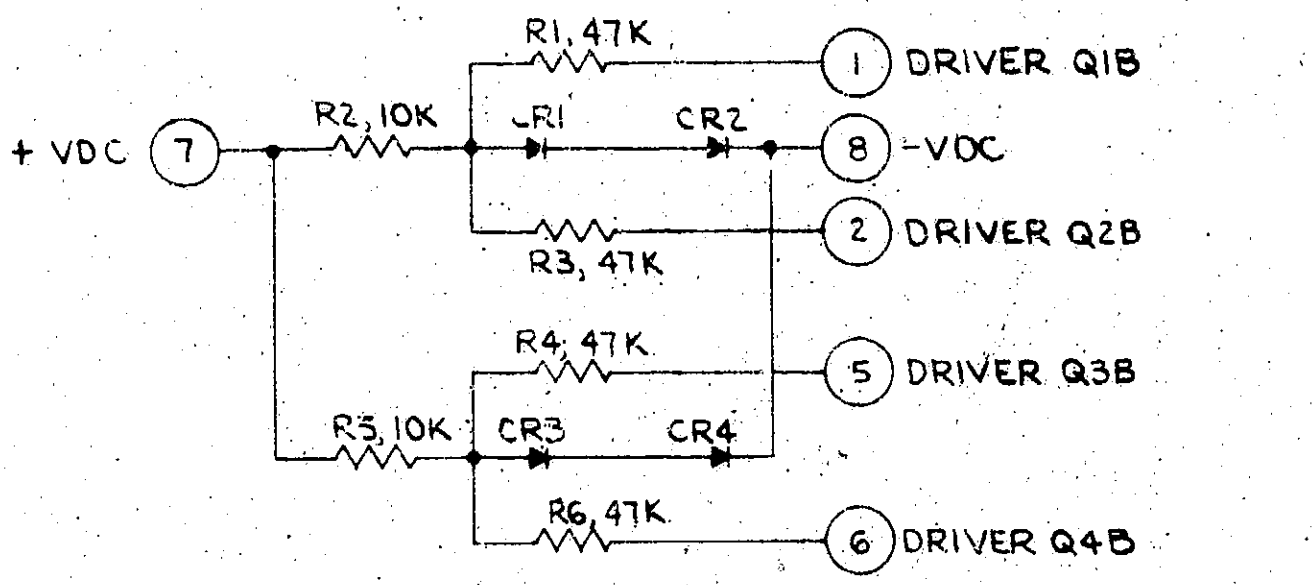


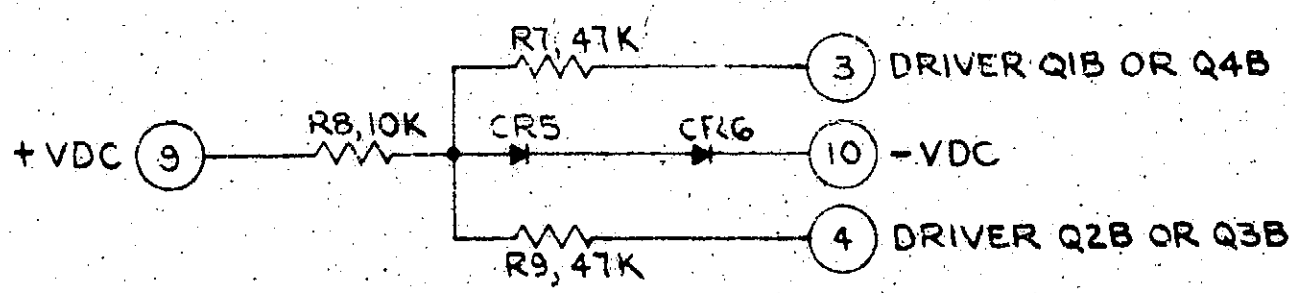


Figure 17. Schematic Diagram of Current Amplifier Bias Terminal Board (TB7, TB8)

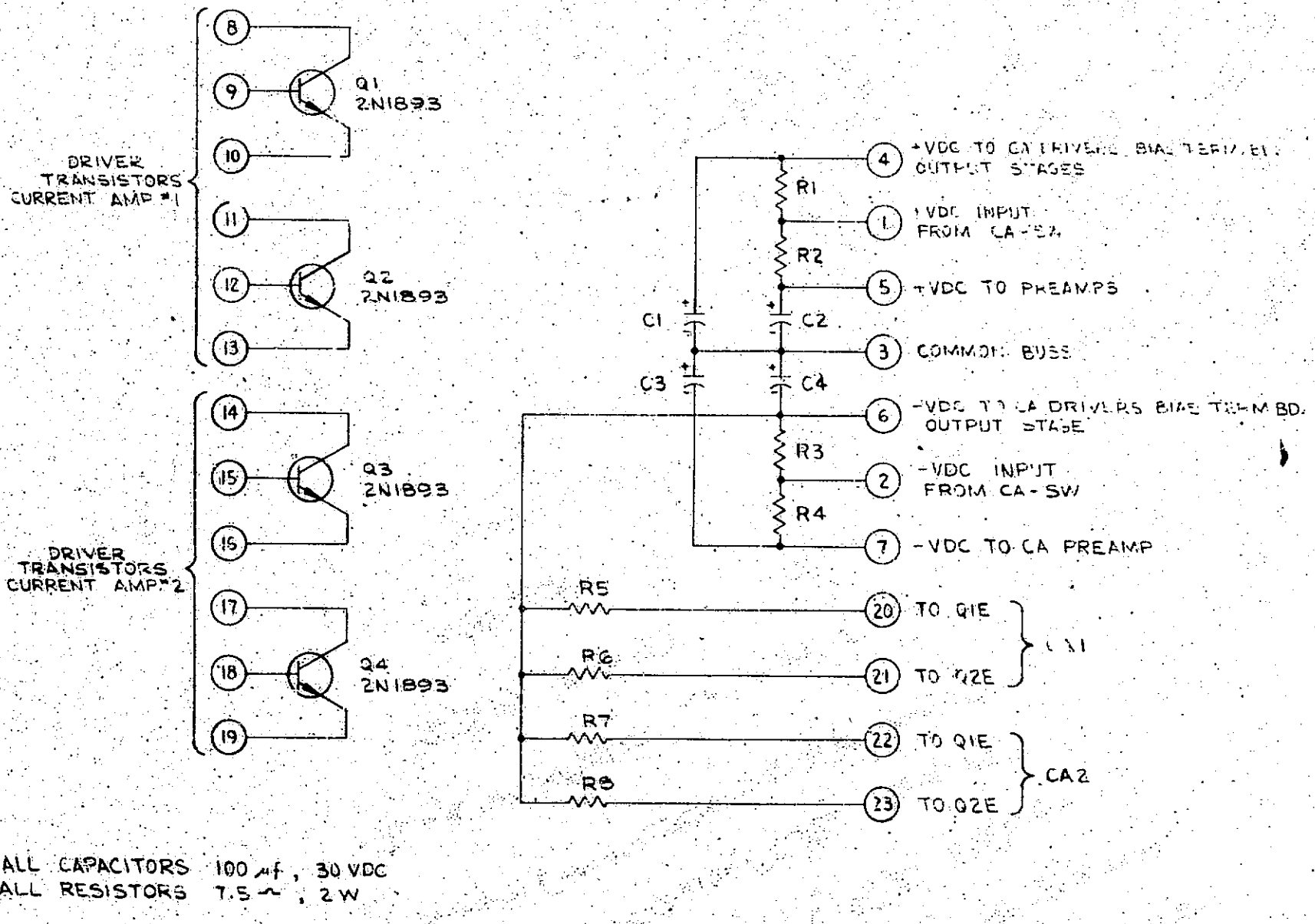


2- ALL CAPACITORS 100 μf, 30 VDC
1- ALL RESISTORS 7.5 ~, 2 W

Figure 18. Schematic Diagram of Current Amplifier, Driver and Decoupling Board

| HONEYWELL PART NO. | RESONANT FREQUENCY OF L1-C1 TANK | NOMINAL VALUE OF L1 |
|---|---|---|
| C13193-6-X | 1250 KC | 135 μh |
| C13193-6-Y | 1510 KC | 92.5 μh |
| C13193-6-Z | 1740 KC | 69.6 μh |

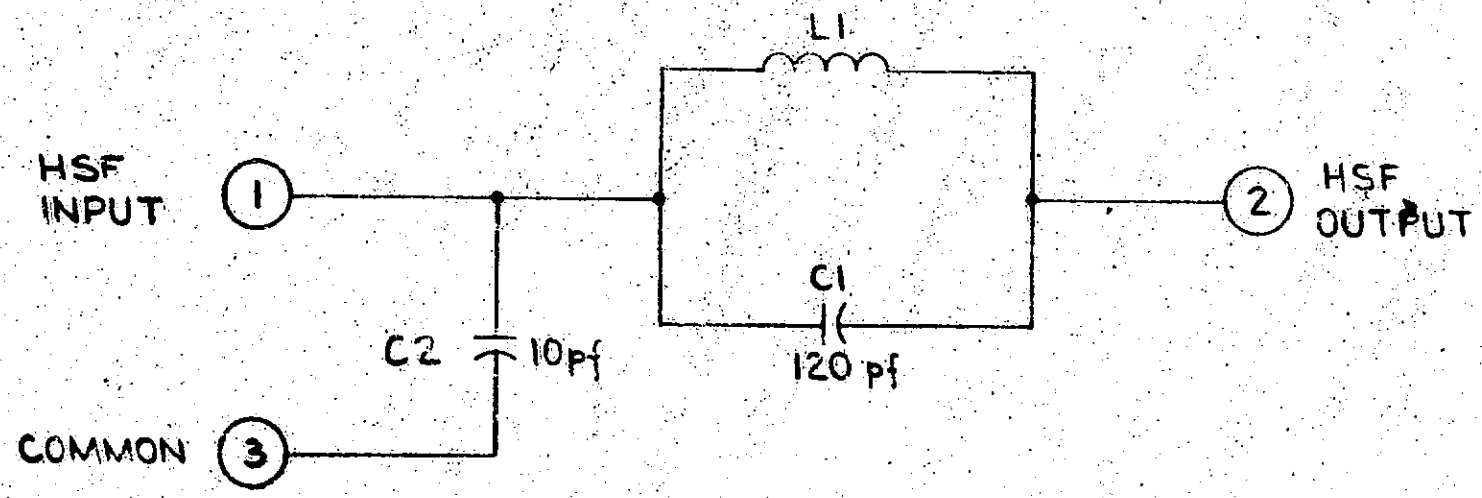


Figure 19. Schematic Diagram of Current Amplifier, Harmonic Suppression Filter Terminal Board

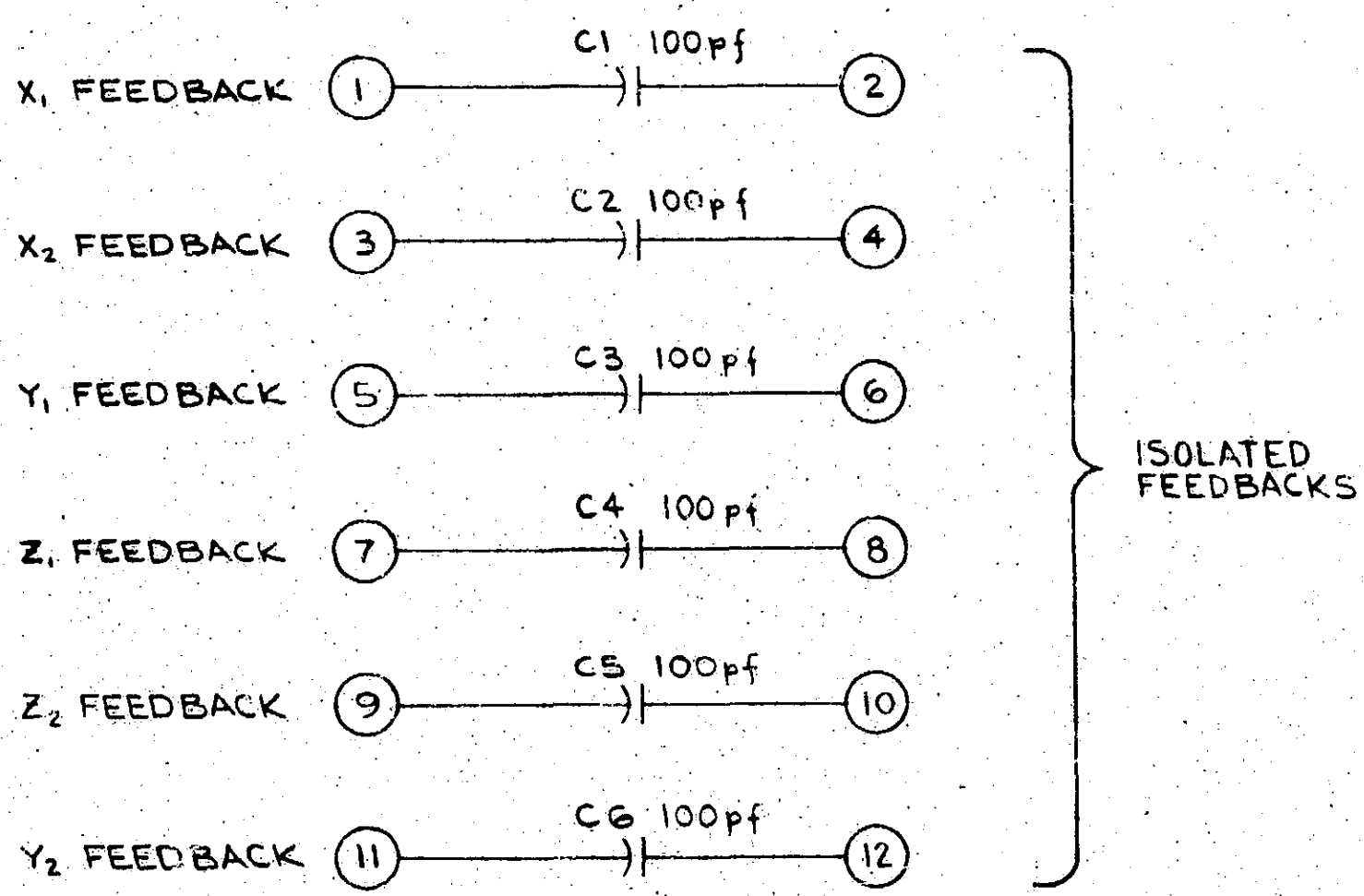


Figure 20. Schematic Diagram of Current Amplifier, Feedback Isolation Terminal Board

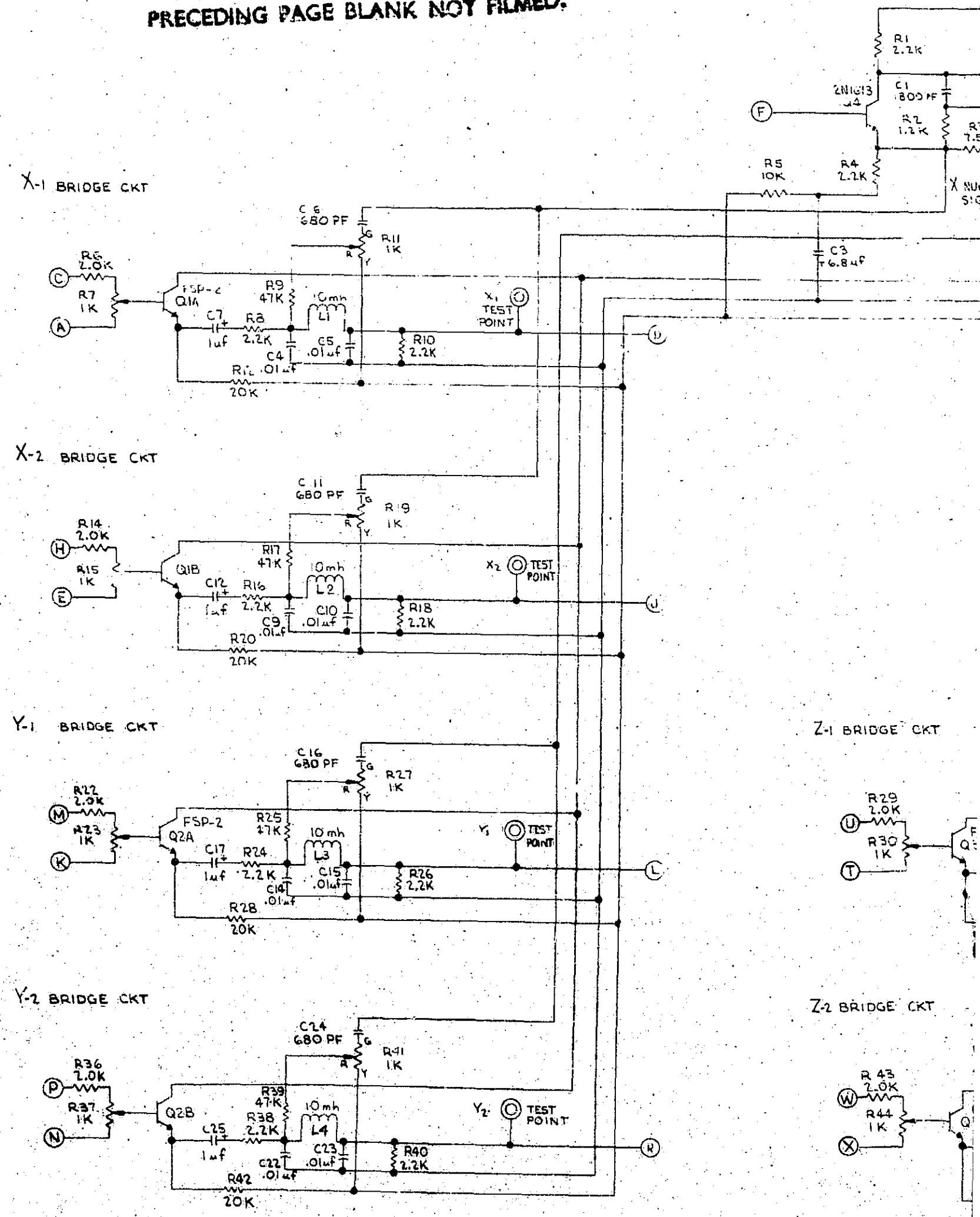


Figure 21.. Capac

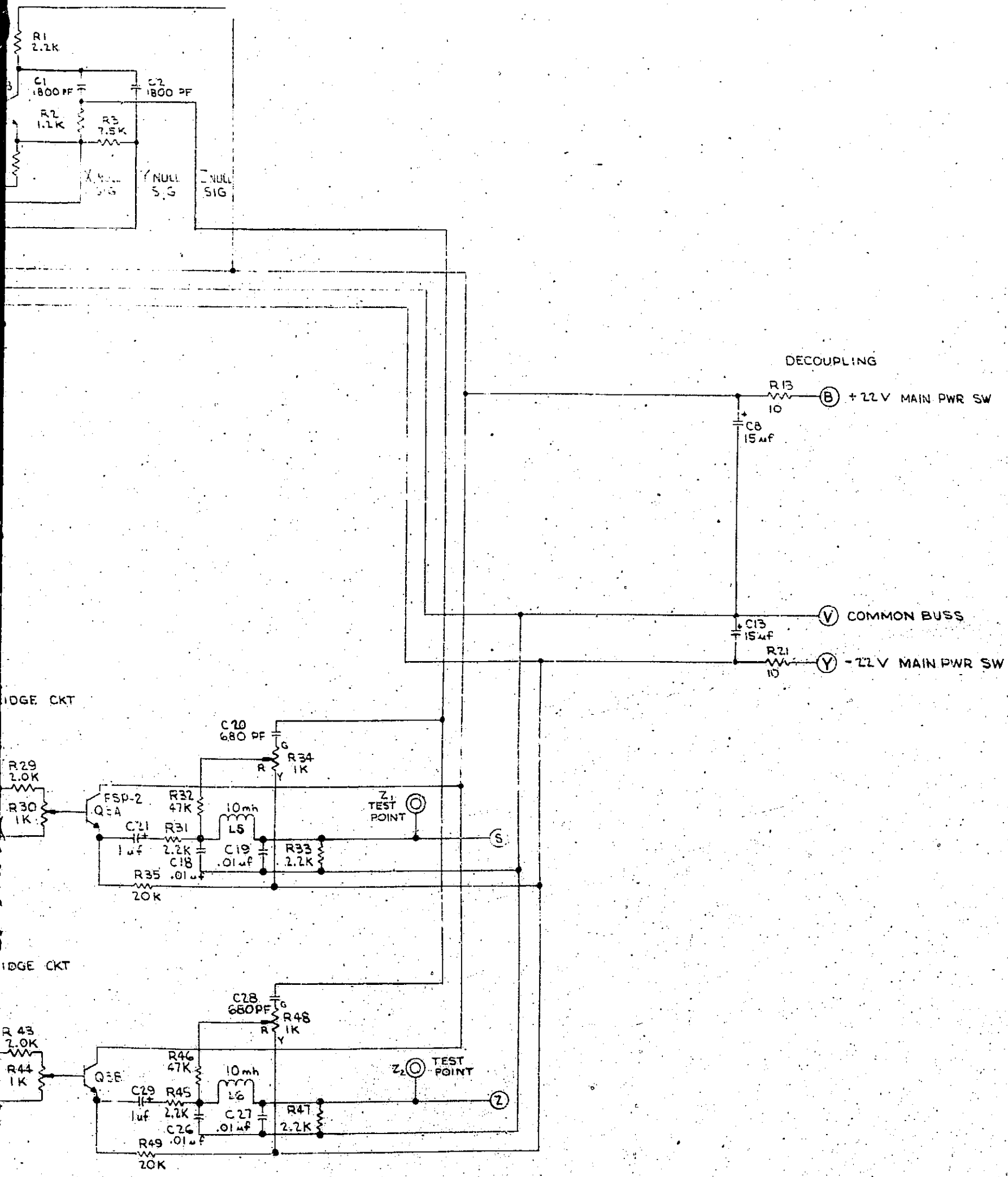




1. Capacitance Bridge

FOLDOUT FRAME 2

C13198-1 X & Y HIT (CIRCUIT CARD)

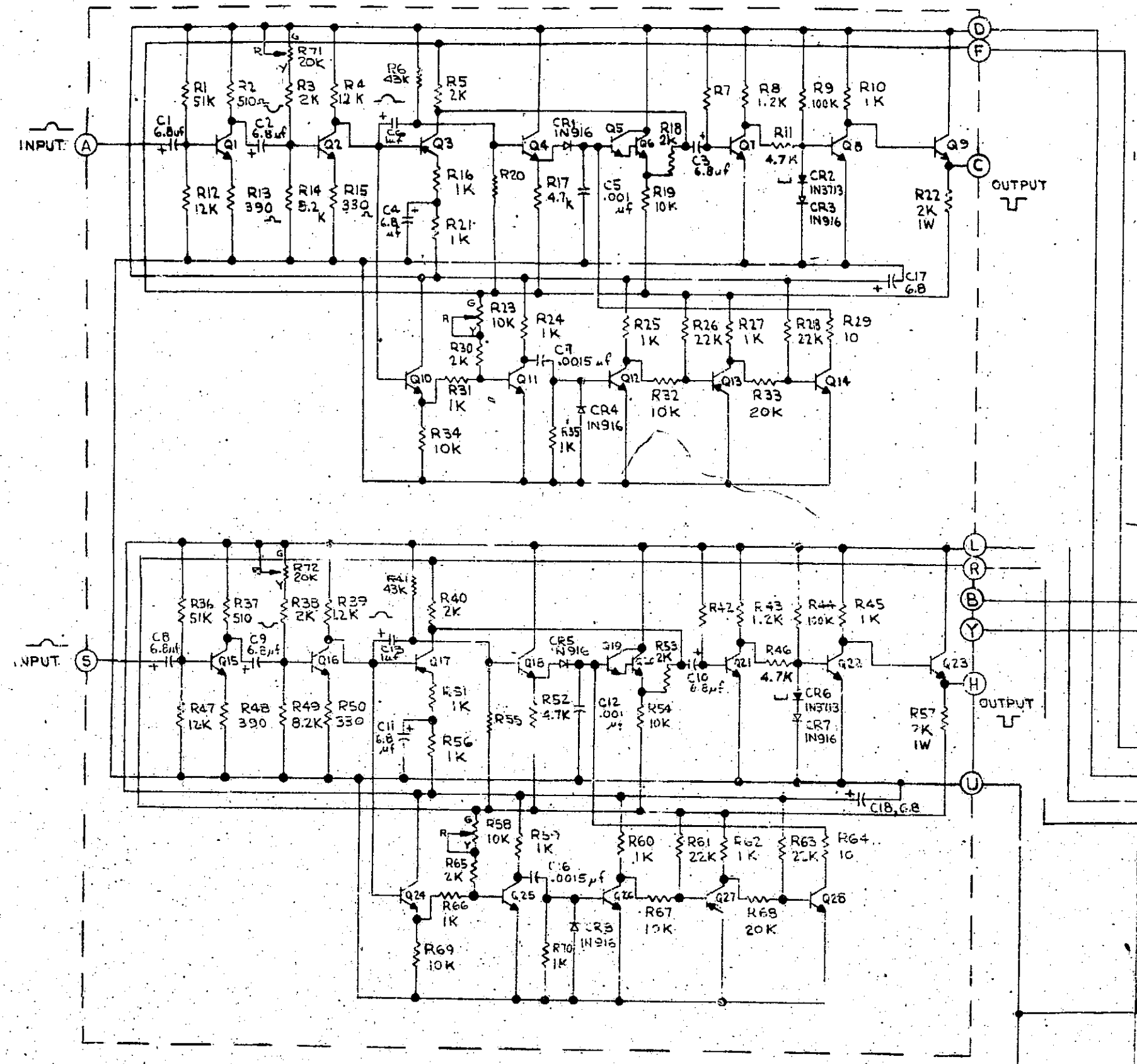


5- POTENTIOMETERS R71, R72 OF C13198-1 & R42 OF C13198-2 ARE LEVEL ADJUST CONTROLS
POTENTIOMETERS R23, R58 OF C13198-1 & R23 OF C13198-2 ARE DISCHARGER ADJUST CONTROLS

4- RESISTORS R7 OF-1, R42 OF-1 AND R7 OF-2 SELECTED TO BIAS Q7 OF-1, Q20 OF-1 AND Q7 OF-2 RESPECTIVELY, JUST INTO SATURATION AT +60°F

5- RESISTORS R20 OF-1, R55 OF-1, AND R20 OF-2 SELECTED TO BIAS EMITTER OF Q4 OF-1, Q18 OF-1 AND Q4 OF-2 RESPECTIVELY, AT +0.5VDC, AT +90°F

2- ZENER DIODES CR5 TO CR10 ARE PS 6817; 15VDC; 400 MW, ON C13198-2

1- TRANSISTOR TYPES

Q3, Q13 ---- 2N1132
Q4, Q10, Q11, Q12, Q14 ---------- 2N697
Q1, Q2, Q5 Q6, Q7, Q8, Q9 ----- 2N834

FOLDOUT FRAME 1

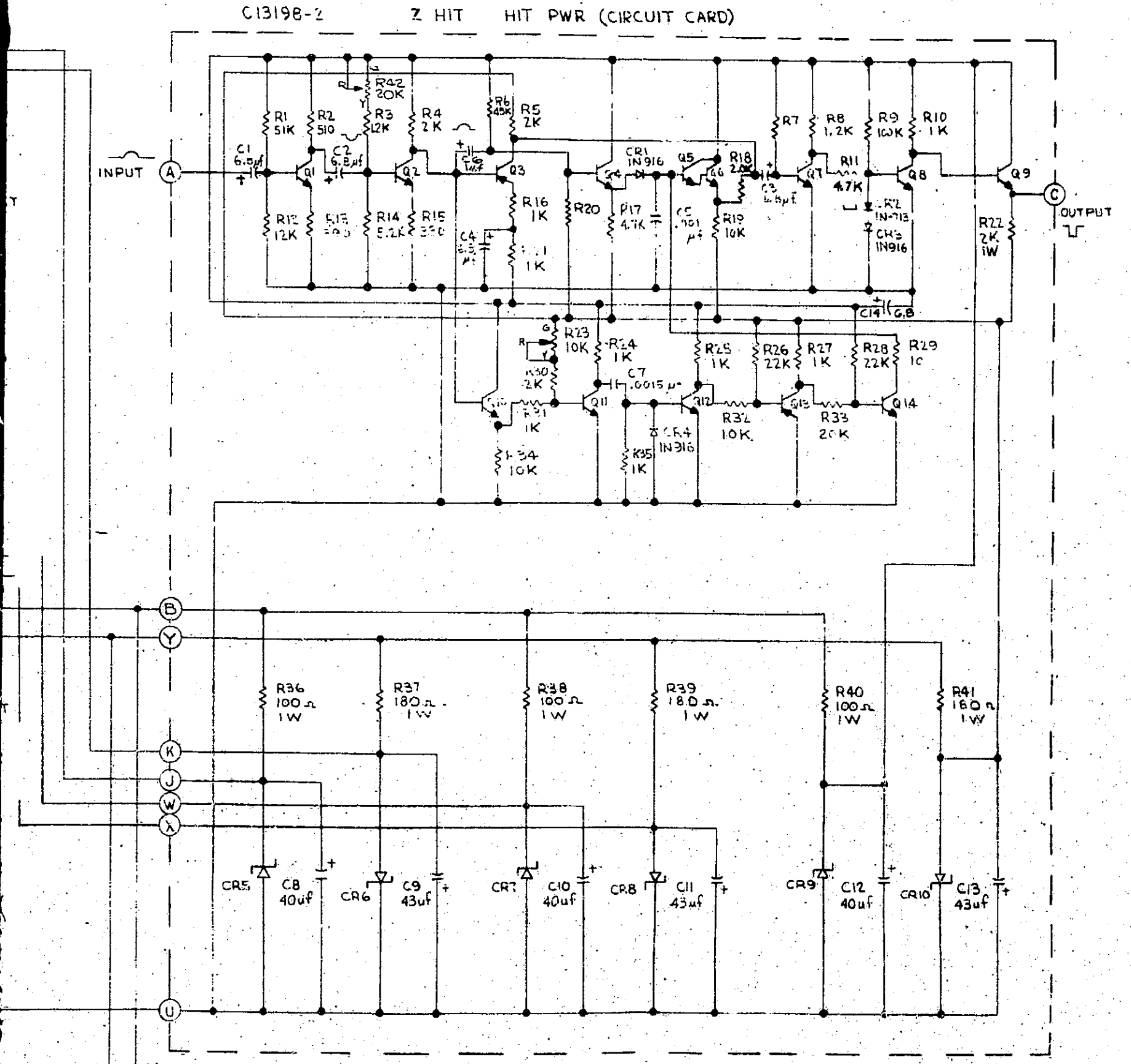


Figure 22. Schematic Diagram of Height-Insensitive Triggers

# SECTION III
# SDMEG SUPPORTING EQUIPMENT

To implement fully the evaluation of the gyro performance in this program, several supporting items were needed. These items are described in this section. Block diagrams of electric and electronic equipment are included.

The major supporting equipment items needed in this program were

- Control panels for gyro functions and associated power supplies
- Automatic-start function sequencer
- Data processing unit and associated power supplies
- Rotatable table about vertical axis
- Leitz dividing head and mounting stand
- Fixture for mounting gyro onto dividing head

Two control consoles were built, each of which housed the suspension power supply and the control function panels. Each console was adapted to receive the auto-start sequencer unit, but can be operated independently of it. The data processing unit was patterned after one built in 1963 for the Air Force and is housed in two racks. A rotatable table used in earlier ESG programs was available for use at Honeywell Aerospace facilities in Minneapolis, and a dividing head was available on a consignment basis at the same facility. A mounting stand and gyro mounting fixture were designed and built for use with the table and dividing head.

## CONTROL CONSOLES

Two control consoles were built under this development contract. Each console contains all of the power supplies and control functions needed to operate the SDMEG. The console consists of a network of panels, all of which are mounted in a 61-inch rack cabinet. A block diagram of the console is shown in Figure 23.

Four panels in each console contain wired units available from vendors:

- Vacuum Panel -- The vacuum panel contains the ion getter pump and flash supplies. Included is an ion gauge for measuring the gyro housing vacuum.

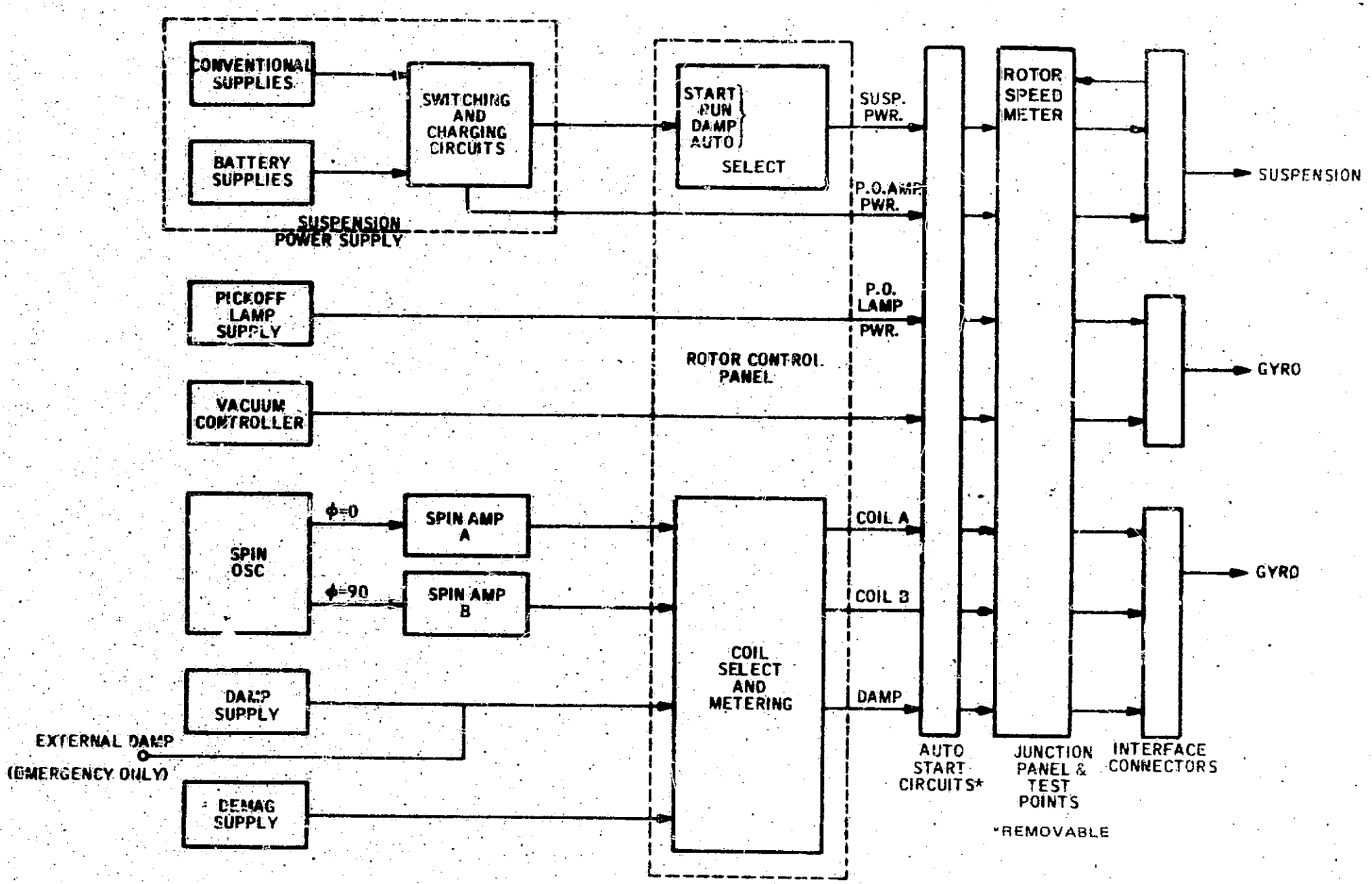


Figure 23. Control Console Block Diagram

- Damp-Demag and Pickoff Lamp Panel -- The power supply for the pickoff lamps is mounted in this panel. A d-c supply for damping and rheostats for controlling demagnetization are included.

- Spin Panels (2) -- The spin supply is a two-phase power supply consisting of two amplifiers and an adjustable oscillator.

Minor wiring was done by Honeywell on these panels to facilitate inter-panel cabling and connections.

Three panels in each console were assembled and completely wired at Honeywell:

- Suspension Power Panel -- The suspension power panel contains the power supplies needed for operating the gyro electronics subassembly.

- Rotor Control Panel -- The operating mode selector switches are mounted on this panel.

- Junction Panel -- This panel provides easy access to all wires leading to the gyro and suspension. Included are test points for measuring capacitance bridge signals and error channel feedback voltages.

Figure 24 shows a front view of the console, complete with the auto-start panel at the top and a blower unit at the bottom. Each console can be operated with or without the auto-start sequencer panel in the console. An interior view of the console is shown in Figure 25; when connected as shown, the auto start is a functional part of the console. The auto start can be electrically removed by interchanging the large cable connections on the left-hand sides of the junction panel and the auto-start sequencer panel. The latter can then be disconnected and physically removed from the console.

Figure 26 shows the suspension power panel in greater detail. The power supplies and emergency batteries can be locked on with the key-operated switch to protect the gyro from an inadvertent shutdown by personnel not familiar with the equipment. The other switches connect the panel-mounted meters into or across the four supply lines. Green indicator lights (lower row) are on when the regular power supplies are energized and available for use. Red indicator lights (upper row) show when the emergency batteries are being used. The arc alarm light is tripped when an excessively high pressure is sensed in the gyro.

The rotor control panel is shown in Figure 27. Meters are mounted for monitoring spin and damping currents. The gyro mode of operation is selected with the switch on the left. A spring-loaded cover protects the switch from

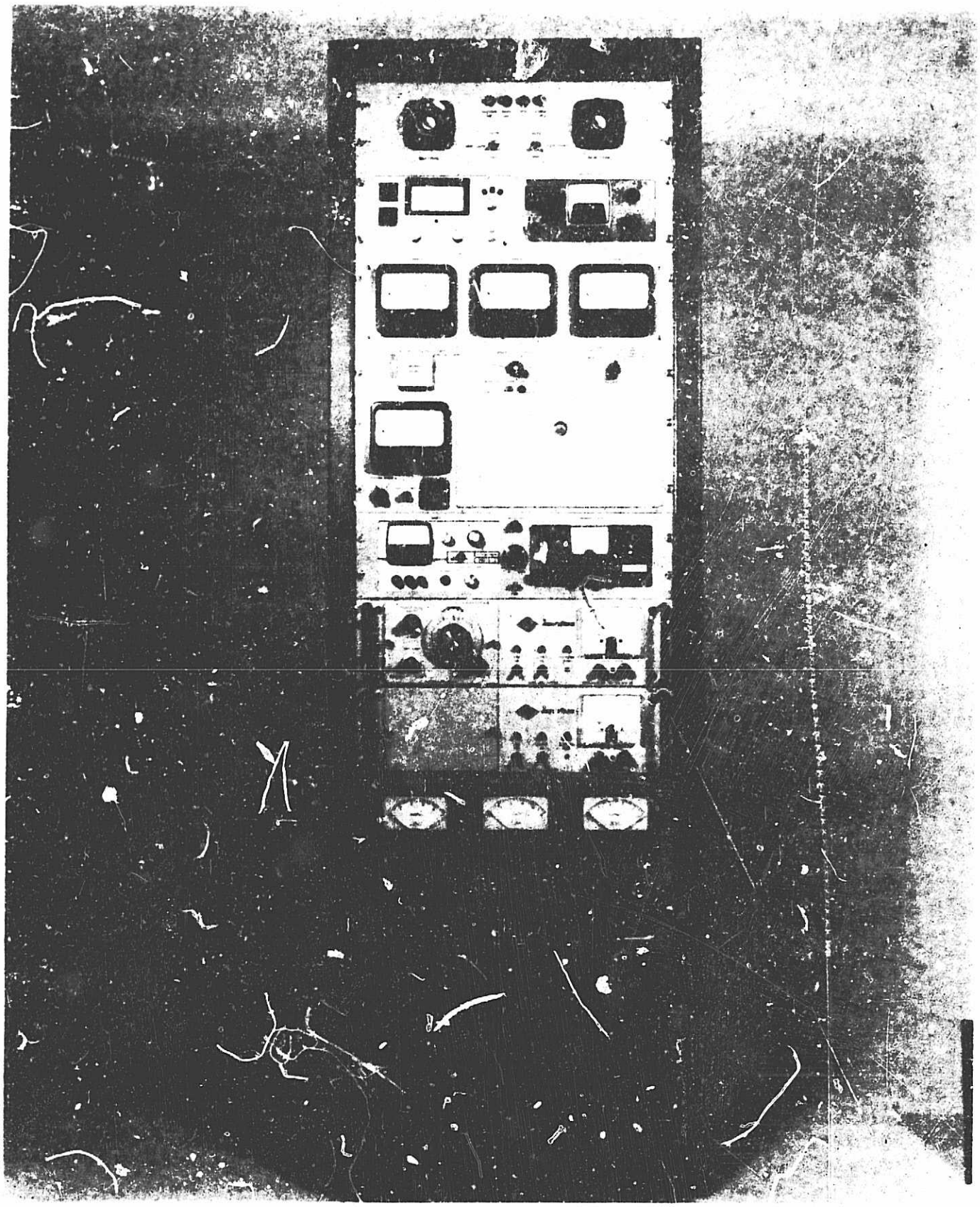

Figure 24. JPL SDMEG Control Console

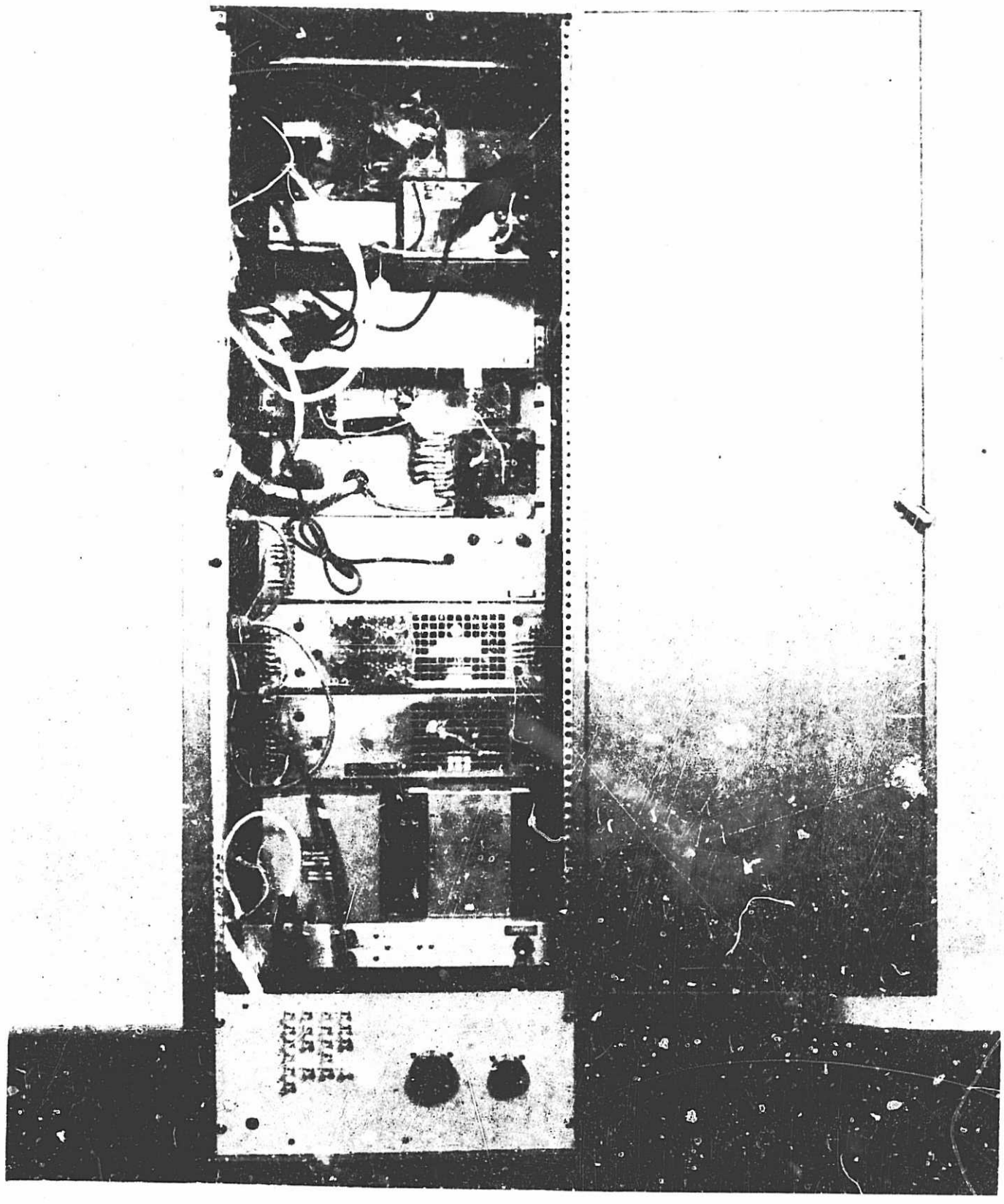

Fig. 21 - 25 Interior View of Control Console

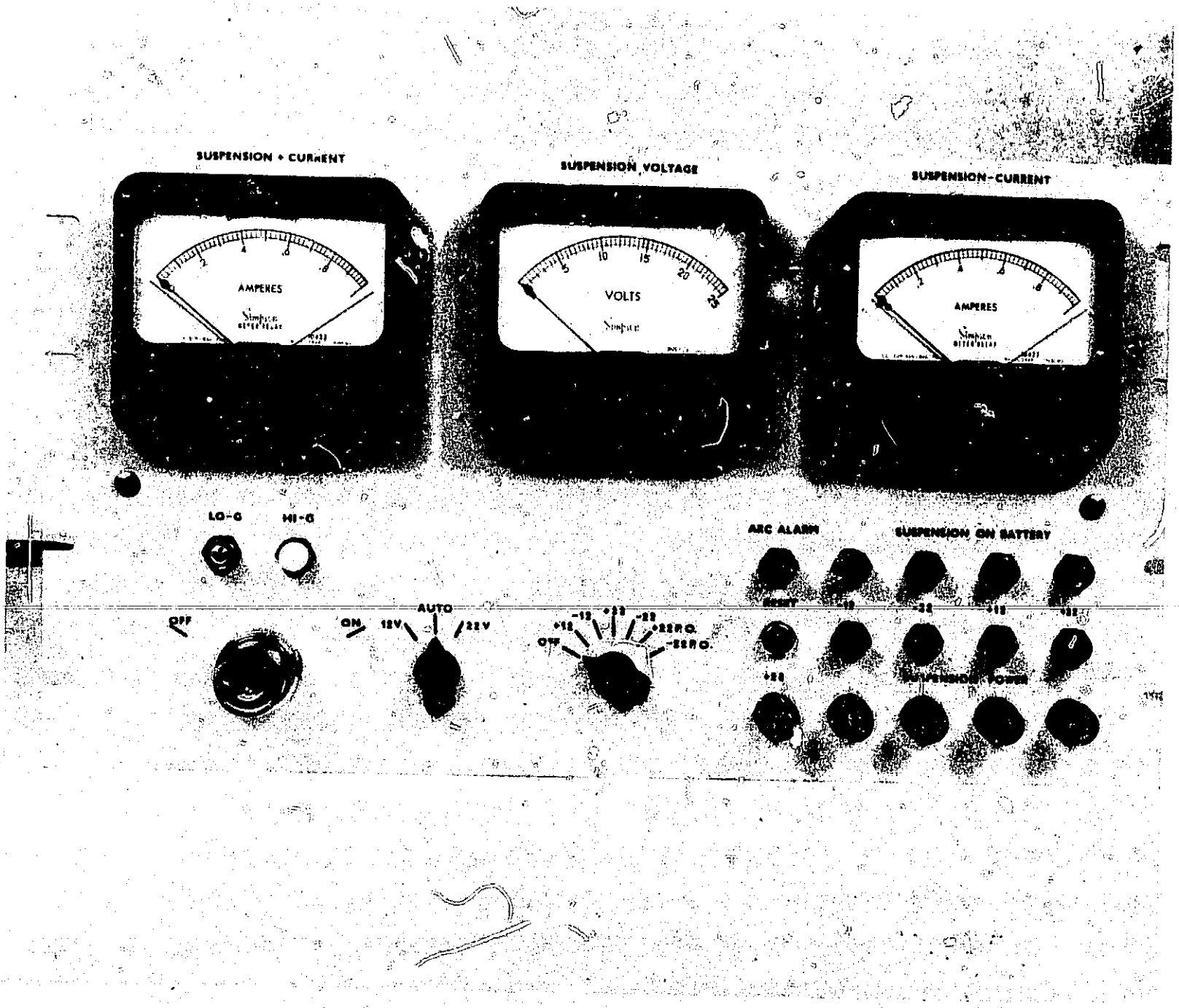


Figure 26. Console Suspension Power Panel

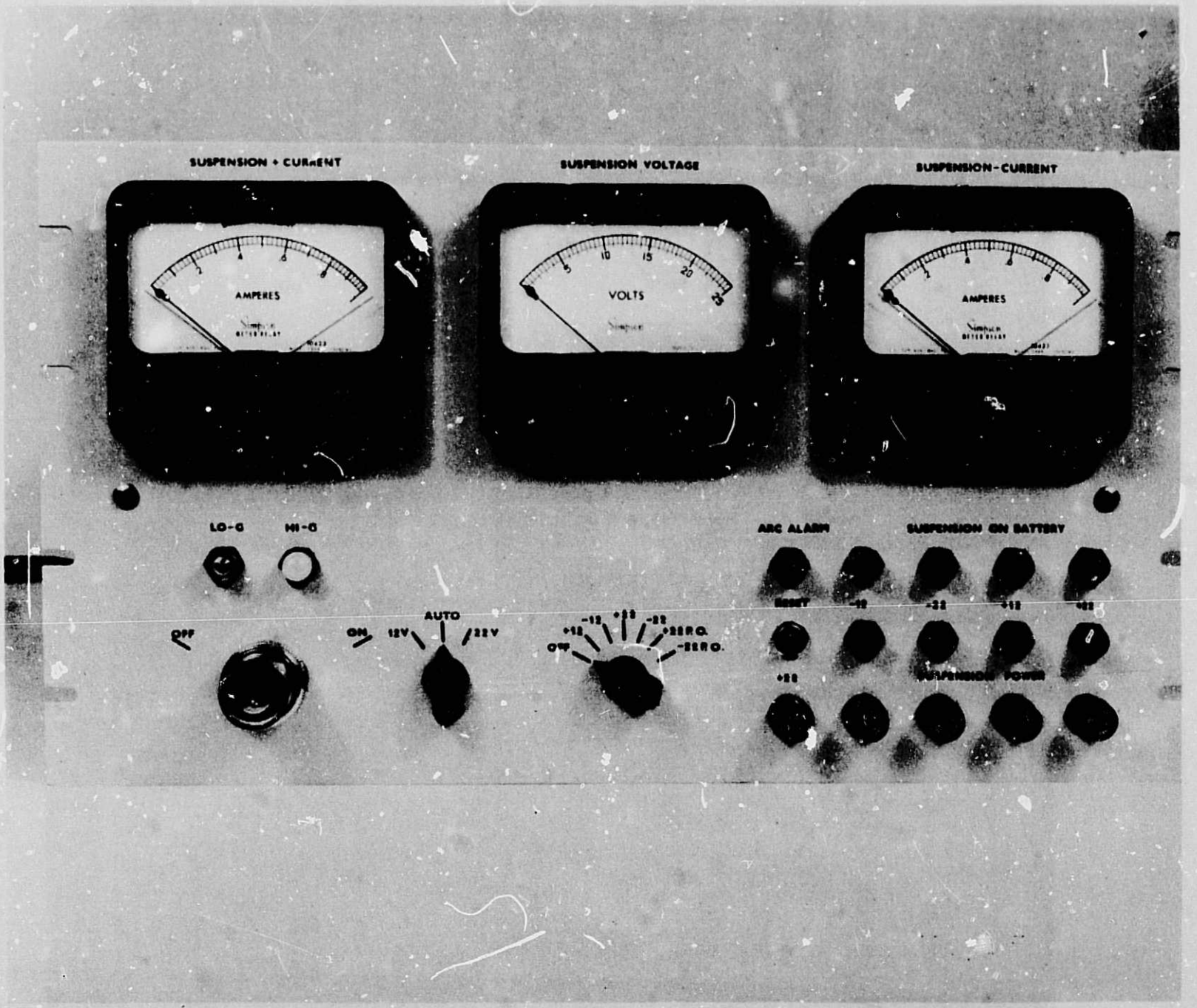


Figure 26. Console Suspension Power Panel

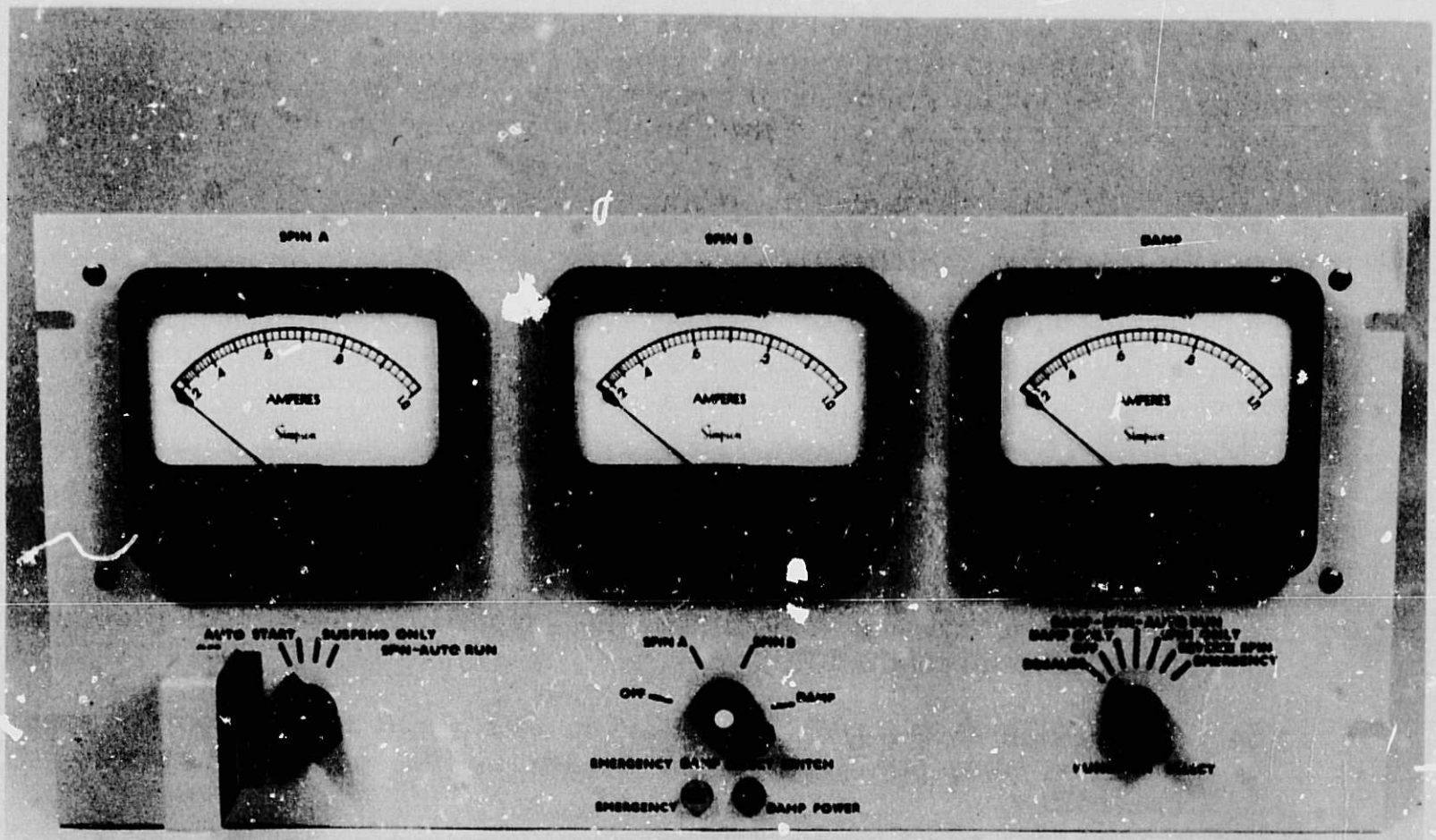


Figure 27. Console Rotor Control Panel

being inadvertently disturbed. When in the "suspend only" position, the spin power lines are not connected to the coils. If excessive pressure is sensed, suspension power is automatically shut off to avoid arcing. When in this mode, the gyro can be left suspended without an operator in attendance. With the switch in the "spin - auto run" position, the spin power lines are connected and the arc alarm trip is locked out.

The center switch directs damping current to the various coils for slowing down the rotor. Either normal damping supply or emergency damping supply (from a battery cart plugged into the panel jacks) is directed by this switch. The function-select switch defines the type of control operation to be performed on the gyro. To avoid dangerous transients, the execution of what operation is selected is governed by use of the rheostats mounted on the power supply units themselves.

## AUTOMATIC-START CIRCUIT

The automatic-start circuit consists of series relay controllers whose action is governed by a set of timers. The assembly is designed to interface with either of the two control consoles built during this program with plug-in connectors and cables.

Referring to the block diagram of Figure 28, the starting sequence may be described as follows:

1) Suspension switch from off to auto start (on rotor control panel) sets the suspension relay controller, the suspension reset controller, and the spin-damp controller.

2) Suspension switch from auto start to auto run (on rotor control panel) turns on pump power and enables a line to the suspension relay controller.

3) When pressure indication is OK, the suspension relay controller operates suspension relay and turns on suspension power line.

4) Lift is or is not a success. If successful, a one-minute delay is energized.

5) If lift is not a success, current and pressure will be high. These quantities are sensed, and, if not back to normal in one second, the suspension reset controller turns off the suspension power, waits for the pressure to return to normal, and then re-energizes the suspension relay.

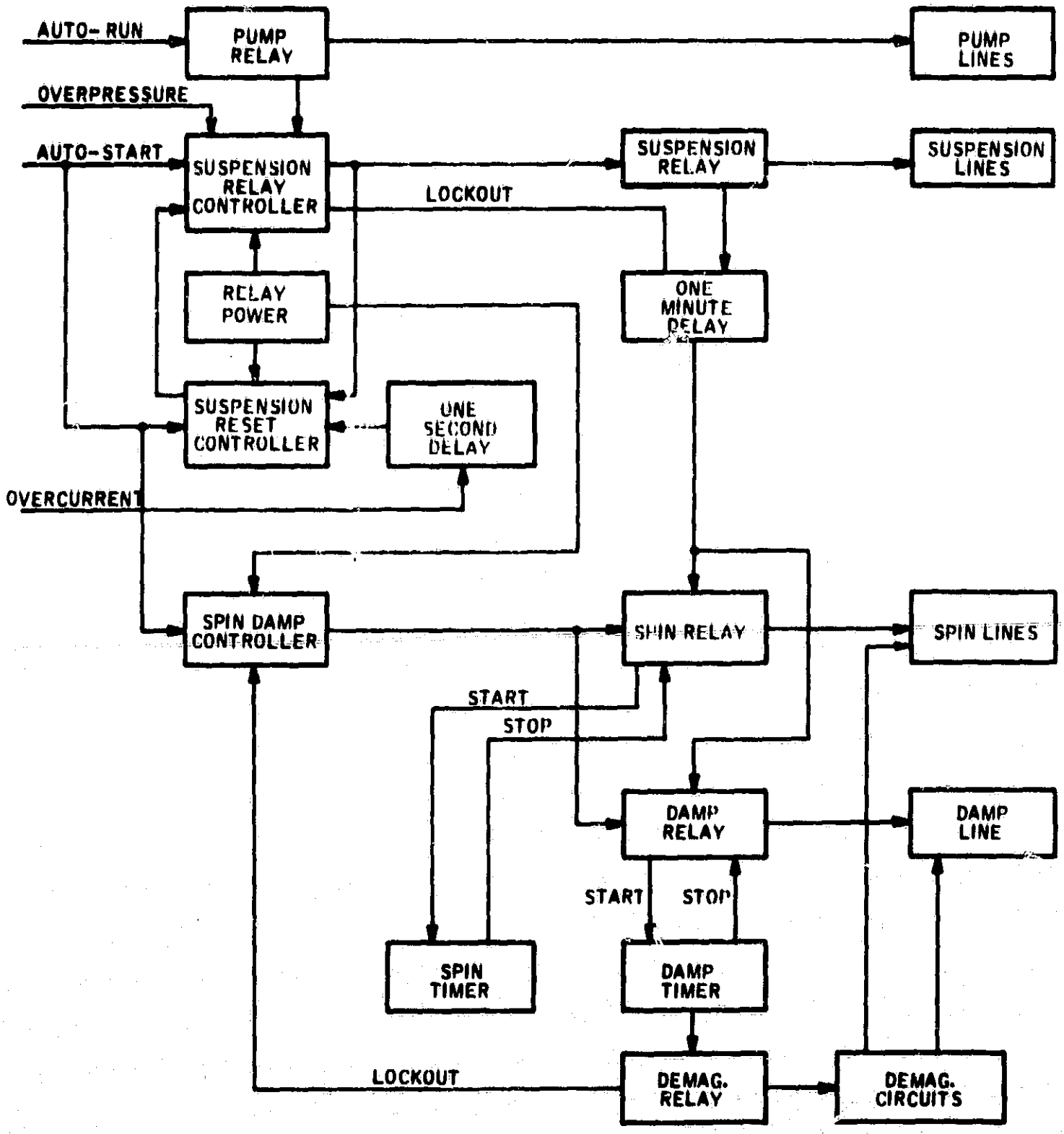


Figure 28. Automatic Start Block Diagram

6) After the one-minute delay time the suspension controller is locked out and a start signal is sent to the spin-damp relay.

7) The spin-damp relay applies spin and damping power simultaneously to the gyro coils. The spin-damp timers are energized.

8) After the spin cycle is complete, the timer opens these lines.

9) After the damp cycle is complete, the timer opens this line and energizes the demagnetize relay which sends a decaying sinusoidal pulse to the gyro coils.

10) When the demagnetize relay drops out (approximately 0.5 second), it locks out the spin-damp relay controller and the starting cycle is complete.

Figure 29 shows the auto-start sequencer assembly. Two switches are mounted to control its operation. To energize the unit, the mode select switch is set in the "auto" position. The start signal described in Step 6 is sent to the spin-damp relay through the spin-damp switch mounted on the front panel; subsequent steps in the starting cycle are performed if this switch is in the "auto" position. Lights are also mounted to indicate the stage of the starting operation.

## DATA PROCESSOR

The data processor records strapdown ESG test data on paper tape by scanning and routing the data to the punch. The paper tape is routed so that page copy of the data is produced immediately by a Flexowriter. A minimum of six data words is recorded, providing time, spin vector direction information, rotor speed, and a test identification. As many as six digitized voltages can be added to the data which are measurements of gyro parameters that are deemed pertinent to the test being conducted. The processor is capable of handling data from two gyros simultaneously. All data processor components are housed in two racks, a 61-inch unit and a 30-inch unit. Figure 30 is a block diagram of the data processor.

### Vendor-Supplied Components

Seven major units making up the data processor were vendor supplied and were used with few or no modifications.

Time Interval Counters (TIC) -- Two Hewlett Packard H0405275A counters measure the time from an input pulse on the START line to an input on the STOP line. These counters are shown in Figure 30 as TICA and TICB. Each

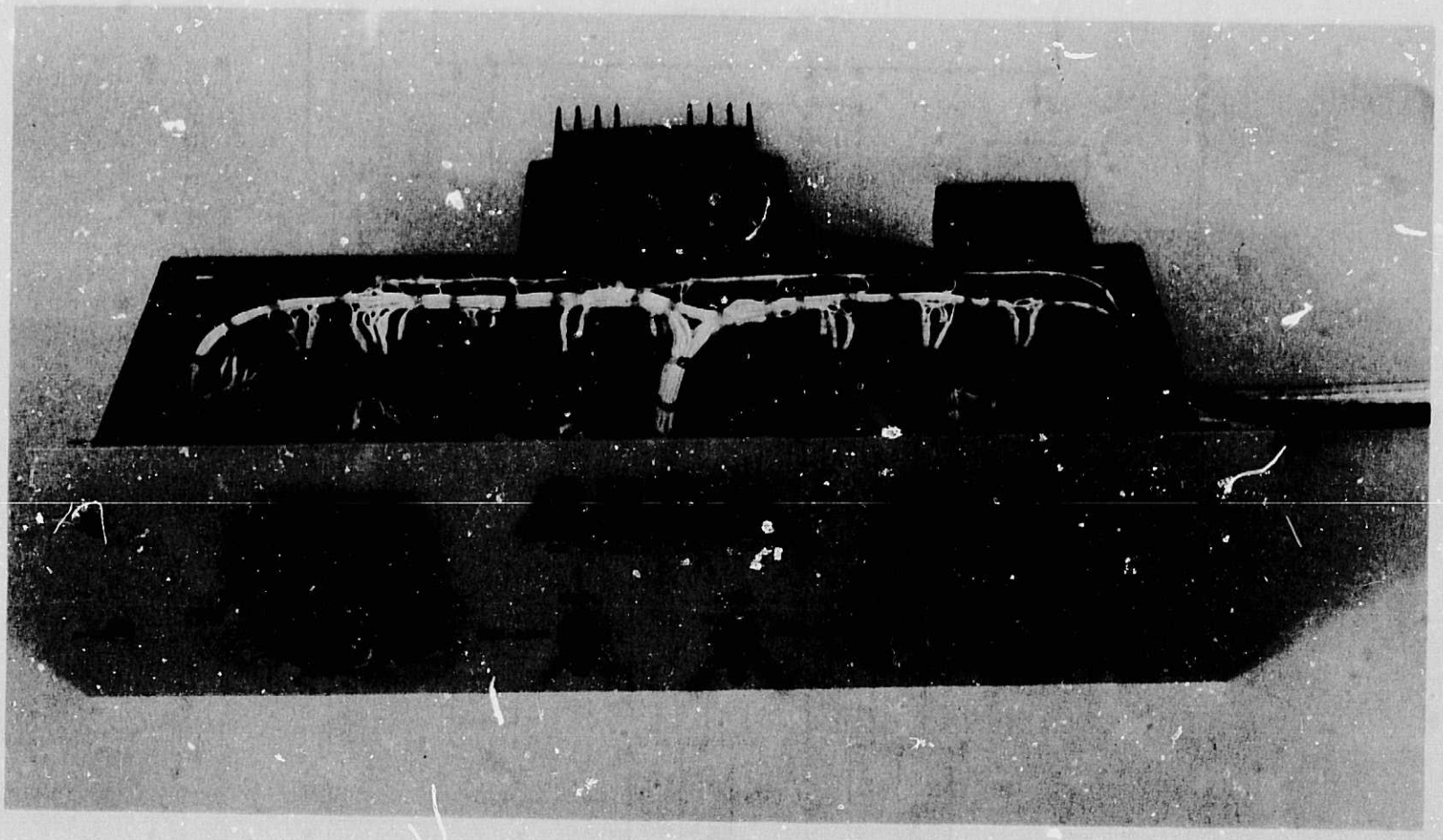

Figure 29. Automatic-Start Sequencer Panel

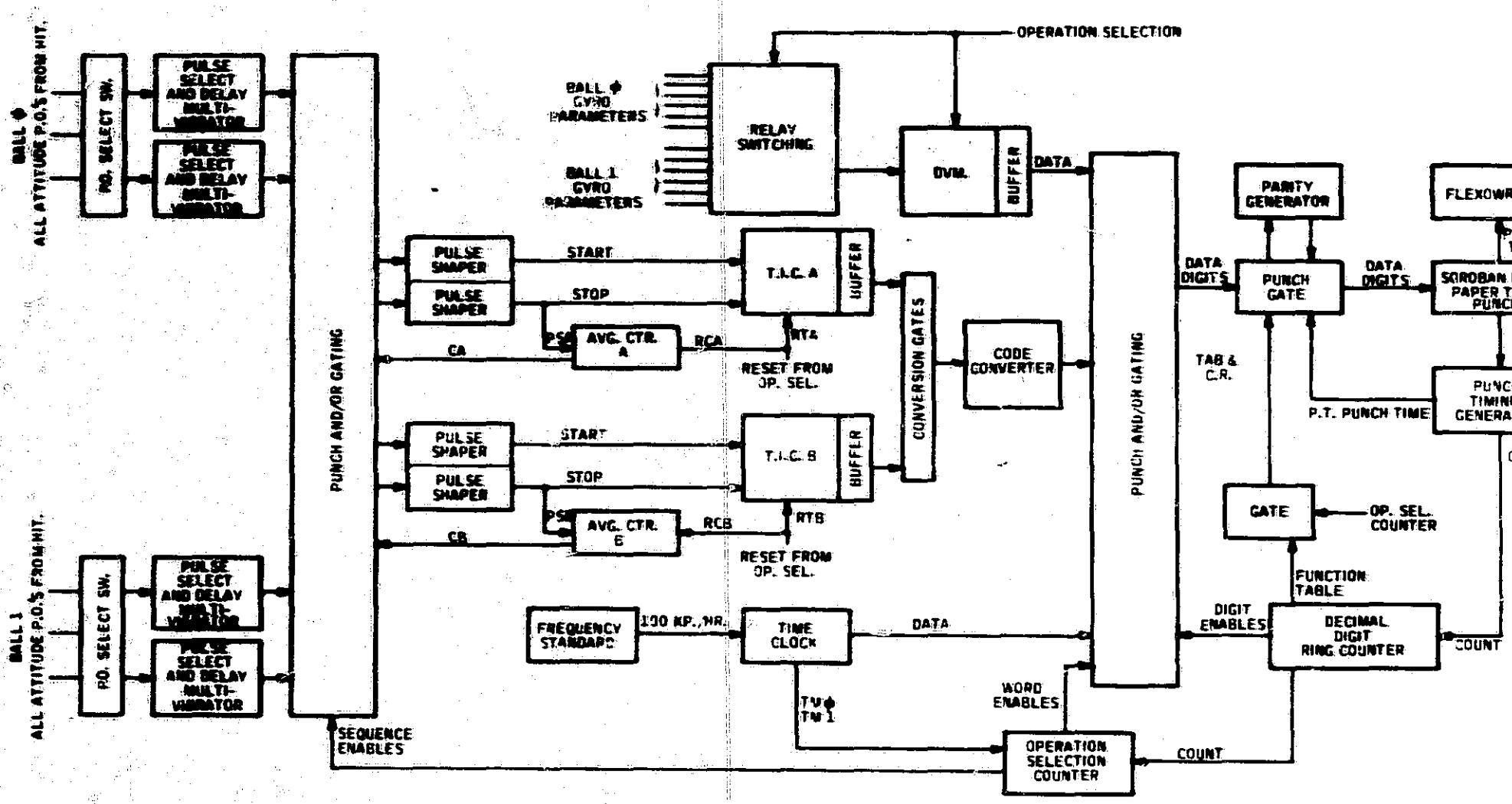


Figure 30. SDMEG Data Processor Block Diagram

counter may be started and stopped several times before it is RESET. The START and STOP pulses are positive-going pulses from -12 volts to ground produced by pulse-shaping circuits in the logic. The RESET pulse is produced by an LC201 level converter logic circuit. The time interval counter (TIC) digital output code is 1-2-2-4 and is changed to 1-2-4-8 code by a section of the data processor logic. The counter was modified to prevent the START pulse lockout flip-flop from inhibiting later START pulses.

Frequency Standard -- The H17-100ER frequency standard is manufactured by Hewlett-Packard. It provides 20-kp/sec,* 100-kp/hr, and -1MHz/sec signals for the data processor. The pulse signals are shifted by LC200 buffer amplifiers into the standard logic levels. The 1-MHz/sec signal is multiplied to 100 MHz/sec in the TIC. The 100-MHz/sec signal is counted in the TIC to provide a 10-nsec time interval resolution. The 100-kp/hr signal drives the logic time clock. The frequency standard has a short-term stability of ±3 parts in $10^8$ and a long-term stability of ±5 parts in $10^8$.

Digital Voltmeter -- The Beckman 4011 RVP digital voltmeter digitizes six measured parameters from each of the two gyros. The voltages are selected by relays in the logic. A relay closure between the READ COMMAND lines causes the meter to balance. After it balances, a PRINT COMMAND signal is sent to the logic. The output of the DVM is 1-2-4-8 binary coded decimal (BCD).

Soroban LP-2-150-P Tape Punch -- The LP-2-150P Soroban punch punches tape at 150 characters per second. The synchronization signal from the punch drives the timing signal generator circuit in the logic. The inputs to the punch are supplied by the punch driver circuits.

The punched code is designed to be compatible with the Friden Flexowriter. The character set punched by the unit consists of the 10 numeric characters, tab, carriage return, and space.

Flexowriter -- A Friden Flexowriter prints out the punched paper tape, an operation used to discover marginal operation as soon as possible and to provide data for real-time plotting during a gyro run. The Friden Flexowriter, Model "SFD" has the following additional characteristics:

- 8-channel
- 16-inch
- Automatic parity check
- Radio interference elimination (includes isolation transformer)
- Tape winder

*kp = kilopulses

- External terminals for control (start, stop) of tape reading
- Tape puncher

A tape-operated microswitch is used to control the Friden when it is reading tape from the Soroban punch. The standard Friden 8-channel SPS code is used.

Tape Drivers, Reels -- Reels for playing out and collecting the tape as it is punched occupy one panel. Included are pulleys and clutches to route the tape through the punch and flexowriter with a minimum risk of damage to the tape.

## Honeywell-Built Components, Logic

Four panels in the data processor were assembled and wired by Honeywell before they were installed into the 61-inch rack. The power supplies for the two logic drawers and the punch solenoids are mounted on two panels and installed in the lower section of the 61-inch rack. The other two units are logic drawers containing Raytheon standard logic cards and some Honeywell-built cards.

Delay Multivibrator -- A delay-multivibrator is used to detect two lines in close succession. When using a cosine pattern as shown in Figures 1 and 2 for reading spin vector direction, an extra line is used to detect which line is crossing the pickoff field of view. Also, a pulse width selector is used to gate through pickoff signals and discriminate against rotor reflectivity variations and arc marks.

Pulse and/or Gating -- The pulse and/or gating block handles all of the high-speed gating of the data processor. The major outputs are the start and stop pulses from the line-crossing detectors which feed the pulse shapers. The high-speed pulse signals from the HIT circuits are gated by the pulse shapers to the time interval counters, under control of the operation selection information.

Pulse Shaper -- Pulse shapers improve the incoming rise time from approximately 100 nsec to approximately 10 nsec to operate the time interval counters. An additional output with slower rise time is provided to toggle the averaging counter each time a start pulse is sent to the time interval counter.

Averaging Counter -- The averaging counter is required to allow the averaging of several $C_1$ and $C_1 + C_2$ intervals. To sum a specific number of intervals, the averaging counter counts the number of start pulses sent to the time interval counter; after the prescribed number of start pulses, a signal is sent to the pulse AND/OR gating to inhibit any more start pulses. As many as ten $C_1$ and $C_1 + C_2$ intervals may be summed. Using this technique, the magnitude of the random errors is scaled by one over the square root of the number of intervals summed.

Time Clock -- The time clock provides the time reference for the data processor. Two time mark signals are provided to indicate when data should be read from Gyro Zero and when from Gyro One. The input to the time clock is a signal from the frequency standard of 100,000 pulses per hour. This frequency is counted down to provide time in tens of hours, hours, tenths of hours, hundreths of hours, thousandths of hours, and ten thousandths of hours. A Nixie readout is provided to indicate time information to thousandths of hours. Digital signals are provided to print out time to an accuracy of ten thousandths of an hour.

Operation Selection Counter -- The operation selection counter provides the main sequence control for the data processor. A signal from the time clock indicates the time to take a data point. The operation selection counter then cycles through the entire reading, causing the correct data to be punched out on the tape.

Decimal Digit Counter -- The decimal counter is a ring counter with eight states. During state zero, a control character (CR or TAB) is punched on the tape. During the next seven states, the decimal digits of the information being recorded are punched on the tape. If the data being punched have less than seven digits, the remaining digits are punched as zeros.

Punch AND/OR Gating -- The punch AND/OR gating is a large gating matrix. With the aid of the operation selection counter, the data source (Gyro Zero or Gyro One) is selected.

Data of the correct logic levels, such as the time clock, may be used by the punch AND/OR gating directly. Other data, such as supplied by the digital voltmeter and the time interval counters, are buffered into the proper logic levels.

Code Conversion Circuitry -- The Hewlett-Packard 100-MHz counters have a 1-2-2-4 BCD output. Since the remainder of the equipment was designed to output 1-2-4-8 BCD code, which is compatible with the Flexowriter, the 1-2-2-4 BCD code must be converted to 1-2-4-8 BCD code. This is the function of the code conversion logic which is a part of the punch gating matrix. The presence of the counter outputs on the matrix causes the code converter to change the code to 1-2-4-8 BCD code. Thus, no additional command or enable circuitry is needed to initiate the conversion.

Punch Gate -- The punch gate takes the four-line signal from the punch AND/OR gating and converts it to an eight-line signal of standard Flexowriter code. The eight-line signals are amplified and sent to the Soroban tape punch.

Time Signal Generator -- To operate at a maximum data rate, the selection of the individual decimal digit must be done under the control of the Soroban tape punch. A signal from the Soroban tape punch drives the timing signal generator. The timing signal generator then stops the decimal digit counter in synchronism

with the Soroban tape punch. To give the proper duty cycle to the data feeding the Soroban tape punch, a punch time signal and an advance signal are generated by the timing signal generator.

Pickoff and Relay Switching -- Seven relays are used to select the proper pickoff from the HIT circuits and to select voltages for the digital voltmeter. The three pickoff signals from the HIT circuits are selected by two front-panel switches. The seven voltage selection relays are switched under the control of the operation selection counter while the voltages are being digitized.

## Paper Tape Format

The tape format is designed to produce a concise, easy-to-read page copy when printed by a Friden Flexowriter. The two ESGs that may be handled by the data processor are designated Gyro Zero and Gyro One. An example of the printed-out format when Gyro One is operated is shown in Figure 31.

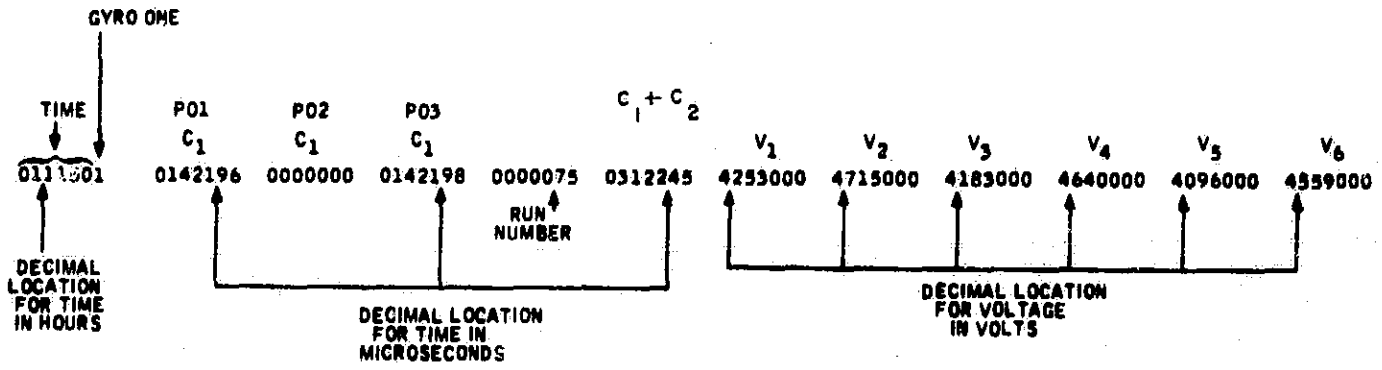


Figure 31. Data Processor Tape Format

Only two $C_1$ measurements are taken at any one time; therefore, one of the three $C_1$ columns will be all zeros. Note that the position of the $C_1$ measurements in the data format indicates which pickoffs are being read.

All words are seven digits; digits which do not contain information are zeros, to simplify the logics. For example, in Figure 31 the three least significant digits in each voltage word are considered to be zero.

## Assembly Description

A front view of the 61-inch rack is shown in Figure 32. At the top of the 61-inch rack are the time interval counters; immediately below them are the logic drawers. Next is the digital voltmeter and the frequency standard. The two power supply panels and a blower unit for ventilation complete the unit. An interior view of this unit is shown in Figure 33. All inter-unit connections are made through the terminals on the bottom panel. The cable from the punch rack is connected at the right; all of the inputs measured or needed are brought in from the electronics subassembly and the control console through the terminals at the left.

Figure 34 shows the units mounted on the 30-inch rack which includes the Soroban punch, the tape handling equipment, and the Flexowriter. Tape is routed through the punch from the right; from there it can be routed directly to the large collection reel on the left side, or to the Flexowriter for a real-time hard copy of the data and the smaller collection reel at the far right. The interior view of this unit is shown in Figure 35, in which motors and clutches for the tape punch and reels can be seen. The cable which connects to the 61-inch rack back panel is shown at the bottom.

Some of the details of the lower logic drawer are shown in Figure 36. To facilitate checkout and maintenance, the lower logic drawer is hinged to swing downward into the position shown.

As a further convenience, several points have been wired to jacks on the front panel.

- A Simulated Pickoff Pulse Input -- The output of an EH-130 generator can be input to the test point. As shown in Figure 37, two circuits have been added to produce simulated HIT pulses and to excite both channels of both gyro inputs. This point is useful in checking out the timing readouts.

- A Timing Pulse Generator Input -- When the circuit shown in Figure 38 is set up and input to this test point, the data processor can be checked out without operating the Soroban punch.

- An External Clock Drive Input -- Use of this test point permits operating the clock at an accelerated speed. This facilitates checkout of the clock timing gates.

- Data Cycle Pulse Output Points -- The pulses which start the data cycle for each gyro (Ball 0 and Ball 1) appear at these points, permitting the synchronization of any peripheral equipment to the processor data cycle.

- Other Output Points -- These provide for checkout of the basic data processor sequences which are essential to its proper operation.

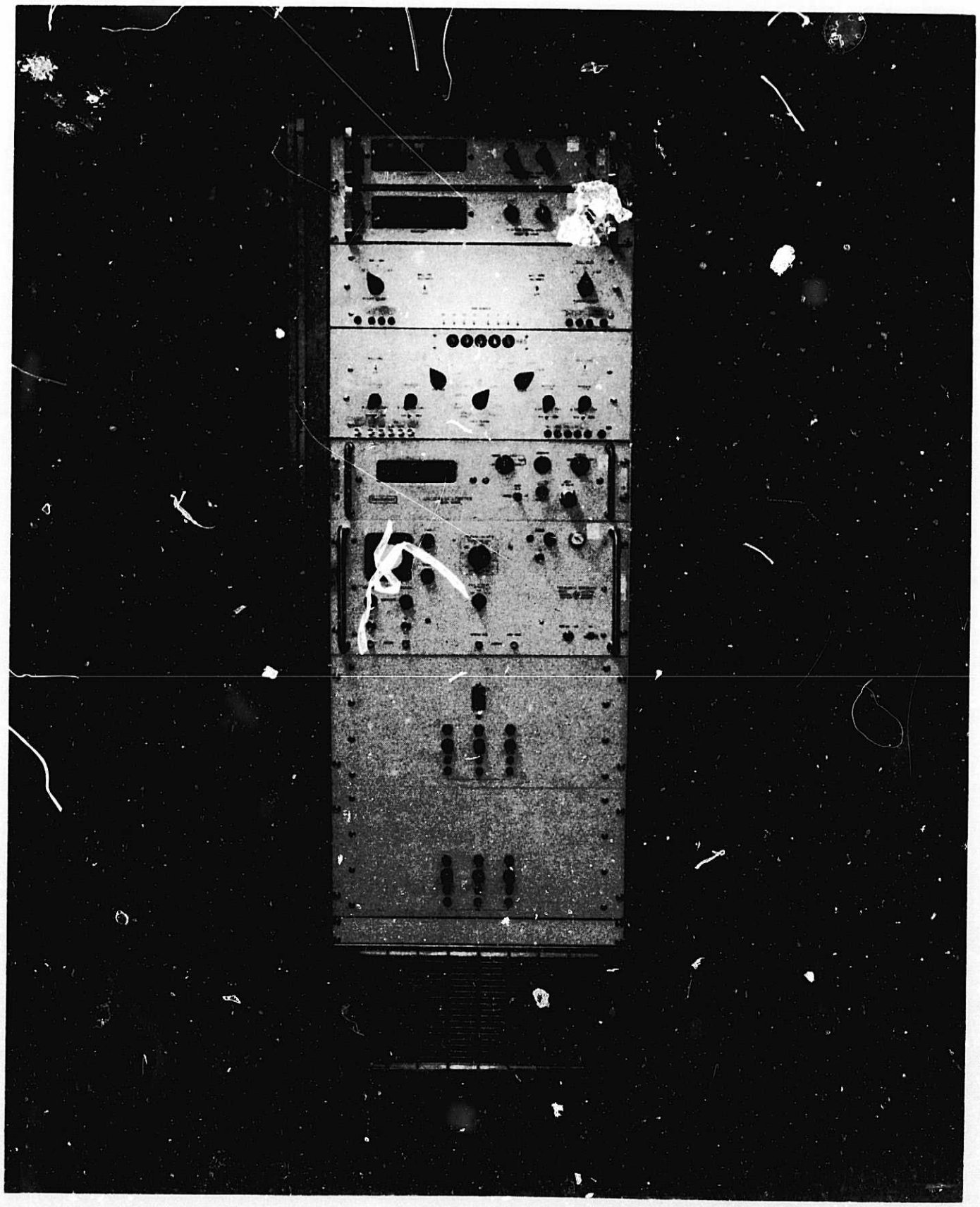

Figure 32. Data Processor, Main Rack

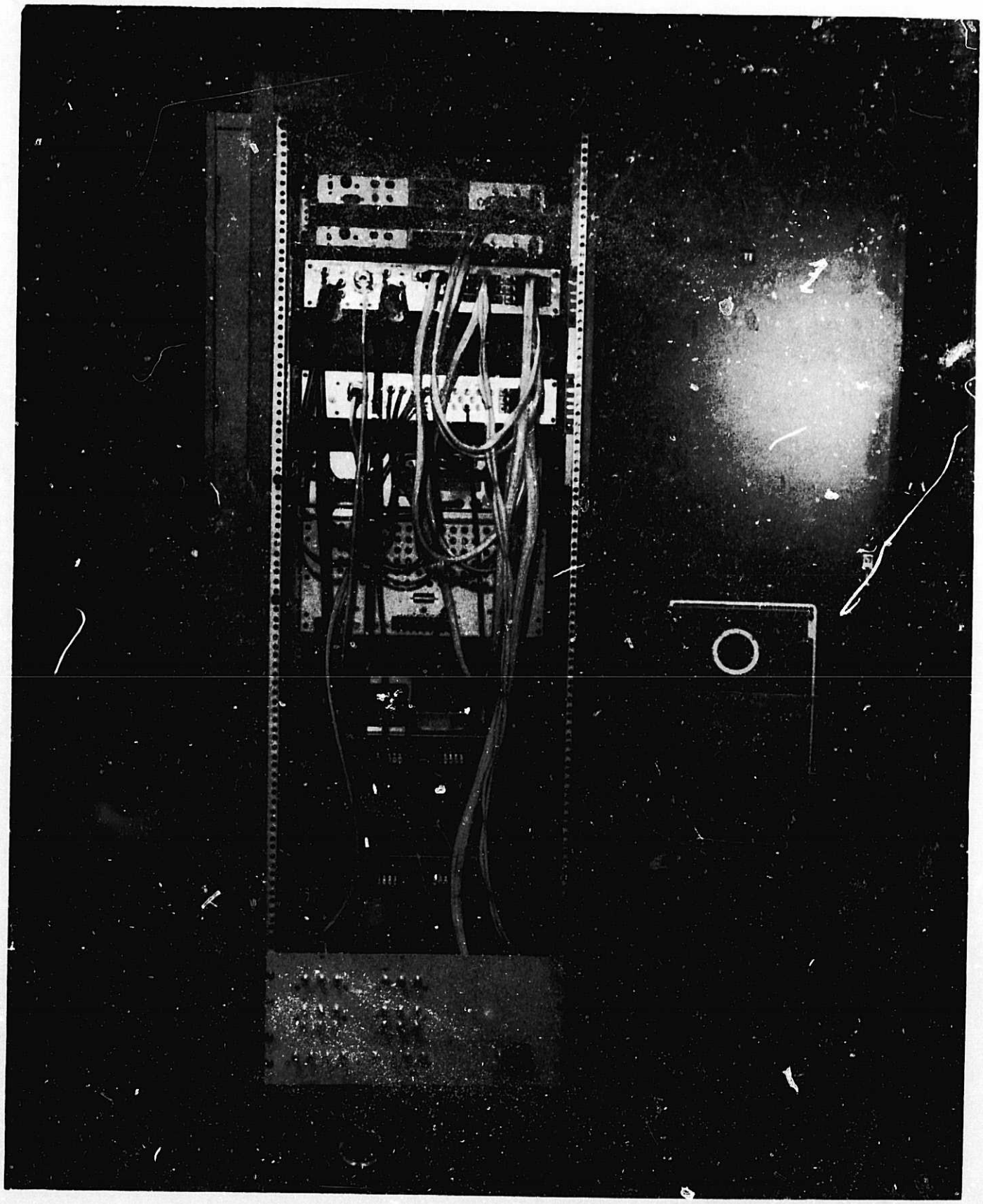

Figure 33. Interior View of Data Processor Main Rack

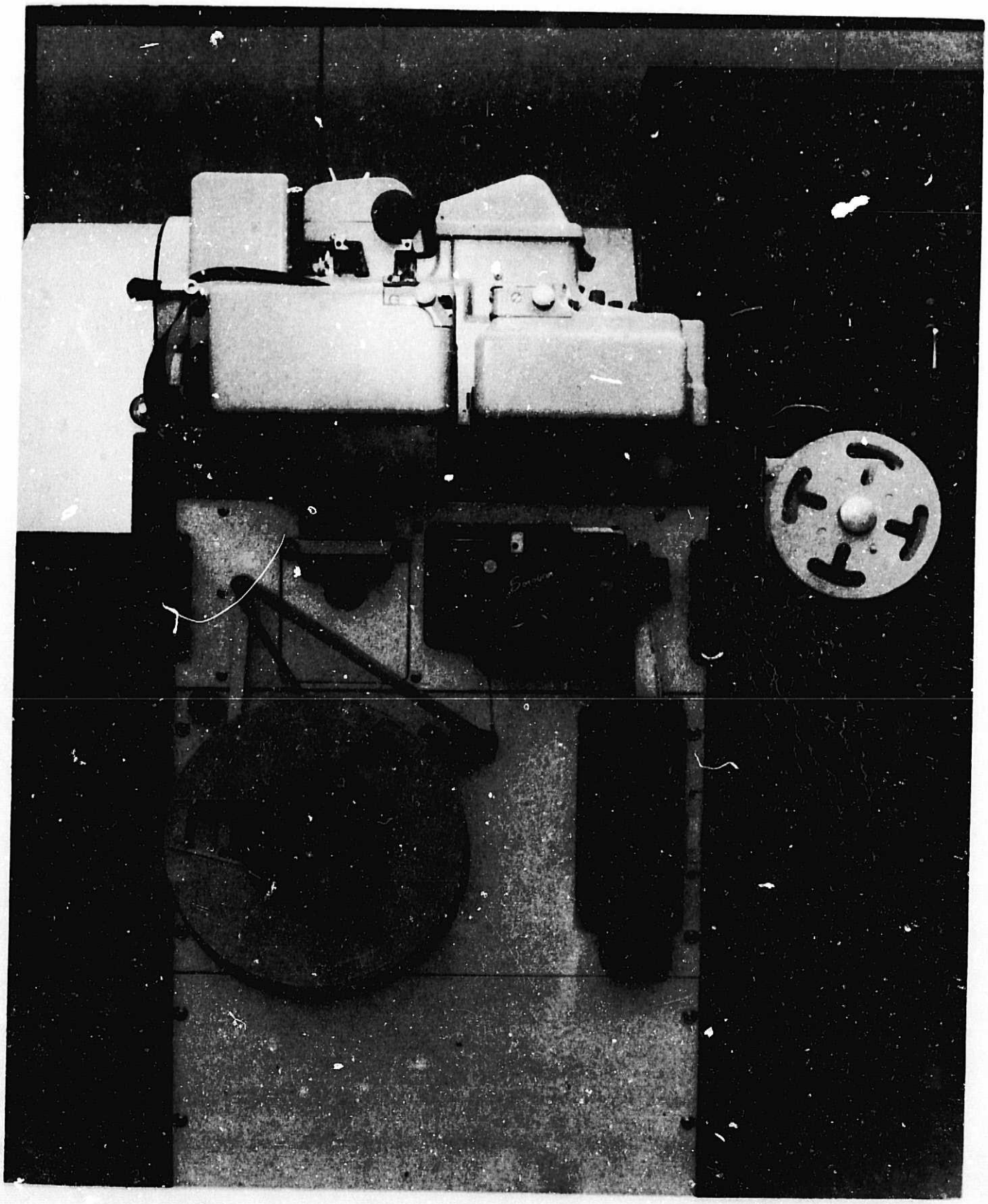

Figure 34. Data Processor Punch Rack

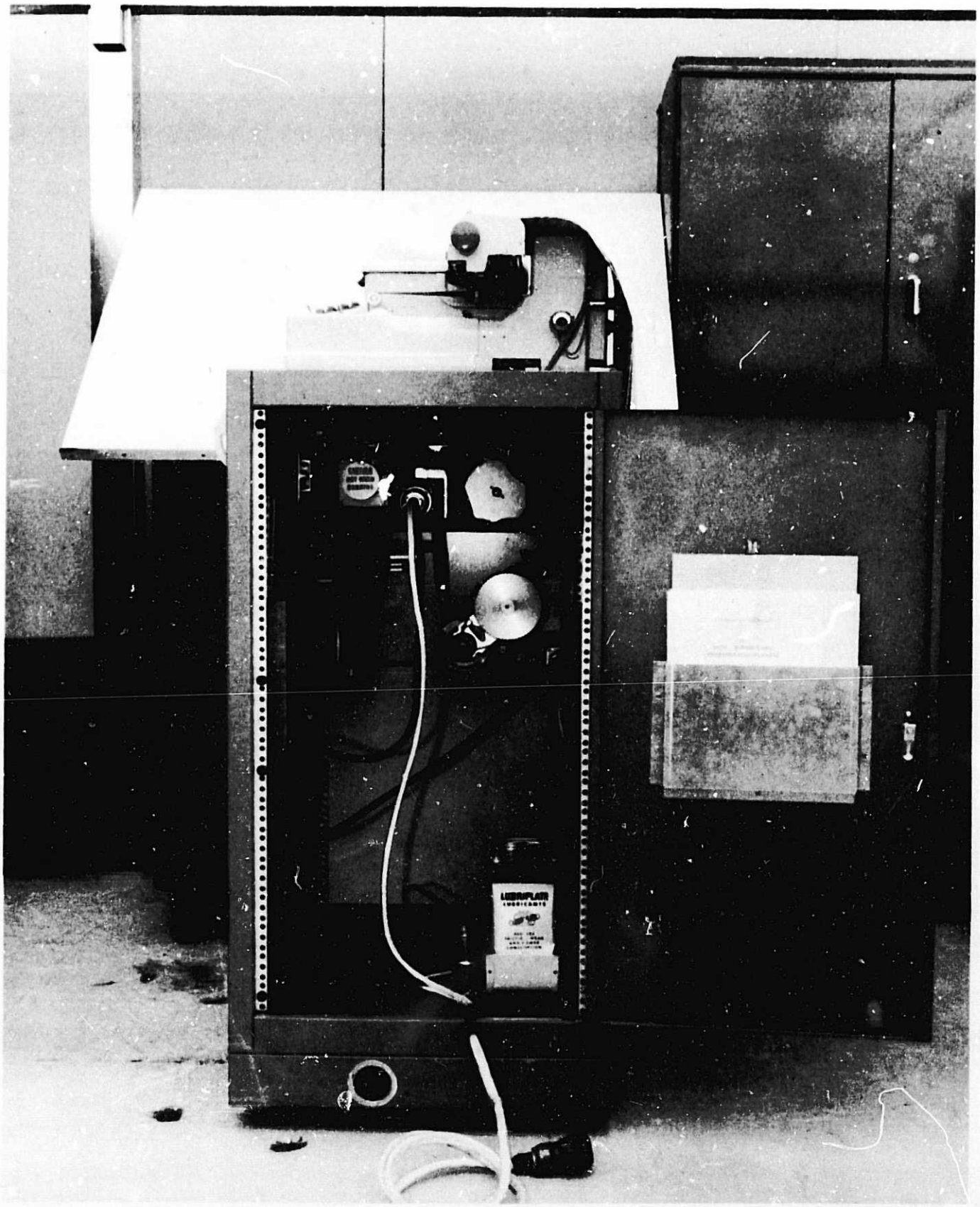

Figure 35. Interior View of Punch Rack

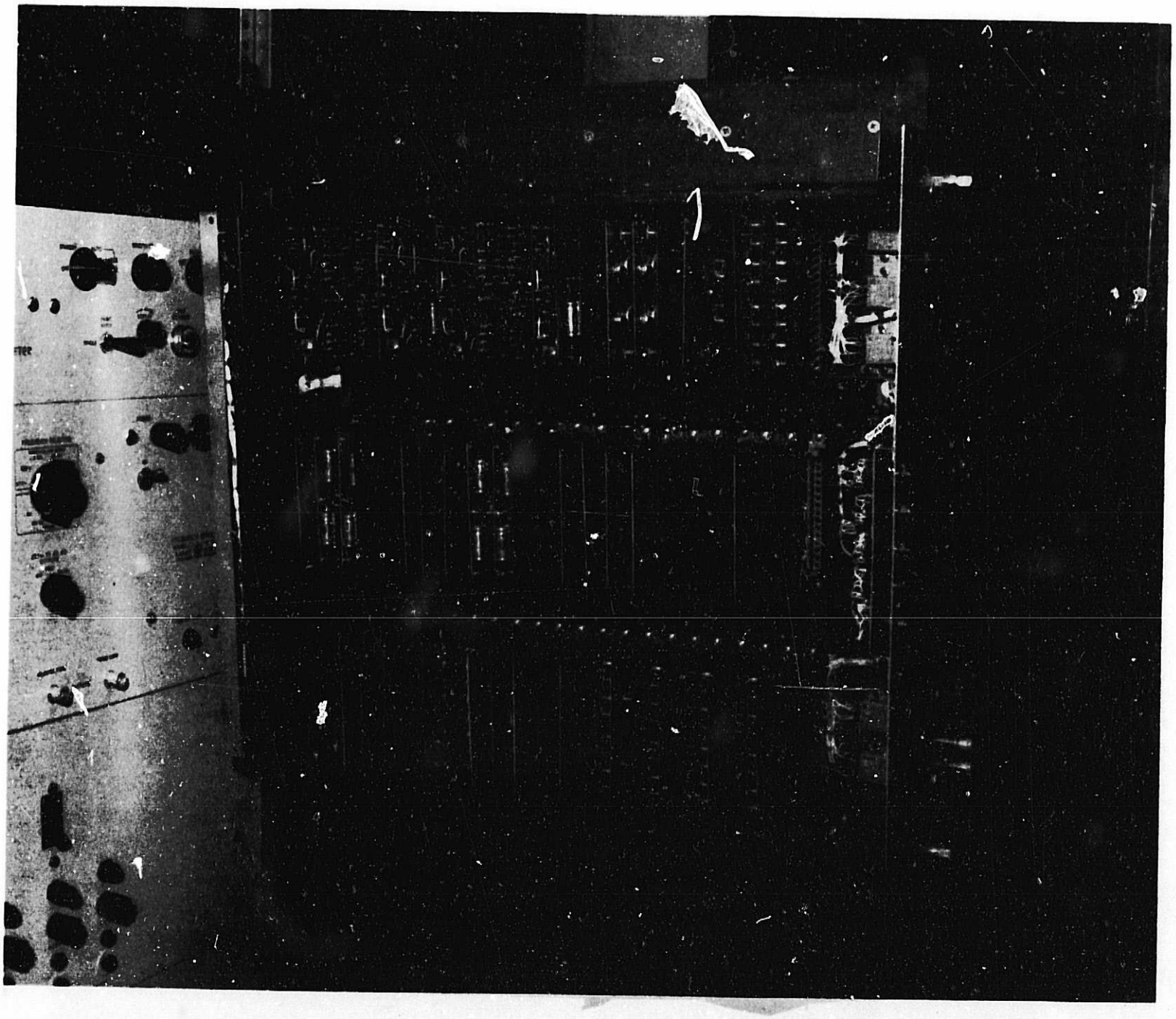

Figure 36. Data Processor Lower Logic Drawer

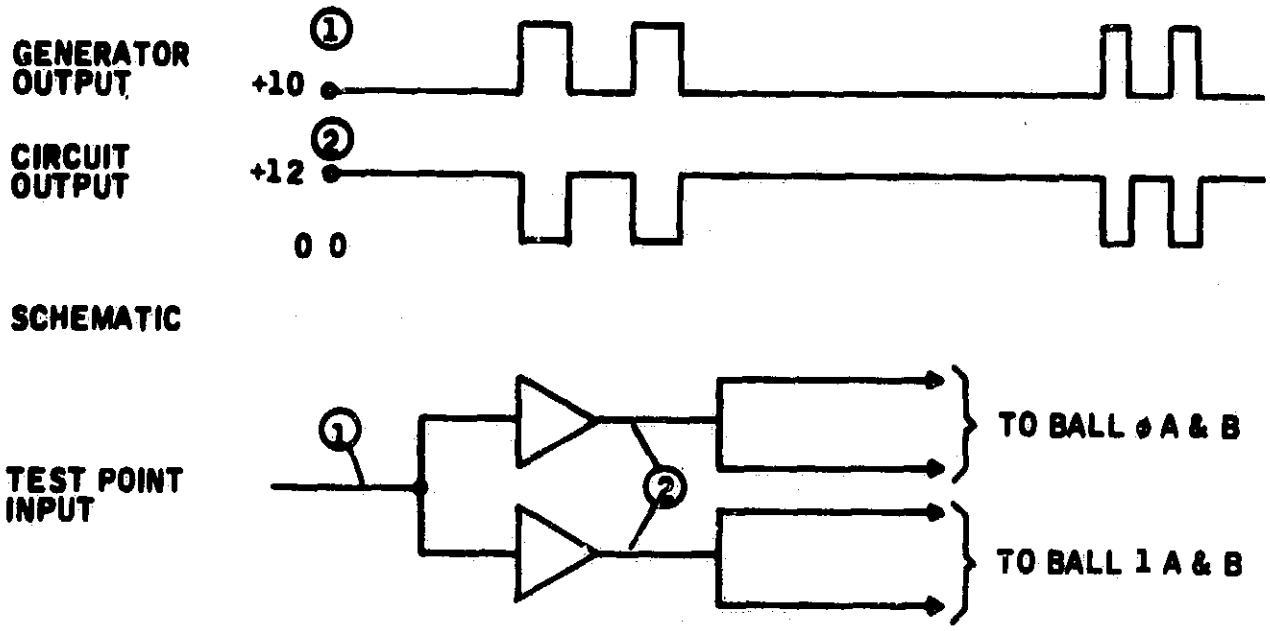


Figure 37. Pickoff Input Simulator Circuit

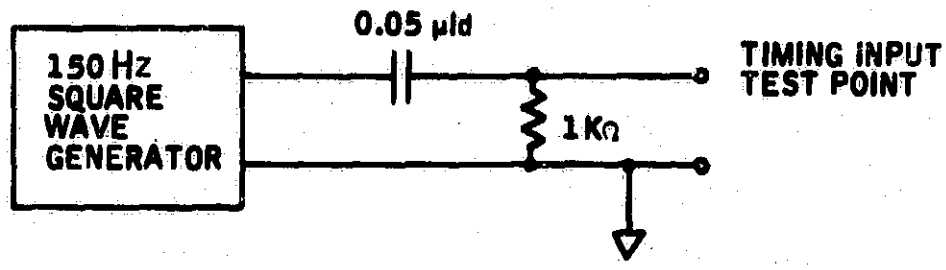


Figure 38. Timing Signal Circuit

## MAGNETIC AMPLIFIER FOR THE DIGITAL VOLTMETER (DVM)

A thermocouple magnetic amplifier was built for amplifying thermocouple outputs to a level satisfactory for input to the digital voltmeter. A block diagram of the amplifier is shown in Figure 39. This unit does not mount into either data processing rack. Figure 40 is a view of the magnetic amplifier chassis without its cover.

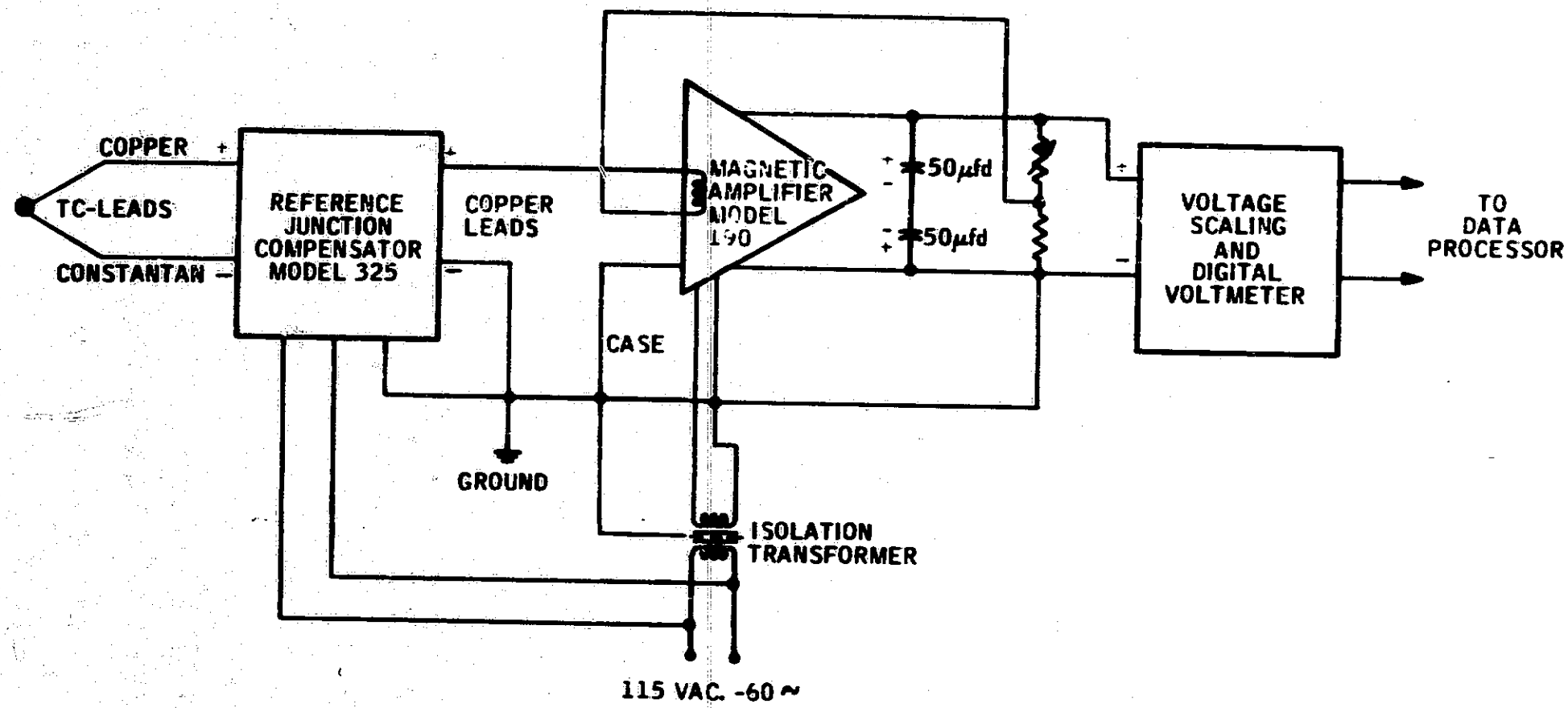


Figure 39. Temperature Recording Using Magnetic Amplifier

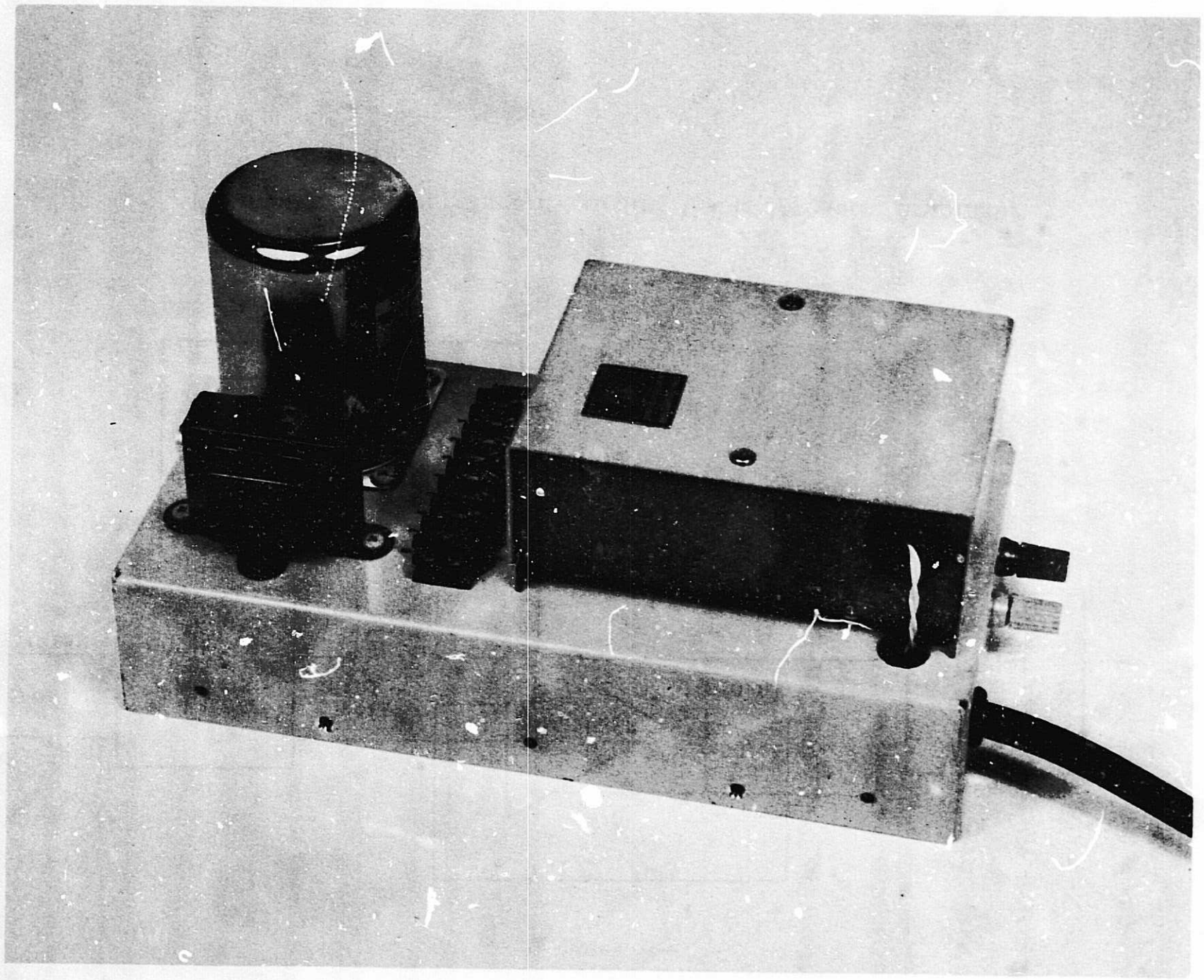

Figure 40. Magnetic Amplifier for DVM Input

# SECTION IV
# SDMEG EVALUATION TESTS

## INTRODUCTION

Major tasks performed under this contract were aimed at evaluating the performance of the SDMEG. Except for drift performance, math model, and readout accuracy evaluation (Sections V and VII), these evaluation tasks are discussed in this section.

These tasks can be subdivided as follows:

- Evaluation of the characteristics of the SDMEG suspension
- Evaluation of the automatic-start concept developed in the feasibility study program
- Determination of the SDMEG acceleration capability and its limiting factors

When evaluating suspension characteristics, such items as transient response, power consumption, and thermal characteristics were determined. These tests were conducted early in the evaluation program prior to the major suspension modification which occurred in 1966. Generally, these tests were not followed up after the modification because the characteristics of a suspension of the modified design were already known.

The automatic-start and acceleration tests were conducted after the modification took place; the results as reported here characterize the gyro in its present form. The starting tests included repeatability tests and simulated case motion in order to define gyro operating factors which are least predictable or most likely to vary if a startup in space is implemented on an ESG. Two such parameters can be defined from these tests, rotor direction of rotation (defined by the sequence of pattern pulses) and final rotor speed. Five acceleration tests were conducted; the results of these tests were satisfactory.

## SUSPENSION TESTS

Early in the program, the SDMEG suspension underwent a number of tests to determine its environmental limitations and power characteristics. The results of these tests are summarized here. The suspension was modified after these tests were completed. Except where noted, the results are considered to be applicable to the modified design.

## Rotor Levitation

The time interval between initial application of power to the suspension circuitry and stabilization of the rotor at the cavity center was observed to be about 50 ms for both high- and low-g mode. This time is governed mainly by the time lag of the suspension power decoupling, the starting characteristic of the 20 KHz carrier frequency oscillator, the time lag of the lag-lead compensation network, and the physical time characteristic of rotor displacement relative to rotor-to-electrode forces. In both modes of operation, the d-c power consumption by the suspension during levitation was 135 watts.

The suspension input current during rotor lifting was measured by observing the voltage drop across a 0.5Ω resistor connected in series with the supply outputs. An oscilliscope was used to monitor the line voltage. Figure 41 shows the upper bounds on the currents measured during several rotor lifts for the high-g mode. An improvement was made in the levitation characteristics by changing a capacitor in the error channel. With the change, the rotor position stabilizes after about 6 ms. The result is a considerably relaxed current profile, as shown in Figure 42. Note the change in the time scale in Figure 42 from Figure 41.

## Suspension Power

The steady-state power consumption is distributed between current amplifiers, error channels, and signal source and capacitance bridges. Table IV shows the power distribution for both the low-g and high-g modes.

The 10-watt power consumption in the low-g mode is somewhat higher than the 6-watt figure obtained in the feasibility study program. This power increase is caused by the following:

- The suspension error channels and signal source are operated from the ±22.5-volt supplies rather than from the ±10-volt supplies used in the feasibility study program.
- The capacitance bridges were added to the suspension in this program.
- The current amplifiers are operating from conventional ±12 vdc supplies rather than ±10 vdc.

The power consumption in the low-g mode could be reduced from the present 10-watt value to some lower value by altering the error channel and signal source transistor biasing networks in conjunction with operating the entire suspension from ±12 vdc.

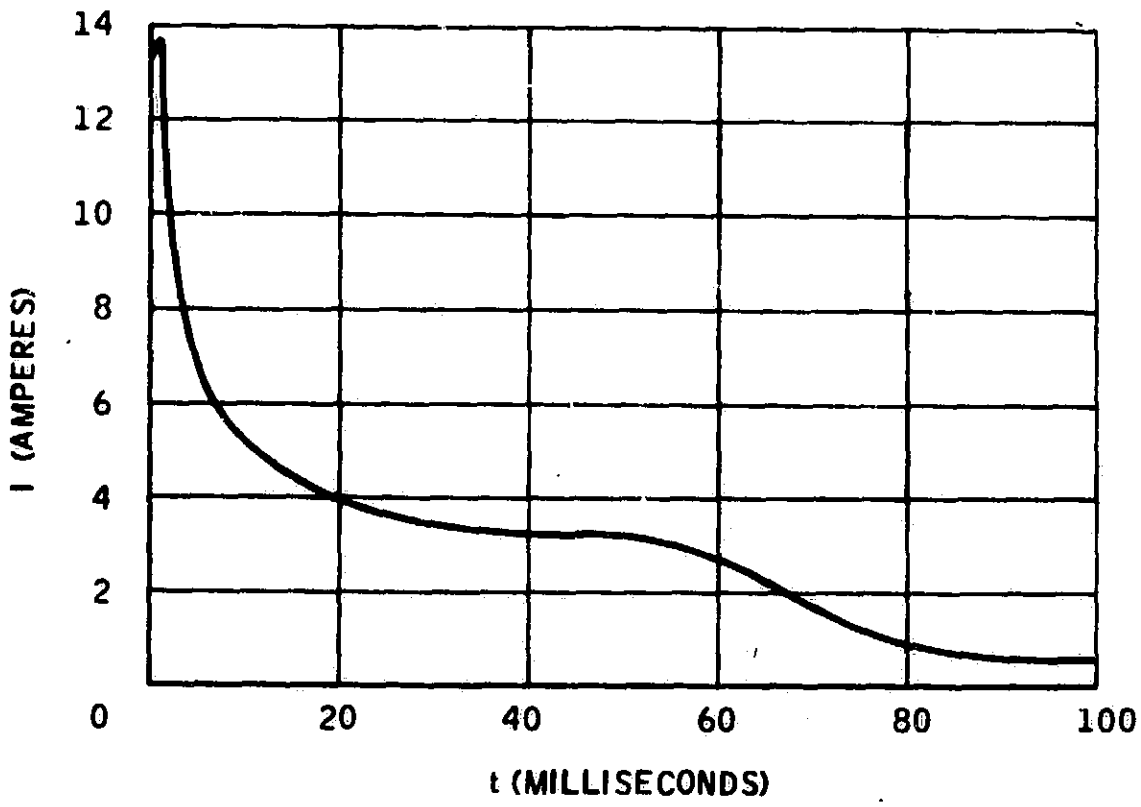


Figure 41. Maximum Value of Suspension Input Current During Rotor Lifting before Error Channel Modification

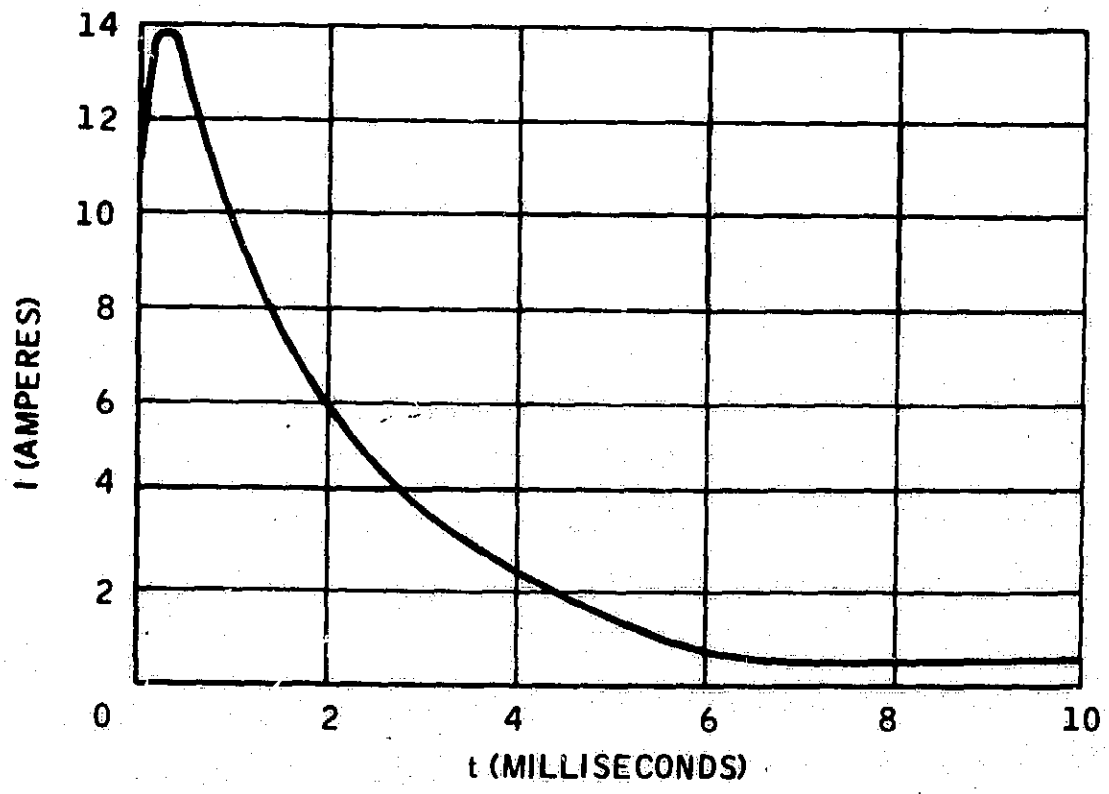


Figure 42. Maximum Value of Suspension Input Current During Rotor Lifting after Error Channel Modification

Table IV. Suspension Power Consumption

| Circuits | 15-g Mode (watts) | 3-g Mode (watts) |
|---|---|---|
| 6 Current Amplifiers | 18.8 | 4.6 |
| 3 Error Channels | 3.3 | 3.3 |
| 1 Signal Source | 1.8 | 1.8 |
| 6 Capacitance Bridges | 0.4 | 0.4 |
| TOTAL | 24.3 | 10.1 |

The suspension modification consisted of adding three high-frequency sensing bridges to the circuits, each drawing power for its operation. Each of these bridges is estimated to draw from 1.0 to 1.5 watts.

## Line Voltage Variations

In the high-g mode, the d-c power supplies were varied from ±16 volts to ±24 volts with no loss of rotor suspension. The actual limits of permissable supply voltages exceed these values since this test was limited by the supplies used.

In the low-g mode, the nominal ±12 vdc supplies were varied from ±7.5 vdc to ±16 vdc with no noticeable effect on the suspension electronics. As in the high-g mode, these numbers represent the range of the power supplies. The suspension capability to withstand supply variations exceeds these values.

## Rotor Sag Measurements

The gyro was mounted on a two-axis table and was oriented such that a specified force axis was at local vertical and the capacitance bridges on that channel were adjusted for a null. The gyro attitude was then changed by 180 degrees with respect to vertical and the capacitance bridge outputs were again measured. This enables a calculation of rotor sag resulting from the 2-g change in input acceleration. The results of this test are shown in Table V.

Table V. Steady-State Rotor Sag Measurements

| Suspension Channel | Average Sag (μ inch/g) | |
|---|---|---|
| | High-g Mode | Low-g Mode |
| X | 15.8 | 102 |
| Y | 17.9 | 104 |
| Z | 18.5 | 95 |

A comparison of these values shows the low-g sag values to be five times the high-g values. This result is expected since the gradient reduction by $\sqrt{5}$ results in acceleration capability and suspension gain reduction by a factor of 5.

The suspension modification provided a substantial reduction in the steady-state sag characteristics. It is estimated that for the high-g mode the steady-state sag is approximately 2 μ inches/g. Furthermore, the suspension gain became independent of preload voltage setting; consequently, the low-g sag increases only by a factor of $\sqrt{5}$, becoming approximately 5 μ inches/g.

Electrical Transient Response

Photographs of the typical response of the suspension to a square wave signal at the error channel modulator input are shown in Figure 43. The time scale on the photographs is 10 ms per square. Three parameters define the response -- overshoot, frequency of oscillation, and damping time. The oscillation frequency in the low-g mode is difficult to measure accurately because the oscillation is damped in less than one cycle (Figure 43b).

Transient response tests were also conducted at reduced and elevated temperatures in both modes of operation. Table VI summarizes the results of all those tests.

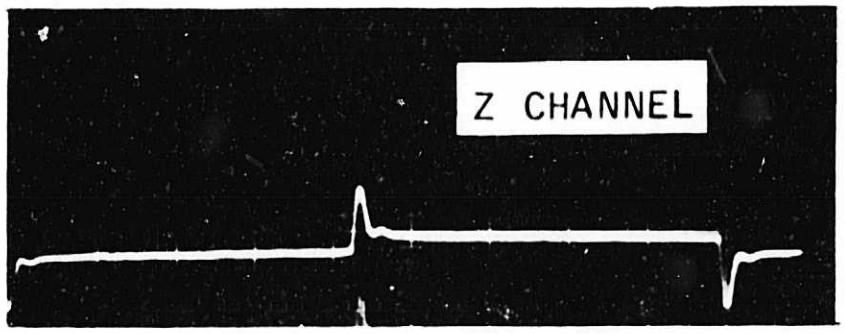


Figure 43a. Temperature Response -- High-g Mode -- Room Temperature

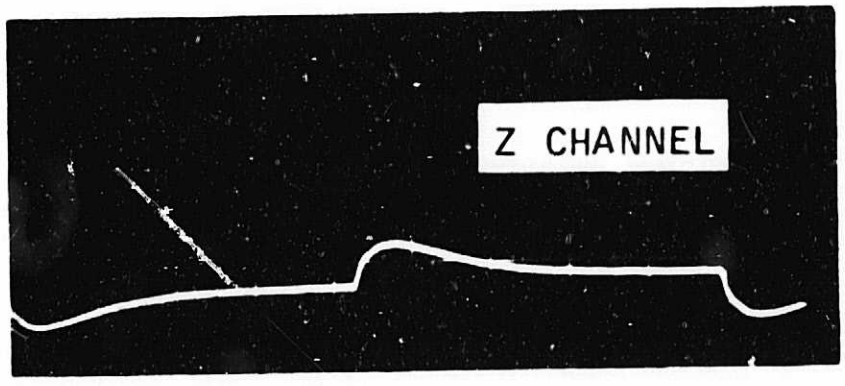


Figure 43b. Temperature Response -- Low-g Mode -- Room Temperature

Table VI. Results of Transient Response Tests

| Suspension Mode | Gyro Temp (°F) | Overshoot (%) | Oscillation Frequency (Hz) | Damping Time (ms) |
|---|---|---|---|---|
| High-g | 60 | 250 | 330 | 6 |
| | 80* | 300 | 300 | 6 |
| | 120 | 300 | 330 | 7 |
| Low-g | 60 | 200 | | 20 |
| | 80* | 150 | | 25 |
| | 120 | 150 | | 25 |

*Temperature at which suspension was tuned for minimum power

## Thermal Transient Tests

The breadboard gyro assembly and suspension electronics were temperature-stabilized at 80°F and then subjected to an ambient temperature of 60°F. A second transient test was conducted, after stabilization at 80°F, with ambient raised to 120°F. The capacitance bridge outputs were monitored and the resulting data were analyzed.

The reduced temperature and elevated temperature test results indicate the following:

- The thermal coefficients of expansion for both the rotor and envelope were calcuated. These values agree with the materials data, 6 microinches per inch-°F for the beryllium rotor and 3.4 microinches per inch-°F for the alumina envelope. This results in a net change in rotor-to-electrode capacitance of +0.12 percent per °F.

- The thermal time constant (time required to change 63 percent of total temperature change) was approximately one hour for the envelope.

- The thermal time constant of the suspended rotor was approximately seven hours.

## Simulated Vibration Tests

A simulated vibration test was performed at room temperature in both the high- and low-g modes. A sinusoidal voltage was fed into the suspension loop at the error channel modulator input. For each frequency the input level was increased until the rotor dropped. The input signal level, feedback signals, capacitance bridge outputs, and low-pass filter outputs were measured at the time of maximum input.

The broken lines of Figure 44 show the rotor sag (frequency response) estimated from the data of these tests for both high- and low-g modes. It can be seen that the suspension servo response is shifted downward by a factor approximately equal to the change in preload acceleration when going from high- to low-g mode. This could be expected, since the servo gain is proportionately reduced in the low-g operating mode.

As for the steady-state sag, the suspension modification caused the frequency response curve to change significantly. For the high-g mode, the curve is similar to that of the Air Force FGG432A1 SDESG suspension. The lower solid line of Figure 44 shows the approximate response curve of the modified suspension in the high-g mode. Based on the nominal differences of servo loop characteristics for high and low g, the upper solid line of Figure 44 was constructed to indicate approximately the suspension frequency response in the low-g mode.

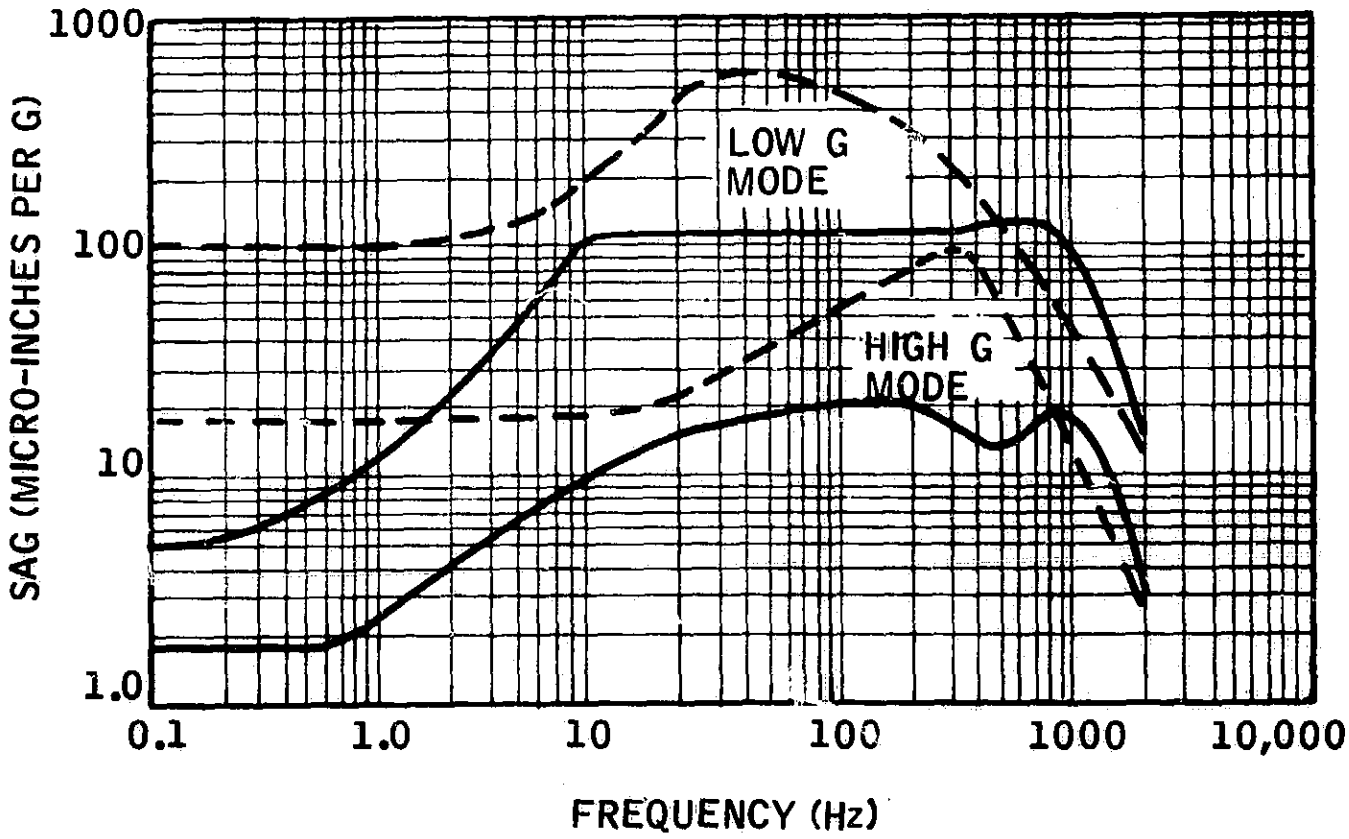


Figure 44. SDMEG Suspension Frequency Response Characteristics

### Suspension Stability

Suspension test results revealed that the suspension electronics functioned correctly with rotor-electrode capacitance variations from +10 to -5.5 percent from tuning capacitance. Before the modification, the suspension servo became unstable when rotor-electrode capacitance exceeded these limits. To remain within these limitations, the range of gyro operating temperature was restricted. In its present form, however, much greater capacitance variations can be tolerated by the suspension.

## AUTOMATIC STARTING TESTS

In 1967 a series of starting tests was conducted on the SDMEG using the automatic start sequencer panel to control the starting functions. The tests were conducted to determine

- Rotor spin-up time and spin-up rates as a function of speed
- Rotor nutation angle (wobble) as a function of damping time
- Repeatability of auto-start cycle
- Effect of case rotation on rotor behavior during the start cycle
- Thermal stabilization time after completion of start cycle

Five static starting tests were conducted -- static in the sense that the damping axis was parallel to the EPA and the case was not moved during the starting cycle. Seven tests were conducted simulating case angular motion, which included both constant and oscillatory movements. After six of the starting tests, the gyro was allowed to drift and the temperature to stabilize for eight or more hours. During this time, the capacitance bridge outputs were monitored along with the gyro temperature to determine when the gyro became thermally stabilized.

### Procedure

For these tests the gyro was mounted on a Leitz dividing head. The dividing head was mounted on a vertical axis table which could be driven at various rates by a motor. For the first five tests the damping axis was in the EPA; for the rest of the tests it was nominally normal to or started normal to the EPA.

The automatic-starting circuit spin timer was set for approximately 26 minutes and the damping timer was set for the maximum time (six hours) for all 12 auto-start tests.

The starting procedure was the same for the 12 start-up tests except for the case angular rates. The spin and damp currents were adjusted while the rotor was down. The automatic start switches were switched to "Auto." The suspension switch was turned to the "start" position and then to the "Auto-Run" position to place the automatic circuits in operation.

The time at which the following events occurred was recorded:

1) Initiation of auto-start sequence

2) Start of spin and damp cycle (the data processor clock was started at this time)

3) End of spin cycle

4) End of damp cycle

The following data were recorded every one-half hour during the tests:

1) Time at which the data were recorded

2) Positive suspension current

3) Negative suspension current

4) Vacuum reading

5) Temperature of gyro foot

6) Positions of vertical axis table (when input rates were applied)

7) Temperature of gyro envelope

8) The rms feedback voltage at the console test points

9) The capacitance sensor output voltages for the first five tests

10) The "gap" sensor meter reading was recorded for the last seven tests

The following data were recorded on the data processor during the auto-start tests:

1) Station time (0.00 hours at the application of spin power)

2) $C_1$ and $C_1 + C_2$ time intervals for the x and y pickoffs

3) A data point was taken every 0.005 hour during spin-up, every 0.02 hour during the damping, and every 0.05 hour during the temperature stabilization period

4) Ten data points were taken every half hour at the 0.0002-hour rate for determining the nutation angle

## Results

Except for one test, the positive end of the rotor became the direction of the positive spin vector. When the negative end was sensed on the exception, the test was restarted.

Rotor Spin-Up -- The spin-up time was calculated using data measured from one of the auto-start tests that had a low initial nutation angle. The spin-up time and the spin-up rate versus speed are shown in Figure 45. The average spin-up rate to 200 rps was about 7.8 rps/min. This rate was obtained with 800 Hz spin currents of 300 ma in coil A and 215 ma in coil B; this spin power was used for all 12 tests. Higher spin-up rates can be obtained with higher spin currents. With 700 ma of 800 Hz spin power applied during previous tests, the spin-up rate is about 17 rps/min.

Rotor Nutation as a Function of Damping Time -- The rotor nutation angle is shown in Figure 46 for one of the static starting tests as a function of damping time. A damping current of 930 ma was used for all tests, except for run number 12 which had 1200 ma of damping current. The damping rates exhibited the same characteristics during all the tests except number 12. Case angular rotations were applied perpendicular to the damping axis in runs 6 through 12, but they did not seem to affect the damping rate. The increased damping current in run 12 increased the damping rate by a factor proportional to the square of the damping current. An empirical equation for the damping time (the time required to reduce the nutation angle to one arc minute) in terms of the initial nutation angle and the damping current, was determined for the gyro. The equation determines the damping time to a point where the wobble decreases to a peak-to-peak value of one arc min.

$$\tau_d = \frac{1.3}{I_d^2} \log_{10} (\nu_o)$$

where

$\tau_d$ = damping time in hours

$I_d$ = damping current in amps

$\nu_o$ = initial rotor nutation in arc minutes

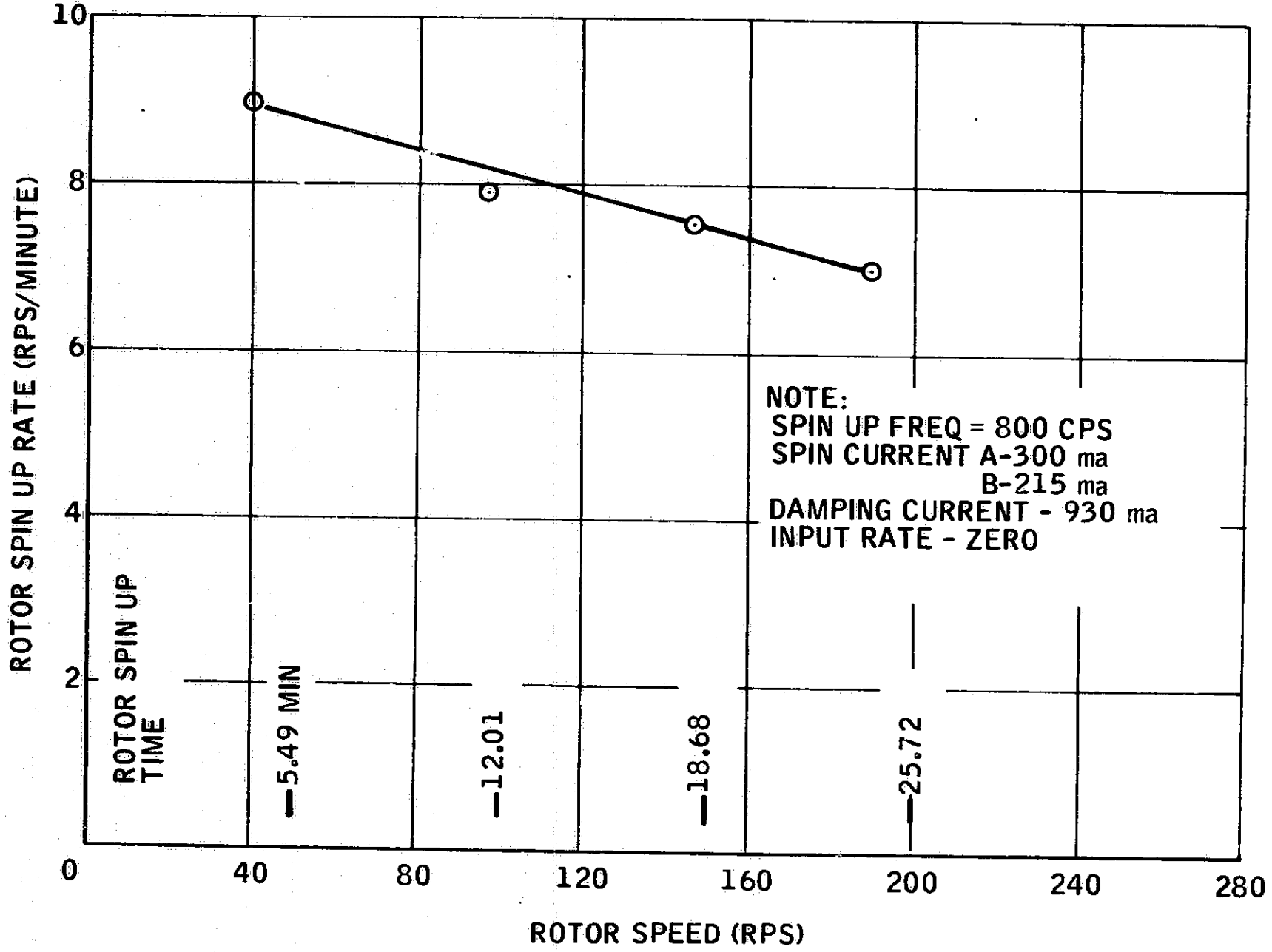


Figure 45. Spin-Up Rate and Spin-Up Time Versus Rotor Speed

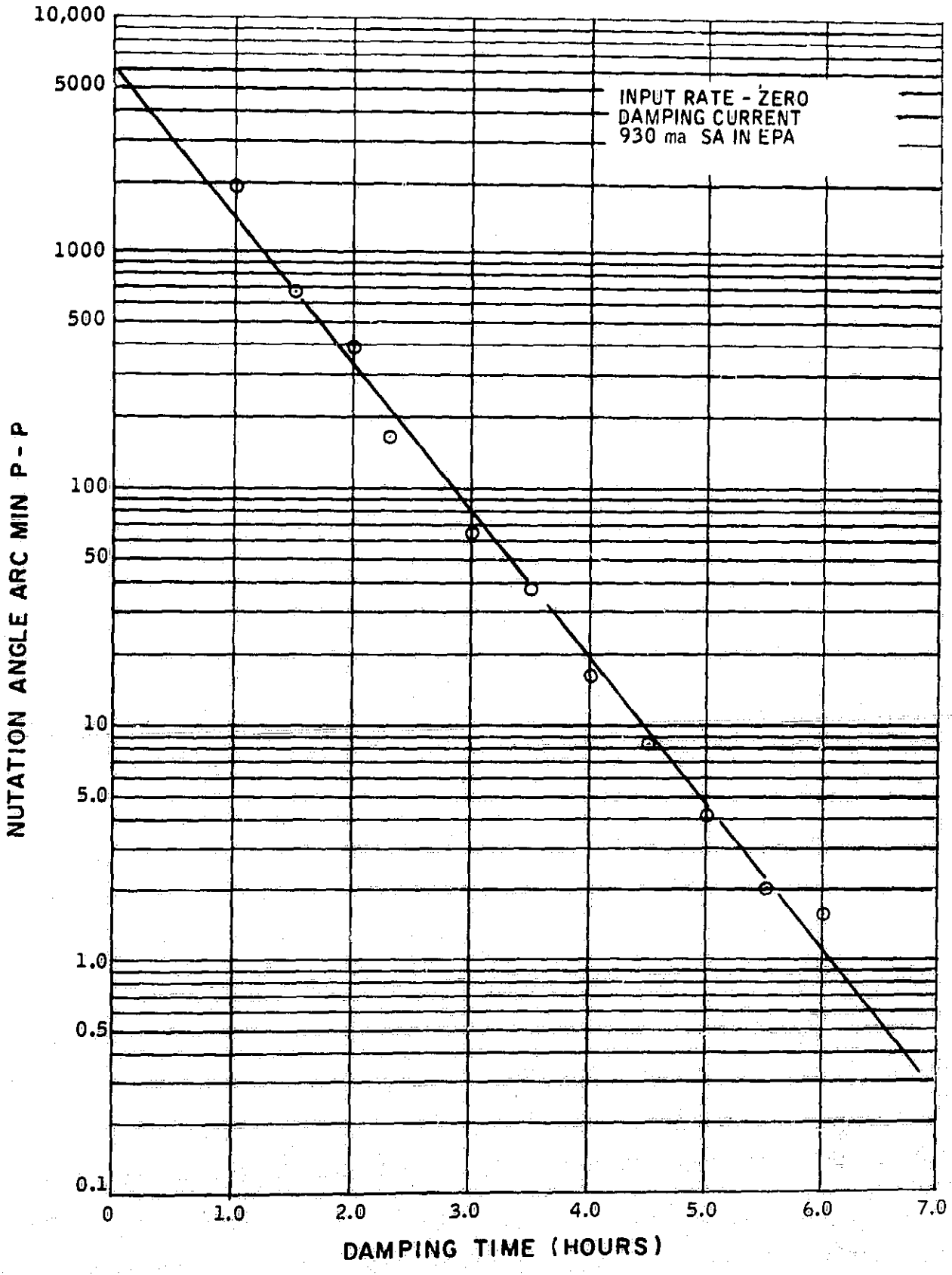


Figure 46. Pickoff Data Scatter versus Damping Time-Auto-Start Test No. 4

With an increase in damping current, the rate of rotor speed loss increases, but the loss over the total required damping time is reduced. This information was obtained from runs 11 and 12 by determining the rate of speed over a portion of each run where the initial and final nutation angles were the same. The results of the calculations are shown in Table VII.

Table VII. Damping Effectiveness

| Damping Current (ma) | Speed Loss (rps/hr) | Damping Time (hr) | Total Speed Loss* (rps) |
|---|---|---|---|
| 930 | 4.17 | 5.22 | 21.8 |
| 1200 | 4.53 | 3.18 | 14.4 |

*Note: The table input rate was about 45 deg/hr for both tests.

Rotor Run-Down Rate as a Function of Nutation Angle -- A plot of rotor run-down rate versus the magnitude of nutation angle is shown in Figure 47. This result was obtained from tests 1 through 5, where the damping axis was parallel to the EPA. The curve shows a high increase in the run-down rate when the nutation angle is greater than 2 to 3° peak-to-peak. All of the starting tests show that the nutation angle is greater than 2 to 3° for approximately the first one to two hours.

Auto-Start Test Repeatability -- The spin-up time for the tests varied from 25 minutes, 42 seconds, to 26 minutes, 16 seconds, a peak-to-peak variation of 2.2 percent. The damping time for the 12 tests varied from 6 hours, 00 minutes, 52 seconds, to 6 hours, 04 minutes, 15 seconds, a variation of 0.9 percent. Neither of the timers was adjusted throughout the test series.

The most noticeable effect of timing variations of the damp and spin-up cycle is the final rotor speed. The spin-up cycle has the most important effect; a two percent difference in spin-up time would change the final speed about 4 rps. A similar change in the damping time would only change the speed about 0.02 rps if the damping axis is along the spin axis, and would increase proportionately if case angular motion leaves these axes nonparallel at the end of the damp cycle.

Case Rotation Effects -- The only observed effect of case rotation was in the final rotor speed. Case angular motion produces a noncoincidence between the damping axis and spin axis throughout most of the damping cycle, resulting in a higher average rundown rate. This effect is shown in Figure 48. The

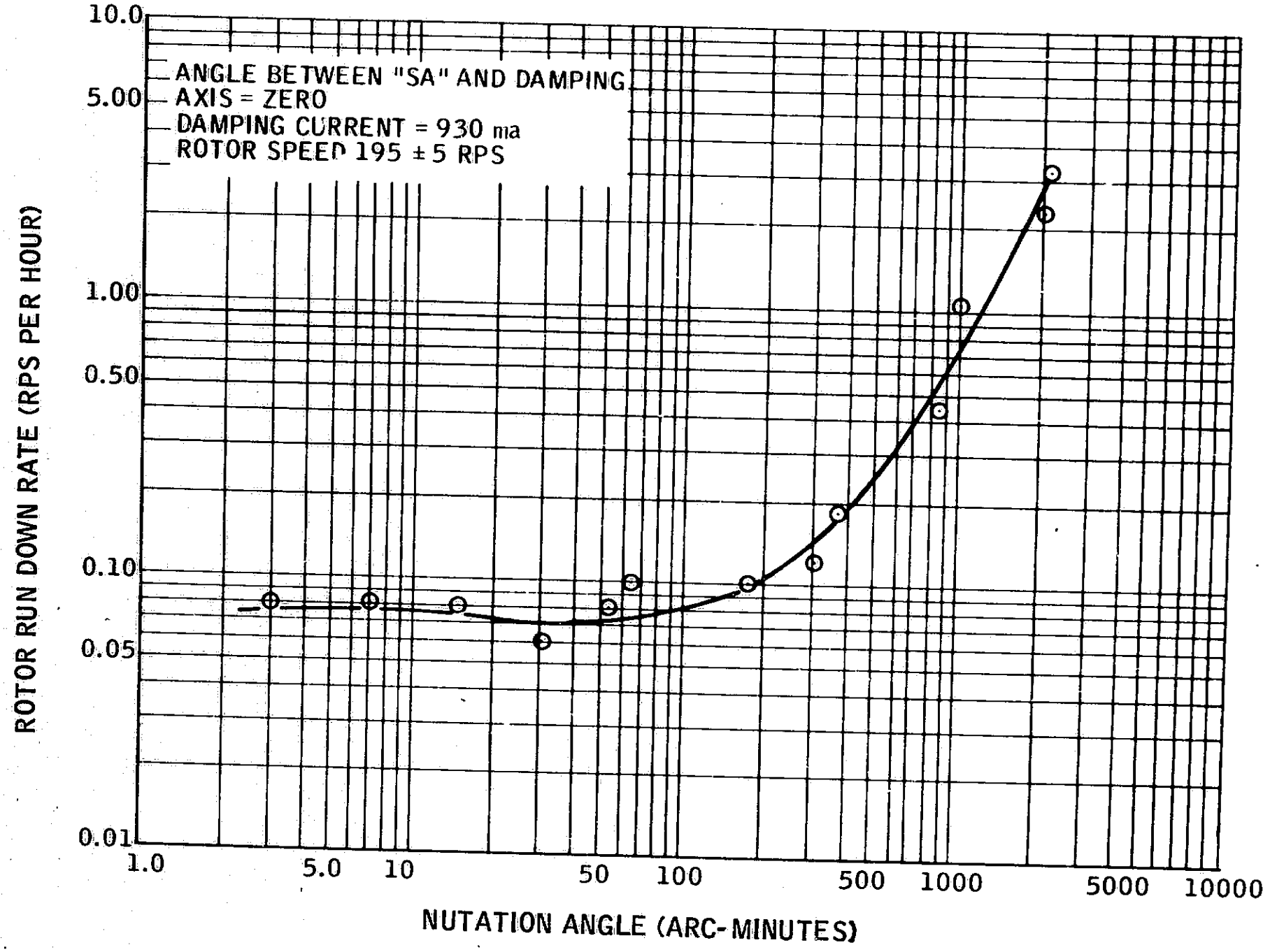


Figure 47. Effect of Nutation Angle on Run Down Rate

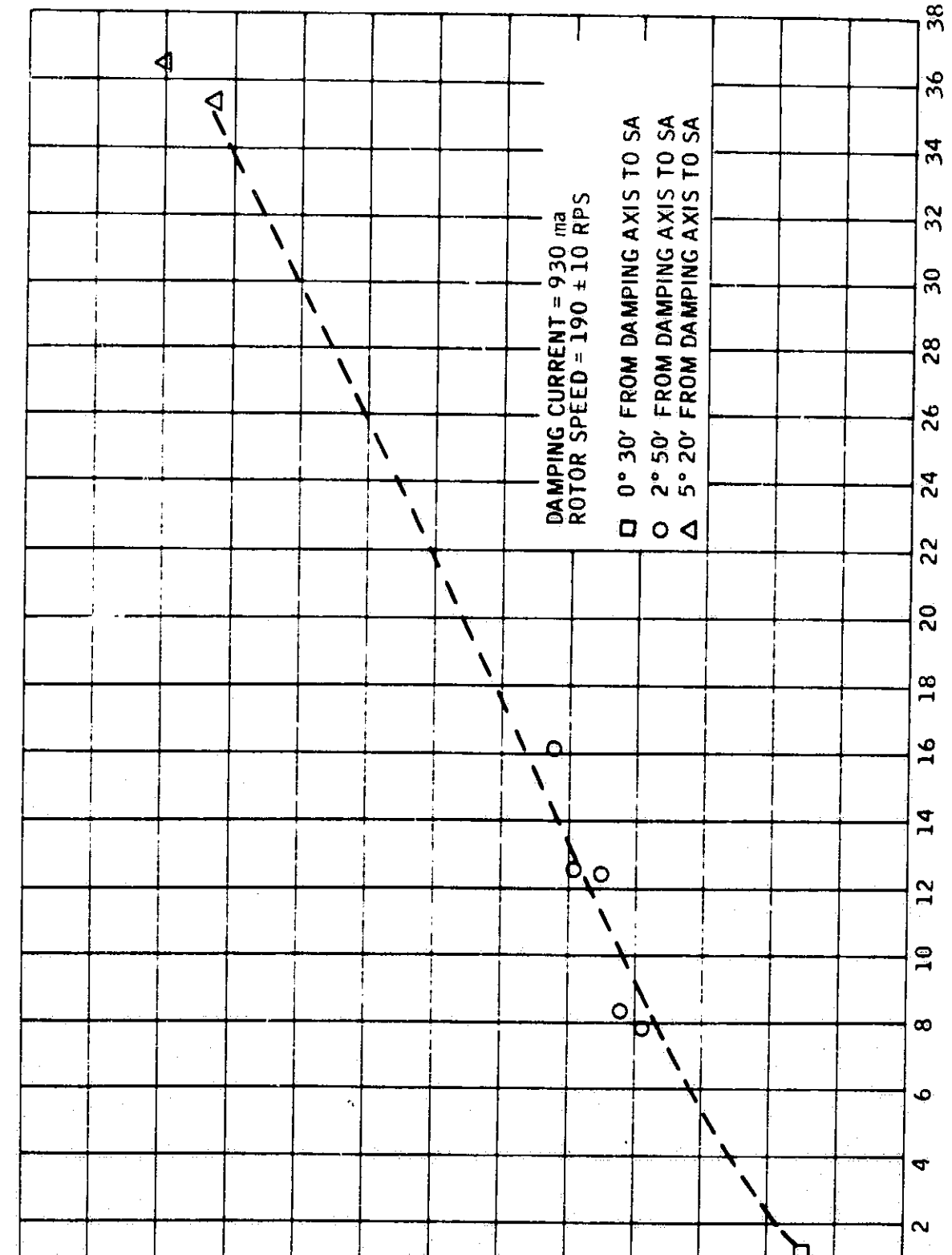


Figure 48. Run Down Rate versus Input Rate

resulting rotor rundown rate is shown as a function of table rate, at a damping current of 930 ma. The angle between the spin axis and the damping axis is almost proportional to the table input rate.

Thermal Stabilization -- To provide some measure of the change of nominal rotor-electrode gap with time, the difference of capacitance sensor outputs from two opposite electrodes was monitored during the thermal stabilization tests. Data from two thermocouples mounted on the gyro subassembly were also recorded. Figure 49 is a plot of the temperature of the two points and the gap indication for one of these tests. The same data recorded for the start sequence prior to the stabilization period are also shown. From the graph, it is seen that stability was reached approximately 16 hours after the start sequence was completed.

The thermal transient tests reported on page 4-7indicated that the thermal time constant of the suspended rotor was measured to be seven hours. The gap indication plotted in Figure 49 agrees very well with this finding. The data shown in this graph indicate that, after 16 hours of stabilization, the difference in temperature between the rotor and envelope was less than 1°F.

## CENTRIFUGE TESTS

To determine the limits of capable acceleration of the SDMEG, the gyro was tested in a centrifuge. The centrifuge test apparatus was set up as shown in Figures 50 and 51. Two special interconnecting cables were used -- one between the control console and the centrifuge 37-pin Cannon, and the other on the centrifuge arm. The cable connection scheme is shown in Figures 52 and 53.

### Procedure

The suspension had been modified to the separate sensing type (see page 2-12) before the centrifuge tests took place. The rotor was suspended and preliminary measurements of feedback voltages were taken directly from both the suspension electronics package and control console. Table VIII summarizes the conditions of the tests performed on the centrifuge.

For each test, the acceleration was increased until the suspension either reached its capability limit or became unstable.

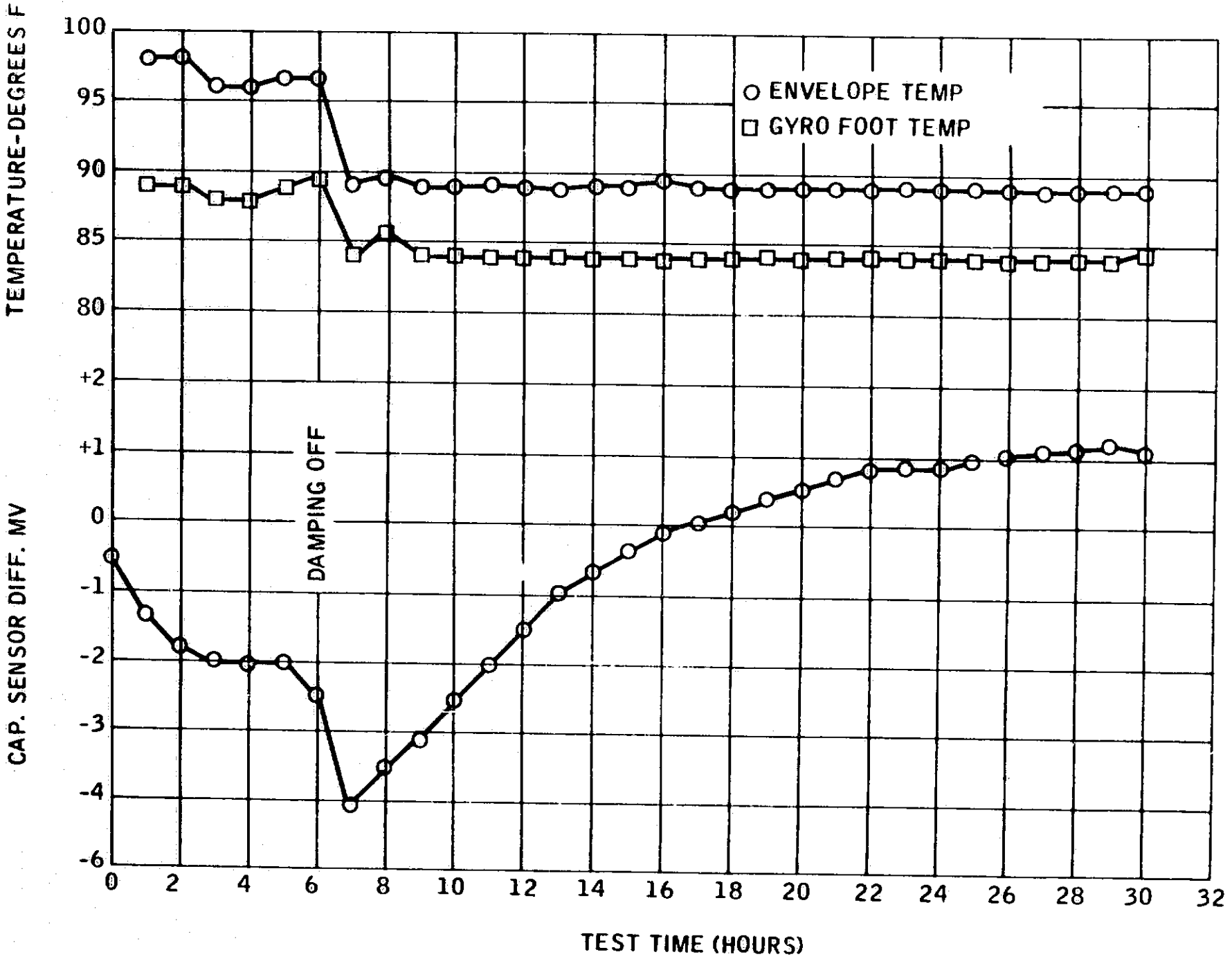


Figure 49. Temperature Stability Test

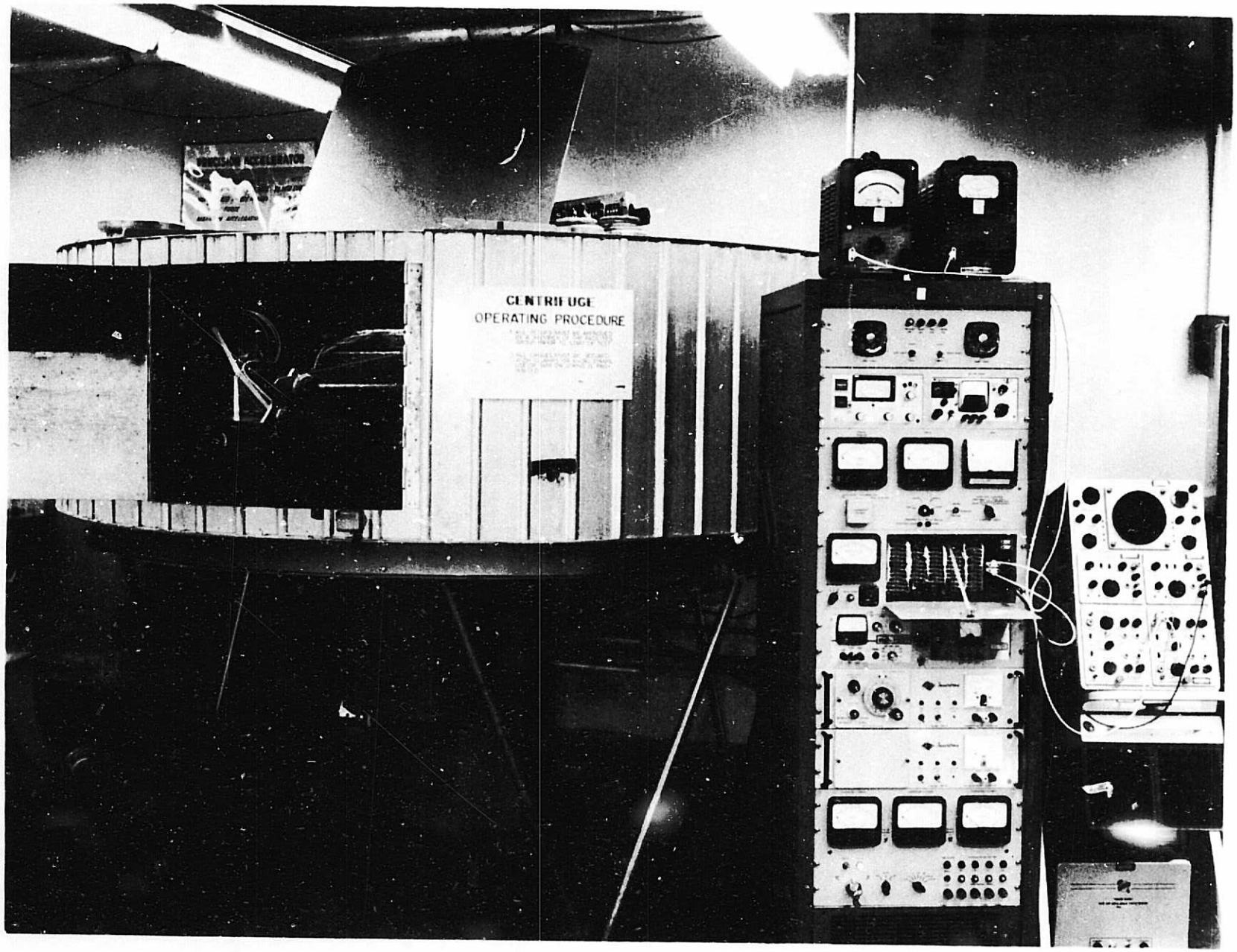


Figure 50. SDMEG Centrifuge Test Set-Up

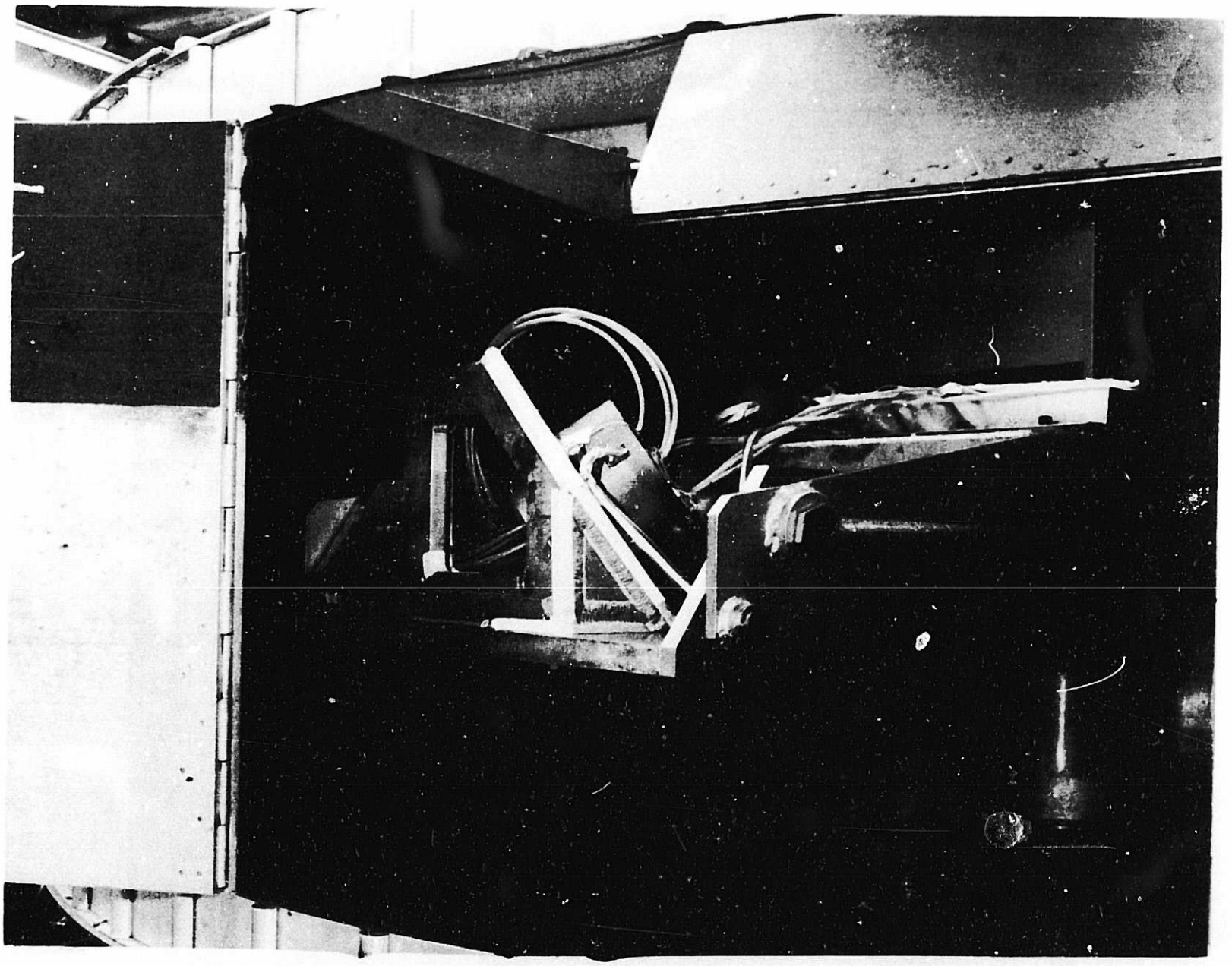

Figure 51. SDMEG Mounted on Centrifuge Arm

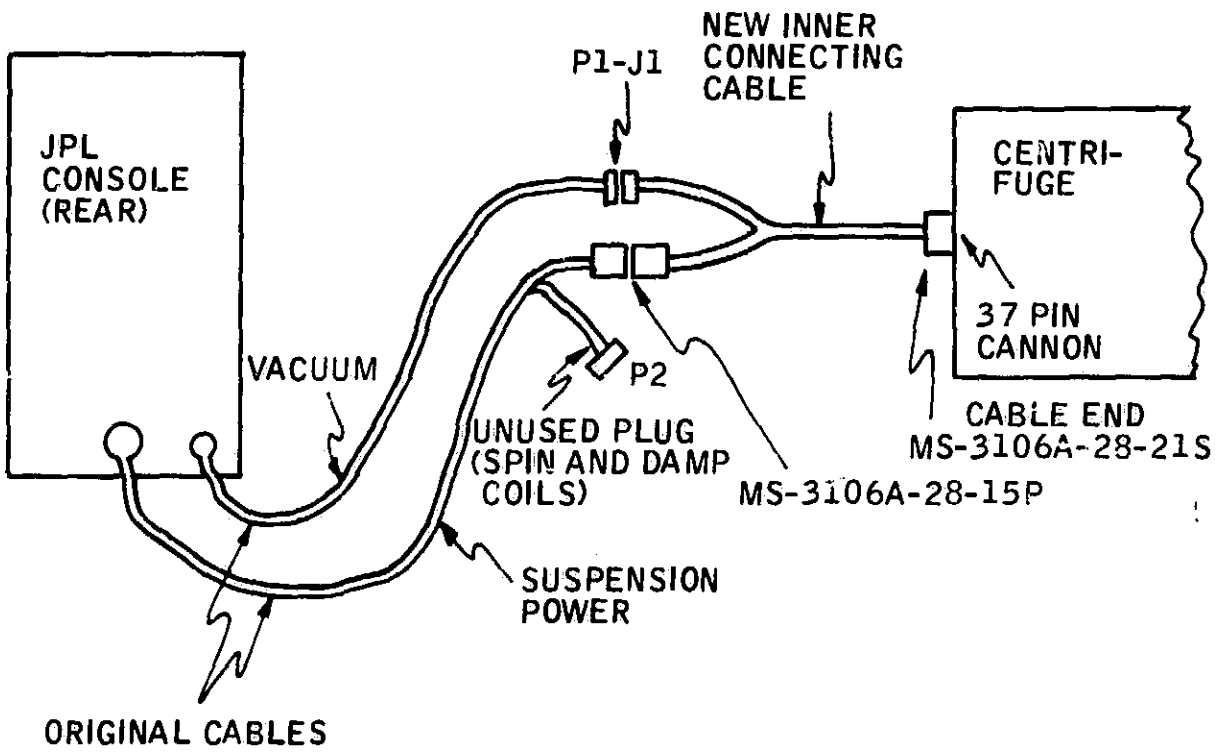


Figure 52. Connections of Vacuum and Suspension Output Cable between Console and Centrifuge

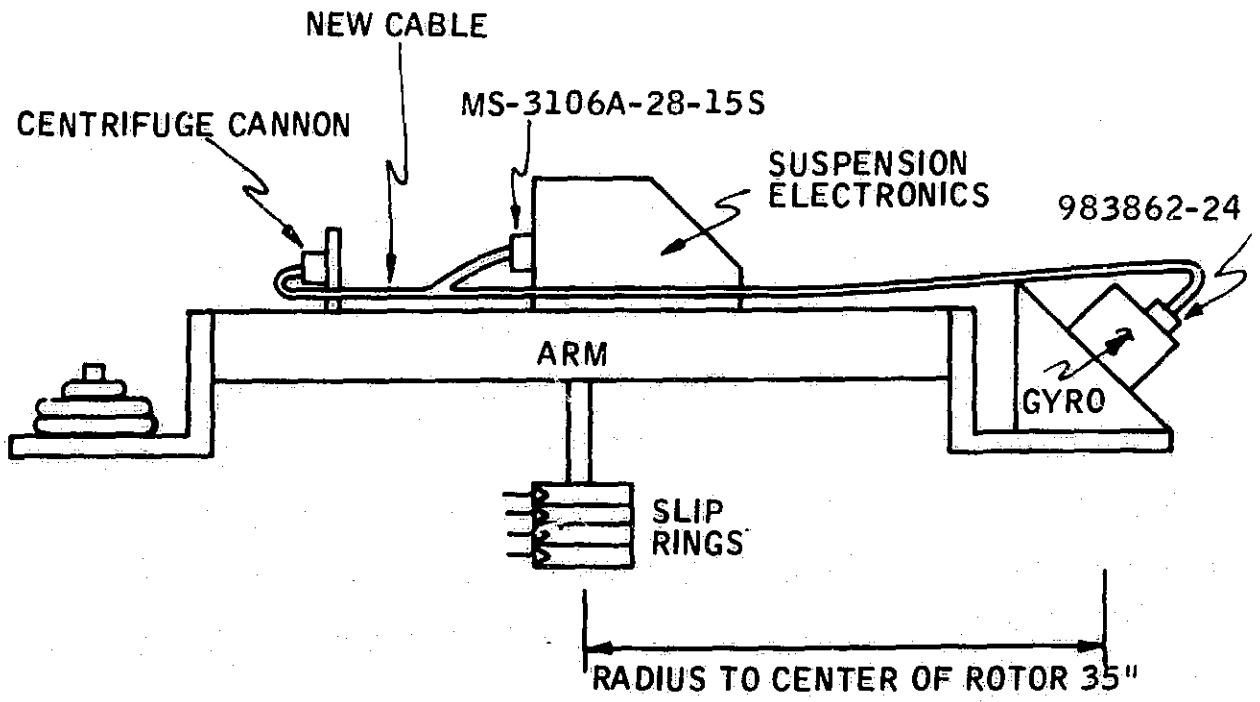


Figure 53. New Cable on Centrifuge Arm

Table VIII
SDMEG Centrifuge Test Parameters

| Test No. | Axis of Acceleration | Gravitational Support Axis | Suspension Bias Level (g) | Power Supply Voltage (v) |
|---|---|---|---|---|
| 1 | -Y | -X Up | Low | ± 22 |
| 2 | -Y | -X Up | High | ± 22 |
| 3 | -Y | -X Up | Low | ± 12 |
| 4 | -Z | -X Up | High | ± 22 |
| 5 | -X | -Y Up | High | ± 22 |

During the five tests, the angular speed of the centrifuge was raised in increments of 3 to 20 rpm. At each level, the following data were recorded:

- Angular speed of centrifuge (rpm)
- Suspension current (positive)
- Suspension current (negative)
- Two isolated feedback test point voltages for the axis under acceleration
- Vacuum indicator reading

The data are given in Tables IX through XIII.

Using the collected data, the following quantities were calculated:

- Acceleration was calculated for each level of centrifuge speed, assuming that the center of the gyro rotor was 35 inches from the center of the centrifuge arm
- Scale factors were determined to compensate for attenuation of feedback voltages read at the console
- Using the scale factors, true feedback voltages were calculated from the readings taken at the console
- Rebalance voltage (which is proportional to rotor sag) was calculated for each level of acceleration

Table IX. Centrifuge Test No. 1 Data 20302-FR

| Centrifuge Speed | Accelera-tion | Vacuum Indication | Suspension +22 v | Current -22 v | Suspension Feedback Voltages | | | | |
|---|---|---|---|---|---|---|---|---|---|
| | | | | | Reading at Console | | Scaled Value | | Rebalance |
| | | | | | -Y Axis | +Y Axis | -Y Axis | +Y Axis | Voltage |
| -- | -- | $3.7 \times 10^{-6}$ mm Hg | 515 ma | 660 ma | 0.07 v p-p | 0.07 v p-p | 3.0 v p-p | 3.0 v p-p | 0 |
| 13.0 rpm | 0.16 g | 3.8 | 520 | 661 | 0.07 | 0.065 | 3.0 | 2.8 | 0.1 v p-p |
| 21.1 | 0.44 | 3.8 | 510 | 660 | 0.08 | 0.05 | 3.4 | 2.1 | 0.65 |
| 30.3 | 0.91 | 3.7 | 510 | 660 | 0.10 | 0.04 | 4.3 | 1.7 | 1.3 |
| 43.9 | 1.9 | 3.7 | 525 | 685 | 0.12 | 0.015 | 5.2 | 0.65 | 2.28 |
| 52.4 | 2.7 | 3.3 | 560 | 710 | 0.15 | -0.015 | 6.5 | -0.65 | 3.58 |
| 61.2 | 3.7 | 3.3 | 600 | 750 | 0.18 | -0.05 | 7.7 | -2.15 | 4.98 |
| 65.2 | 4.2 | 3.2 | 620 | 775 | 0.20 | -0.65 | 8.6 | -2.8 | 5.7 |
| 69.8 | 4.9 | 3.2 | 645 | 800 | 0.22 | -0.085 | 9.5 | -3.75 | 6.68 |
| 75.0 | 5.1 | 3.2 | 680 | 825 | 0.24 | -0.11 | 10.0 | -4.75 | 7.38 |
| 79.8 | 6.3 | 3.2 | 720 | 865 | 0.27 | -0.13 | 11.6 | -5.6 | 8.6 |
| 85.0 | 7.2 | 3.1 | 765 | 890 | 0.30 | -0.17 | 12.9 | -7.3 | 10.1 |
| 90.6 | 8.2 | 3.1 | 840 | 950 | 0.33 | -0.20 | 14.2 | -8.6 | 11.4 |
| 93 | 8.6 | Limit Reached | | | | | | | |

Scale Factors: -Y Axis = 43
+Y Axis = 43

## Table X. Centrifuge Test No. 2 Data

| Centrifuge Speed | Accelera-tion | Vacuum Indication | Suspension +22 v | Current -22 v | Suspension Feedback Voltages | | | | |
|---|---|---|---|---|---|---|---|---|---|
| | | | | | Reading at Console | | Scaled Value | | Rebalance Voltage |
| | | | | | -Y Axis | +Y Axis | -Y Axis | +Y Axis | |
| --- | --- | $3.5 \times 10^{-6}$ mm Hg | 860 ma | 1000 ma | 0.15 v p-p | 0.16 v p-p | 5.9 v p-p | 6.1 v p-p | 0.1 v p-p |
| 21.2 rpm | 0.44 g | 3.5 | 870 | 1000 | 0.16 | 0.15 | 6.25 | 5.7 | 0.28 |
| 40.8 | 1.6 | 3.4 | 852 | 1000 | 0.18 | 0.14 | 7.05 | 5.3 | 0.88 |
| 62.2 | 3.8 | 3.4 | 860 | 996 | 0.21 | 0.11 | 8.2 | 4.2 | 2.0 |
| 71.2 | 5.0 | 3.3 | 850 | 1000 | 0.23 | 0.09 | 9.0 | 3.4 | 2.8 |
| 81.1 | 6.5 | 3.2 | 850 | 1000 | 0.25 | 0.07 | 9.75 | 2.65 | 3.55 |
| 91.4 | 8.3 | 3.2 | 880 | 1020 | 0.28 | 0.035 | 10.9 | 1.3 | 4.8 |
| 95.2 | 9.0 | 3.2 | 890 | 1036 | 0.29 | 0.03 | 11.3 | 1.1 | 5.1 |
| 100.1 | 9.9 | 3.1 | 920 | 1060 | 0.315 | 0.00 | 12.3 | 0 | 6.15 |
| | (Stopped, phase change in +Y Axis Feedback) | | | | | | | | |

Scale Factors: -Y Axis = 39
+Y Axis = 38

## Table XI. Centrifuge Test No. 3 Data

| Centrifuge Speed | Accelera-tion | Vacuum Indication | Suspension ±12 v | Current -12 v | Suspension Feedback Voltages | | | | |
|---|---|---|---|---|---|---|---|---|---|
| | | | | | Reading at Console | | Scaled Voltage | | Rebalance |
| | | | | | -Y Axis | +Y Axis | -Y Axis | +Y Axis | Voltage |
| --- | --- | $4 \times 10^{-6}$ mm Hg | 310 ma | 305 ma | 0.07 v p-p | 0.07 v p-p | 3.0 v p-p | 3.0 v p-p | 0 |
| 19.6 rpm | 0.39 g | 4 | 305 | 302 | 0.08 | 0.06 | 3.4 | 2.6 | 0.4 v p-p |
| 39.1 | 1.5 | 3.8 | 320 | 310 | 0.115 | 0.025 | 4.95 | 1.1 | 1.98 |
| 45.5 | 2.0 | 3.7 | 338 | 330 | 0.13 | 0.01 | 5.6 | 0.43 | 2.59 |
| 58.7 | 3.4 | 3.6 | 380 | 375 | 0.17 | -0.03 | 7.3 | -1.3 | 4.3 |
| 69.3 | 4.8 | 3.6 | 423 | 418 | 0.21 | -0.08 | 9.05 | -3.4 | 6.2 |
| 77.5 | 6.0 | Limit Reached | | | | | | | |

Scale Factors: -Y Axis = 43
+Y Axis = 43

## Table XII. Centrifuge Test No. 4 Data 20302-FR

| Centrifuge Speed | Accelera-tion | Vacuum Indication | Suspension +22 v | Current -22 v | Suspension Feedback Voltages | | | | |
|---|---|---|---|---|---|---|---|---|---|
| | | | | | Reading at Console | | Scaled Value | | Rebalance |
| | | | | | -Z Axis | +Z Axis | | | Voltage |
| -- | -- | 6.8 x 10 mm Hg | 860 ma | 1000 ma | 0.16 v p-p | 0.14 v p-p | 7.35 v p-p | 6.5 v p-p | 0.42 v p-p |
| 20.0 rpm | 0.4 g | 6.1 | 860 | 1000 | 0.17 | 0.13 | 7.8 | 6.0 | 0.9 |
| 40.2 | 1.6 | 5.9 | 880 | 1000 | 0.18 | 0.12 | 8.2 | 5.5 | 1.35 |
| 52.4 | 2.7 | 5 | 880 | 1010 | 0.20 | 0.11 | 9.2 | 5.0 | 2.05 |
| 63.6 | 4.0 | 4 | 880 | 1016 | 0.22 | 0.09 | 10.1 | 4.15 | 3.0 |
| 71.5 | 5.1 | 4 | 890 | 1030 | 0.23 | 0.08 | 10.6 | 3.7 | 3.95 |
| 81.9 | 6.7 | 4 | 900 | 1040 | 0.25 | 0.06 | 11.5 | 2.8 | 4.35 |
| 92.1 | 8.4 | 4 | 920 | 1060 | 0.28 | 0.035 | 12.9 | 1.6 | 5.65 |
| 95.5 | 9.0 | 4 | 920 | 1060 | 0.29 | 0.03 | 13.3 | 1.4 | 5.95 |
| 100.7 | 10.0 | 4 | 940 | 1080 | 0.31 | 0.015 | 14.2 | 0.69 | 6.75 |
| 105.3 | 11.0 | 4 | 954 | 1084 | 0.32 | 0.01 | 14.7 | 0.46 | 7.12 |
| | | Lost vacuum protection @ 102 rpm | | | | | | | |

Scale Factors: -Z Axis = 46
+Z Axis = 46

## Table XIII. Centrifuge Test No. 5 Data

| Centrifuge Speed | Accelera-tion | Vacuum Indication | Suspension 22 v | Current -22 v | Suspension Feedback Voltages | | | | |
|---|---|---|---|---|---|---|---|---|---|
| | | | | | Reading at Console | | Scaled Value | | Rebalance |
| | | | | | -X Axis | +XAxis | -X Axis | +X Acis | Voltage |
| --- | --- | $4 \times 10^{-6}$ mm Hg | 860 ma | 1000 ma | 0.16 v p-p | 0.16 v p-p | 6.4 v p-p | 6.4 v p-p | 0 |
| 20.9 rpm | 0.42 g | 4 | 860 | 1000 | 0.17 | 0.15 | 6.8 | 6.0 | 0.4 v p-p |
| 39.6 | 1.6 | 4 | 870 | 1000 | 0.19 | 0.14 | 7.6 | 5.6 | 1.0 |
| 63.0 | 3.9 | 4 | 880 | 1000 | 0.22 | 0.11 | 8.8 | 4.4 | 2.2 |
| 73.4 | 5.4 | 4 | 886 | 1020 | 0.24 | 0.09 | 9.6 | 3.6 | 3.0 |
| 81.6 | 6.6 | 4 | 920 | 1030 | 0.26 | 0.07 | 10.0 | 2.8 | 3.6 |
| 92.8 | 8.6 | 4 | 960 | 1080 | 0.29 | 0.04 | 11.6 | 1.6 | 5.0 |
| 101.9 | 10.2 | 4 | 1000 | 1120 | 0.31 | 0.02 | 12.4 | 0.8 | 5.8 |
| 106.0 | 11.2 | 4 | 1020 | 1160 | 0.33 | 0.00 | 13.2 | 0.0 | 6.6 |
| 111.2 | 12.3 | 4 | 1040 | 1180 | 0.35 | -0.02 | -14.0 | -0.8 | 7.4 |
| 118 | 13.7 | Feedback currents pegged | | | | | | | |

Scale Factors: -X Axis = 40
+X Axis = 40

For each test, the rebalance voltage was plotted against the acceleration. The graphs are shown in Figures 54 to 58.

Results

Test 1 - (+Y outward, Low-g Mode, ±22 v Supply) -- The suspension supported the rotor against 8.6 g before its limit was reached.

Test 2 - (+Y outward, High-g Mode, ±22 v Supply) -- The suspension withstood 9.9 g before the test was stopped because of a phase change in the feedback voltage at terminal 10.

Test 3 - (+Y outward, Low-g Mode, ±12 v Supply) -- The suspension supported the rotor against 6.0 g before reaching its limit.

Test 4 - (+Z outward, High-g Mode, ±22 v Supply) -- The suspension withstood 11.0 g, at which point the test was stopped because vacuum protection was lost. The vacuum-indicating meter read negative pressures; the cause is not known. At this level of acceleration, the feedback voltages indicated that the suspension was close to its limit.

Test 5 - (+X outward, High-g Mode, ±22 v Supply) -- The suspension withstood 13.7 g, at which point all meters indicating feedback currents pegged for unknown reasons. No evidence of arcing was present, since the vacuum remained constant; thus, it is assumed that the rotor remained suspended. The test was terminated at this point.

Conclusions

Suspension acceleration limits were reached only in the low-g mode tests (Tests 1 and 3). None of the high-g mode tests was terminated at the gyro acceleration limits. Test 2 was terminated at a feedback null because it was a suspension condition not previously reached in the high-g mode. Results of Test 5 (where the test was continued through the feedback null) indicate that Test 2 could have been continued to higher acceleration levels if other factors had not been considered in the decision to terminate.

In addition to being measured on the meters, the feedback signals were also monitored on oscilloscopes. At the termination points of the high-g mode tests, these monitors indicated that the tests should be terminated to avoid catastrophic damage to the suspension and gyro. Subsequent tests with the suspension on the dummy load indicated that the maximum voltage of the output

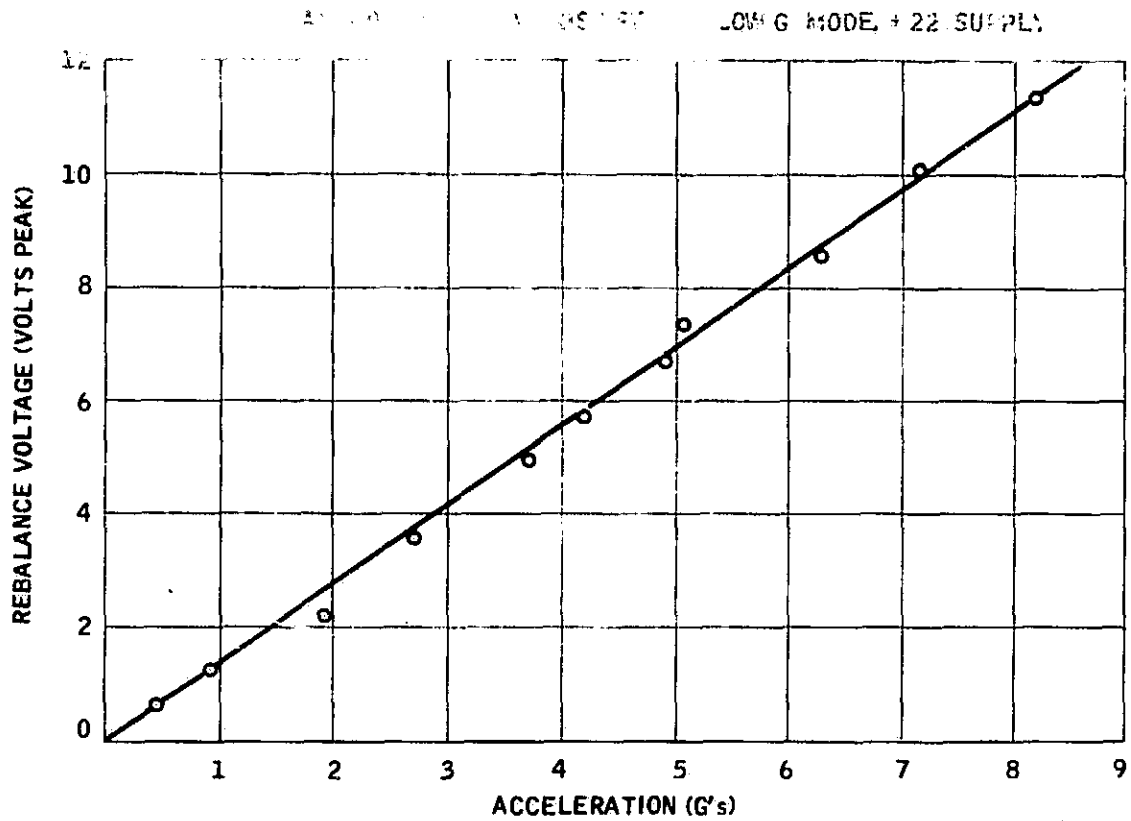


Figure 54. Results of Centrifuge Test No. 1

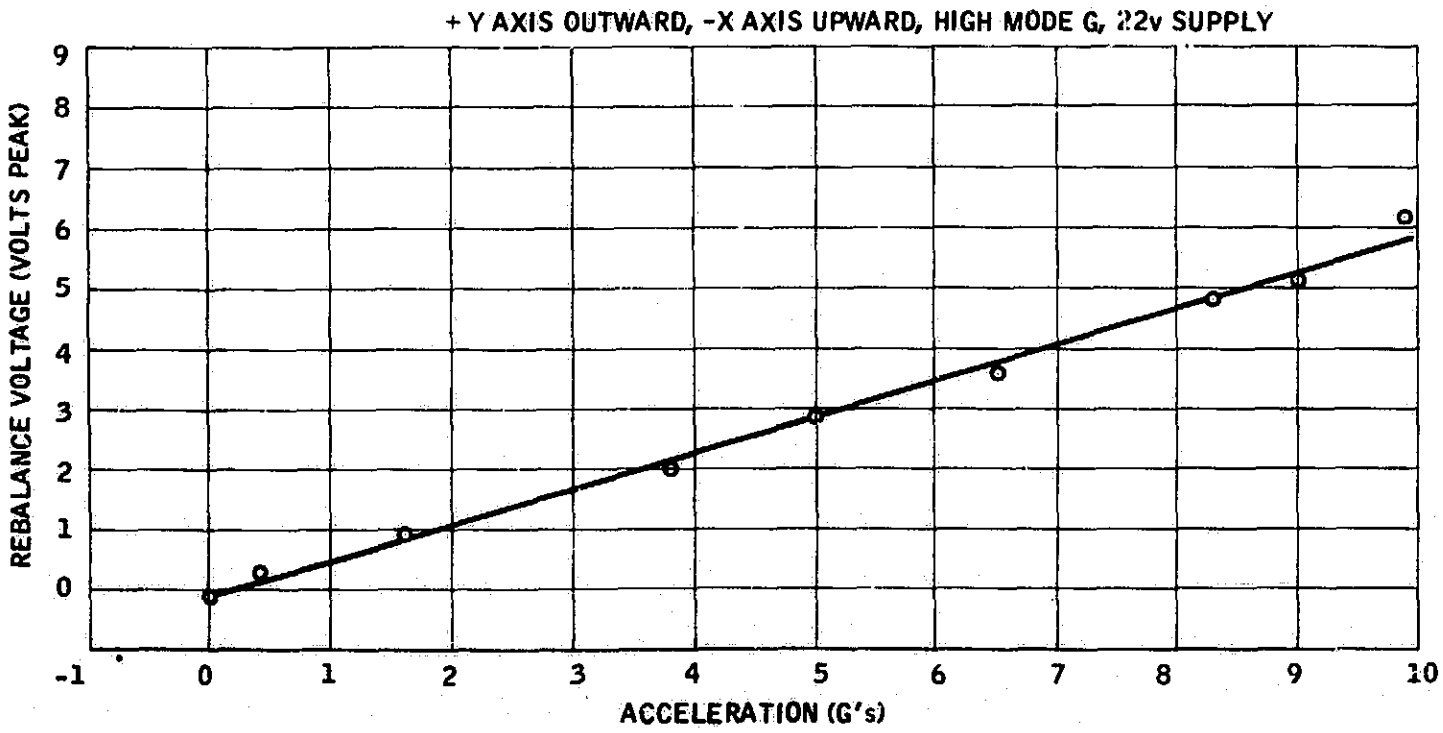


Figure 55. Results of Centrifuge Test No. 2

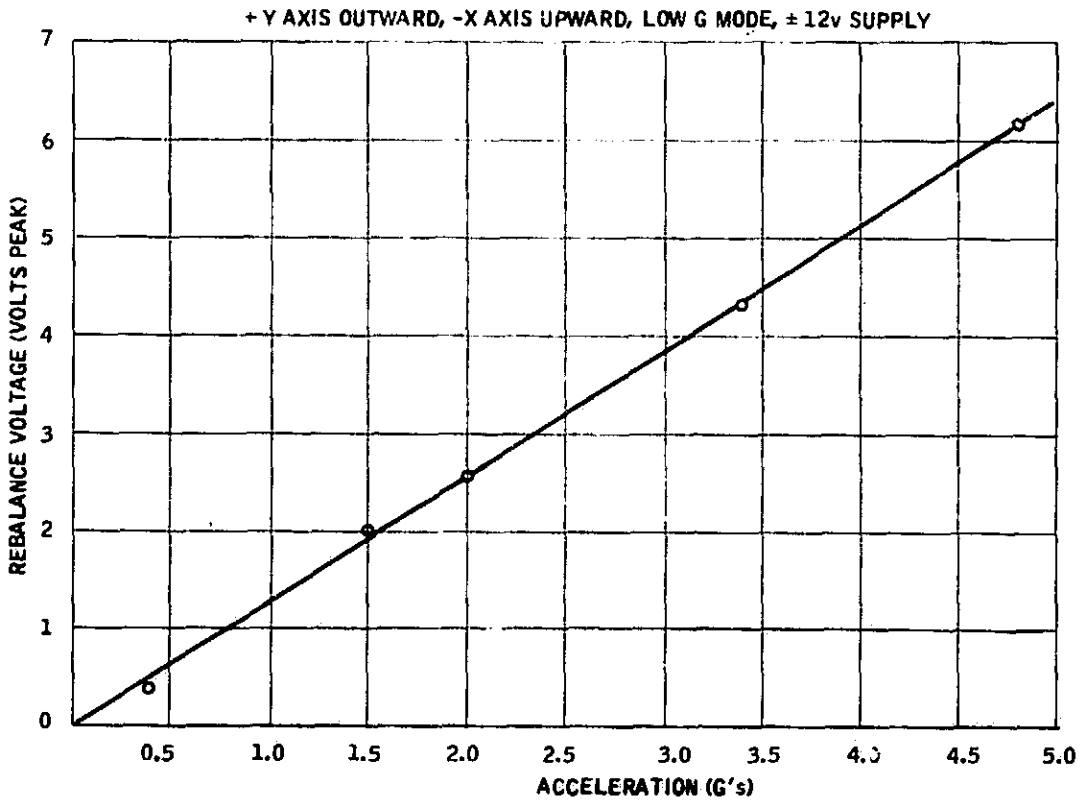


Figure 56. Results of Centrifuge Test No. 3

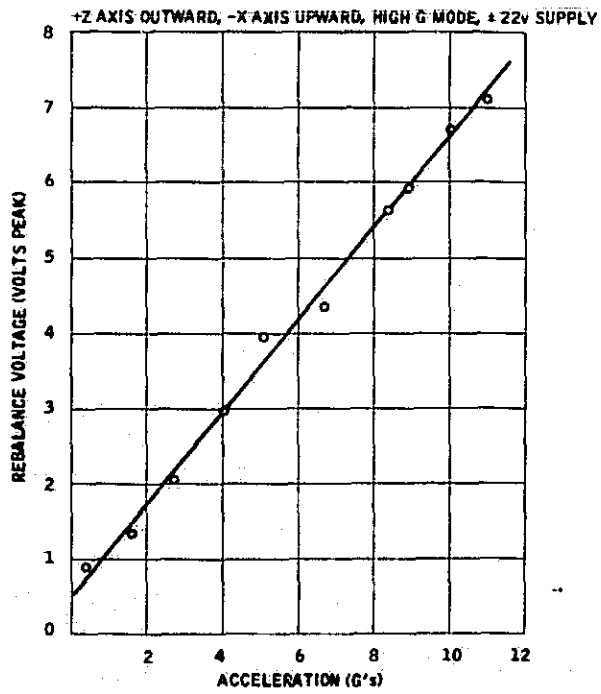


Figure 57. Results of Centrifuge Test No. 4

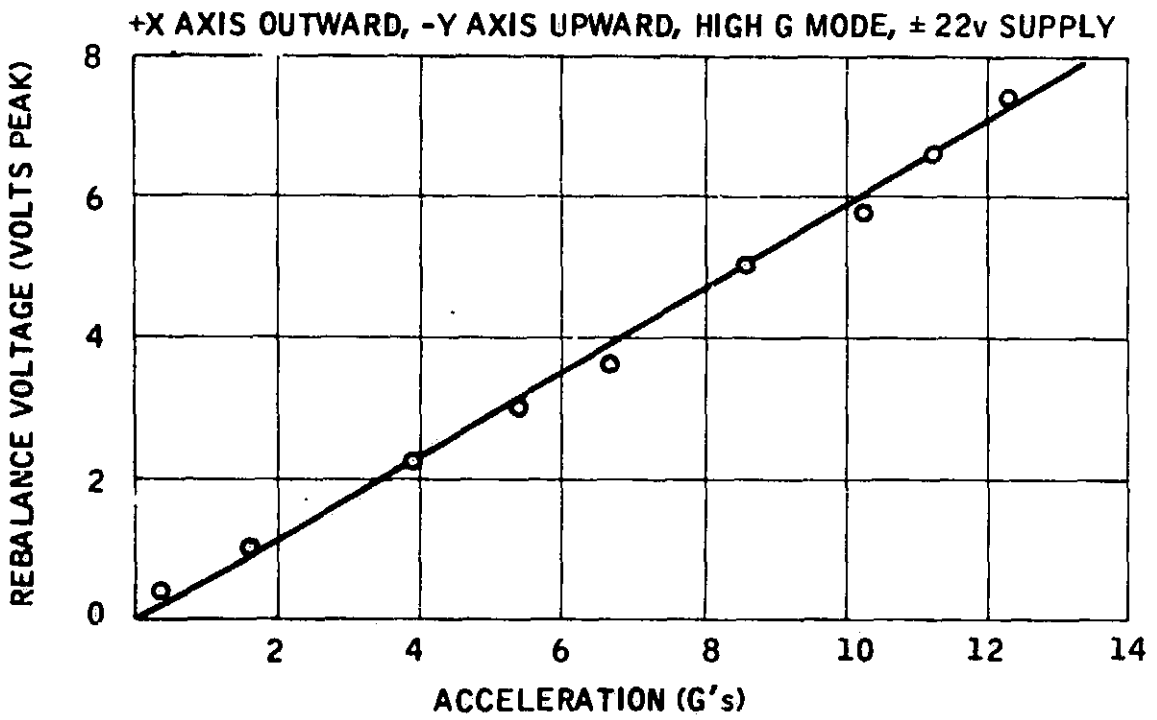


Figure 58. Results of Centrifuge Test Number 5

transformers was limited by the breakdown between coil windings. At present, breakdown appears to have been the factor which limited the results of these centrifuge tests.

There is a strong possibility that the output transformers were slightly damaged when, with the original suspension circuit design, suspension failures occurred with attendant large transient voltages. This is supported by tests conducted on the suspension system of the gyro built under JPL Contract No. 951148. Those tests showed that the output transformers of that suspension were capable of producing voltages compatible with 15-g support before encountering corona problems.

The results of the first test is truly noteworthy for low-g mode. The other low-g mode test utilized the ±12 volt supply for the output circuits; since this was the only change from the first low-g test, the maximum acceleration attained in the third test appears to be limited by the available supply voltage.

# SECTION V
# SDMEG READOUT SYSTEM

## INTRODUCTION

The ESG readout system is an important subsystem of the gyro. This section briefly describes the readout system of the SDMEG, and sources of reading error are summarized.

To accurately evaluate the drift performance and torque model of the SDMEG, it was important that spin vector components with respect to case axis coordinates be calculated accurately. For this reason, considerable attention was devoted in this program to two important aspects of this calculation:

- Specifying the location of the optical axis of each pickoff
- Defining the coefficients of the equation which yields the the direction cosine between each pickoff axis and the spin vector

The remainder of this section discusses the techniques which were developed and evaluated in this program for calibrating these readout parameters.

## READOUT SYSTEM DESCRIPTION

A block diagram of the SDMEG readout system is shown in Figure 59. The passage of readout information through the system and the sequence of operations with or on the information is indicated. Also shown is the location of the important readout components in the gyro test setup.

The heart of the readout system is the pickoff which is pictured in Figure 60. The pickoff consists of a lamp, the optics which include lenses and a beamsplitter, a photosensor for converting the optical signal into an electrical signal, and a preamplifier. The surface of the spinning rotor is either reflective or diffuse; the reflectivity of the surface determines the amplitude of the signal received by the photosensor. The signal is amplified and transmitted to the pulse-shaping electronics (HIT) by the preamplifier.

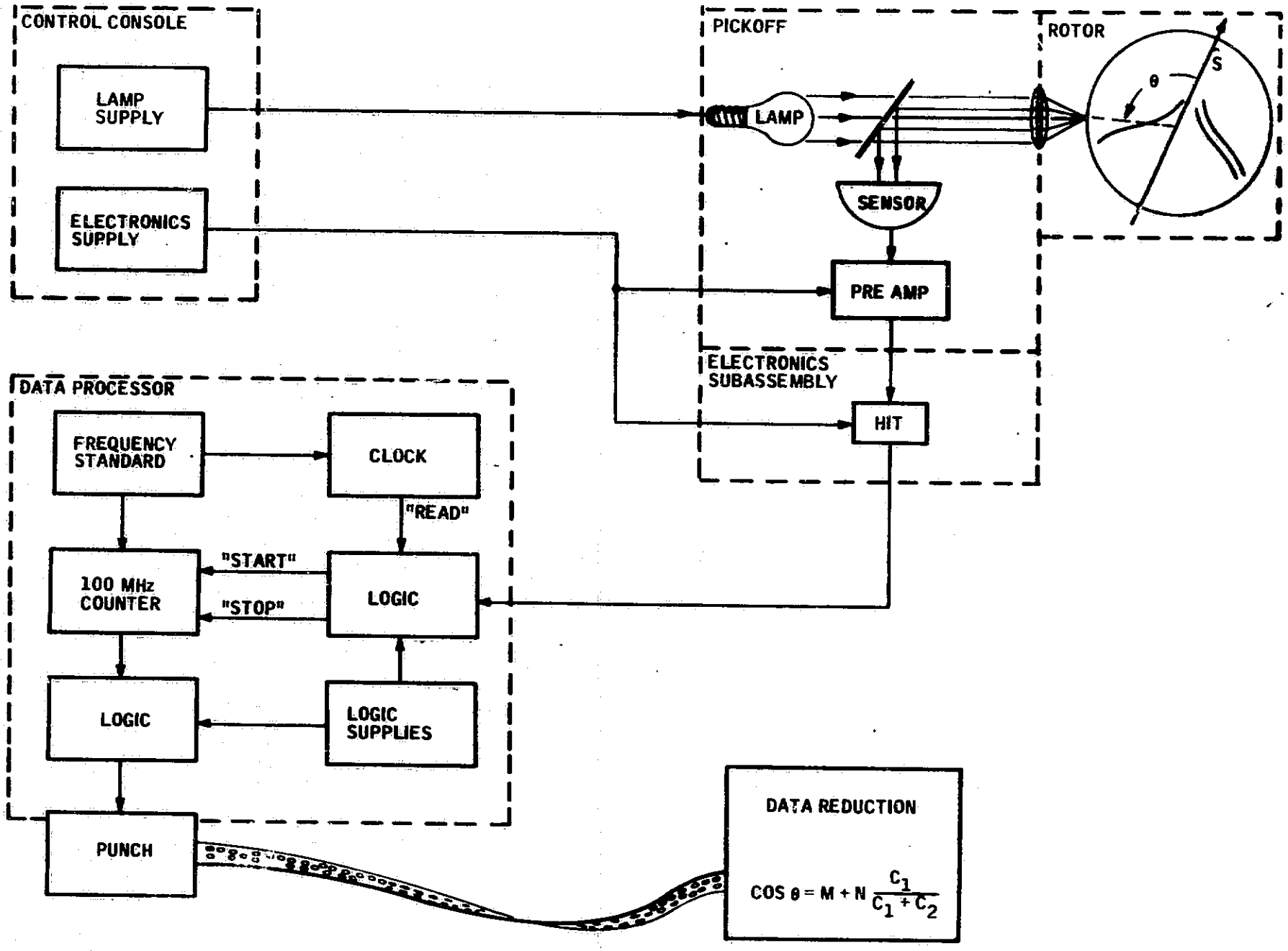


Figure 59. SDMEG Readout System Block Diagram

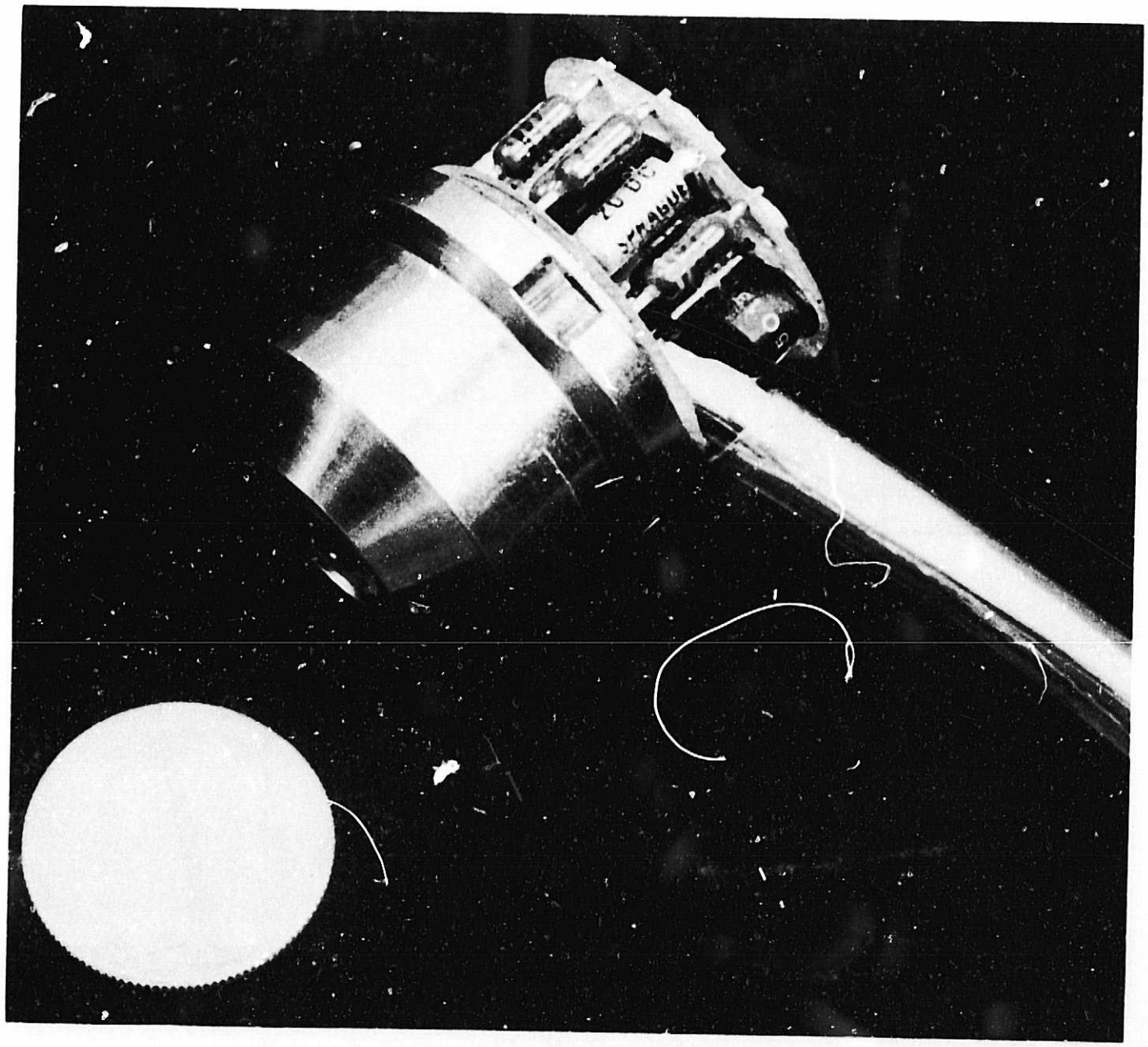

Figure 60. SDMEG Pickoff

The high-speed pulses generated by the HIT are received by the data processor logic, which sorts and uses the pulses for gating the pulse counters. High-precision clock pulses are counted by these counters; the counts which are recorded on paper tape provide a measure of the time interval between the pulses from the HIT. These time-interval measurements are used to calculate the phase angle between the portion of pattern lines viewed by the pickoff. The spin axis-pickoff axis direction cosine is then calculated using the characterization function of the pattern lines.

## Sources of Readout Error

A number of components of the readout system are potential sources of error. A detailed treatment of these sources is available in the literature;[1] consequently, these sources are only summarized.

Rotor Pattern -- Three types of error are associated with the patterning process. Generally, there is a pattern axis which should be coincident with or at a specific angle with the spin axis. Deviations are caused by patterning fixture misalignment and by uncertainties in the location of the spin axis at the time of patterning. Play in the application tool linkage, or an error in the master, can produce errors while applying the pattern. High-frequency (with angle) error is the result of imperfect control of line edge sharpness.

Rotor Surface -- Variations in the reflectivity of the rotor surface affect the amplitude of the sensor output; such variations occur from polishing variations or variations in the rotor material grain structure. Of greater significance is the presence of surface blemishes as the result of arcing between the rotor and the electrodes.

Optics -- Variations in the optics which affect the sensor output are potential sources of error. An important factor is the lamp luminosity which should remain constant throughout the operation of the gyro. Variations of illumination over the field of view, or irregularities in the field of view, can cause a deviation which is sensitive to the pattern line slope and its angle of approach.

Electronic -- Potential electronic sources of error include rise time variations of the photosensor, amplifier noise, and variations in triggering time. The digitizing process of the counters produces a least count resolution uncertainty in the data.

Other Sources -- Two important sources of readout error cannot be identified with specific components. One is uncertainty and instabilities in the location of each pickoff axis. This information must be precisely known for accurate use of the direction cosine information.

---

1. Research in Electrically Supported Vacuum Gyroscope, Volume IV; NASA CR 86125, November 1968, Section II.

The second source is a computational buildup associated with the strategy of obtaining three direction cosines out of data from two pickoffs using the direction cosine identity for an orthogonal set of coordinates. This effect, denoted as the third direction cosine error, is not an error per se; it is an amplification of other errors which may be present. As such, it is reduced or removed once the effects of other sources are reduced or removed.

## Reduction and Control of Error Effects

During the feasiblity study program attention was directed toward reducing the effects of readout error by:

- Development of a height insensitive trigger (HIT) to reduce the effect of reflectivity and lamp output variations
- Investigation of the effect of various polishing techniques and materials on the final rotor surface finish.
- Pickoff optics improvement

Each reaped benefits in improving the accuracy and dependability of the readout system. The most notable item is the HIT, which is described here in greater detail.

Reflectivity variations and changes in lamp output appear as short-term and long-term changes in pulse height. If the trigger occurs at a fixed voltage, a time interval error ($\Delta T$) results, as shown in Figure 61.

Since the basic electronic trigger circuits are voltage-sensitive, some method of compensation is desired to remove this error source. One method is by compensating the trigger device to render it sensitive to a fixed proportion of height rather than a fixed voltage. This is the purpose of the HIT. The block diagram of the HIT is shown in Figure 62, and the waveforms are shown in Figure 63. The basic operation is as follows.

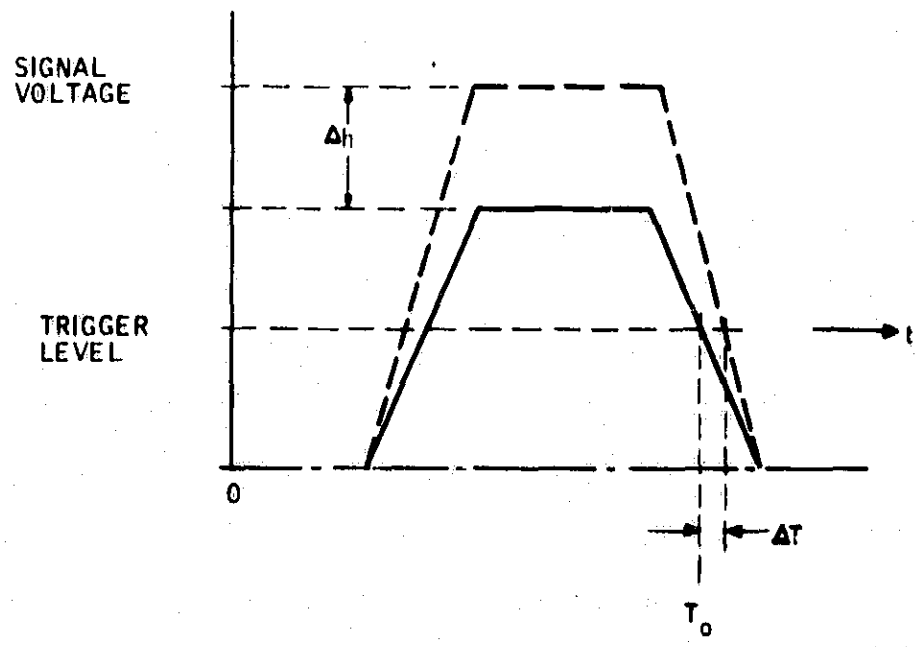


Figure 61. Error from Fixed Trigger Level

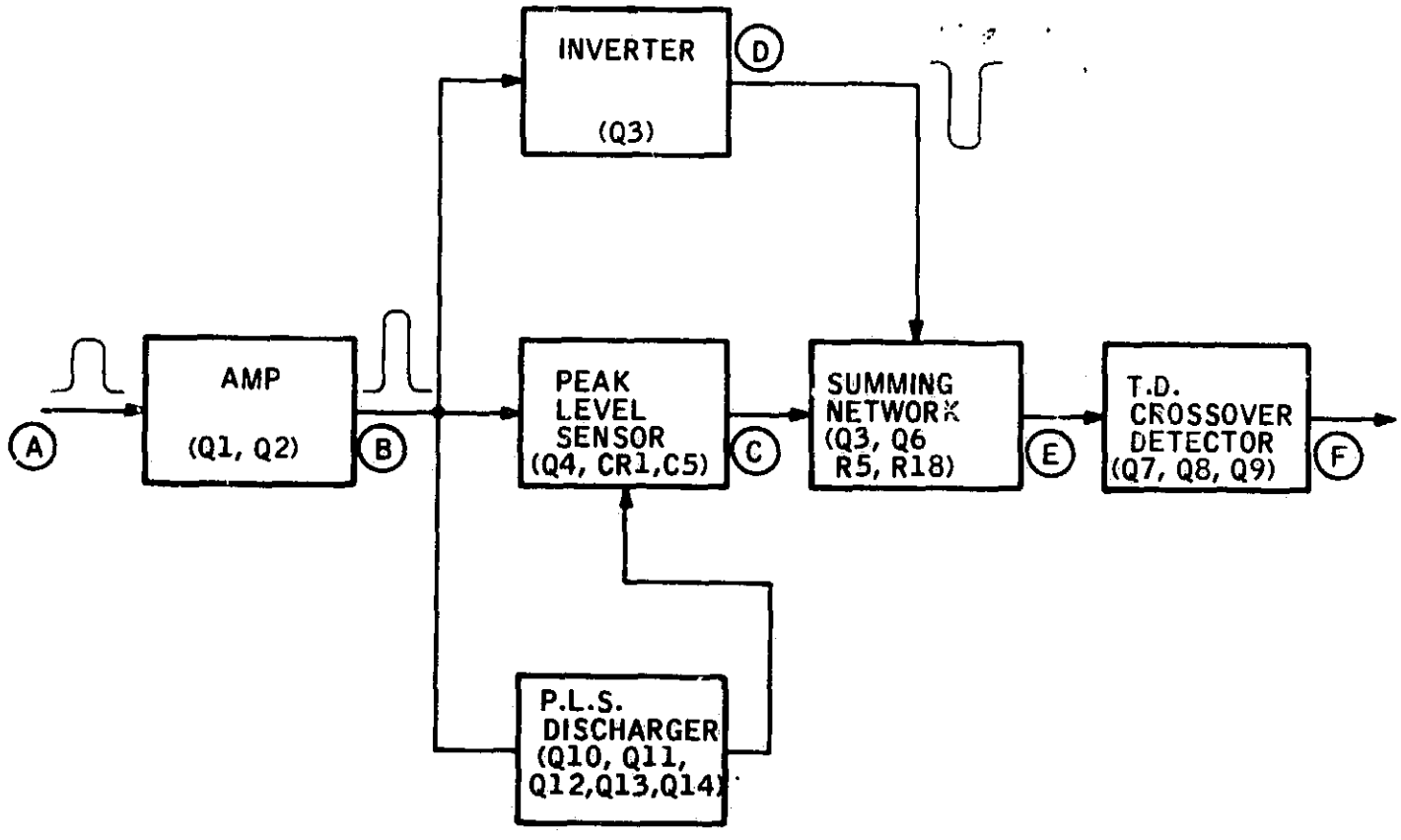


Figure 62. Block Diagram of HIT Circuit

The input pulse is amplified; the amplified pulse is sent to a peak level sensor that samples the peak voltage (flat top) of the input pulse and holds it. The amplified input pulse is then subtracted from one-half of the output of the peak level sensor. The zero-volt crossing of the resultant signal is a fixed percentage (nominally 50 percent) of the incoming pulse height. The zero-crossing signal is amplified to increase the slope of the zero crossing, and the zero crossing is then sensed by a tunnel diode threshold detector circuit. The trailing edge of the output pulse is the time mark used to control the time interval counters. The input pulse is differentiated and clipped, amplified, and used to discharge the voltage level sensor so it can accurately sample the peak voltage of the next input pulse.

At the same time that the suspension was modified, several modifications were incorporated into the HIT circuits (see Figure 22 for the schematic):

- The emitter bias resistor of the output emitter follower was returned to the -15 vdc supply rather than to ground. This allows the output stage to drive a 3K resistive load in the data processor with negligible signal attenuation.

- A level adjust control (R71, R72 of C13198-1, and R42 of C13198-2) was added to the circuit. Adjustment of R71 changes the bias on Q2, which then sets the level of input signal required to produce an output. The level adjust control permits any extraneous pulses below the set amplitude to be rejected.

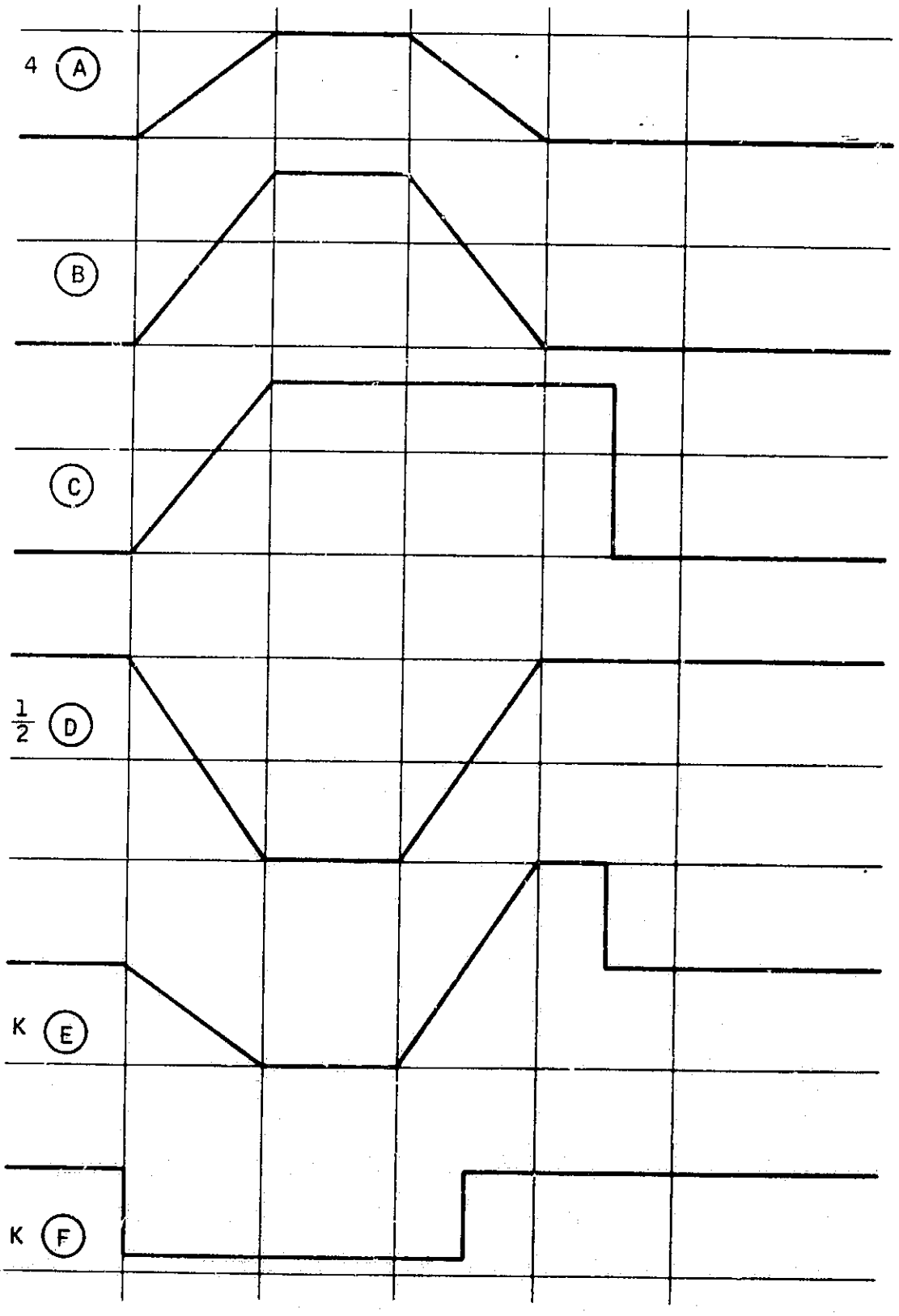


Figure 63 HIT Circuit Waveforms

- More power decoupling on the +15 vdc was added to the HIT cards. This improved the output wave forms.

- The summing network, Q3 and Q6 into Q7, was simplified.

- Capacitive coupling on the base of Q4 was added to produce a bias on the peak level sensor (Q4 driving CR1 and C5) independent of the level control adjustment.

Recent developments in reducing the effects of readout errors are in the use of faster electronic components in the HIT and the data processor gating logic. Compared to other effects, the effect of electronic sources of error is presently not significant. Another improvement is the incorporation of a levitation circuit in the suspension. This limits the output voltages to safe levels during lift and prevents surface blemishes from arcs.

Based on data gathered in this program, the remaining significant errors are patterning errors, pickoff alignment uncertainties, and computational buildup. During this program, procedural experiments were conducted in calibrating parameters which deal directly with these effects. The effectiveness of these procedures has been evaluated; they are discussed below.

## PICKOFF ALIGNMENT, ADJUSTMENT, AND CALIBRATION

In the alignment procedure used, the rotor is spun up to nominal operating speed, and the rotor pattern is used to determine when the pickoffs are aligned to a gyro case reference axis. This method is a nulling process and does not require an accurately calibrated pattern. Two of the pickoffs are adjusted to be parallel with the two gyro reference mirrors. The third pickoff is adjusted to be perpendicular to the plane determined by the normals of the gyro reference mirrors. The angle between the mirror normals is measured, thereby allowing the pickoff orientations to be defined with respect to an orthogonal reference determined by the mirrors.

The equipment used for the pickoff alignments consists of:

- Vertical axis turn table (TS 204)
- Lietz dividing head
- Gyro mounting fixture
- Gyro control console and readout system
- Theodolite, holding fixture, and level vial
- Pentaprism and holding fixture

The equipment is set up as shown in Figure 64.

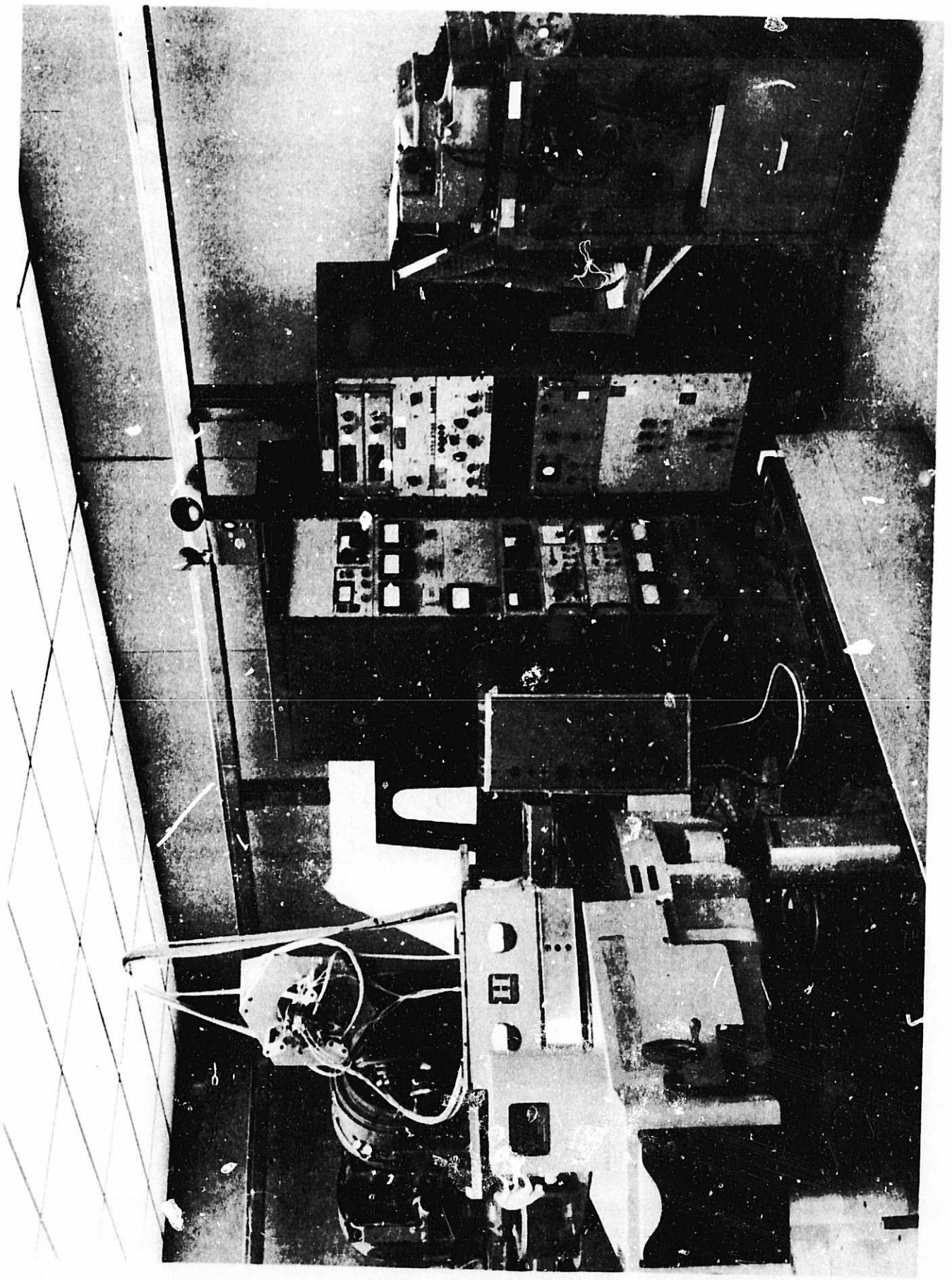

Failure 64. Pickoff Alignment Station

The Lietz dividing head is mounted on the vertical axis table with the dividing spindle axis horizontal and located so that the gyro reference mirror normals may be positioned parallel and colinear with the vertical table axis. The gyro holding fixture is mounted on the dividing head face plate so that the X and Y mirror normals are nominally perpendicular to the spindle axis (for X and Y pickoff alignment).

The pentaprism is mounted on a holding fixture which spans the vertical axis table. The gyro reference mirror can then be viewed by the theodolite through the pentaprism. The Z pickoff alignment is facilitated by adjusting the turn table so that its axis of rotation is vertical. This adjustment can be checked with the level vial mounted on the table.

Procedure

1) Using the dividing head tilt adjustment and vertical axis table, position the gyro so that the spin coil axis is approximately parallel to the EPA.

2) Perform the necessary prespin checks and spin-damp procedure to bring the rotor to operating speed.

3) After the rotor is at operating speed, adjust the spindle and tilt axis of the dividing head (in the case of the X and Y pickoffs) to make the mirror axis parallel to the axis of the vertical table (observing the coning of the mirror normal with the theodolite and pentaprism). For the Z pickoff, adjust the spindle and tilt axes so that the mirror normals are perpendicular to the table axis (horizontal when the table axis is vertical).

4) Adjust the position of the pickoff being aligned so that this pickoff reads a constant rotor colatitude (within the threshold of adjustment) when the table is rotated 360 degrees.

5) When making the final trim adjustments, it is usually necessary to plot count readings against table position to separate the direction and magnitude of adjustments from gyro drift.

6) Final data: If the pickoff cannot be satisfactorily aligned or if the desired readout accuracy exceeds the trim adjustment threshold, data are then taken for calibrating the existing misalignment for computer compensation. Data are recorded from the pickoff whose alignment is being calibrated and from a second pickoff for use as a phase reference.

7) Record data for two complete table revolutions.

8) Record data again for two complete table revolutions in the opposite direction from that of Step 7.

Data Reduction

The data recorded in Steps 7 and 8 for each pickoff (a total of six sets) are punched on cards in preparation for input to a stepwise regression program which was available from the Honeywell Scientific Computing Library. Each set includes two table revolutions to check the repeatability of the count data and to provide a more reliable determination of the constant portion of spin vector drift. By correlating the results in opposite directions, the apparent misalignment caused by spin vector drift from electric torque can be detected and removed from the results of the regression for pickoff misalignment.

The spin vector drift can be detected as follows: Let $C_x$ and $C_y$ denote the misalignment of the Z axis pickoff in the directions of the X and Y coordinates, as denoted by the pickoffs. With respect to some table reference angle, the change in the direction cosine of the Z pickoff can be denoted by

$$\Delta\lambda_z = C_x \sin\phi + C_y \cos\phi$$

where $\phi$ is the table angle from reference. Let the components of an electric torque be such that the change in the direction cosine from this torque is

$$\Delta\lambda_z = \frac{1}{H} \int_0^t (L_1 \sin\phi + L_2 \cos\phi)\, dt$$

where H is the rotor angular momentum. When the table rotates in one direction at a constant rate $\omega$, then $\phi = \omega_1 t$. If both misalignment and torque are present, then

$$(\Delta\lambda_z)_1 = \left(C_x + \frac{L_2}{H\omega_1}\right) \sin\omega_1 t + \left(C_y - \frac{L_1}{H\omega_1}\right) \cos\omega_1 t$$

The coefficients $\left(C_x + \frac{L_2}{H\omega_1}\right)$ and $\left(C_y - \frac{L_1}{H\omega_1}\right)$ are determined by regression on data taken with the table rotating in this direction. With the table rotating in the opposite direction, $\phi = -\omega_2 t$ ($\omega_2 > 0$). Then

$$(\Delta\lambda_z)_2 = \left(-C_x + \frac{L_2}{H\omega_2}\right) \sin\omega_2 t + \left(C_y + \frac{L_1}{H\omega_2}\right) \cos\omega_2 t$$

The coefficients $\left(-C_x + \frac{L_2}{H\omega_2}\right)$ and $\left(C_y + \frac{L_1}{H\omega_2}\right)$ are determined by regression on data. One can then separate $C_x$ from $\frac{L_2}{H}$ and $C_y$ from $\frac{L_1}{H}$ by appropriate manipulation of these coefficients. In practice it has been found that $L_1$, $L_2$ and $|\omega_2 - \omega_1|$ are small enough that, in the separation process, the assumption that $\omega_1 = \omega_2$ has a negligible effect on the results for $C_x$ and $C_y$.

Useful Residual Information

This pickoff alignment adjustment and calibration procedure utilizes the gyro in actual operating conditions; consequently, the alignment parameters obtained from this procedure define where the "operating axis" of the pickoff is located. This axis is best defined as the center of illumination of the spot on the rotor surface; as such, it is sensitive to irregularities caused by illumination variations or field-of-view irregularities. By using data gathered under actual operating conditions, some of these irregularities are automatically taken into account in the alignment adjustment and calibration.

Other irregularities sensitive to the pattern slope and direction of approach would also be included in the alignment calibration data. The residuals can be monitored for such irregularities while reducing the data for alignment parameters; an example would be checking the data for a repeatable second harmonic content. The same combinatorial technique can be used for separating second harmonic effects caused by spin vector drift. When the data have been monitored for these effects, the magnitude of these results as a rule have been within or slightly larger than the noise level of the data.

## PATTERN LINE CALIBRATION

Three sources of error associated with the pattern line and the pattern application process were delineated earlier in this section. To reduce the effects of the errors, the nominal line equation was expanded so that nonrandom errors in the pattern could be computer compensated. The line equation for perfectly applied cosine pattern lines is of the form

$$\cos\theta = M_o \frac{C_1}{C_1 + C_2} - N_o \tag{1}$$

where $M_o$ and $N_o$ are design constants. The equation was modified to read

$$\cos\theta = M \frac{C_1}{C_1 + C_2} - N + P_2\psi^2 + P_3\psi^3 + P_4\psi^4 + P_5\psi^5 \tag{2}$$

where

$$\psi = \frac{C_1}{C_1 + C_2} - 0.5$$

and M and N as well as the P's are constants determined by least squares fitting of data.

## Data Sources and Errors

Two sources of data have been used for calibrating the coefficients:

- Microscope data after pattern application before the rotor is removed from the patterning fixture
- Pickoff data from the assembled gyro after the pickoffs have been aligned

The results of these calibrations were tested on drift test data with varying degrees of success. The measurement of success was in terms of the magnitude of steps noted in the inertial space spin vector data at the times that the pickoff modes change -- the smaller the steps, the greater the degree of success.

When checked out with drift test data by this method, coefficients from both sources of data showed good success for some gyros and little success for others. Even when corrected for deviations in three-pickoff checkpoint results (described later in this section), neither source provided distinctly better results than the other. On the basis of this finding, it was necessary to further elaborate on one of the existing data collection procedures, or develop new procedures, which accurately take into account inherent uncertainties or errors of the existing procedures.

Either source of data is, of course, not without error. The microscope data are measured about the pattern axis, not the spin axis; it must be corrected for pattern axis - spin axis misalignment. Nor is there any assurance that the microscope data correlate with pickoff data obtained at the same point. The pickoff data are referenced to known dividing head spindle axis increments. It must not only be corrected for spin vector drift, but some absolute reference must be established to specify the true spin axis-pickoff axis angle for each data point used in the calibration.

## Useful Error Compensation Techniques

Spin vector drift can be estimated over a series of data points taken during a scan at fixed spindle axis increments by returning to some previous spindle axis setting after the scan is completed. As long as the scan is neither too large nor too lengthy, a constant drift with time can be assumed without incurring intolerable error.

Both microscope and pickoff data can be corrected with data taken at certain spin vector "check points". Such a check point is illustrated in Figure 65. The Z-axis pickoff is positioned to view the equator (as is best determined by known pattern characteristics at the time), and the spin axis is positioned between the X and Y pickoffs. Data are recorded when the $C_1$ counts from the X and Y pickoffs are equal. The two pickoffs are known to be reading the same colatitude (denoted by $\theta_{ab}$ in Figure 65). From the pickoff alignment calibration and the angle between mirror normals, the angle $\tau_{ab}$ can be calculated. Using trigonometric relationships, one can assert that

$$\cos \frac{\tau_{ab}}{2} = \frac{\cos \theta_{ab}}{\cos \sigma}$$

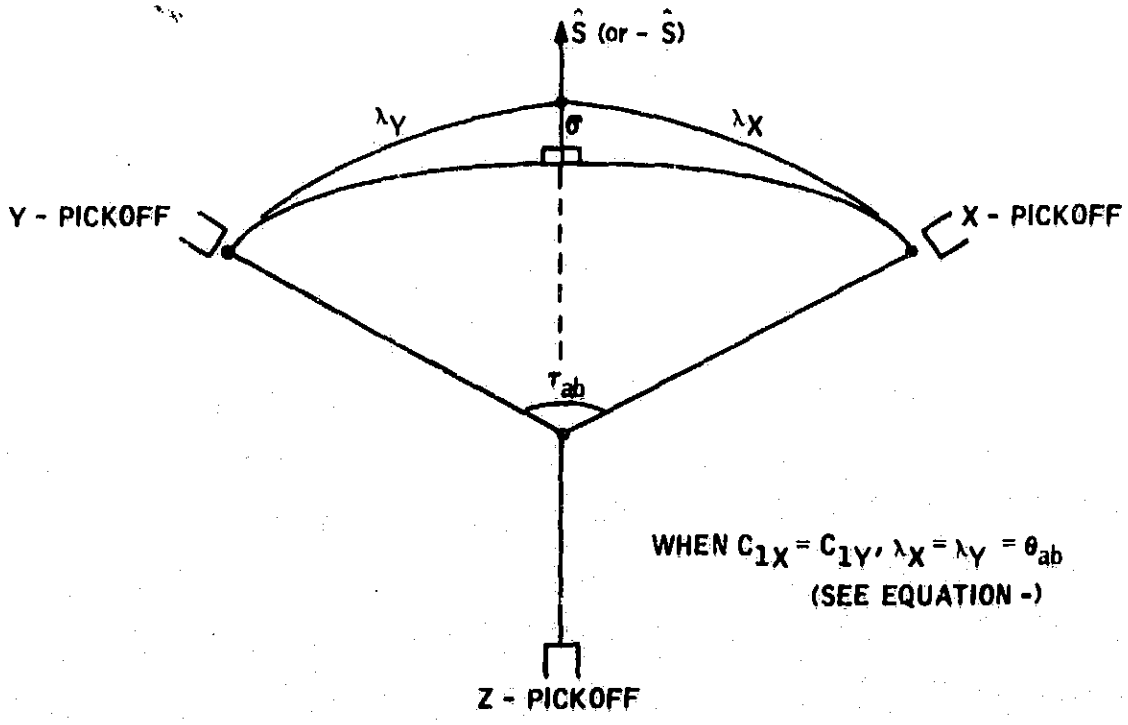


Figure 65. Pattern Line Checkpoint Position, Two Pickoffs

The greatest uncertainty in this equation is the value of $\sigma$ which is the combination of

- The deviation of the Z pickoff view from the true rotor equator
- The component of Z pickoff misalignment in the direction of the spin axis

However, by positioning the Z pickoff nominally on the equator, the effect of this uncertainty is minimized (since $\cos \sigma \simeq 1$ over a relatively wide range of $\sigma \sim 0$).

This process establishes a specific ratio of $\frac{C_1}{C_1 + C_2}$ to a specific angle $\theta_{ab}$; if exactly equal $C_1$ counts are not achieved, one can use the average of the X and Ȳ $C_1$ counts for the numerator of the count ratio with good accuracy. (The only nonrandom error is the change of line slope; over a small range which exceeds the expected resolution of adjustment this is not expected to exceed the random error.) A second check point can be obtained using the same pickoffs with the rotor positioned anti-parallel [midway between the (-X) and (-Y) axes] to that shown in Figure 65. With such a checkpoint on each end of the pattern one can check the accuracy of, and make appropriate adjustments to, either microscope or pickoff data.

Other pairs of checkpoints occur with the spin vector aligned between the X and Z pickoffs and the Y and Z pickoffs. Additional useful checkpoints occur when the spin axis is positioned so that one pickoff views a pattern extremity, a second the other extremity, and the third the equator. Still another useful checkpoint is realized at a different colatitude by adjusting the spin vector direction in the envelope so that all three pickoffs yield nearly equal $C_1$ counts and an average count ratio. Figure 66 shows this situation when the three pickoff axes and mirrors are perfectly aligned. The spin axis is nominally parallel to the housing axis; each pickoff is $\cos^{-1} \pm \sqrt{\frac{1}{3}}$ for that axis. The average count ratio can be identified with that colatitude angle.

If the pickoff and mirror alignment are not perfect, the colatitude angle identified with the equalized count ratio is slightly different. It can nevertheless be determined by calculating the component of misalignment of each pickoff along the housing axis, subtracting the component from $\cos^{-1} \pm \sqrt{\frac{1}{3}}$, and averaging the results. For small deviations in the range of pickoff misalignments, linear averaging is sufficiently accurate.

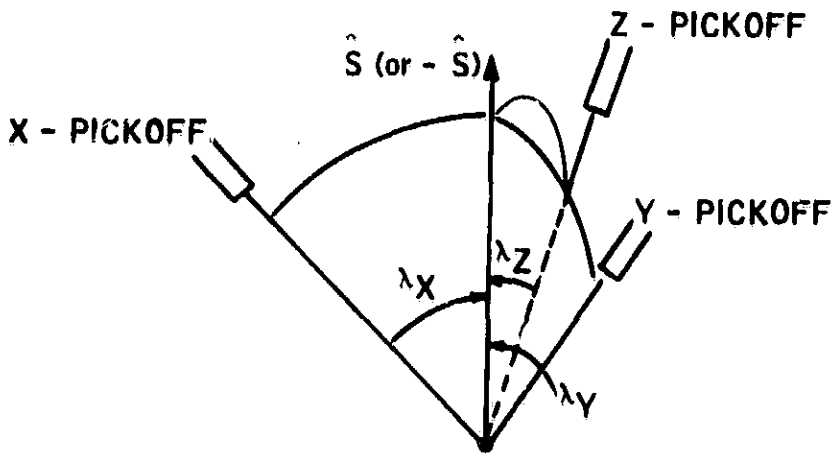


WHEN $C_{1X} = C_{1Y} = C_{1Z}$, $\lambda_X = \lambda_Y = \lambda_Z = \cos^{-1}\sqrt{\frac{1}{3}}$ (or $\cos^{-1} -\sqrt{\frac{1}{3}}$)

Figure 66. Pattern Line Checkpoint Position, Two Pickoffs

## Third Direction Cosine Considerations

The effect that errors in direction cosines calculated from count data have on the third direction cosine calculation has been treated in the literature[2]. Not only is that error sensitive to the other errors but also the direction cosines themselves. The error can be amplified as the pickoffs being read view portions of the pattern remote from the equator.

Large errors can be avoided in the choice of pickoffs used, when a choice is available. In this case, the error is minimized when the two pickoffs nearest the equator are used. This principle has been adopted in the procedure for conducting drift tests on the SDMEG.

The same effect has recently been taken into consideration in developing pattern line calibration procedures. The amplification factor in the third direction cosine calculation can be balanced with a mechanization equation which describes the pattern lines more precisely and in greater detail at

2. Ibid; Section IV.

the pattern extremes than at the equator. The expanded form of the mechanization (Equation 2) is amenable to such a description. All terms are relatively significant when the count ratio is very small or very large; in the middle range $\left(\frac{C_1}{C_1 + C_2} \sim 0.5\right)$ only the first two terms are relatively significant. To provide the greater detail at the pattern extremities, the scanning increment is reduced, resulting in a greater density of data points from these regions.

## Pattern Line Calibration Procedure

The procedure outlined here is one that proved successful for the FGG379A1 S/N 1 SDMEG built under JPL contract 951148 and transferred to the drift performance evaluation program. This procedure was first implemented in April 1968. Pickoff data are used because, like the pickoff alignment procedure, those data are obtained from the gyro under actual operating conditions. Except for the theodolite and the pentaprism, the same appratus as that used in pickoff alignment adjustment and calibration is used for pattern line calibration.

1) To provide a convenient rotation reference, the gyro is mounted and shimmed on the dividing head so that a mirror normal is parallel to the spindle axis. The dividing head is mounted on the vertical axis turn table.

2) Accurately align the damping axis parallel to the EPA. Perform the spin-damp procedure to operating speed.

3) Position the gyro case with respect to the spin vector so that the $C_1$ counts from all three pickoffs are as nearly equal as possible within limits of adjustment. Repeat for the opposite rotor hemisphere.

4) Reposition the table and tilt axes so that the spindle axis is nominally perpendicular to the spin axis.

5) Measure the angle between the averaged count ratios obtained in Step 3 by positioning one of the pickoffs at each of the count ratios obtained and reading the spindle axis scale at each setting.

6) Position the same pickoff midway between the two settings of Step 5. This should establish the count ratio at the equator. To reduce the effect of drift, it may be necessary to repeat this and the previous step.

7) Scan the pattern 1 degree on each side of the equatorial count ratic position in 10-minute increments. Start and end with the same spindle axis setting to provide a correction for drift.

8) Scan the entire pattern in 5-degree increments. Start at the equatorial count ratio position and scan to one extremity, and return to starting spindle axis setting. Repeat for other extremity, readjusting starting position for drift if necessary.

9) Readjust starting position at the equatorial count ratio. Rotate spindle axis 30 degrees and scan in 1-degree increments to the end of the pattern. Return to starting spindle position at equator. Repeat for the other extremity.

10) Adjust case to the three two-pickoff checkpoint positions for each combination of pickoff pairs - two positions with both pickoffs reading the same pattern extremity (one for each extremity) and one position with the pickoffs reading opposite extremities. The third pickoff, positioned nominally at the equator for each setting, is also read for calculating $\sigma$ of Figure 65.

11) For determining pattern limits, scan each pattern extremity in 2-minute increments until the pattern is lost. Start about 20 to 30 minutes from the discrenible end of pattern to check the linearity or mechanization accuracy of the extremities.

12) Shut down gyro and reduce data. Only the 5-degree and 1-degree data are used in regressing for coefficients; it is first corrected for spin vector drift, using a linear interpolation with time. Drift during each scan is estimated from the change in count ratio for the identical dividing head settings at the beginning and end of each scan with the aid of the 10 minute increment scan obtained in Step 7.

13) Using the coefficients obtained from the 5-degree and 1-degree scans, spin vector colatitude angles are calculated using all checkpoint data and 2 minute scans obtained in Steps 3, 10, and 11. Compare the results with what these angles should be from knowledge of pickoff alignments. Make necessary corrections to the 5-degree and 1-degree scans and obtain a corrected set of coefficients. Repeat this step until satisfactory results are obtained.

It should be observed that only one-third (or less) of the data used for finding coefficients comes from the region between the colatitude angles of 60 degrees and 120 degrees, which covers two-thirds of the patterned region. The other two-thirds are recorded from the pattern extremities.

The coefficients obtained using this procedure were used for reducing the data of 17 drift tests conducted in 1968 and 1969. The steps noted in the data of these tests were two minutes or less in over 70 percent of the cases. None of the steps exceeded three minutes of arc.

# SECTION VI
# SDESG DATA ANALYSIS COMPUTER PROGRAMS

## INTRODUCTION

A major task of the SDMEG development and evaluation program was to prepare and develop software for reduction and to analyze drift test data from the gyro. Programs were written for use on the H-1800 computer located at the Honeywell Aerospace facilities in Minneapolis and on the IBM 7094 computer located at JPL. Primary development of the programs took place on the H-1800 version of the programs; when they were satisfactorily checked out with data, duplicate programs were modified for the 7094 and were checked out with data at JPL.

## SOFTWARE SYSTEM DEVELOPMENT

A total of seven computer programs were developed under this contract. The designations and titles of these programs are

- SM1100 - Edit and Initial Calculations
- SM2200 - Transformation of Coordinates
- SM3700 - Manual Edit
- SM4000 - Math Model and Regression
- SM6100 - Performance
- SM7000 - Data Simulation
- SMPLOT - Plotting of Data

The data analysis system structure and the flow of data through the system are diagrammed for the H-1800 in Figure 67. Except for SMPLOT, all of the programs are operational on the 7094 computer.

The first six programs were developed, coded, and checked out in 1965. Documentation drafts of these programs were prepared in early 1966. The first drift test data became available late in 1966. From the results of these test data, the math model was expanded and reorganized; appropriate modifications were made in Programs SM4000 and SM7000. In 1967 duplicates of these six programs were modified for running on the 7094 computer at JPL. The program documentation (Honeywell R-ED 1749) was published 1 July 1967.

Program SMPLOT was developed in 1968 for use with the Honeywell Aerospace machine plotting facility in Minneapolis. This program expedited the

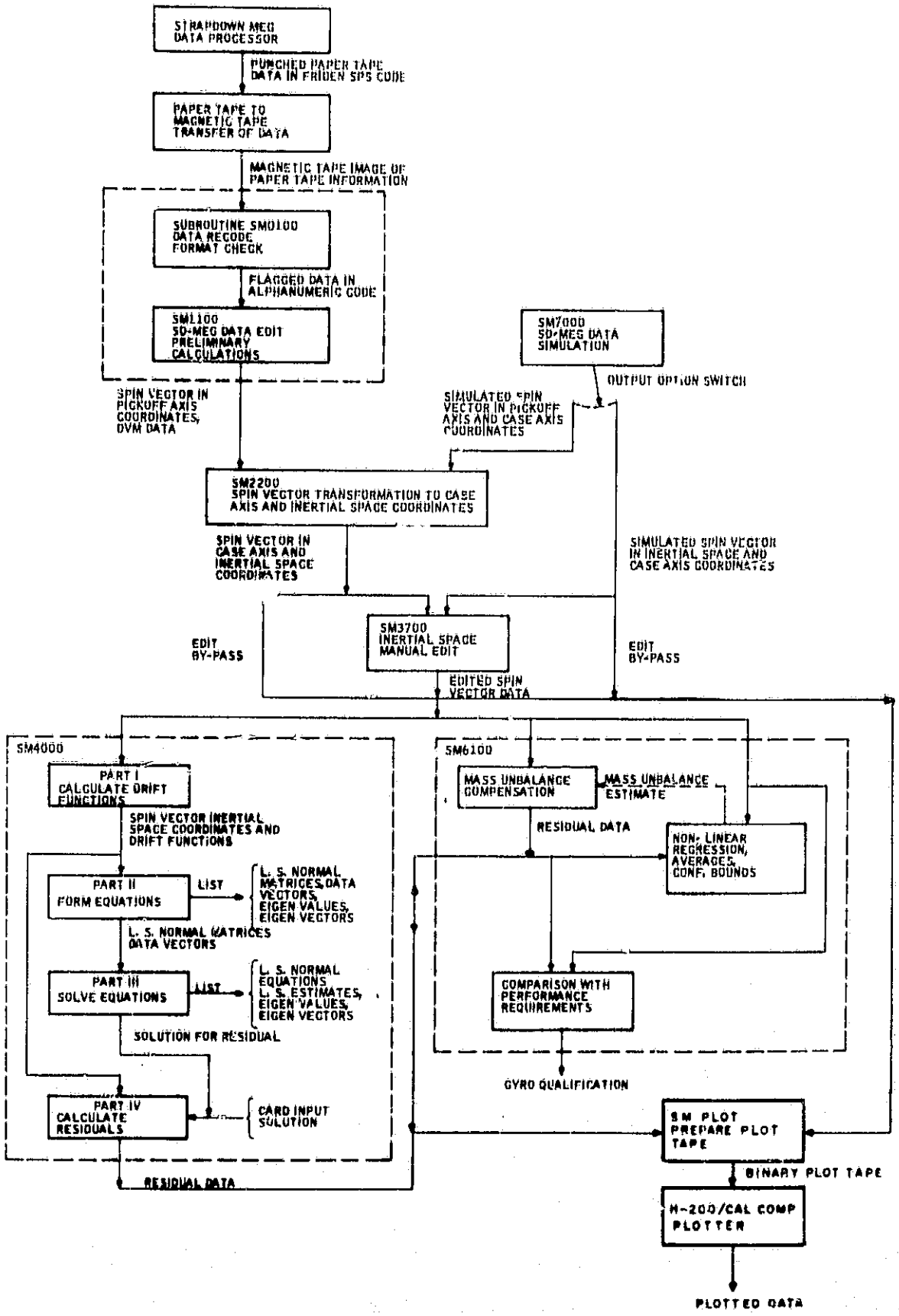


Figure 67. SDMEG Drift Data Analysis System for H-1800 Computer

overall analysis effort on 17 drift tests conducted on the FGG379A1 S/N SDMEG which started in April 1968 and ended in January 1969.

## PROGRAM OPERATIONS

The basic operations of each program are summarized in the remainder of this section. Included in these summaries are options available to the analyst and some guidelines in preparing the card-input data to these programs. Since details of the program operations and card input formats are described in the documentation, these items are not duplicated here.

### Preliminary Gyro Data

To implement fully and precisely the capabilities of these programs, a number of parameters about the gyro under test must be known. For bookkeeping purposes, there are several means of identifying the gyro. Such parameters as the rotor, housing vacuum, run number, and the dates and times of the drift test can be entered on the standard header which is created by Program 3M1100 and is duplicated on the output tapes and listings by the other programs. However, it is not necessary to have these data to operate the programs.

There are critical gyro parameters which must be known. These parameters are

- Rotor pattern mechanization parameters
- Angle between the two mirrors mounted on the pump end of the gyro housing
- Alignment of the pickoffs with respect to the mirrors
- Rotor pattern limits
- Rotor moment of inertia
- Rotor optimum speed (optional)
- Digital voltmeter sensitivity coefficients (optional)

These parameter are either measured directly, or procedures are followed to calculate them. Throughout this program, methods were devised for taking data used for estimating the pickoff alignments and pattern constants. Estimates were obtained using a stepwise regression program available from the Honeywell Computer Sciences Library; however, a significant amount of hand preparation of the data is required to obtain precise estimates of these parameters.

A nominal estimate of the moment of inertia is sufficient for these programs; it is only necessary that the value of inertia used be the same throughout the system of programs. Pattern limit parameters serve as an editing function; as such, they are not as critical as the other parameters. The optimum rotor speed is useful only if the change of rotor speed over a normal drift test period causes significant changes in spin vector drift characteristics.

The data processing unit which punches test data on paper tape may or may not include a digital voltmeter which can be used to measure such additional items as suspension currents, vacuum pump current, and thermocouple currents. Voltages representing these measurements are digitized and punched on tape. If the voltmeter is used, the conversion constants which relate the recordings directly to the parameters measured are needed.

## Program SM1100 - Edit and Initial Calculations

In addition to editing the data, this program controls the operation of Subroutine SM0100. Data from several drift tests can be batch processed by this subroutine, which numbers the data events sequentially, converts the data into an alphanumeric code, and checks the data for errors in format. The event numbers, recoded data, and format information are printed out on an intermediate tape which is usually saved for later use.

The output of the subroutine is then processed by the main program. The portion of data on the intermediate tape to be processed is defined by card input. If any errors in the format of a data event are detected, the event is rejected. If the format is correct, the data is unpacked and the initial computations are made. Spin vector components (direction cosines) in pickoff axis coordinates are calculated from the cosine pattern mechanization constants. If digital voltmeter measurements were recorded, the quantitative values of the parameters which these measurements represent are also calculated. Data events are also rejected if any of the following criteria are not satisfied:

- (Optional) The time elapsed between this event and the previously accepted event is equal to or greater than a quantity which is specified by the analyst.
- Two and only two "$C_1$" measurements are nonzero.
- Each ratio $C_1/[C_1 + C_2]$ is less than unity.
- The rotor speed calculation does not exceed 1000 rps.
- The direction cosines come within bounds which are determined by the rotor pattern limits.

- (Optional) The sum of the squares of the direction cosines calculated from the counter information does not exceed unity by a quantity proportional to the pattern uncertainty and the error in pickoff alignment.

Data events accepted by this program are recorded on tape which is saved for input to the next program.

Options available to the analyst include:

- Whether to run only the subroutine, only the main program, or both. The subroutine is used if the intermediate data tape has not been created or is not available. In practice, both subroutine and main program may be run sequentially if data from one drift test are to be processed.

- Whether to produce the standard header on the output tape.

- Whether to use the time increment edit. Sometimes it is desirable or necessary to record data at shorter intervals than is desired in the analysis. This option (which may also be exercised in Program SM3700) serves as a convenient means to delete these points.

- Whether to use the third direction cosine edit. This option may be useful if noisy data are encountered and if compensation for pickoff misalignments is not used in Program SM2200. In practice, if the pattern limit parameters are reasonably precise, this option is unnecessary.

There is a provision in the header for indicating the starting and ending rotor speeds as well as the length of the drift test. These parameters are used to calculate the rundown time constant which is added to the header.

A seven-digit identification number is formed for each data point. This identification number consists of the gyro station number (the last digit of the first data word), the run number (the last two digits of the fifth data word), and the four-digit event number assigned by Subroutine SM0100. This number is carried through subsequent test data outputs to aid in identifying and sorting listings.

### Program SM2200 - Coordinate Transformation of Spin Vector Components

This program transforms the spin vector data into those sets of coordinates used for analysis by the SDMEG math model and gyro performance programs.

Only the inertial space components of the spin vector are used in the gyro performance program (SM6100); however, the math model program (SM4000) uses both inertial space components and the components of a test set of coordinates fixed with respect to the gyro housing. Program SM2200 must therefore prepare the data in two sets of orthogonal coordinates--one fixed to the gyro and one fixed in inertial space--and record the spin vector data on a magnetic tape which is saved for input to the gyro performance and math model programs.

The case axis coordinates, defined by the normals of the mirrors mounted on the gyro, are used as the set of gyro-fixed coordinates in the math model program. Since the pickoffs are aligned to be as nearly coincident as possible with them, the calculation of spin vector components in case axis coordinates reduces to a compensation for any misalignment of the pickoffs. Three spin vector components (direction cosines $\alpha, \beta, \gamma$) are calculated from information provided by two pickoffs, from the orthogonality identify and from sign continuity criteria.

Inertial space components of the spin vector are obtained by performing a series of coordinate rotations on the spin vector components in case axis coordinates. Because it is relatively easy to define the orientation of the gyro with respect to the vertical axis, the first three rotations transform the spin vector data into a set of coordinates whose orientation is determined by the vertical axis and the earth's polar axis (EPA). Two more rotations from this intermediate set of coordinates complete the transformation to inertial space coordinates.

Several alignment parameters are needed by the program.

- Test station latitude
- Elevation angles of the envelope mirror normals
- Azimuth angle of one of the mirror normals
- Angle between the mirror normals
- Whether the elevation of the Z-axis pickoff is positive, negative, or zero

The conventions adopted are such that elevation angles are positively signed if the positively directed case axes (defined by the pickoff end) are above the horizontal plane. Thus, if mirror normals are defined to be directed outward from the case, the elevation angles of these normals are positive if they are below the horizontal plane. The azimuth angle of an outward mirror normal is measured with respect to west, and is positive if it is north of west.

Options available to the analyst include

- Choice of input data from Program SM1100 or Program SM7000
- Which mirror azimuth angle is input
- Whether to compensate for alignment errors

The data usually processed are the output of Program SM1100; however, the simulation program can output data compatible for input to Program SM2200. This alternative has been employed for checking out the programs.

The azimuth angle of either mirror normal may be used. In principle, the more precise measurement is obtained from the normal closer to the horizontal plane. If both are accessible for azimuth measurement, the Y-axis mirror aximuth ($\psi'_m$) is preferred because it is used directly in the program. If the X-axis mirror aximuth ($\psi_m$) is input, $\psi'_m$ is calculated from it and the other alignment parameters.

Compensation for pickoff misalignments should be employed if their misalignments exceed the accuracy desired in the SM2200 output data or if the nonorthogonality of the mirrors exceeds the desired accuracy. If compensation is employed, the misalignments of the pickoff axes are to be provided by card input, in the form of direction cosines with respect to the mirror normals. The program automatically adjusts the X-axis pickoff misalignment for mirror nonorthogonality. Misalignment of the Z-axis pickoff is measured with respect to the axis orthogonal to the mirror normal plane.

From the input data and the misalignments, two direction cosines are uniquely determined. The magnitude of the third direction cosine is calculated from the orthogonality identity

$$\alpha^2 + \beta^2 + \gamma^2 \equiv 1$$

The sign of the third direction cosine is determined from a sign continuity criterion which assumes that counter data are taken from the two pickoffs viewing areas nearest the rotor equator throughout the test. If the test is carried out in this fashion, the sign of the third direction cosine never changes, for the sign of any cosine would change while the pickoff associated with that cosine is being used.

Exceptions to the sign selection criterion can occur, and the input data must be examined for these exceptions. The selection process must first be initialized; a positive sign is assumed by program for the third direction cosine for the first data point unless it is cited as an exception by the card input. If the test is not correctly carried out, and the sign of the third direction cosine does change, the first data point with the change of sign must be cited as an exception.

The program checks the validity of the sign that it carries through the data by comparing that sign with the sign of the cosine from counter data when the combination of pickoffs used changes. Such a change is detected by a change in the counter code number which follows station time in the data. If this sign check fails, the program stops. Erroneous data points adjacent to the change in pickoff combination can generate a false failure; for such occasions, other data points must be cited as exceptions to prevent a sign check failure.

Data points for which the sign of the third direction cosine is to change from that of previous data points are itemized in cards 14 through (14 + K), where K is the number of points itemized, in the order that the points appear in the data. The counter code of the data point is also entered as a further check. The number K is entered in the correct location on card 2 of the input.

For the transformation to inertial space, a value for time zero must be selected and input to the program. The inertial space base vectors are indexed so that the X-component of the spin axis coordinates is nominally zero and the Y-component is positive. The selection of time zero is fundamentally one at which it is convenient for the indexing to occur. To reduce the effect of noise, several data points are averaged for the indexing, the points being located symmetrically about time zero. The number of points on each side of time zero to be averaged is entered on card 2.

The span of data points averaged in the time zero indexing should all have the same counter code. This counter code, together with the sign of the third direction cosine of these data points, is entered with time zero on card 9. Because the 7094 computer does not have backspacing capability, the time of the first data point of the series to be averaged must also be entered on card 9 of the 7094 version of SM2200.

In addition to the spin vector case axis components (direction cosines) and inertial space components, the seven-digit data point identification, station time, and counter code are printed on the output. The last column is "SM2200" to identify the program from which the output came.

## Program SM3700 - Inertial Space Manual Edit

Specific events may be deleted from the data of a drift run by the use of this program. It accepts as input the output of Programs SM2200, SM7000, and SM3700. The output of this program is the same as the input, except that the events specified for deletion are absent. Deleted events are recorded on a separate tape for listing. To identify the output, the last two digits in the last column are changed to "37." If the data is an edited version of SM2200, for example, the right hand column reads "SM2237." Single events or blocks of events may be deleted with the use of this program. It may also delete an event when the time interval between it and the last accepted event is less than a quantity specified by the analyst.

## Program SM7000 - Data Simulation

This program simulates SDESG spin vector data for the purposes of checking out the data analysis system programming and evaluating the capabilities of the math model and gyro performance programs under various drift test conditions. A vector differential equation based on the SDESG torque model is solved by an iterative method in case axis coordinates. Spin vector components at specific time intervals are determined from this iteration and, at the option of the analyst, are transformed into pickoff axis coordinates or into inertial space coordinates. By simulating data in pickoff axis coordinates, it is possible to generate an output which can be used as input to Program SM2200 so that the calculations performed in that program may be checked out. Simulations in inertial space coordinates may be used to check out Program SM3700 and the math model and performance programs.

Options available to the analyst include

- Simulation of SM1100 or SM2200 output data
- Superposition of random noise to the data
- Initialization of the simulation with spin vector case axis components, or inertial space components
- Simulation of misaligned pickoffs, if SM1100 output is simulated
- Application of a rotor speed dependency on certain torque coefficients

When random noise is superimposed, the noise level ($1\sigma$) and the number of random numbers to be summed are input. The latter provides a means of altering the randomness from one run to another.

The standard header (set up by SM1100) is simulated in SM7000 also, but with the gyro identification information excluded. Nevertheless, this header information is not required for actual execution of the program. When SM1100 output is simulated, SM7000 calculates and prints out the input angles in the header. This expedites the formation of the SM2200 card input.

The output of SM7000 is identified according to whether SM1100 output or SM2200 output is simulated. For identifying SM1100 simulated output, the identification "SM7011" appears; for SM2200 output, "SM7022" is used.

Program SM4000 - Math Model and Regression

This program is capable of obtaining least squares estimates for any of the 30 torque coefficients, the three alignment error coefficients, and the three initial condition error coefficients that make up the SDMEG math model. Constraints may be imposed on any combination of coefficients after the estimates are obtained; the residual drift is calculated and recorded on magnetic tape which can be processed by the performance program.

The program is divided into four parts

I Calculate drift functions (or variables)

II Form least squares normal equations

III Solve equations for coefficients

IV Calculate residual data

Each part may be run individually, if the data needed by any part is available. The program also contains a subroutine which calculates the eigenvalues and eigenvectors of a matrix. This subroutine can be used to evaluate the condition of the least squares normal equations, even though a solution to the equations may not be available.

In Part I, the value of the drift functions is calculated for each event in the raw inertial space data and is recorded on a binary tape for use in Parts II and IV of the program. Since the math model is a vector model, three scalar functions are calculated for each of the 36 coefficients in the math model, one function for each inertial space coordinate. Under normal conditions, only one pass through this part of the program is necessary.

The least squares normal equations are formed in Part II by summing the required products of the drift functions which are recorded on tape by Part I. If certain standard constraints are to be used in estimating the coefficients, or if any coefficients are to be deleted from the regression, these constraints or deletions may be so specified at this time and utilized to decrease the order of the least squares normal matrices and their corresponding data vectors. (There is one matrix and one data vector for each coordinate axis in inertial space.) The eigenvalues and eigenvectors of the matrices are then calculated and recorded with the matrices and vectors on a tape for listing. The program is designed so that several passes may be made through Part II, in order that a set of equations may be formed for each combination of constraints and deletions that may be desired. A set of matrices and data vectors is recorded on a binary tape for each pass through Part II.

For Part III, a set of equations recorded by Part II is selected for solution. Coefficients may be deleted and constraints may be imposed on the solution by the method of Lagrange multipliers before the equations are solved. Four

sets of estimates may be obtained from the three matrices; three sets are "scalar" sets, each of which minimize the component of error along one of the inertial space coordinate axes, and the fourth set is a "vector" set which minimizes the vector magnitude of the error. A solution is not attempted if the determinant of the matrix is less than some value specified by the analyst. Eigenvalues and eigenvectors of the matrix are also calculated if the determinant or the matrix does not exceed a value specified by the analyst. Sets of matrices may be combined (added together) to improve the condition of the matrix and the quality of the solution. All of the matrices must be on one tape to make the combination; also, only one solution which minimizes the vector magnitude of the error is obtained for the combination.

The residual spin vector data are calculated and are recorded on tape in Part IV, if a solution is available from Part III or if a solution is furnished by card input. The solution which minimizes vector error is used for the residual calculation, if this solution is available and if no other solution is specified by the analyst. The format of the residual output is such that the residual can be processed by the performance program.

Options for the analyst include

- Accounting for the dependency of second harmonic coefficients on rotor speed
- Using rotor speed data or an interpolation table in forming the torque model functions
- Definition of the data interval over which a solution for coefficients is sought
- Whether the matrices that minimize the scalar components of error, the matrix that minimizes the vector error, or both, are to be analyzed with eigenvalues and eigenvectors and/or solved for coefficients
- The choice of solution for calculating residuals

To expedite the formulation of card input for Part I, SM2200 prints out the three alignment rotation angles in the header. These angles are merely copied onto cards 3 to 5 in the order printed in the header. Compensation for speed sensitivity of second-harmonic coefficients is recommended only if the rundown rate is relatively high and if the data indicate a sensitivity of coefficients to rotor speed. The rotor speed table is necessary if erroneous values of rotor speed appear in the data. In principle, if erroneous data points appear as a result of noise, the spin vector components are also in error and the points should be deleted for this reason. Erroneous rotor speed data would occur if the number of revolutions averaged differs from the number input to SM1100 or if it changes during the test. In this event, a rotor speed table should be used.

The option of examining and/or solving matrices that minimize scalar error is referred to as a "multivariate" option, while the error vector minimization option is referred to as a univariate option. The multivariate option was made available but has not been useful because these matrices have been found to be ill-conditioned to a greater degree than the univariate option matrix (which is the sum of the three multivariate option matrices). On the 7094 version, memory size limitations have dictated that the multivariate option be removed. On the H-1800 version, the multivariate option is not available when matrices are combined.

Constraints may be imposed on the solution (in Part III) by a powerful method using Lagrange multipliers. Constraint equations may be written in the generalized form

$$\sum_{j=1}^{n} b_{mj} C_j = g_m$$

To add this constraint to the solution matrix, the subscript j is entered in the "column" portion of Card 4 of Part III, while $b_{mj}$ is entered in the "coefficient" portion. Only nonzero elements are entered. When all the $b_{mj}$'s of a constraint equation have been entered, the program is signaled by entering a zero in the "column" portion of the next card. In the "coefficient" portion of the same card, $g_m$ is entered.

Each constraint equation adds another row and column to the matrix, even though the constraint reduces the degrees of freedom in the solution. Allowance for constraints rapidly expands the array size and can impose serious limitations on the program. For this reason, the standard constraints (which evolve from the fact that the torque vector is orthogonal to the spin vector) are added in Part II by making approximate linear combinations of functions and by reducing the order of the matrix as well as the degrees of freedom. The standard constraints are particularly amenable to this method because the $b_{mj}$'s are independent of the torque model and of the $C_j$'s, because the $b_{mj}$'s are either +1 or -1, and because $g_m$ is always zero.

When residuals are to be calculated, a four-digit identification is input for identifying the output. The last data word of the output is "SM4XXXX," the last four columns being the digits which are input.

## Program SM6100 - Performance

Program SM1100 consists of three subprograms which may be run individually or sequentially. The basic functions of the subprograms are to

- Remove drift which appears to be produced by axial mass unbalance torque from the raw inertial space data

- Perform a nonlinear regression and calculates averages and confidence bounds

- Compare the raw or residual drift with the gyro performance specifications

The mass unbalance compensation is based on an approximate closed form solution to the equations of motion for an axially unbalanced, earth-fixed gyro. Included in the solution is a compensation (to a first approximation) for any change in mass unbalance drift caused by loss of rotor speed. The residual drift is calculated and recorded on a tape for processing by the other subprograms. This subprogram does not estimate the mass unbalance to be removed; the mass unbalance and speed-loss coefficient are furnished to the program by cards. However, the compensation subprogram receives an estimate of mass unbalance from the nonlinear regression subprogram if the regression is performed first on the raw drift data. This estimate is based on that part of drift observed in the data which mass unbalance produces; it cannot distinguish between actual mass unbalance and another source of drift which looks like mass unbalance. Consequently, there is not necessarily a direct correlation of the mass unbalance estimate from this program with that of SM4000.

The nonlinear regression subprogram fits each axis of the input data to the following characterization equation:

$$C = C_1 + C_2 (t_s - t_o) + C_3 (t_3 - t_o)^2 + \sum_{n=1}^{5} \left[ C_{(2n+2)} \sin n\,\omega_c (t_s - t_o) + C_{(2n+3)} \cos n\,\omega_c (t_s - t_o) \right]$$

where $t_o$ and $\omega_c$ are specified by the analyst. Any coefficient on any axis may be deleted from the regression. To reduce the effect of readout noise on the graphs, hourly averages of the data are calculated. Hourly averages of the model (from the characterization equation), the residual, and confidence bounds on the model are also calculated and recorded for listing.

In the performance comparison subprogram, the difference between the magnitude of the actual spin vector drift and the drift permitted by the original performance requirements is calculated and recorded. This comparison can be indexed to several different "starting times" throughout a drift run. The sign of the difference determines whether the drift requirements are satisfied, while the magnitude of the difference determines the margin of satisfaction or nonsatisfaction.

Options available to the analyst include

- The subprograms to operate and the sequence of operation
- Whether or not to compensate for change of mass unbalance drift due to loss of speed
- The choice of mass unbalance torque, the spin vector closure period ($\omega_c$), or the estimate from the nonlinear analysis subprogram for calculating mass unbalance compensation parameters.
- Whether mass unbalance prediction or case axis components are printed on the output of the mass unbalance compensation subprogram
- Selection of drift performance parameters and index times in the performance comparison subprogram
- Whether uncompensated (SM2200, SM3700, or SM7000 output) data or residual (SM4000 or mass unbalance subprogram) data are input to the nonlinear regression and performance comparison subprogram

If an estimate of the mass unbalance is desired from the nonlinear analysis subprogram and the data drift compensated for this estimate, the nonlinear analysis subprogram is executed first on the uncompensated data. Otherwise, the linear analysis subprogram uses residual data as input if they are available.

In the performance comparison subprogram, the vector magnitude of the drift from the specified index time is compared with the performance specification. The characterization equations of the performance specification are tailored to the original requirements of the FGG379A1 SDMEG; the parameters are input by cards to provide flexibility to the analyst.

## Program SMPLOT - Plotting of Data

This program accepts as input the output tapes from Programs SM2200, SM3700, SM4000, and SM6100, and the SM2200 simulated output of SM7000. Program SMPLOT then generates a tape (called the plot tape) containing the necessary information for creating plots of the input data. The portions of data to be plotted are defined by the last four digits of the first and last event number. Provision is made to select the correct set of data on a stacked tape (which can be created by SM4000) by the last four characters of the output identification, the last column appearing on the input data records.

To minimize the tape handling, the data to be plotted are stored as a large array in core. If averages of data points are to be plotted, means of N data points (where N is defined by card input) are stored in core memory. Maxima and minima of all array columns are determined for proper scaling of the plots on the paper.

The program is sufficiently versatile to generate any foreseeable plots. Examples of what may be plotted are

- Raw data $X_{es}$, $Y_{es}$, or $Z_{es}$ versus time
- Residual data $X_r$, $Y_r$, $Z_r$ versus time
- RSS of raw or residual data versus time
- Raw or residual locus plots; i.e., $X_{es}$ versus $Y_{es}$
- Direction cosines $\alpha$, $\beta$, $\gamma$ versus time
- Rotor speed versus time

Parameters in inertial space coordinates are converted to suitable angular dimensions. At the option of the analyst, plots of different components can be stacked against a common time axis (such as $\alpha$, $\beta$, $\gamma$ versus time). Scales are determined from the data; however, maximum sensitivity limits are included to avoid an excessive blow-up of small raw or residual drift.

As many as four data tapes can be mounted and used as input. (Five work tapes can be mounted on the H-1800, but one is reserved for the plot tape.) After the plot tape is prepared, it is mounted on the H200 computer which drives the Calcomp plotter according to the information recorded on the plot tape.

# SECTION VII

# SDMEG MATH MODEL AND DRIFT PERFORMANCE

## INTRODUCTION

A major task of this contract was to evaluate the drift performance of the gyro and to study its drift characteristics. A drift study conducted during the feasibility study program indicated that mass unbalance would be the dominant source of drift for the SDMEG. Early drift tests in this program supported this conclusion; however, these tests also showed that electric torque was a major source of drift which would dominate the drift performance of a gyro with a low mass unbalance, or of a gyro whose suspension operated in the high-g mode to maintain support against high-incident acceleration.

These test results shifted greater emphasis onto the study of the drift torque model and its characteristics. Added to the mass unbalance and second harmonic (ellipsoidal rotor) electric torque model were third and fourth harmonics of rotor shape contribution to electric torque. Recent studies[3] have indicated this to be inadequate; however, this torque model was found to be sufficient to satisfactorily account for the drift observed in individual drift tests conducted on all recently built SDMEG and similar units at Honeywell facilities in Minneapolis.

The prolificity of torque coefficients created by the torque model expansion posed a serious calibration problem. Although care was taken to avoid including linearly dependent sets of terms in the torque model, the least squares normal matrix of equations was not adequately conditioned to provide a complete and reliable set of coefficients from the data of any given drift test. For this reason, a study was conducted with simulated drift test data on how the condition of the matrix may best be improved. Since this study had an important bearing on how test data for the torque model evaluation were collected and reduced, this simulation study is discussed in this section.

Once the data collection and reduction procedure was defined from the simulation study, a series of drift tests was conducted to follow up and check the conclusions of this study with actual test data. The set of coefficients obtained from this follow-up were sufficiently reliable to predict at least 75 percent of the drift observed in those tests of this series not involved in the calibration.

---

3. Research in Electrically Supported Vacuum Gyroscope, Volume II; NASA CR 86123, November 1968.

The tests involved in this follow-up were part of a series of 17 tests conducted for a study of the drift and electric torque characteristics of the FGG379A1 S/N 1 SDMEG. A qualitative discussion of the results of this investigation are included in this section. JPL document GTD 900-165 requires that drift test results and torque coefficients obtained from data be classified. This information is contained in the attachment to this report.

## THE SDMEG MATH MODEL

In the feasibility study program, drift from rotor mass unbalance torque and the electric torque developed on an ellipsoidal rotor was estimated. Two types of electric torque were considered, a primary torque and a secondary torque resulting from rotor miscentering which develops from suspension adjustment uncertainties and rotor sag (acceleration-sensitive displacement). The equation for all of these effects is included in the SDMEG math model. During this program several other electric torque factors were added:

- Electric torque developed on a third harmonic (pear shaped) rotor
- Electric torque developed on a fourth harmonic rotor
- Electrode assembly error effects

Electrode assembly errors do not specifically add terms to the torque model as set up for the math model and regression program (SM4000); instead, it imposed alterations on the size of the coefficients and their sensitivities to the gyro acceleration parameters.

The torque model reads as follows:

$$\vec{L} = L_1 \hat{i}_c + L_2 \hat{j}_c + L_3 \hat{k}_c$$

$$L_1 = C_{10}\beta + C_{11}\gamma + C_{12}\beta\gamma^2 + C_{13}\beta^2\gamma + C_{14}\beta\gamma^3 + C_{15}\beta^3\gamma + C_{16}\beta\gamma + C_{17}(\gamma^2-\beta^2) + C_{18}\alpha\beta + C_{19}\alpha\gamma$$

$$L_2 = C_{20}\gamma + C_{21}\alpha + C_{22}\alpha^2\gamma + C_{23}\alpha\gamma^2 , C_{24}\alpha^3\gamma + C_{25}\alpha\gamma^3 + C_{26}\alpha\gamma + C_{27}\alpha\beta + C_{28}(\alpha^2-\gamma^2) + C_{29}\beta\gamma$$

$$L_3 = C_{30}\alpha + C_{31}\beta + C_{32}\alpha\beta^2 + C_{33}\alpha^2\beta + C_{34}\alpha\beta^3 + C_{35}\alpha^3\beta + C_{36}\alpha\beta + C_{37}\alpha\gamma + C_{38}\beta\gamma + C_{39}(\beta^2-\alpha^2)$$

where

$$C_{10} = (\frac{\mu}{g} - 0.662\ M\ a_3)\ a_z$$

$$C_{11} = -(\frac{\mu}{g} - 0.662\ M\ a_3)\ a_y$$

$$C_{12} = Ma_3\ (0.906\ a_z - 3.75\ \frac{a_o Z_c}{h} + A_6)$$

$$C_{13} = Ma_3\ (0.906\ a_y - 3.75\ \frac{a_o Y_c}{h} + A_7)$$

$$C_{14} = Ma_o\ a_4\ B_1$$

$$C_{15} = Ma_o\ a_4\ B_2$$

$$C_{16} = Mr\epsilon\ (0.69\ \frac{a_y^2 - a_z^2}{a_o} + A_4) + Ma_4\ a_o\ B_4$$

$$C_{17} = Mr\epsilon\ (0.529\ \frac{Y_c a_z + Z_c a_y}{h} + A_1)$$

$$C_{18} = -Mr\epsilon\ (0.529\ \frac{X_c a_z + Z_c a_x}{h} + A_2)$$

$$C_{19} = Mr\epsilon\ (0.529\ \frac{X_c a_y + Y_c a_x}{h} + A_3)$$

$$C_{20} = (\frac{\mu}{g} - 0.662\ Ma_3)\ a_x$$

$$C_{21} = -C_{10}$$

$$C_{22} = Ma_3\ (0.906\ a_x - 3.75\ \frac{a_o X_c}{h} + A_8)$$

$$C_{23} = -C_{12}$$

$$C_{24} = Ma_o\ a_4\ B_3$$

$$C_{25} = -C_{14}$$

$$C_{26} = Mr\epsilon\ (0.69\ \frac{a_z^2 - a_x^2}{a_o} + A_5) + Ma_x\ a_o\ B_5$$

$$C_{27} = C_{17}$$

$$C_{28} = -C_{18}$$

$$C_{29} = -C_{19}$$

$$C_{30} = -C_{11}$$

$$C_{31} = -C_{20}$$

$$C_{32} = -C_{13}$$

$$C_{33} = -C_{22}$$

$$C_{34} = -C_{15}$$

$$C_{35} = -C_{24}$$

$$C_{36} = -(C_{16} + C_{26})$$

$$C_{37} = -C_{17}$$

$$C_{38} = -C_{18}$$

$$C_{39} = C_{19}$$

The symbols used in defining the torque model are

| | |
|---|---|
| $A_1, A_2, \ldots\ldots A_8$ | Unspecified products of electrode error integrals and acceleration parameters. |
| $a_o$ | Gyro acceleration capability. |
| $a_3, a_4$ | Third-and fourth-harmonic perturbations in rotor shape. |
| $a_x, a_y, a_z$ | Components of acceleration along $\hat{i}_c$, $\hat{j}_c$, $\hat{k}_c$ respectively. |

| | |
|---|---|
| $B_1, B_2, \ldots\ldots B_5$ | Unspecified electrode error integrals |
| $C_{10}, C_{11} \ldots\ldots C_{39}$ | Torque coefficients |
| $g$ | Magnitude of gravitational acceleration |
| $h$ | Nominal rotor-electrode gap |
| $\hat{i}_c, \hat{j}_c, \hat{k}_c$ | Case axis coordinate unit vectors |
| $L_1, L_2, L_3$ | Torque components in case axis coordinates |
| $\vec{L}$ | Torque vector |
| $M$ | Rotor mass |
| $r$ | Rotor radius |
| $\hat{S}$ | Spin axis unit vector |
| $\mu = M\ell g$ | Rotor axial unbalance, where $\ell$ is the axial component of the displacement of the center of mass |
| $X_c, Y_c, Z_c$ | Components of rotor displacement in case axis coordinates |
| $\alpha, \beta, \gamma$ | Spin vector components along $\hat{i}_c, \hat{j}_c, \hat{k}_c$, respectively |
| $\epsilon$ | Rotor ellipticity (second harmonic) |

In this definition of the torque model,

$$\vec{L} \cdot \hat{S} = 0$$

i. e., the sources of torque making up the model do not cause the rotor to change speed. This is the direct result of the assumption that the outer rotor shape is a body of revolution about the spin axis. This equation leads to the introduction of standard constraints to the mathematical model (Part II of SM4000). At the option of the analyst, these constraints are introduced at the time that the least squares normal matrix is formed in such a manner so as to reduce the order of the matrix. Table XIV defines the sets of constraints and indicates how the constraints are introduced.

Table XIV. Math Model Constraints

| Set | Sources of Torque | Constraint Equations | How $Q_k^*$ is Reduced | | |
|---|---|---|---|---|---|
| | | | Replace | With | Delete |
| I | Mass Unbalance | $C_{10} + C_{21} = 0$ | $Q_{k10}$ | $Q_{k10} - Q_{k21}$ | $Q_{k21}$ |
| | 3rd Harm. Primary | $C_{11} + C_{30} = 0$ | $Q_{k11}$ | $Q_{k11} - Q_{30}$ | $Q_{k30}$ |
| | 3rd Harm. Translation | $C_{20} + C_{31} = 0$ | $Q_{k20}$ | $Q_{k20} - Q_{k31}$ | $Q_{k31}$ |
| II | 3rd Harmonic | $C_{12} + C_{23} = 0$ | $Q_{k12}$ | $Q_{k12} - Q_{k23}$ | $Q_{k23}$ |
| | Primary Torque | $C_{13} + C_{32} = 0$ | $Q_{k13}$ | $Q_{k13} - Q_{k32}$ | $Q_{k32}$ |
| | Rotor Translation | $C_{22} + C_{33} = 0$ | $Q_{k23}$ | $Q_{k22} - Q_{k33}$ | $Q_{k33}$ |
| III | 4th Harmonic | $C_{14} + C_{25} = 0$ | $Q_{k14}$ | $Q_{k14} - Q_{k25}$ | $Q_{k25}$ |
| | Primary Torque | $C_{15} + C_{34} = 0$ | $Q_{k15}$ | $Q_{k15} - Q_{k34}$ | $Q_{k34}$ |
| | | $C_{24} + C_{35} = 0$ | $Q_{k24}$ | $Q_{k24} - Q_{k35}$ | $Q_{k35}$ |
| IV | Elliptic Rotor: Primary Torque | $C_{16} + C_{26} + C_{36} = 0$ | $Q_{k16}$ | $Q_{k16} - Q_{k36}$ | |
| | Electrode Errors | | $Q_{k26}$ | $Q_{k26} - Q_{k36}$ | $Q_{k36}$ |
| V | Elliptic Rotor: Rotor Translation Electrode Errors | $C_{17} + C_{37} = C_{17} - C_{27} = 0$ | $Q_{i7}$ | $Q_{17} + Q_{27} - Q_{37}$ | $Q_{27}$, $Q_{37}$ |
| VI | | $C_{28} + C_{18} = C_{28} - C_{38} = 0$ | $Q_{k18}$ | $Q_{k18} - Q_{k28} - Q_{k38}$ | $Q_{k28}$, $Q_{k38}$ |
| VII | | $C_{39} + C_{29} = C_{39} - C_{19} = 0$ | $Q_{k19}$ | $Q_{k19} - Q_{k29} + Q_{k39}$ | $Q_{k29}$, $Q_{k39}$ |

* $Q_k$ is the M by 39 matrix of data functions, where M is the number of data points in the regression interval. The least squares normal matrix is $A_k = Q_k{}^t Q_k$.

The first digit of the subscript denotes the axis of the coefficient (1 for x, 2 for y, 3 for z). The second digit denotes the type of coefficient as follows:

0, 1 denotes mass unbalance

2, 3 denotes third-harmonic rotor shape coefficients

| | |
|---|---|
| 4, 5 | denotes fourth-harmonic rotor shape coefficients |
| 6 | denotes primary coefficients, ellipsoidal rotor |
| 7, 8, 9 | denotes translation coefficients, ellipsoidal rotor |

It should be noted that the type of coefficient can be ascertained from the sums of the powers of $\alpha$, $\beta$, $\gamma$. (Mass unbalance is equivalent to the "fundamental" rotor shape distortion.) To facilitate communication of the torque model with the regression matrices in SM4000, the subscript, read as a two-digit number, denotes the column and row to which the coefficient is assigned in the regression matrix; i.e., $C_{15}$ and its associated function are assigned to the fifteenth row and column. The first nine columns and rows do not have torque coefficients assigned to them; instead, they contain the rest of the math model as follows:

$C_1$ is the initial condition error in the $X_{es}$ axis

$C_2$ is the initial condition error in the $Y_{es}$ axis

$C_3$ is the initial condition error in the $Z_{es}$ axis

$C_4$ is the gyro alignment error $\Delta\rho$

$C_5$ is the gyro alignment error $\Delta\sigma$

$C_6$ is the gyro alignment error $\Delta\chi$

$C_7$, $C_8$, and $C_9$ are not assigned

The model and constraint arrangement is such that, when all constraints are used, columns 27 through 39 are deleted from the matrices $(Q_k)$, thus reducing the least squares normal matrix to a 26 x 26 array. In ordinary practice, the coefficients will be constrained or deleted in the formation of $(Q_k)$, but occasionally there may be an exception. The rows vacated by the use of standard constraints are available for any LaGrange Multiplier constraints that may have to be added later. These constraints are now added in columns and rows 27 through 39 when they are available; in this way the memory requirements of the program to handle the arrays do not become excessively large.

## MATH MODEL CALIBRATION STUDY

### Background

The inability to accomplish a complete calibration of the SDMEG torque coefficients from the data of early drift tests demonstrated the need for a

study on how a complete calibration of the math model may be obtained from drift test data. Such a study was conducted in this program. The primary goal was a set of parameters for two drift tests (or more if necessary) which can be conducted in the Minneapolis test laboratory and provide a complete calibration of math model. Secondary goals of the study were to determine the effect of random raise and of math model-torque model noncorrelation on the results of the calibration.

Drift simulations were used for several reasons:

- There is better control over the contents of the test data and the test conditions.
- A priori knowledge of the torque coefficients enables a better assessment of the ability of the regression program to calculate torque coefficients.
- The expenditure of time and funds to produce data for the study is minimized with simulations.
- A computer program which simulates data already existed. The program (SM7000) solves the SDMEG equations of motion and outputs it in a form for input to the other SDESG data reduction programs.

The torque model assumed for generating the simulated data was the same model to which the data was fitted in the regression. Consequently, the nominal results of the study could then be effectively utilized only if the actual gyro torque model correlates with the assumed model. To evaluate the effect of noncorrelation, it was necessary to include in the data some effect not accounted for in the regression. This was accomplished by deleting from the regression nonzero simulation coefficients. The results of the remaining coefficients were then compared with the nominal results.

## Role of Test Parameters

When more than one test is used to calibrate the math model for one set of coefficients, care must be exercised to assure that the coefficients do not change during these tests. In the form that the math model takes in the regression program (SM4000), the coefficients are sensitive to changes in

- Rotor speed
- Gyro temperature
- Acceleration capability
- Direction of laboratory gravity vector

However, variations can be produced in the data without changing the torque coefficients by changes in

- Spin vector locus in inertial space
- Azimuthal orientation of the gyro case housing

By producing variations in the data of two or more tests without changing the coefficients, it was theorized that a sufficiently conditioned least squares normal matrix might be obtained by forming the sum of least squares normal matrices obtained from the data of each test. Such a procedure can be implemented so as not to be contradictory to the theory of the least squares fitting technique. If the combined matrix does become sufficiently conditioned, a complete set of coefficients can be obtained with reasonable confidence bounds for each.

Even within these constraints on the simulations, there remained considerable latitude in the choice of test parameters. They were selected from other considerations:

- The nature of the math model is such that for each test it was desirable that the spin axis become relatively coincident with each case axis within each closure period.
- Since the math model is acceleration sensitive, it was desirable that one case axis be parallel to or anti-parallel to the gravity axis for subsequent gyro model studies.
- The simulations should be sufficiently realistic that their simulated conditions can be duplicated at the Honeywell test facility in Minneapolis.

## Procedure

The following set of test parameters was selected as the best compromise to all of the desired constraints:

- One force axis oriented parallel to the vertical axis for both tests
- The other force axes oriented symmetrically about the north-south vertical plane for each test
- Spin vector locus bounded by two concentric cones whose axes of revolution are parallel to the EPA, one cone passing through the vertical force axis and the other passing through both horizontal force axes

- A rotation about the vertical axis by 180 degrees between tests
- No change of locus between tests

The decision to simulate an azimuthal rotation rather than a change of locus was based on laboratory operations considerations; the spin vector torquing to a new locus disturbs operating conditions more than a case rotation.

The spin vector locus bounding cone which passes through the vertical axis has a vertex angle equal to the colatitude of the test station. The vertex angle of the other can be calculated from the geometry of the right spherical triangle shown in Figure 68.

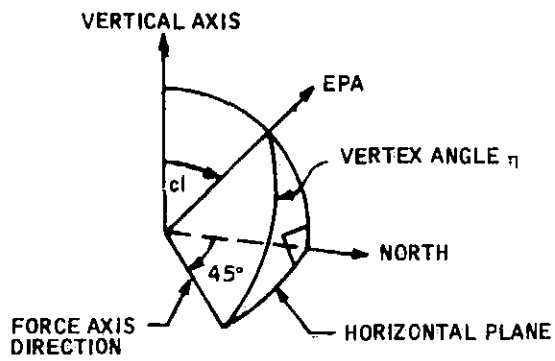


$$\cos \eta = \cos\left(\frac{\pi}{2} - cl\right) \cos\frac{\pi}{4} = \frac{\sin(cl)}{\sqrt{2}}$$

Figure 68. Vertex Angle Geometry

At the Minneapolis test station, the colatitude is nearly 45 degrees; the second vertex angle is , therefore, approximately 60 degrees. The spherical annulus which defines the desired position of the unit spin vector terminus is 15 degrees wide. At the 45-degree locus, the spin vector goes through the vertical force axis and misses the horizontal axes by 15 degrees; at the 60-degree locus, the spin vector goes through both horizontal axes, but misses the vertical axis by 15 degrees. The intermediate loci provide weighted compromises of these extremes.

Four sets of drift simulation runs were prepared, each following the test parameters outlined above. Except for numerical changes in the coefficients and the superposition of random noise, Runs 3 and 4 are identical to Runs 1 and 2. Runs 5 and 6 were prepared with the same coefficients as Runs 1 and 2; the case azimuthal orientation for these were 90 degrees from that of Runs 1 and 2. The fourth set, Runs 7 and 8, differed from Runs 1 and 2 in that the vertex angle of the locus was 45 degrees.

## Simulation Study Results

Least squares normal matrices were formed from the data of Runs 1 and 2. They were solved separately for all coefficients, then combined for another solution of coefficients. The solutions are given in Table XV. The condition of the combined matrix shows a dramatic improvement over that of the separate matrices; this improvement is not only shown in the solution but also in the matrix determinants which is also given in Table XV .

The superposition of random noise in Runs 3 and 4 caused some differences in the solution from their simulated values. Nevertheless, these differences are deemed tolerable; they did not detract from the effectiveness of solving the combined matrix for coefficients.

Several pairwise combinations of matrices from Runs 1, 2, 5, and 6 were solved for coefficients. Whether the azimuthal orientation differed by 90 or 180 degrees seemed to matter very little; the solution of each combination differed from the simulated values by negligible margins.

In evaluating the effects of noncorrelation between the math model and the gyro drift model, the case in which the math model does not contain torque terms which occur in the drift model is of greatest interest. In the case that the math model contains more torque terms than occur in the drift model is of greatest interest. In the case that the math model contains more torque terms than occur in the drift model, a well conditioned matrix will yield zero, or nearly zero, for the "missing" terms. Some coefficients in Runs 3 and 4 were deliberately set to zero to demonstrate this.

Certain coefficients were selected and deleted from the solution of various combinations of matrices from Runs 1, 2, 5, and 6. The combinations selected were such that $\underline{L} \cdot \underline{S}$ remained zero, the reason being that this constraint is likely to apply also to any coefficients missing from the model. The solutions for the remaining coefficients did not agree as well with their simulated values as when all coefficients were solved.

The existence of gyro drift factors not included in the math model can be detected by

- Examining the residual for nonrandom or repeatable error
- Checking the degree to which the model fit the data in the regression interval

The simulation study indicated another method of detecting noncorrelation. This consisted of conducting three or more tests, each differing only in azimuthal orientation, and comparing solutions from the several combinations therefrom. If there is a noncorrelation problem, these solutions would not agree. The results of such a comparison are shown in Table XVI.

Table XV. Comparison of Solutions from Separate and Combined Matrices; Effect of Random Noise

| Source | Coefficient | Simulation | Separate Solutions Run 1 | Separate Solutions Run 2 | Combine 1 and 2 Solution | Combine 1 and 2 Change | Combine Runs 3 and 4 Simulation | Combine Runs 3 and 4 Solution | Combine Runs 3 and 4 Change |
|---|---|---|---|---|---|---|---|---|---|
| Determinant of Matrix | | | $7\times10^{-10}$ | $4\times10^{-11}$ | $5\times10^{17}$ | | | $7\times10^{17}$ | |
| Mass Unbalance | $C_{10}=-C_{21}$ | 0.12500 dem | 0.10562 | -0.03300 | 0.12500 | 0.00000 | -0.09300 | -0.09291 | 0.00009 |
| | $C_{20}=-C_{31}$ | -0.00800 | -0.02155 | 0.10222 | -0.00800 | 0.00000 | 0.01700 | 0.01791 | 0.00091 |
| | $C_{30}=-C_{11}$ | -0.01500 | -0.00149 | -0.12451 | -0.01500 | 0.00000 | -0.02100 | -0.02050 | 0.00050 |
| Third Harmonic | $C_{12}=-C_{23}$ | -0.06500 | -0.06564 | -0.07108 | -0.06498 | 0.00002 | -0.04700 | -0.04937 | -0.00037 |
| | $C_{22}=-C_{33}$ | 0.02000 | 0.02027 | 0.01981 | 0.02000 | 0.00000 | -0.03100 | -0.03116 | -0.00016 |
| | $C_{32}=-C_{13}$ | 0.03000 | 0.03028 | 0.02972 | 0.03000 | 0.00000 | -0.07100 | -0.07089 | 0.00011 |
| Fourth Harmonic | $C_{14}=-C_{25}$ | 0.07000 | 0.07040 | 0.07388 | 0.06997 | -0.00003 | -0.08600 | -0.08261 | 0.00339 |
| | $C_{24}=-C_{35}$ | 0.07500 | 0.07501 | 0.07565 | 0.07501 | 0.00001 | -0.07500 | -0.07378 | 0.00122 |
| | $C_{34}=-C_{15}$ | 0.08000 | 0.08019 | 0.08096 | 0.08000 | 0.00000 | 0.06900 | 0.06664 | -0.00236 |
| Ell. Rotor, Primary | $C_{16}$ | 0.02000 | 0.03462 | 0.14112 | 0.02000 | 0.00000 | -0.01300 | -0.01421 | -0.00121 |
| | $C_{26}$ | 0.02500 | 0.01025 | -0.09477 | 0.02500 | 0.00000 | 0.00000 | 0.00015 | 0.00015 |
| | $C_{36}$ | -0.04500 | -0.01487 | -0.04635 | -0.04500 | 0.00000 | 0.01300 | 0.01406 | 0.00106 |
| Ell. Rotor, Translation | $C_{17}=C_{27}=-C_{37}$ | 0.00300 | 0.02243 | -0.15511 | 0.00300 | 0.00000 | -0.01200 | -0.01220 | -0.00020 |
| | $C_{18}=-C_{28}=-C_{38}$ | -0.00500 | 0.01447 | -0.16414 | -0.00500 | 0.00000 | 0.00000 | -0.00012 | -0.00012 |
| | $C_{19}=-C_{29}=C_{39}$ | -0.00800 | 0.00553 | 0.10225 | -0.00800 | 0.00000 | 0.00200 | 0.00208 | 0.00008 |
| Alignment Errors | $\Delta\phi$ | 0.00 min | 0.00 | 0.00 | 0.00 | 0.00 | 0.50 | 0.97 | 0.47 |
| | $\Delta\gamma$ | 0.00 | -0.02 | 0.02 | 0.00 | 0.00 | 0.30 | -0.07 | -0.37 |
| | $\Delta\psi$ | 0.00 | 0.00 | 0.00 | 0.00 | 0.00 | -0.83 | -0.77 | 0.06 |
| Initial Condition Errors | $\Delta x$ | 0.00 | 0.01 | 0.00 | 0.00 | 0.00 | 1.17 | 0.46 | 0.71 |
| | $\Delta y$ | 0.00 | -0.01 | -0.01 | 0.00 | 0.00 | 0.07 | -0.01 | -0.08 |
| | $\Delta z$ | 0.00 | 0.02 | 0.01 | 0.00 | 0.00 | -0.38 | 0.09 | 0.47 |
| RMS of Change | | | | | | | | | |
| Torque Coefficients (dem) | | | | | | 0.00001 | | | 0.00122 |
| I.C. & Align. Errors (min) | | | | | | 0.00 | | | 0.43 |
| Fit over Reg. Intervals | $\sigma_s$ (min) | | | | | | | 0.92 | |

# Table XVI. Solutions Resulting from Deletion of $C_{14}$ and $C_{25}$

| Source | Coefficient | Simulation | Combine 1 and 2 | | Combine 1 and 6 | | Combine 1, 2, 6 | | Combine 1, 2, 5, 6 | |
|---|---|---|---|---|---|---|---|---|---|---|
| | | | Solution | Change | Solution | Change | Solution | Change | Solution | Change |
| Mass Unbalance | $C_{10}=-C_{21}$ | 0.12500 dcm | 0.12213 | -0.00287 | 0.12177 | -0.00323 | 0.12206 | -0.00294 | 0.12204 | 0.00296 |
| | $C_{20}=-C_{31}$ | -0.00800 | -0.00765 | 0.00035 | -0.00770 | 0.00030 | -0.00791 | 0.00009 | -0.00789 | 0.00011 |
| | $C_{30}=-C_{11}$ | -0.01500 | -0.01512 | -0.00012 | -0.01527 | -0.00027 | -0.01516 | -0.00016 | -0.01519 | -0.00019 |
| Third Harmonic | $C_{12}=-C_{23}$ | -0.06500 | -0.07547 | -0.01047 | -0.00254 | 0.06246 | -0.00171 | 0.06328 | -0.00166 | 0.06334 |
| | $C_{22}=-C_{33}$ | 0.02000 | 0.01985 | -0.00015 | 0.01777 | -0.00223 | 0.01969 | -0.00031 | 0.02031 | 0.00031 |
| | $C_{32}=-C_{13}$ | 0.03000 | 0.03033 | 0.00033 | 0.03052 | 0.00052 | 0.03086 | 0.00086 | 0.03073 | 0.00073 |
| Fourth Harmonic | $C_{14}=-C_{25}$ | 0.07000 | -------- | | -------- | | -------- | | -------- | |
| | $C_{24}=-C_{35}$ | 0.07500 | 0.08124 | 0.00624 | 0.08487 | 0.00987 | 0.08104 | 0.00604 | 0.08030 | 0.00530 |
| | $C_{34}=-C_{15}$ | 0.08000 | 0.08639 | 0.00639 | 0.08073 | 0.00073 | 0.08370 | 0.00370 | 0.08493 | 0.00493 |
| Ell. Rotor, Primary | $C_{16}$ | 0.02000 | 0.02008 | 0.00008 | 0.01910 | -0.00090 | 0.01978 | -0.00022 | 0.02016 | 0.00016 |
| | $C_{26}$ | 0.02500 | 0.02507 | 0.00007 | 0.02273 | -0.00227 | 0.02440 | -0.00060 | 0.02468 | -0.00032 |
| | $C_{36}$ | -0.04500 | -0.04515 | -0.00015 | -0.04182 | 0.00318 | -0.04418 | 0.00082 | -0.04484 | 0.00016 |
| Ell. Rotor, Translation | $C_{17}=C_{27}=-C_{37}$ | 0.00300 | 0.00290 | -0.00010 | 0.00288 | -0.00012 | 0.00300 | 0.00000 | 0.00298 | -0.00002 |
| | $C_{18}=-C_{28}=-C_{38}$ | -0.00500 | -0.00522 | -0.00022 | -0.00447 | 0.00053 | -0.00502 | -0.00002 | -0.00515 | -0.00015 |
| | $C_{19}=-C_{29}=C_{39}$ | -0.00800 | -0.00849 | -0.00049 | -0.00806 | -0.00006 | -0.00801 | -0.00001 | -0.00802 | -0.00002 |
| Alignment Errors | $\Delta\rho$ | 0.00 min | 0.10 | 0.10 | -0.06 | -0.06 | -0.01 | -0.01 | 0.04 | 0.04 |
| | $\Delta\sigma$ | 0.00 | 0.01 | 0.01 | 0.05 | 0.05 | 0.03 | 0.03 | 0.01 | 0.01 |
| | $\Delta\psi$ | 0.00 | 0.01 | 0.01 | -0.02 | -0.02 | 0.02 | 0.02 | 0.01 | 0.01 |
| Initial Condition Errors | $\Delta x$ | 0.00 | 0.00 | 0.00 | 0.06 | 0.06 | 0.09 | 0.09 | 0.05 | 0.05 |
| | $\Delta y$ | 0.00 | -0.04 | -0.04 | -0.04 | -0.04 | 0.00 | 0.00 | -0.02 | -0.02 |
| | $\Delta z$ | 0.00 | 0.07 | 0.07 | 0.06 | 0.06 | -0.02 | -0.02 | 0.02 | 0.02 |
| RMS of Change | | | | | | | | | | |
| Torque Coefficients (dcm) | | | | 0.00376 | | 0.01697 | | 0.01704 | | 0.01705 |
| I.C. & Align. Errors (min) | | | | 0.05 | | 0.05 | | 0.04 | | 0.03 |
| Fit over Reg. Intervals | $\sigma_s$ (min) | 0.00 | 0.27 | 0.27 | 0.27 | 0.27 | 0.28 | 0.28 | 0.28 | 0.28 |

## EVALUATION OF CALIBRATION TECHNIQUE

The simulation study was followed up with a series of six drift tests as soon as a gyro became available for testing. Figure 69 diagrams the case azimuth and spin vector locus for each of these tests. The first four tests, Runs 116 - 119, duplicated the parameters duplicated in Runs 1, 2, 5, and 6. The fifth and sixth tests differed from Run 116 only in spin vector locus. Run 120 had a 60-degree vertex angle but was south, instead of north, of the equatorial plane. Run 121 was conducted strictly for prediction purposes; the spin vector was initialized about 1 degree from the EPA.

Various combinations of matrices from the data of the first five drift tests were solved for coefficients and the solutions were compared. Generally there was good agreement; the greatest variability noted was in the fourth harmonic coefficients. These solutions were also tested by predicting the drift in tests whose data were not used in the solution for those coefficients. For all tests except for the EPA locus test, the prediction error was less than 15 percent of the total drift. For this test the prediction error was 35 percent of the total drift or less.

The set of coefficients which provided the most precise predictions on all of the tests came from the combination of data from Runs 116 and 120, where the difference in test parameters was in spin vector locus. This combination predicted over 90 percent of the drift observed in Runs 117, 118, and 119, and 80 percent of the drift of Run 121. In the case of Runs 117, 118, and 119, the prediction error of these coefficients and the deviation of rotor speed in these runs from that of Runs 116 and 120 were correlated. Whether there was a relationship between these two deviations was not determined.

## TORQUE MODEL EVALUATION PROGRAM

After the mathematical model calibration procedure had been verified with the analytical results of these six tests, 11 more tests were conducted to evaluate

- Sensitivity of the coefficients to suspension preload
- Sensitivity of the coefficients to rotor speed
- The dependence of the torque model to the gravity vector components

The calibration test parameters were patterned after that of Runs 116 and 120, namely to change only the locus and to make no change in azimuthal orientation of the case. Runs 116 and 120 were employed as the control tests for the rotor speed and suspension mode sensitivity tests; they were also used to develop the gyro torque model using acceleration components as variable parameters.

TOP VIEW Z-AXIS IS TOWARD READER FOR EACH ORIENTATION

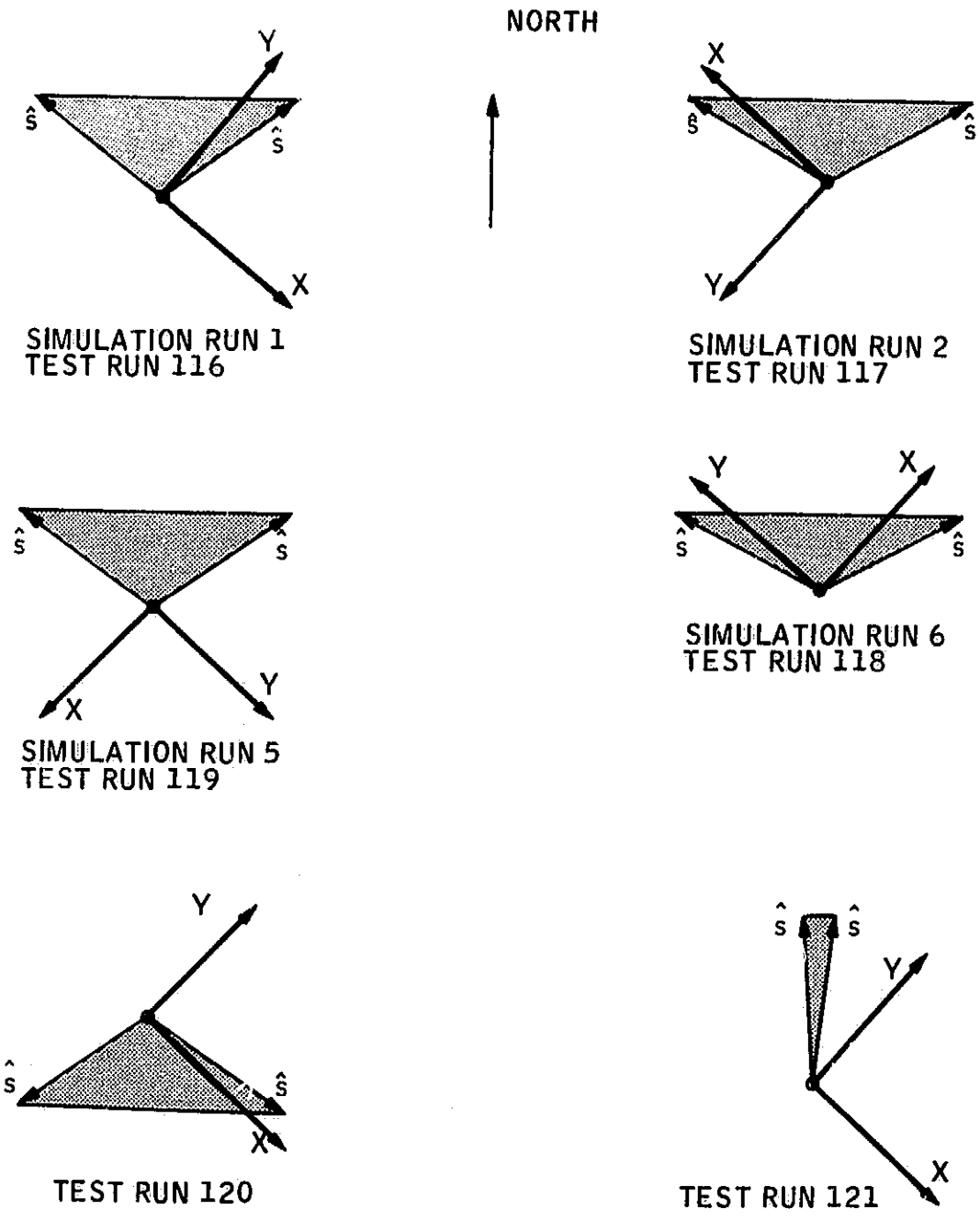


Figure 69. Case Orientations and Spin Vector Loci for Simulation Study and Gyro Follow-up Tests

The parameters of the 13 tests used to study the gyro torque model are summarized in Table XVII.

The sequence of the tests was determined by what was considered more important to learn about the torque model. The gravity vector dependence was considered most important; consequently, the first four tests were conducted with gravity vector - case axis orientations which differed from that for Runs 116 and 120. This was followed by the two tests with the suspension in the high-g mode. The seventh test, Run 128, was conducted with the spin vector locus coincident with the housing split and with the suspension in the low-g mode. There was no second test conducted to combine with this test for a complete solution of coefficients; this test was subsequently used as a prediction test for the gravity vector model. Partial solutions were obtained whose coefficients could be compared with the gravity vector model prediction.

The remaining four tests were not conducted immediately after the conclusion of Run 128. A four-week shutdown period followed Run 128 so that

- The control console and data processing unit could receive regular maintenance
- The data reduction on the tests thus far conducted could proceed

The rotor speed sensitivity tests were then conducted. Another shutdown then followed, during which the reduction of data on the tests conducted thus far was completed.

During the reduction of the gravity vector test data, it became apparent that at least two more tests were needed to enable separation of linear gravity component terms from quadratic terms as well as from constant terms. An anomaly also developed in the solution for coefficients with the Y case axis directed upward. More test data were considered warranted to further investigate this anomaly. To satisfy both needs, the final two tests were conducted with the Y case axis directed nominally downward.

## Suspension Preload Sensitivity

In comparing the torque coefficients obtained from the high-g mode test data with the coefficients of Runs 116 and 120, one must keep in mind that the magnitude of some sources of torque not included in the math model are likely to increase with suspension preload. Consequently, the effect of noncorrelation between the math model and the gyro torque model may also be greater. A modest degradation was noted in the fit of the model to the data; however, this degradation was not as large as one might expect. One could infer, as an example, that the fit would degrade with preload acceleration if the noncorrelation effects are caused by electric torques not included in the math model.

# Table XVII. Summary of Torque Model Evaluation Tests

| Run Number | Date of Start | Length of Test (hr) | Purpose of Test | Test Locus | Susp. Mode | Rotor Speed | | Gravity Components | | | Case Azimuth | | Remarks |
|---|---|---|---|---|---|---|---|---|---|---|---|---|---|
| | | | | | | Start | End | $g_x = \hat{G}\cdot\hat{i}_c$ | $g_y = \hat{G}\cdot\hat{j}_c$ | $g_z = \hat{G}\cdot\hat{k}_c$ | | | |
| 116 | 4-16-68 | 72.10 | Gravity vector along Z axis ($k_c$ Up) | 60°-N | Low g | 199.66 | 198.81 | 0.0 | 0.0 | -1.0 | $\hat{i}_c$ - SE | $\hat{j}_c$ - NE | Simulation follow-up Test 1 |
| 120 | 4-29-68 | 71.20 | | 60°-S | Low g | 199.63 | 198.87 | 0.0 | 0.0 | -1.0 | $\hat{i}_c$ - SE | $\hat{j}_c$ - NE | Simulation follow-up Test 5 |
| 122 | 7-29-68 | 63.45 | Gravity vector along X axis ($i_c$ Up) | 60°-N | Low g | 199.90 | 199.07 | -1.0 | 0.0 | 0.0 | $\hat{j}_c$ - SE | $\hat{k}_c$ - NE | |
| 123 | 8-5-68 | 61.20 | | 60°-S | Low g | 199.80 | 199.10 | -1.0 | 0.0 | 0.0 | $\hat{j}_c$ - SE | $k_c$ - NE | |
| 124 | 8-12-68 | 77.75 | Gravity vector along Y axis ($j_c$ Up) | 60°-N | Low g | 199.86 | 198.91 | 0.0 | -1.0 | 0.0 | $\hat{i}_c$ - SE | $\hat{k}_c$ - SW | Frequency standard malfunction |
| 125 | 8-19-68 | 60.85 | | 60°-S | Low g | 199.89 | 199.11 | 0.0 | -1.0 | 0.0 | $\hat{i}_c$ - SE | $\hat{k}_c$ - SW | |
| 126 | 8-22-68 | 50.45 | Suspension preload sensitivity | 60°-N | High g | 199.90 | 199.29 | 0.0 | 0.0 | -1.0 | $\hat{i}_c$ - SE | $\hat{j}_c$ - NE | Runs 116 and 120 are control tests |
| 127 | 8-25-68 | 55.40 | | 60°-S | High g | 199.87 | 199.28 | 0.0 | 0.0 | -1.0 | $\hat{i}_c$ - SE | $j_c$ - NE | |
| 128 | 8-27-68 | 49.65 | Spin vector locus in plane of housing split | Eq. plane | Low g | 199.93 | 199.32 | 0.11952 | 0.11952 | 0.98562 | $\hat{i}_c$ - SE | $\hat{j}_c$ - SW | Partial calibration prediction |
| 129 | 10-7-68 | 67.10 | Rotor speed sensitivity | 60°-N | Low g | 179.89 | 179.14 | 0.0 | 0.0 | -1.0 | $\hat{i}_c$ - SW | $\hat{j}_c$ - SE | Runs 116 and 120 are control tests |
| 130 | 10-14-68 | 62.35 | | 60°-S | Low g | 179.35 | 178.74 | 0.0 | -1.0 | -1.0 | $\hat{i}_c$ - SW | $\hat{j}_c$ - SE | |
| 131 | 1-14-69 | 51.03 | Gravity vector along Y axis ($j_c$ Down) | 54°-N | Low g | 199.24 | 198.61 | 0.11952 | 0.98562 | -0.11952 | $\hat{i}_c$ - SE | $\hat{k}_c$ - NE | Case axes in spin vector locus |
| 132 | 1-21-69 | 54.95 | | 54°-S | Low g | 199.39 | 198.73 | 0.11952 | 0.98562 | -0.11952 | $\hat{i}_c$ - SE | $\hat{k}_c$ - NE | |

Instead, the results show the degradation to scale more closely with the square root of preload voltage, or the fourth root of preload acceleration.

The analytical results of the high-g mode tests showed the fourth harmonic coefficients to be directly proportional to the preload acceleration. It is worthy to note that only the fourth harmonic coefficients show such a direct sensitivity. The ellipsoidal rotor coefficients showed definite changes which qualitatively support the characterization of these coefficients as given in the theoretical torque model.

An increase was noted in the translation coefficients. In addition to the influence of noncorrelation, such changes can be attributed to the presence of electrode assembly errors and to a change of rotor displacement produced by the change of suspension operating mode. The only likely change of displacement is that attributed to rotor sag, an effect which was rendered negligible by the suspension modification.

To the extent that it could be ascertained from these tests, the mass unbalance and third harmonic coefficients showed no sensitivity to the suspension preload. Earlier tests on another SDMEG assembly showed some third harmonic sensitivity to preload. In view of the uncertainties of solving for coefficients from the data of one test, considerable doubt must be placed on those test results.

## Rotor Speed Sensitivity

The analytical results of the rotor speed sensitivity tests showed significant increases in the ellipsoidal rotor coefficients at the reduced operating speed of 180 rps. All of the other tests in the program were conducted at a speed of just under 200 rps; the Indiron measurements of rotor shape indicated the optimum speed of the rotor to be slightly above 200 rps. The increases noted are, therefore, in agreement with the theory.

No significant changes were noted in the mass unbalance and third harmonic coefficients. The results of earlier tests also show no obvious sensitivity of these coefficients with speed. These observations are also in agreement with theory. Modest changes were noted in the fourth harmonic coefficients. Such changes are not in conflict with the idea that the centrifugal (symmetric) distortion of rotor shape would affect the other even harmonics as well as the second.

## Gravity Vector Test Results

According to the theory, the mass unbalance and third harmonic coefficients are primarily linear functions of the gravity components, while the fourth harmonic and the primary terms of the ellipsoidal rotor coefficients are

quadratic functions of the gravity components. By comparing the coefficients from tests with a case axis upward with those from tests with the same case axis downward, one evaluates to what extent the analytical results from data support the theory. A comparison of the results with the Y axis upward (Runs 124 and 125) with those with the Y axis nominally downward (Runs 131 and 132) tends to support the theory. Exact comparisons cannot be made because in the latter tests the Y axis was not directly downward. Other uncertainties, particularly the solution anomaly noted in Run 124 and 125 and noncorrelation uncertainties, tend to cloud the results of these comparisons. Even so, no behavior directly in conflict with the theory is in evidence.

A deterministic gravity vector model was developed from the results of the four pairs of gravity vector tests. From this model, a set of prediction coefficients was calculated from the gravity components of Run 128. The drift predicted by these coefficients was removed from the data of Run 128. The ratio of residual error to uncompensated error was approximately 25 percent with this prediction.

## Conclusions

Despite some uncertainty which existed in the estimation of torque coefficients in this study, useful insights were gained about the nature of the SDMEG torque model. In general, the sensitivities of the drift predicted by the theory to the gravity vector, rotor speed, and suspension preload were substantiated by the test results. With the model in the form given earlier in this section, a major portion of the FGG379A1 S/N 1 SDMEG drift can be predicted in 1-g acceleration environments or less.

Some uncertainty existed in the estimation for torque coefficients on the FGG379A1 S/N 1 SDMEG. That there is uncertainty is evidenced by a nonrandom error remaining in the data of Run 121 when predicting with various solutions for coefficients from Runs 116 through 120. This error represents 25 percent of the uncompensated drift of Run 121; nevertheless, as long as a nonrandom component remains in a residual, there remains the potential for improving the prediction to remove the nonrandom element.

Further evidence of uncertainty is shown by a similar nonrandom error in the residual of Run 128. Here the residual represents a larger component of the uncompensated drift; however, the gravity vector was an added variable as contrasted with Runs 116 through 121 where its direction remained invariant throughout. Other evidence of uncertainty can be noted when the test data are examined closely. Steps can be detected at points where the readout mode changes, and relatively high-frequency noise in spin vector inertial space data can be observed.

If the direct effect of the sources of uncertainty can be measured in terms of the variability of the torque coefficients, it can then be concluded that the third harmonic coefficients were the most vulnerable to errors. To more accurately

characterize the drift of the gyro tested in this program, it is necessary that greater stability and consistency be achieved in this important set of coefficients.

In view of what was learned from the calibration study with simulations and from observations on the test data, three likely sources of uncertainty emerge. They are

- The existence of a source (or sources) of gyro drift not included in the math model
- Greater than average noise in the output of one of the pickoffs of the gyro tested
- Inaccuracies in the pattern line mechanization coefficients

It is doubtful that the noise by itself produced significant errors in the coefficients, nor can anything be done to reduce the noise for subsequent analyses conducted on the data. The noise had a greater influence in the pattern mechanization coefficients; through this factor the noise played a more significant role in the calibration error.

Further studies of the drift data with an expanded math model would be useful and has the potential of improving the predictability of the gyro drift. Recommendations for further studies are outlined in the next section. A more accurate calibration for the pattern mechanization coefficients should be obtained before such studies are attempted. Greater accuracy would be enhanced in the mechanization by taking steps to reduce the noise level of the y-axis pickoff before taking line calibration data.

In addition to reducing the error of such prediction tests as Runs 121 and 128, it is hoped that continued studies would provide answers to some questions which arose from this gyro torque model study. An important question is represented in the results from analysis of the data of Runs 124 and 125, with the case y axis parallel to the gravity vector. The results for the mass unbalance coefficients differed from the pattern set by all previous gravity vector tests (Runs 116 through 123) in two important respects:

- The direction of the torque vector from this set of coefficients is not perpendicular to the gravity axis. In the other tests, the direction of torque could be constrained in the horizontal plane without degrading the fit.
- That component perpendicular to the gravity axis had a scale factor K, where

$$\vec{L} = K(\vec{g} \times \hat{S})$$

which was significantly different from the results of the other tests.

Runs 131 and 132 were conducted to further investigate this anomaly as well to provide some information on the $g^2$ sensitivity of the coefficients. Analysis of the data from these tests provided results for the mass unbalance coefficients. These data were more consistent with the results of Runs 116 through 123, than with Runs 124 and 125. The scale factor K differed significantly from those of Runs 116 through 123, but not as much as that from Runs 124 and 125.

If one postulates that the mass unbalance coefficients are specified only by rotor mass unbalance and the odd harmonics of rotor shape (no rotor miscentering or housing assembly errors), the torque represented by the six mass unbalance coefficients should then be constrained normal to the gravity vector. All of the test results, except those for Runs 124 and 125, support this postulate.

The anamalous result of Runs 124 and 125 could be caused by rotor miscentering or assembly errors. If either is present, they should also indicate their presence, according to the theory, in the elliptic rotor coefficients. In particular, assembly errors would cause the primary terms to increase with suspension preload. No significant increase was noted in these terms in the results of the high-g suspension mode tests.

Another question which arose in the gyro torque study is the behavior of the fourth harmonic coefficients. A comparison of the high-g mode test results with the others shows that they increased in proportion to the preload acceleration (or the square of the bias voltage). The torque theory predicts that their dependence on preload acceleration should be consistent with the second harmonic primary terms. If a true fourth harmonic in rotor shape is being modeled, they would decrease with increase in suspension preload, unless gross housing assembly errors exist.

The answer to both questions may lie in an expansion of the math model to include terms which produce significant drift in the FGG379A1 S/N 1 SDMEG. One must be selective in choosing the terms to add, lest a prolificity of terms result in a linearly dependent subset of terms for which a unique solution is unattainable. Clues to what sources of torque are significant are available in the analytical results from data of this gyro as well as other strapdown ESG units. The departure of the sensitivity of the fourth harmonic coefficients from that predicted by the theory offers an important clue in that the source of torque is an electric torque sensitive to fields produced by a single electrode or adjacent electrodes, or a sum of fields of an opposite pair. The torque does not appear to be sensitive to the difference of fields of opposite pairs, which characterize odd harmonic primary terms, or the difference of the sums of fields of two opposite pairs, which characterize the even harmonic primary terms.

Localized rotor surface anomalies can produce such a torque; an example of such an anomaly is the rotor pattern. Earlier analytical work has predicted

the presence of electric torque if the patterned area represents a significant anomaly of the surface and if the line of travel of the pattern edge (such as the end of the pattern line) dwells in an inter-electrode gap. For the SDMEG, one can show somewhat heuristically that when this occurs the spin vector orientation is one where the drift predicted by the fourth harmonic model is most significant (i.e., slightly removed from a case axis). This suggests that it would be useful to develop a mathematical model for pattern torque, or take steps to further reduce its effect.

On the other hand, since fourth harmonic seemed to fit this torque relatively well, it appears that other rotor shape harmonics could be added and the combination be used to model the torque. Such a technique appears to have been successful in related strapdown ESG data analysis efforts.[4]

---

[4]Strapdown Electrostatic Gyro Inertial Navigation System Feasibility Development, Technical Report AFAL-TR-68-286, Vol. II, Honeywell Inc., November 1968 Classified Confidential

# SECTION VIII

# CONCLUSIONS AND RECOMMENDATIONS

## SUMMARY OF ACCOMPLISHMENTS IN THE DEVELOPMENT AND EVALUATION PROGRAM

Evaluation tests performed on the FGG379A1 SDMEG units were aimed at determining the capability of the gyro to provide attitude reference information for a spacecraft system. These tests are basically grouped into suspension environment tests, automatic starting tests, and gyro performance tests. The results of these tests are briefly summarized here.

Environment tests determined the capability of the suspension to maintain rotor support under thermal and acceleration environments. The suspension performed well during the static acceleration and simulated vibration tests. The thermal tests indicated that the SDMEG is limited in its operating temperature range; modifications to the suspension subsequent to these tests substantially increased the operating temeprature range.

Automatic starting tests demonstrated the feasibility of starting the gyro after launch into space, even when small case rotations occur during the starting process. There were two variables noted in these tests - rotor direction (also denoted in earlier reports as an "upside-down rotor") and final rotor speed. Both of these variables are considered resolvable items with further development of the SDMEG.

SDMEG performance evaluation tests were originally intended to concentrate on investigating the drift characteristics of the gyro. Some attention was diverted to two important prerequisites to evaluating the SDMEG drift characteristics - readout parameter calibration and test and data reduction procedures for accurately calibrating the math model coefficients. The important goals in each of these areas were accomplished.

Accuracy in the readout parameters was needed to yield reliable results in the evaluation of drift characteristics. While sufficient accuracy was obtained to provide meaningful results, the data indicates that there is potential for further improvement.

The test and data reduction procedures were developed with the aid of computer-simulated data and verified later with SDMEG test data before proceeding with the SDMEG drift test program. A calibration of the math model coefficients was developed from these tests and was found to be capable of predicting from 60 to 90 % of the drift of other tests not involved in the calibration. Generally, the drift behavior of the gyro was found to be consistent with that predicted from the ESG torque theory.

## SDMEG FUTURE DEVELOPMENT

In the test and data reduction procedures study conducted with computer simulations, some attention was focused on the effect that significant gyro torque terms missing from the math model would have on the calibration. Significant deviations were noted in the estimates for some of the coefficients that remained. Some evidence of such deviations was noted later in the drift evaluation program. This suggests that the math model as it now stands is insufficient for complete characterization of the SDMEG drift.

An examination of the results of the drift evaluation program suggests two areas of study to improve the completeness of the math model:

- Inclusion of additional rotor shape harmonics. In-depth analytical studies have already been completed in this area[5]; all that remains is to consolidate the terms in a format that is compatible with calibration from data.

- Pattern torque theory. Relatively little analysis has been conducted on the effects the surface anomaly produced by applying a pattern to the rotor has on gyro drift. There is evidence that more analytical study of these effects is needed.

Once additional terms are included, the existing SDMEG data can be used for calibrating the math model as well as any data collected on a future drift evaluation program.

The attitude reference accuracy requirement of a spacecraft employing the SDMEG is likely to be such that further improvements will be needed in the SDMEG readout system. This was the specific subject of a recent study[6]; consequently, the results of this study can be applied directly to the SDMEG. An intriguing result of this study was how a significant improvement in accuracy can be achieved by modifying the readout strategy to use three pickoffs when available and two only when necessary. (Present strategy is to use the best two when a choice is available.) The patterned region of the rotor is then modified to optimize this strategy. This improvement was projected without any specific improvements elsewhere in the system.

Other suggestions for readout improvement from this study appear to be worthy of further work. An important area for development is in improving the accuracy and contrast of the pattern line edge on the rotor. Some suggestions for improving edge accuracy are:

---

[5] Research in Electrically Supported Vacuum Gyroscope, Volume II NASA CR 86123, November 1968

[6] Research in Electrically Supported Vacuum Gyroscope, Volume IV; NASA CR 86125, November 1968

- Use of laser beam methods in applying the pattern to the rotor.

- Coating or alloying the rotor with another material to improve surface reflectivity contrast between patterned and unpatterned regions.

Improvements in the finished pattern line edge will effect a significant improvement in system accuracy.

In the time that has passed since the design of the readout system, a number of new products and concepts have been developed, particularly in the field of electronics. All aspects of the readout optics and electronics can be examined in the contest of new developments for possible reductions in size, weight, and power consumption. As an example, the 100 MHz counters which are a part of the readout processing electronics must be replaced with spaceworthy versions or discarded in favor of a more suitable type of phase angle measurement apparatus. Other improvements which may be made in the readout system can include:

- Improving the speed and effectiveness of the height insensitive trigger

- Improving the effectiveness of the pickoff shielding

- Examining all circuits and structural design of the components to reduce their susceptibility to spacecraft acceleration and thermal environments

Throughout the test programs there were many opportunities to compare the operating characteristics of the SDMEG with those of other ESG designs. The system of spin and damping coils of the SDMEG was designed to expend minimum energy to accomplish their tasks. It was noted in the automatic starting tests that several hours were required to damp out rotor nutation. In more recent gyro designs the plane of the coils intersects the rotor surface; these designs show greater efficiency in the spin and damp operations. Such a modification would be worthwhile on the SDMEG which would reduce the energy expended to start the gyro as well as the starting time.

The results of the automatic starting tests provided confidence that the SDMEG could be started by an automatic sequencer. The success of these tests was limited in that the rotor was not spunup in the same direction everytime and that the final rotor speed was not the same in every test. Neither of these factors is an insurmountable obstacle for starting the SDMEG under automatic control. One can add a device which monitors rotor speed and cuts off a final spinup cycle when the desired speed is reached.

The SDMEG feasibility study program conducted prior to the development and evaluation program included consideration of the problem of incorrect direction of rotor spin.

A solution to this problem was suggested as a result of that study; i.e., the use of a bidirectional rotor. Another solution is the use of instantaneous rotating fields in the plane normal to the damping coil axis to erect the correct end of a unidirectional rotor into that hemisphere which assures spinup in the desired direction. This concept was successfully implemented in a gimbaled version of the ESG and can in principle be implemented in the SDMEG. Each of these solutions has a significant impact on the rotor pattern design. The bidirectional rotor requires that both edges of a pattern line be accurately applied while the erection method requires that a large area of the rotor surface have a diffuse finish. Any success in the development of new pattern torque study suggested earlier would have an important influence on the choice of solutions. Further study and experimentation may also suggest other solutions to this problem.

Many of the SDMEG design concepts are based on surviving launch environment with the rotor not supported. This choice permits launch with minimum damage to the rotor and housing parts. Other critical gyro components must be capable of surviving launch regardless of whether the rotor is electrically supported during launch. Two specific gyro components are the vacuum pump and the pickoffs. It is recommended that acceleration hardened versions of these components be developed and followed up by acceleration, vibration, and shock tests in a follow-up SDMEG program.

In this evaluation program, thermal tolerance testing was concentrated on the capability of the suspension to operate and to maintain rotor levitation over a range of temperatures and through thermal transients. However, more information is needed on the sensitivity of the pickoff output signals, the pickoff alignment, and the gyro torque coefficients to temperature. Theremal tolerance tests on these parameters are recommended in future work on the SDMEG.

The study of the impact of new products and concepts should not be limited to the readout system. Significant advances in ESG suspension technology have been achieved since the SDMEG suspension was designed, built, and modified. There is potential now for updating and simplifying the SDMEG suspension circuits, thus cutting down on the number of parts which make up the suspension and as a consequence increasing its reliability. Another benefit of such an effort is the reduction of suspension power, an important consideration for a spacecraft system.

## SDMEG FOR FLIGHT TESTS

While this activity in readout accuracy and SDMEG torque model improvement proceeds, preparations can begin for actual flight testing of the SDMEG. Limitations on evaluating the applicability of the SDMEG for space missions on earth are imposed by the earth's gravitational environment. It is believed that this limitation has been nearly reached in this program.

The drift test results have indicated that during flight testing the suspension preload should be reduced to that needed to support the rotor in the space environment. Recent studies have been conducted on the concept of a suspension whose preload varies with the demands of the environment; such a suspension has been developed and tested under Honeywell sponsorship. For the SDMEG flight tests, a suspension of this type is recommended.

Other preparations for flight tests would include designing, building, and testing flight test versions of SDMEG piece parts and components. This would be followed by pre-flight tests on two SDMEG gyros.